Title
Corrosion Performance of Steel and Nickel Alloys in Elevated Temperature Solar Salt

Author
Dong, Andrew Lianghan

Publication Date
2023

Peer reviewed|Thesis/dissertation

Corrosion Performance of Steel and Nickel Alloys in Elevated Temperature Solar Salt

By

Andrew Lianghan Dong

A dissertation submitted in partial satisfaction of the

requirements for the degree of

Doctor of Philosophy

in

Engineering – Nuclear Engineering

in the

Graduate Division

of the

University of California, Berkeley

Committee in charge:

Professor Peter Hosemann, Chair
Professor Raluca O. Scarlat
Professor Thomas M. Devine

Summer 2023

Abstract

Corrosion Performance of Steel and Nickel Alloys in Elevated Temperature Solar Salt

by

Andrew Lianghan Dong

Doctor of Philosophy in Engineering – Nuclear Engineering

University of California, Berkeley

Professor Peter Hosemann, Chair

Nitrate molten salts are widely used in applications requiring high temperature heat transfer and thermal energy storage such as in the chemical and metal industries and in concentrated solar power plants. Recently, several advanced nuclear reactor designs have proposed the use of nitrate salt as an intermediate loop or thermal energy storage system. In doing so, nitrate salt is aimed to be operated at temperatures above the current max operating limits around 570°C. At these elevated temperatures, corrosion rates of materials in molten nitrate salt environments have been observed to markedly increase, owing in large part to the decomposition of the nitrate salt. While significant research has been conducted regarding elevated temperature corrosion of materials in nitrate salt, particularly rare are long-term, elevated temperature corrosion studies which enable more detailed understanding of the interplay between nitrate salt decomposition and material corrosion behavior.

In this dissertation, the corrosion performance of steel and nickel alloys in elevated temperature Solar Salt (60wt% sodium nitrate, 40wt% potassium nitrate) was investigated. Chapter 3 describes the results from a multi-alloy corrosion experiment conducted at 630°C for 600hr. Twelve different materials were investigated, revealing significantly better corrosion performance for alumina-forming austenitic steel and nickel alloys when compared to typical stainless steels such as 316SS. This is followed by a relatively brief Chapter 4 in which 316SS was exposed in Solar Salt for 645hr at elevated temperatures ranging from 570°C-650°C. Through this temperature scoping study, a temperature inflection point was discerned in the rate of increased corrosion of 316SS, hinting at a change in the rate controlling process for corrosion within the salt.

The heart of the dissertation revolves around a long-term corrosion study (Chapter 5) conducted on 316SS and Alloy 601 at a range of elevated temperatures up to 5000hr. Microscopy revealed a complex evolution in corrosion scale morphology exhibited by the materials as a function of both temperature and time. Solar Salt was found to become more corrosive over time to fresh samples, and over-nitriding of the metal surface was readily observed. These and other results were synthesized in a proposed corrosion mechanism for 316SS and 601 in elevated temperature Solar Salt with significant implications for the use of these and other related materials in molten nitrate salt applications.

To everyone along the way,

No matter how big or how small

Table of Contents

List of Figures iv
List of Tables xii
Acknowledgements xiii
Chapter 1 – Introduction 1
1.1. Next Generation Nuclear Reactors 1
1.2. Nitrate Salt 2
1.3. Corrosion 4
1.4. Corrosion in Solar Salt 7
1.5. Nitrate Salt Decomposition and Elevated Temperature Corrosion in Solar Salt 9
Chapter 2 – Dissertation Scope and Research Questions 13
Chapter 3 – Multi-Alloy Corrosion Study 14
3.1. Background 14
3.2. Materials and Methods 14
3.2.1. Materials 14
3.2.2. Corrosion Setup 16
3.2.3. Experiment Set 1 17
3.2.4. Experiment Set 2 19
3.2.5. Post-Corrosion Examination 21
3.3. Results 21
3.3.1. Weight Change Corrosion Rates 21
3.3.2. Corrosion Scale Microscopy 26
3.4. Discussion 46
3.4.1. Comparison of Weight Change vs. Oxide Depth Corrosion Rates 46
3.4.2. Summary of Corrosion Scale Morphologies 47
3.4.3. General Protectiveness of Major Alloying Elements 50
3.5. Conclusion 51
Chapter 4 – Temperature Range Corrosion Study 53
4.1. Background 53
4.2. Materials and Methods 53
4.3. Results 54

4.4. Discussion 56
4.4.1. Arrhenius Analysis on Temperature 56
4.4.2. Refinement of Partially Submerged Corrosion Rates 57
4.5. Conclusion 58
Chapter 5 – Long-Term Corrosion Study 60
5.1. Background 60
5.2. Materials and Methods 63
5.2.1. Materials 63
5.2.2. Corrosion Setup 69
5.2.3. Mid-Experiment Changes 70
5.2.4. Mid-Experiment Temperature Excursions 71
5.2.5. Post Corrosion Examination 72
5.3. Results 73
5.3.1. Weight Change Corrosion Rates 73
5.3.2. Post-Extraction Sample Surfaces 79
5.3.3. Scanning Electron Microscopy 82
5.3.4. Transmission Electron Microscopy 103
5.3.5. Electron Backscatter Diffraction 121
5.3.6. XRD of Corroded Sample Surfaces 122
5.3.7. Nitrate Salt Analysis 124
5.4. Discussion 131
5.4.1. Corrosion Rate Time Dependencies 131
5.4.2. Corrosion Scale Morphology and Evolution 132
5.4.3. Over-Nitriding of the Bulk Material Surface 133
5.4.4. Corrosion Mechanism for 316H and 601 in Elevated Temperature Solar Salt 134
5.5. Conclusion 138
Chapter 6 – Overall Dissertation Conclusion 140
References 143

List of Figures

Figure 1.1: Expected temperature and irradiation dose requirements for in-core structural materials for current and advanced reactor designs.[1] 1
Figure 1.2: Schematic of general energy flow in current (left) and alternative (right) designs of nuclear power systems.[2] 2
Figure 1.3: $NaNO_3$-KNO_3 binary phase diagram with the Solar Salt composition annotated. Adapted from Zhang et al. 2003.[14] 4
Figure 1.4: Standard free energies of formation for metal oxides of common alloying elements in structural materials as a function of temperature and oxygen partial pressure.[15] 5
Figure 1.5: Proposed corrosion mechanism for 316Ti in Solar Salt at 560°C.[34] 8
Figure 1.6: Microstructure of a) a nickel-aluminide coating on P91 steel[30] and b) an iron-aluminide coating on 304SS[39] used in high temperature nitrate salt corrosion experiments. 8
Figure 1.7: Phase stability diagram for the Na-O-N system at 900K (solid) with metal oxide and sodium-metal-oxide stability boundaries for Fe, Cr, and Ni (dotted).[86] 11
Figure 1.8: 3D plot of 316SS corrosion rate data in elevated temperature Solar Salt available from literature (top). Pseudo-2D corrosion rate vs. temperature (a) and corrosion rate vs. time (b) plots obtained from rotating the overall 3D plot. 12
Figure 3.1: Five duplicate corrosion vessels utilized for Solar Salt corrosion experiments. 16
Figure 3.2: Schematic of an individual corrosion vessel used in the corrosion experiments. 17
Figure 3.3: Examples of the coupon dimensions for experiment set 1. Left: 1-inch diameter sample machined from N60 rod. Right: 10cm sample machined from sheet. 18
Figure 3.4: Schematic of a corrosion vessel for experiment set 1 with samples hanging from the vessel head. 19
Figure 3.5: Examples of the coupon dimensions for experiment set 2. Left: 3.5cm medium-sized sample. Right: 2cm small-sized sample. 20
Figure 3.6: Schematic of a corrosion vessel for experiment set 2 with the 60-sample holder used for hanging samples. 20
Figure 3.7: Comparison of weight change corrosion rates of the various alloys exposed to 630°C Solar Salt for 600hr. 22
Figure 3.8: Comparison of weight change corrosion rates of the various alloys exposed to 600°C and 630°C Solar Salt for 600hr. 23
Figure 3.9: Images of samples post-extraction from multi-alloy corrosion experiments. a) From the vessel containing the N60 sample exhibiting 380µm/yr corrosion rate. b) From the vessel containing the N60 sample exhibiting 45.8µm/yr corrosion rate. 25
Figure 3.10: 316SS sample exposed to 0.46wt% Cl^- specification salt at 630°C for 600hr. Both sides showed obvious signs of flaking post-extraction, examples of which are pointed to by red arrows. Patches of white are solidified nitrate salt. 26
Figure 3.11: Alloys corroded in 630°C Solar Salt for 600hr in preparation for microscopy. Top row from left to right: 316SS, 709, Aluminide 316SS, 601, 617, 214, 224, 233, N60. Bottom row from left to right: AFA-OCB, AFA-OCF, AFA-OCL. 27

Figure 3.12: SEM image and EDS elemental maps for 316SS exposed to 630°C Solar Salt for 600hr. 4000x magnification. 31
Figure 3.13: SEM image and EDS elemental maps for Alloy 709 exposed to 630°C Solar Salt for 600hr. 4000x magnification. 32
Figure 3.14: SEM image and EDS elemental maps for N60 exposed to 630°C Solar Salt for 600hr. 1000x magnification. Note that the corrosion scale is significantly larger than that of the other alloys and that the magnification is different. 33
Figure 3.15: SEM image and EDS elemental maps along the metal-oxide boundary for N60 exposed to 630°C Solar Salt for 600hr. 4000x magnification. 34
Figure 3.16: SEM image and EDS elemental maps for AFA-OCB exposed to 630°C Solar Salt for 600hr. 4000x magnification. 35
Figure 3.17: SEM image and EDS elemental maps for AFA-OCF exposed to 630°C Solar Salt for 600hr. 4000x magnification. 36
Figure 3.18: SEM image and EDS elemental maps for AFA-OCL exposed to 630°C Solar Salt for 600hr. 4000x magnification. 37
Figure 3.19: SEM image and EDS elemental maps for Alloy 601 exposed to 630°C Solar Salt for 600hr. 4000x magnification. 38
Figure 3.20: SEM image and EDS elemental maps for Alloy 617 exposed to 630°C Solar Salt for 600hr. 4000x magnification. 39
Figure 3.21: SEM image and EDS elemental maps for Alloy 214 exposed to 630°C Solar Salt for 600hr. 4000x magnification. 40
Figure 3.22: SEM image and EDS elemental maps for Alloy 224 exposed to 630°C Solar Salt for 600hr. 4000x magnification. 41
Figure 3.23: SEM image and EDS elemental maps for Alloy 233 exposed to 630°C Solar Salt for 600hr. 4000x magnification. 42
Figure 3.24: SEM image and EDS elemental maps for aluminide coating exposed to 630°C Solar Salt for 600hr. 4000x magnification. 43
Figure 3.25: SEM image and EDS elemental maps for the meniscus region of Alloy 709 exposed to 630°C Solar Salt for 600hr along with an optical image of the associated area (top left). 4000x magnification. 44
Figure 3.26: Cracking of the aluminide coating observed during microscopy. 45
Figure 3.27: Comparison between corrosion rates obtained via SEM images vs. those obtained via weight change. 46
Figure 3.28: Separation of the oxide layer along the metal-oxide interface observed for the corroded N60 sample. 47
Figure 4.1: Schematic of a corrosion vessel for the temperature range corrosion study with some samples hanging fully submerged within the salt and other samples fully in the gas space. 54
Figure 4.2: Weight change corrosion rates of 316SS in Solar Salt (salt exposed and gas space) vs. temperature. 55

Figure 4.3: Extreme flaking observed from a 316SS sample exposed to 650°C Solar Salt during post-extraction storage..... 56
Figure 4.4: Arrhenius plot of the weight change corrosion rates of 316SS in Solar Salt for 645hr. 600hr datapoints from Chapter 3 are highlighted in blue..... 57
Figure 4.5: Estimated 316SS weight change corrosion rates for partially submerged samples obtained through gas space corrosion correction (dots) compared to previously reported data from Chapter 3 (bars). 58
Figure 5.1: Diagram describing corrosion layer behavior under the Linear, Parabolic, and Logarithmic Laws. 61
Figure 5.2: Schematic of hypothetical corrosion data following Linear, Parabolic, or Logarithmic corrosion time dependencies. X is a parameter such as corrosion thickness, weight gain, or weight loss. 61
Figure 5.3: Corrosion depth vs. time plots of 316SS corrosion in elevated temperature Solar Salt. Datapoints extracted by Dong from literature data in [86,88–90]. 62
Figure 5.4: Examples of the 1.8cm length corrosion coupons used in the long-term corrosion study. From left to right: 316H, 316-REF, 601, WM, AutWeld front, AutWeld back, and aluminide coating. 64
Figure 5.5: EBSD Euler (left) and phase (right) maps obtained for 316H. 1000x magnification. . 65
Figure 5.6: EBSD Euler (left) and phase (right) maps obtained for 316-REF. 1000x magnification. 65
Figure 5.7: EBSD Euler (left) and phase (right) maps obtained for 601. 1000x magnification..... 65
Figure 5.8: EBSD Euler (left) and phase (right) maps obtained for WM. 1000x magnification.... 66
Figure 5.9: EBSD Euler (left) and phase (right) maps obtained for AutWeld. 1000x magnification. 66
Figure 5.10: SEM image and EDS elemental maps of as-received aluminide coating on 316H. 1500x magnification..... 67
Figure 5.11: SEM image and EDS elemental maps of the intermetallic region in as-received aluminide coating on 316H. 2500x magnification. 68
Figure 5.12: Schematic of a corrosion vessel for the long-term corrosion study with the 60-sample holder used for hanging samples. 69
Figure 5.13: Schematic of a corrosion vessel for the long-term corrosion study with the addition of continuously submerged samples in the 620°C, 630°C, and 650°C experiments. 71
Figure 5.14: 1000hr weight change corrosion rates vs. extraction time for the 316-REF samples. 74
Figure 5.15: Weight change corrosion rates of 316H vs. temperature and exposure time..... 75
Figure 5.16: Weight change corrosion rates of 601 vs. temperature and exposure time. 76
Figure 5.17: Weight change corrosion rates of WM vs. temperature and exposure time. 77
Figure 5.18: Weight change corrosion rates of AutWeld vs. temperature and exposure time.. 78
Figure 5.19: Weight change corrosion rates of aluminide coating vs. temperature and exposure time. 79

Figure 5.20: 316H samples post-exposure to Solar Salt. Temperatures from top to bottom: 590°C, 600°C, 620°C, 630°C, 650°C. Exposure times from left to right: 500hr, 1000hr, 2000hr, 3000hr, 4000hr, 5000hr. 80
Figure 5.21: 601 samples post-exposure to Solar Salt. Temperatures from top to bottom: 590°C, 600°C, 620°C, 630°C, 650°C. Exposure times from left to right: 500hr, 1000hr, 2000hr, 3000hr, 4000hr, 5000hr. No 2000hr or 4000hr samples were generated for 620°C and 650°C. 81
Figure 5.22: AL316H samples post-exposure to Solar Salt. Temperatures from top to bottom: 620°C, 650°C. Exposure times from left to right: 1000hr, 2500hr, 4500hr. 82
Figure 5.23: AL316H samples after salt was cleaned off revealing coloration as a function of temperature and time. An unexposed aluminide sample is shown on the left. Temperatures from top to bottom: 620°C, 650°C. Exposure times from left to right: 1000hr, 2500hr, 4500hr. 82
Figure 5.24: Corroded sample exhibiting significant nitrate salt blooming that obstructs microscopy of the corrosion scale. 83
Figure 5.25: Matrix of corrosion scales observed on 316H as a function of temperature and exposure time. 2500x magnification. 86
Figure 5.26: SEM image and EDS elemental maps for 316H exposed to 600°C Solar Salt for 5000hr. 2500x magnification. 87
Figure 5.27: SEM image and EDS elemental maps for 316H exposed to 650°C Solar Salt for 5000hr. 2500x magnification. 88
Figure 5.28: Matrix of corrosion scales observed on 601 as a function of temperature and exposure time. 5000x magnification. 89
Figure 5.29: SEM image and EDS elemental maps for 601 exposed to 600°C Solar Salt for 5000hr. 5000x magnification. 90
Figure 5.30: SEM image and EDS elemental maps for 601 exposed to 650°C Solar Salt for 5000hr. 5000x magnification. 91
Figure 5.31: Matrix of corrosion scales observed on WM as a function of temperature and exposure time. 2500x magnification. 92
Figure 5.32: SEM image and EDS elemental maps for WM exposed to 600°C Solar Salt for 5000hr. 2500x magnification. A piece of completely de-adhered oxide layer can be observed on the right side of the image. 93
Figure 5.33: SEM image and EDS elemental maps for WM exposed to 650°C Solar Salt for 5000hr. 2500x magnification. 94
Figure 5.34: Matrix of corrosion scales observed on AutWeld as a function of temperature and exposure time. 2500x magnification. 95
Figure 5.35: SEM image and EDS elemental maps for a spalled off oxide region of AutWeld exposed to 600°C Solar Salt for 4000hr. 2500x magnification. 96
Figure 5.36: SEM image and EDS elemental maps for a spalled off oxide region of AutWeld exposed to 650°C Solar Salt for 4000hr. 2500x magnification. 97
Figure 5.37: Matrix of corrosion scales observed on 316-REF as a function of temperature and exposure time. 2500x magnification. 98

Figure 5.38: SEM image and EDS elemental maps for 316-REF exposed to 600°C Solar Salt for 4000hr. 2500x magnification. 99
Figure 5.39: SEM image and EDS elemental maps for 316-REF exposed to 650°C Solar Salt for 4000hr. 2500x magnification. 100
Figure 5.40: SEM image and EDS elemental maps for the near surface bulk metal region of 316-REF exposed to 650°C Solar Salt for 4000hr. 10000x magnification. 101
Figure 5.41: SEM image and EDS elemental maps for AL316H exposed to 650°C Solar Salt for 4500hr. 2500x magnification. 102
Figure 5.42: Aluminide coating sample exhibiting significant cracking. 2500x magnification... 103
Figure 5.43: Aluminide coating sample exhibiting surface flaking. 5000x magnification. 103
Figure 5.44: TEM image and EDS elemental maps of the corrosion scale for 316H exposed to 600°C Solar Salt for 5000hr. 5000x magnification. 105
Figure 5.45: TEM image and EDS elemental maps of the bulk surface region for 316H exposed to 600°C Solar Salt for 5000hr revealing the presence of significant Cr (and Mn) denuded regions within the near surface metal. 5000x magnification. 106
Figure 5.46: TEM image and EDS elemental maps of the bulk surface region for 601 exposed to 650°C Solar Salt for 3000hr revealing the presence of significant Cr (and Mn) denuded regions within the near surface metal. 20000x magnification. 107
Figure 5.47: TEM image and EDS elemental maps of the innermost oxide region for 316H exposed to 650°C Solar Salt for 5000hr. 5000x magnification. The red box indicates the region imaged in Figure 5.48. Yellow box indicates the region where the Ni-rich phase diffraction pattern was taken in Figure 5.58. 108
Figure 5.48: TEM image and EDS elemental maps of the bulk surface region for 316H exposed to 650°C Solar Salt for 5000hr indicating the presence of acicular CrN phases. 20000x magnification. 109
Figure 5.49: TEM image and EDS elemental maps of the corrosion scale for 601 exposed to 650°C Solar Salt for 1000hr. 5000x magnification. The red box indicates the region imaged in Figure 5.50. 110
Figure 5.50: TEM image and EDS elemental maps of the bulk surface region for 601 exposed to 650°C Solar Salt for 1000hr indicating the presence of acicular CrN phases. 20000x magnification. 111
Figure 5.51: TEM image and EDS elemental maps of the bulk surface region containing a grain boundary for 316H exposed to 630°C Solar Salt for 5000hr indicating the presence of CrN, Mo, and oxide phases. 20000x magnification. 112
Figure 5.52: TEM image and EDS elemental maps of the bulk surface region for 601 exposed to 600°C Solar Salt for 5000hr indicating the presence of AlN and Al_2O_3 as well as Cr diffusion and Cr_2O_3 formation through bulk volume channels. 20000x magnification. 113
Figure 5.53: TEM image and EDS elemental maps of the intermediate iron oxide region for 316H exposed to 650°C Solar Salt for 5000hr revealing the presence of significant clusters of Ni-rich phases. 5000x magnification. 114

Figure 5.54: TEM image and EDS elemental maps of the bulk surface region for 601 exposed to 650°C Solar Salt for 5000hr detailing the transition from CrN within the bulk metal into Cr_2O_3 in the inner oxide layers. 20000x magnification. 115
Figure 5.55: TEM image and EDS elemental maps of the outermost oxide region for 316H exposed to 650°C Solar Salt for 1000hr and revealing the presence of significant voids and through-thickness cracking within the oxide layer. 5000x magnification. 116
Figure 5.56: TEM image and EDS elemental maps of the corrosion scale for 601 exposed to 630°C Solar Salt for 5000hr revealing the presence of a significant Ni surface phase. 5000x magnification. The red box indicates the region imaged in Figure 5.57. 117
Figure 5.57: TEM image and EDS elemental maps of the Ni surface phase on 601 exposed to 630°C Solar Salt for 5000hr additionally revealing the presence of Mo and Cu phases. 20000x magnification. The Mo EDS map was taken in the region surrounding the green box on the TEM image. 118
Figure 5.58: a) TEM image of inner oxide region of 316H exposed to 650°C Solar Salt for 5000hr. 40000x magnification (higher magnification of same region in Figure 5.47). The red box indicates the area where diffraction pattern b) was taken. b) Ni FCC diffraction pattern from the Ni phase in the oxide layer revealing its metallic nature. [011] zone axis. 119
Figure 5.59: a) TEM image of Ni surface phase on 601 exposed to 630°C Solar Salt for 5000hr (from Figure 5.57). 20000x magnification. The yellow box indicates the area where diffraction pattern b) was taken. b) Ni FCC diffraction pattern from the Ni surface phase revealing its metallic nature. [013] zone axis. 119
Figure 5.60: a) TEM image of Ni surface phase on 601 exposed to 630°C Solar Salt for 5000hr (from Figure 5.57). 20000x magnification. The yellow box indicates the area where diffraction pattern b) was taken. b) Mo BCC diffraction pattern from the Mo phase in the oxide layer revealing its metallic nature. [011] zone axis. 120
Figure 5.61: a) TEM image of Ni surface phase on 601 exposed to 630°C Solar Salt for 5000hr (from Figure 5.57). 20000x magnification. The yellow box indicates the area where diffraction pattern b) was taken. b) Cu FCC diffraction pattern from the Cu phase in the oxide layer revealing its metallic nature. [011] zone axis. 120
Figure 5.62: EBSD Euler (left) and phase (right) maps obtained for 316-REF exposed to 600°C Solar Salt for 1000hr. 2500x magnification. 121
Figure 5.63: EBSD Euler (left) and phase (right) maps obtained for 316-REF exposed to 650°C Solar Salt for 4000hr. 2500x magnification. 122
Figure 5.64: a) TEM image of 316H exposed to 650°C Solar Salt for 3000hr. 5000x magnification. The red box indicates the area where diffraction pattern b) was taken. b) Fe BCC diffraction pattern from the near surface bulk metal region revealing its transformation into ferrite. [-111] zone axis. 122
Figure 5.65: XRD of a 601 sample exposed to 650°C Solar Salt for 5000hr exhibiting $NaFeO_2$ on its surface. 123

Figure 5.66: Solid nitrate salt samples taken from 590°C experiment from left to right: after initial bakeout, 500hr, 1000hr, 1000hr fresh salt bakeout, 2000hr, 3000hr, 4000hr, and 5000hr. 125
Figure 5.67: Solid nitrate salt samples taken from 600°C experiment from left to right: after initial bakeout, 500hr, 1000hr, 1000hr fresh salt bakeout, 2000hr, 3000hr, 4000hr, and 5000hr. 125
Figure 5.68: Solid nitrate salt samples taken from 620°C experiment from left to right: after initial bakeout, 500hr, 1000hr, 1000hr fresh salt bakeout, 2000hr, 3000hr, 4000hr, and 5000hr. 126
Figure 5.69: Solid nitrate salt samples taken from 630°C experiment from left to right: after initial bakeout, 500hr, 1000hr, 1000hr fresh salt bakeout, 2000hr, 3000hr, 4000hr, and 5000hr. 126
Figure 5.70: Solid nitrate salt samples taken from 650°C experiment from left to right: after initial bakeout, 500hr, 1000hr, 1000hr fresh salt bakeout, 2000hr, 3000hr, 4000hr, and 5000hr. 126
Figure 5.71: Aqueous nitrate salt samples taken from 590°C experiment from left to right: after initial bakeout, 500hr, 1000hr, 1000hr fresh salt bakeout, 2000hr, 3000hr, 4000hr, and 5000hr. 127
Figure 5.72: Aqueous nitrate salt samples taken from 600°C experiment from left to right: after initial bakeout, 500hr, 1000hr, 1000hr fresh salt bakeout, 2000hr, 3000hr, 4000hr, and 5000hr. 127
Figure 5.73: Aqueous nitrate salt samples taken from 620°C experiment from left to right: after initial bakeout, 500hr, 1000hr, 1000hr fresh salt bakeout, 2000hr, 3000hr, 4000hr, and 5000hr. 127
Figure 5.74: Aqueous nitrate salt samples taken from 630°C experiment from left to right: after initial bakeout, 500hr, 1000hr, 1000hr fresh salt bakeout, 2000hr, 3000hr, 4000hr, and 5000hr. 128
Figure 5.75: Aqueous nitrate salt samples taken from 650°C experiment from left to right: after initial bakeout, 500hr, 1000hr, 1000hr fresh salt bakeout, 2000hr, 3000hr, 4000hr, and 5000hr. 128
Figure 5.76: Nitrite concentration (rest nitrate) in salt as a function of temperature and time. 129
Figure 5.77: Alkalinity of salt as a function of temperature and time. 130
Figure 5.78: Dissolved chromium in nitrate salt as a function of temperature and time. Resolution limit 5ppm. 130
Figure 5.79: Solar Salt corrosion time dependencies obtained for 316H from 590°C to 650°C. 131
Figure 5.80: Solar Salt corrosion time dependencies obtained for 601 from 590°C to 650°C. .. 132
Figure 5.81: Simplified schematic of the corrosion mechanism for 316SS in high temperature (≲570°C) Solar Salt. 134
Figure 5.82: Schematic of the corrosion mechanism of 316SS in elevated temperature Solar Salt. 136

Figure 5.83: Schematic of the corrosion mechanism of 601 in elevated temperature Solar Salt. 137

List of Tables

Table 3.1: Nominal composition of alloys used during the multi-alloy corrosion study. 15
Table 3.2: Impurity specifications for the nitrate salt used in this study. 18
Table 3.3: Weight change corrosion rates of the various alloys exposed to 630°C Solar Salt for 600hr. 22
Table 3.4: Weight change corrosion rates of the various alloys exposed to 600°C Solar Salt for 600hr. 23
Table 3.5: Summary of corrosion scale morphologies exhibited by materials corroded in 630°C Solar Salt for 600hr. Layers that were observed to separate during microscopy are highlighted in orange. 48
Table 3.6: The alloy compositions along with the weight change corrosion rates obtained for the various alloys. 49
Table 4.1: Weight change corrosion rates of 316SS in Solar Salt (salt exposed and gas space) vs. temperature. 55
Table 5.1: Nominal composition of alloys used during the long-term corrosion study. 64
Table 5.2: Comparison between 316-REF and AutWeld weight change corrosion rates. 78
Table 5.3: Presence of $NaFeO_2$ revealed via XRD on 316H and 601 samples corroded in elevated temperature Solar Salt as a function of temperature and time. 124

Acknowledgements

They say it takes a village, but truly it feels like much more. This journey could not have been possible without the support of so many others including those from the supposedly forgotten past and those from the obvious present:

I would like to thank the University of California, Berkeley for all the memories I've been able to accrue over my total of eight years here. I want to thank the many professors I've learned from for providing me with the knowledge to make an impact in the world. I truly feel well-equipped for whatever lays in front of me.

I would like to thank my advisor Professor Peter Hosemann for being willing to deal with another four years of my antics despite an initial four years of me as an undergraduate. Your guidance has truly shaped my academic journey and solidified my interest in the sciences and engineering. I would similarly like to thank the rest of my dissertation committee, Professor Raluca Scarlat and Professor Thomas Devine, for their expertise and instruction directly relevant to this dissertation research.

I would like to thank Kairos Power, the Nuclear Regulatory Commission, and the National Center for Electron Microscopy for their support throughout my PhD be it through fellowships, access to equipment, and/or expertise.

I would like to thank my research groupmates including but very much not limited to Hi, Jeff, Joey, Evan, Franziska, Sarah, and Rasheed. Along with the many others from the greater nuclear engineering department, you all were such great mentors and peers to look up to and learn from during my studies. Similarly, I would like to thank AJ and Jeff for dealing with my lab shenanigans as well as the other various scientists and scholars in the group who expanded my scientific horizons. To those coming after, I know you all will go on to do great things, and I hope I was helpful to you at least to a fraction of the degree others were for me.

I would like to thank my quarantine buddies for keeping me sane and maintaining a sense of community while the greater community was fractured.

I would like to thank the many many others that came before I started my PhD whose friendship, advice, instruction, and encouragement were crucial during my academic formative years and in developing my eventual pursuits. I particularly want to thank Mr. Morrison whose high school physics classes were the only reason I even considered studying nuclear engineering in the first place.

Finally, I would like to thank my nuclear family, for which I have somehow earned your unwavering support in pursuing this degree.

I can only hope to make you all proud.

Chapter 1 – Introduction

1.1. Next Generation Nuclear Reactors

Next generation nuclear reactors (generally known as Gen IV) are advanced reactor designs envisioned as successors to current nuclear reactors. Since the formation of the Generation IV International Forum (GIF) in 2000, significant efforts globally have been made in maturing advanced reactor designs for commercial development including several national, multinational, and private ventures. Six general reactor concepts were originally highlighted by the GIF: the gas-cooled fast reactor (GFR), the lead-cooled fast reactor (LFR), the molten salt reactor (MSR), the sodium-cooled fast reactor (SFR), the supercritical-water-cooled reactor (SCWR), and the very high-temperature reactor (VHTR). All designs mark a major departure from the typically water-cooled Generation II and III reactors in operation today.

In general, Gen IV reactor designs aim to increase overall plant safety, efficiency, and cost when compared to currently operational reactors. To do so, these reactors envision the use of novel passive safety systems, fuel designs, coolant chemistries, and operating conditions among many other varied changes. Materials to be employed in these reactors will therefore be subjected to different and likely more extreme environments such as increased temperature and irradiation dose (Figure 1.1). As a result, significant research is required to both develop and ensure materials exist that can withstand these anticipated harsh environments.

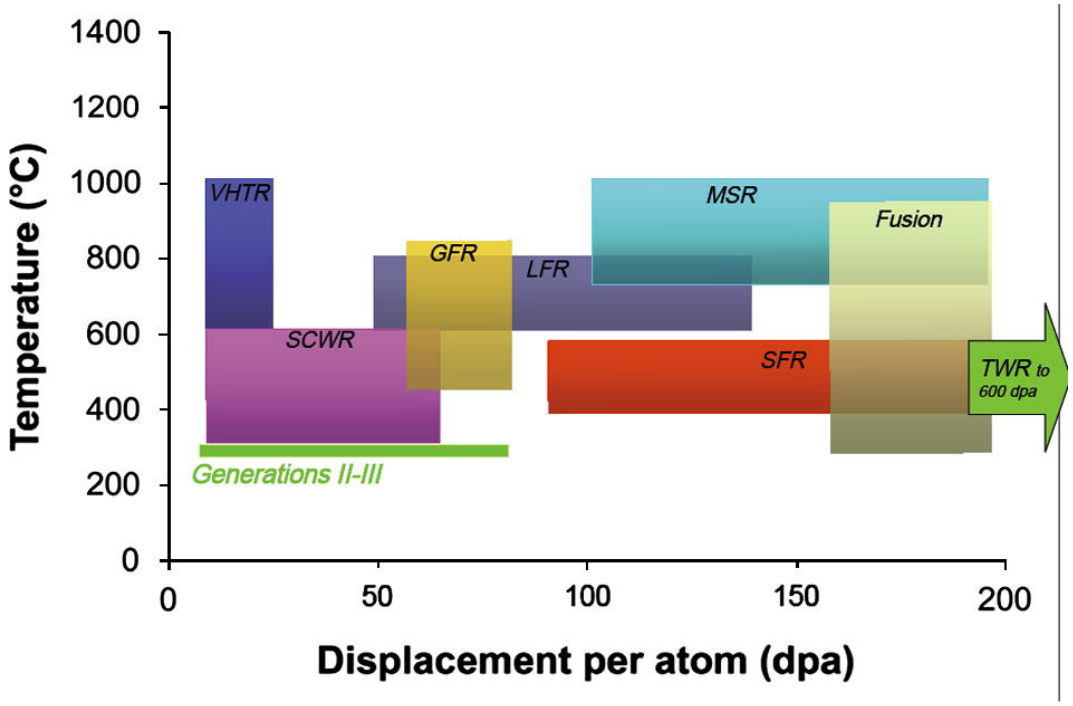

Figure 1.1: Expected temperature and irradiation dose requirements for in-core structural materials for current and advanced reactor designs.[1]

A major update in the design paradigm for advanced nuclear reactors has been the inclusion of a heat storage system (or in general an intermediate loop) separating the nuclear reactor from the power generation block as described in Figure 1.2.[2,3] A dedicated heat storage

system increases overall plant economics by enabling greater flexibility in nuclear cogeneration of electricity and heat as well as by providing dispatchable electricity in a market with increasing variable electricity generation. Regardless of the inclusion of a dedicated heat storage system, the presence of an intermediate loop alone enables significant decoupling of the nuclear reactor block from the power generation system. As a result, the power block of a nuclear power plant can potentially be built to more normal industry standards, reducing costs and making use of efficiency gains in the greater power generation industry. Finally, the thermal mass provided by the intermediate loop acts as an additional thermal buffer during plant operation, and the intermediate loop itself can also be employed as a barrier to radionuclide release.

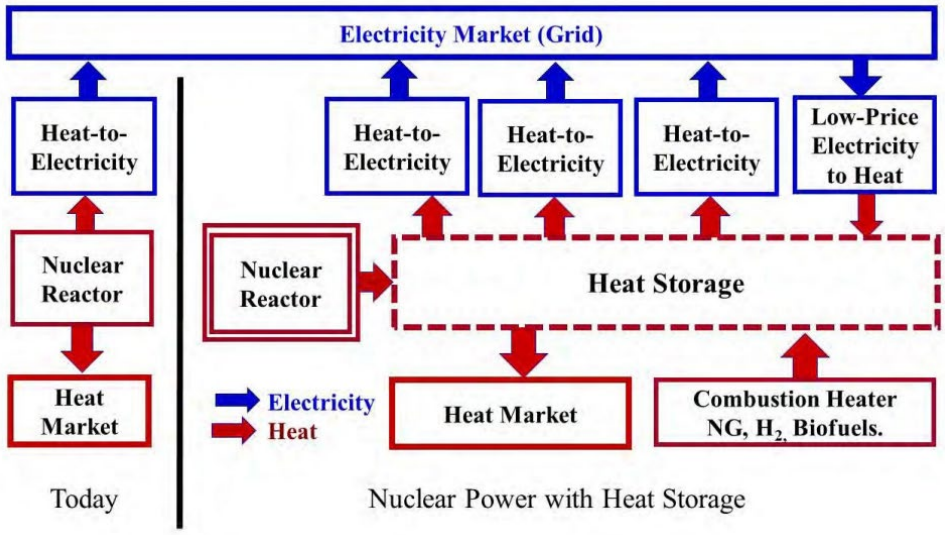

Figure 1.2: Schematic of general energy flow in current (left) and alternative (right) designs of nuclear power systems.[2]

Molten salts (the namesake for molten salt reactors) are generally considered for these intermediate loops and other thermal energy storage systems due to their high volumetric heat capacity, heat transfer properties, thermal stability, high boiling point, and large temperature operating ranges. Many variants and their properties are summarized in Caraballo et al. 2021.[4] There are a wide range of different molten salt chemistries being explored including those that are carbonate-, chloride-, fluoride-, and nitrate-based. As an example, molten salt reactor designs typically employ fluoride-based salts in the nuclear reactor due to chemistry and neutronics considerations.[5,6] Several advanced reactor designs including sodium fast reactors, molten salt reactors (solid and dissolved fuel variants), high temperature gas reactors, and fusion machines propose the use of nitrate salts as an intermediate loop and/or heat storage system.[7–10]

1.2. Nitrate Salt

Nitrate salts (NO_3^-) such as $NaNO_3$, KNO_3, and HITEC (53wt% KNO_3, 40wt% $NaNO_2$, and 7wt% $NaNO_3$) have been used for many decades as a high-temperature heat transfer medium in the chemical and metal industries.[11,12] In more recent decades, nitrate salts have been used in the concentrated solar power industry as the heat storage medium in central receiving towers. The specific salt composition used in this application is a mixture of 60wt% $NaNO_3$ and 40wt%

KNO_3 (now known as "Solar Salt"). In addition to the desirable high temperature and heat transfer properties common across many molten salts, nitrate salts have particular advantages in that they are nonflammable, nontoxic at low temperatures (it is commonly used as a preservative in foodstuffs), and extremely soluble in water. This has significant benefits in safety and handling of these salts when compared to other molten salt compositions. Given its extensive use in the chemical, metal, and now concentrated solar industries, nitrate salt is also relatively economical.

As mentioned in Section 1.1., nitrate salt (and specifically Solar Salt in some instances) is now being considered for use in intermediate loops and heat storage systems in advanced nuclear reactor designs. In these nuclear applications, the nitrate salt system can act as a barrier to radionuclide transfer through inhibiting diffusion, collecting species, or simply acting as another layer before the power generation loop. For example, transfer of tritium (^3H or T) generated in the nuclear reactor can be inhibited by the nitrate salt system in the following ways:[13]

1. Through the formation of oxide layers on materials in contact with the nitrate salt that hinder tritium diffusion.
2. Through the conversion of tritium (which would diffuse to the nitrate salt intermediate system as tritiated hydrogen gas, T_2) into tritiated water (T_2O, which has reduced diffusion rates):
   a) $NaNO_3 + T_2 \rightarrow NaNO_2 + T_2O$
   b) $T_2 + \frac{1}{2}O_2^* \rightarrow T_2O$
   *From $NaNO_3 \leftrightarrow NaNO_2 + \frac{1}{2}O_2$ as will be described in Section 1.5.
3. Through stripping tritiated water from the nitrate salt loop (which is preferable compared to tritium reaching the power generation loop).

For the rest of the dissertation, discussion about nitrate salt will be primarily focused on the Solar Salt composition, though details are relevant to nitrate salts in general. It is of note that the Solar Salt mixture (60wt% $NaNO_3$ and 40wt% KNO_3) is off the eutectic composition (44wt% $NaNO_3$ and 56wt% KNO_3) for binary sodium nitrate and potassium nitrate. Figure 1.3 shows the $NaNO_3$-KNO_3 binary phase diagram with the Solar Salt composition annotated. This off-eutectic composition results in Solar Salt having a melting point of around 238°C vs. 222°C for the eutectic mixture. This trade in roughly 20°C in melting temperature is made in favor of increased economics from utilizing more sodium nitrate which is less expensive than potassium nitrate. While lower melting point molten salts add buffer to potential freeze excursions during operation, Solar Salt already has a very low melting point relative to other molten salts and it is less of an issue for advanced nuclear reactor designs that would be operating well in excess of 300°C. As will be discussed in later sections, issues surrounding the use of nitrate salt in nuclear and other applications predominantly stem from its upper operating temperature limit.

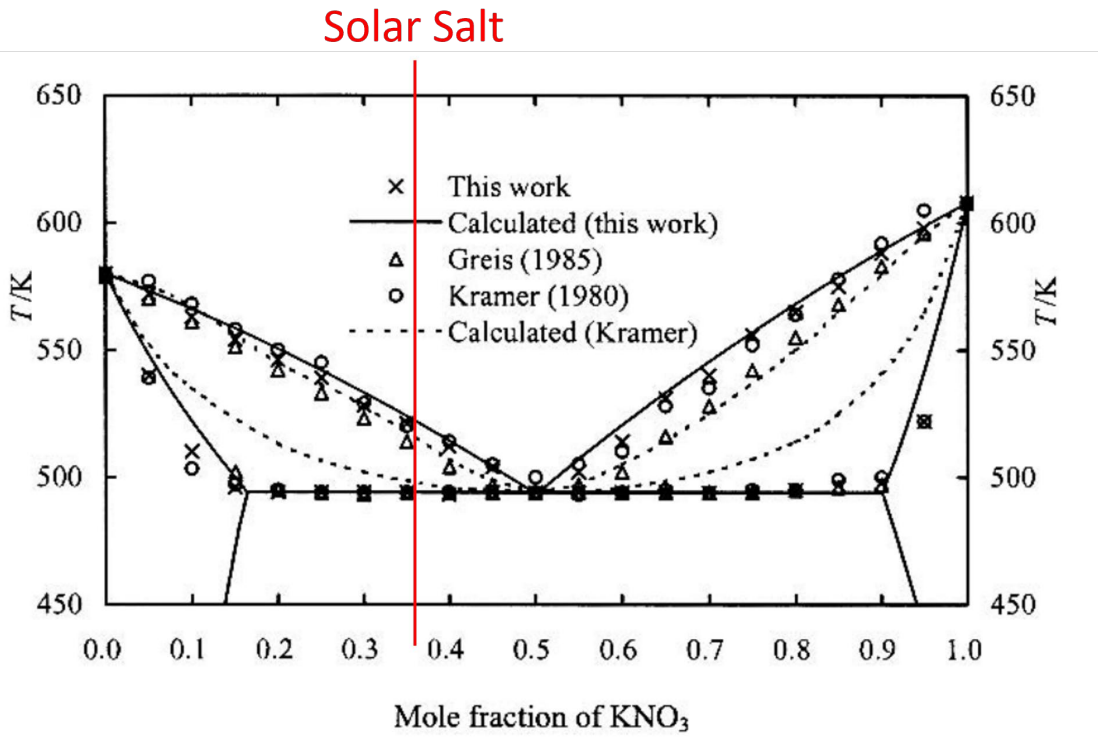

Figure 1.3: $NaNO_3$-KNO_3 binary phase diagram with the Solar Salt composition annotated. Adapted from Zhang et al. 2003.[14]

1.3. Corrosion

Corrosion is a general term that describes the degradation of material through reaction with their environment. As a material corrodes, its strength and other properties can be severely compromised, making corrosion one of the main issues surrounding the long-term performance of components. A way to investigate the cause of corrosion is through understanding the thermodynamics surrounding corrosion reactions. Figure 1.4 shows the standard free energies of formation for oxides of many common structural material alloying elements. Negative free energies mean that it is energetically favorable for oxygen to react with metals to form metal oxides. In other words, there is a thermodynamic driving force for alloy corrosion in environments that contain sufficient oxygen. Understanding the potential reactions and associated thermodynamics surrounding an application environment can guide strategies to control the rate of corrosion in components.

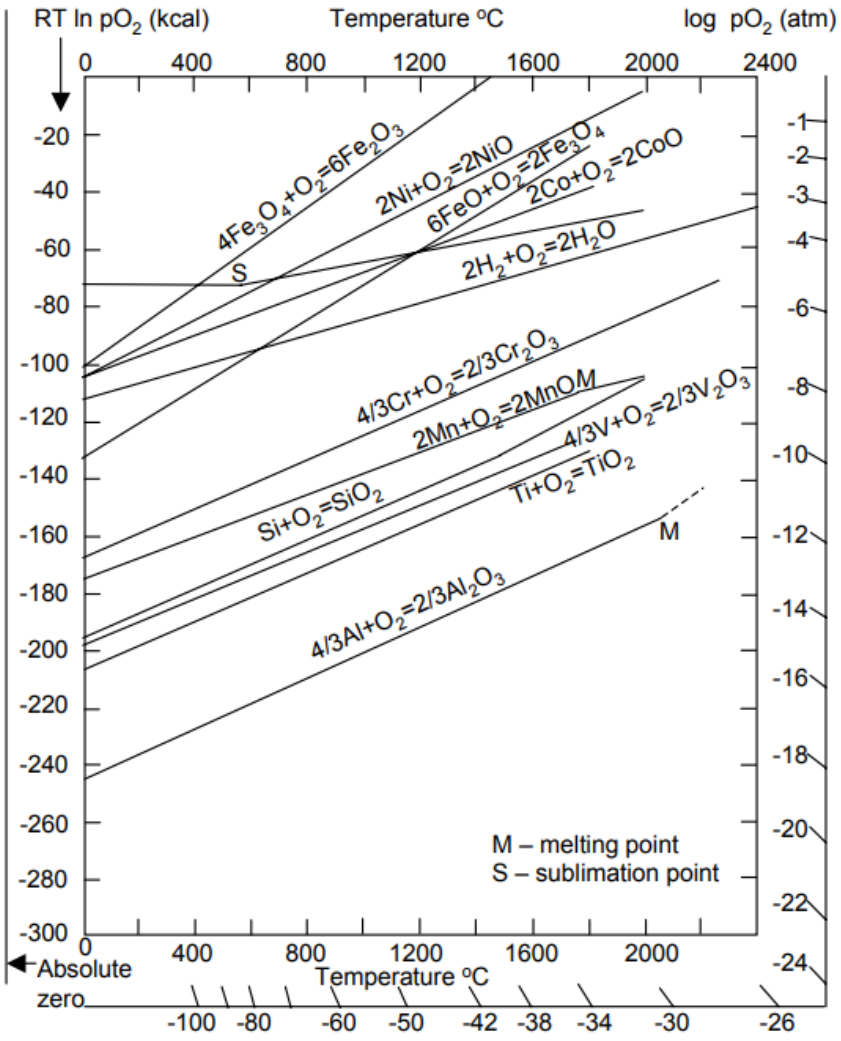

Figure 1.4: Standard free energies of formation for metal oxides of common alloying elements in structural materials as a function of temperature and oxygen partial pressure.[15]

However, while thermodynamics can explain why corrosion may be expected, the extent of corrosion is dictated by the kinetics of the various corrosion reactions that may occur. In oxidizing environments, the corrosion resistance of materials generally depends on the protectiveness of the oxide layers that form on the surface, or more precisely, the materials' ability to form a passivation layer. In order to passivate, a corrosion layer needs to be both stable and nonporous to prevent further penetration of the corrosive medium and diffusion of alloying elements. For example, iron oxides (Fe_2O_3 and Fe_3O_4) form arrangements in environments that are chemically stable but often porous. Porous oxide layers tend to de-adhere or spall off, further exposing the base material underneath and thus are not totally protective. As a result, cast iron and low alloy steels can readily be observed to rust significantly when exposed to air and aqueous environments. Instead of relying on iron oxides, stainless steels are alloyed with a significant amount of chromium to utilize chromia (Cr_2O_3) as a passivating corrosion layer in oxidizing environments. The lower limit in Cr concentration in stainless steel to make it "stainless" is around 12% and can be described via percolation theory.[16] In forming a passivating layer (which

can be nanometers thin[17]), further corrosion is reduced through limiting aspects such as chemical kinetics, mass transfer, and charge transfer for corrosion reactions.

Many different corrosion mechanisms exist and can have significant influence on the corrosion of materials for a given application, a few of which are described here:

Impurity driven corrosion describes the heavy impact that impurities such as moisture, gas species, and certain elements can have within an operating environment. These impurities act as additional reactants that can open additional reaction pathways to react with the material and/or disrupt the ability of a material to form a passivating layer.[18–20] While impurities may be consumed in the process (thus limiting the total extent of corrosion caused by their presence), impurities can often be introduced into the environment through many avenues such as leaks, maintenance, or even normal operation. For molten salts such as the chloride and fluoride salts considered for use as coolants in advanced nuclear reactors, impurities are expected to dominate corrosion of structural alloys rather than the pure salt constituents.[21,22]

Thermal gradient driven corrosion is a phenomenon that can occur in thermal energy systems due to mass transport between regions of different temperature. For example, in molten salt loops, molten salt will flow from a hot leg that has stored the thermal energy generated from a source (like nuclear fuel) and transfer heat to a power generator to form a cold leg. Temperature differentials between the hot and cold leg can be several hundred degrees Celsius in magnitude for power generation systems. In addition to the thermal stresses and different corrosion environments this imposes, solubility limits of species in the heat transfer medium can be heavily altered by the differences in temperature. If solubility limits of a corroded species within a loop are reached (such as through long-term operation), deposition of material can preferentially occur in one region of the loop which then enables further corrosion in another region.[23] Not only does this enable the possibility of continual corrosion within the loop, buildup of deposited material can severely impact the flow and overall function of the loop.

Galvanic corrosion is a mechanism that highlights the electrochemical aspect of corrosion and occurs when differing metals are put in contact within an electrolyte such that electrical flow can occur. The differing electrode potentials between the different metals results in the formation of an electrochemical cell in which the more reactive metal acts as an anode and the more noble metal as a cathode. The electropotential difference causes a driving force that accelerates corrosion on the anode metal while protecting the cathode. Due to this, corrosion of a component can occur more rapidly than usual if for instance it is inadvertently put in intimate contact with a more noble material. Knowledge of this phenomenon, however, is also the basis of corrosion protection strategies such as sacrificial zinc anodes on steel ships and cathodic protection of underground piping.

In summary, corrosion depends heavily on both the material in question and the overall environment. Detailed understanding of the various variables affecting corrosion performance is necessary to select suitable materials for a given application.

1.4. Corrosion in Solar Salt

Nitrate salt is an oxidizing corrosion environment resulting in the formation of metal oxide corrosion layers for metallic materials. Contrary to many other oxidizing environments, chromia does not act as a passivating corrosion layer in nitrate salts. This is due to the formation of chromate species from chromium metal and chromium oxide that are highly soluble in nitrate salt:[24,25]

- Chromium Oxide Reaction: $Cr_2O_3 + 5NO_3^- \rightarrow 2CrO_4^{2-} + NO_2^- + 4NO_2$
- Chromium Metal Reaction (two-step):
    1) $2Cr + 7NO_3^- \rightarrow Cr_2O_7^{2-} + 5NO_2^- + 2NO_2$
    2) $Cr_2O_7^{2-} + 2NO_2^- \rightarrow 2CrO_4^{2-} + NO_2 + NO$

Molybdenum, manganese, and tungsten are also known to form similar soluble species.[26–28] In contrast, iron and nickel do not form soluble species[29] and thus iron oxides and nickel form the primary corrosion layers for steel and nickel alloys in nitrate salt with differing degrees of protectiveness.

Owing to extensive development for use in concentrated solar power, significant literature exists regarding the corrosion of metals in Solar Salt up to temperatures around 570°C (the maximum operating temperature for central receiving towers in concentrated solar power plants). These include corrosion studies on a wide variety of steel and nickel alloys with nickel alloys generally performing better than steel alloys.[30–57] 316SS is the alloy used in concentrated solar power central receivers using Solar Salt[58] and is also the alloy most investigated in Solar Salt corrosion studies.

Figure 1.5 shows the proposed corrosion mechanism for 316Ti (a Ti-doped variant of 316SS) in 560°C Solar Salt. In general, the corrosion oxide layer arrangement is as follows: an outermost Fe_2O_3 layer followed by, in order, a Fe_3O_4 layer, a $FeCr_2O_4$ spinel layer, and a Cr_2O_3 before the bulk metal. As noted earlier, Cr_2O_3 is extremely soluble within nitrate salt, so the formation of the Cr_2O_3 layer is only stable if a sufficiently protective layer of iron oxides is present on top. Also noted in the mechanism is the impact of the gas space atmosphere on potential reactions relevant to corrosion and this will be discussed in Section 1.5. Finally, the presence of Cl^- impurities within the salt are shown which can induce additional corrosion through hindering the adherence of the oxide layers on the metal surface.[34,59,60]

A subclass of steel and nickel alloys known as alumina-forming alloys (AFA, or alumina-forming austenitic alloys for steel variants) have also been investigated for use in Solar Salt.[49,55,61–63] As their name suggests, these alloys incorporate significant concentrations of aluminum as an alloying element to take advantage of the formation of highly protective alumina (Al_2O_3). Alumina is chemically stable in nitrate salt and is often used as the crucible material for nitrate salt experiments. AFA alloys are being developed due to their potential for superior high-temperature corrosion resistance in oxidizing environments compared to alloys typically relying on a chromia-based protective surface oxide.[64–67] Given that chromia is not a reliable passivating layer in nitrate salt environments, AFA alloys are potentially an attractive option for high temperature nitrate salt applications.

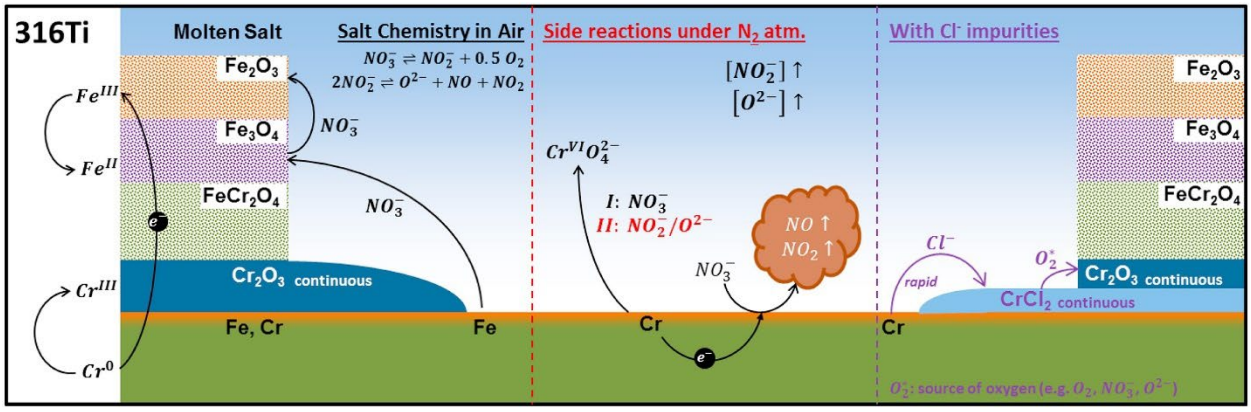

Figure 1.5: Proposed corrosion mechanism for 316Ti in Solar Salt at 560°C.[34]

Beyond tailoring bulk material compositions for corrosion performance, coatings on material surfaces are another method for protecting materials from corrosion. One such coating of interest to nitrate salt applications is aluminide which can be produced through a variety of methods including pulsed electron beam (GESA), selective laser melting (SLM), laser metal deposition (LMD), and pack cementation techniques. These methods incorporate aluminum into/onto the metal surface to form an aluminum intermetallic (M_xAl_y, where M is another metal element) as the outer layer. Using pack cementation as an example, depending on the temperature and duration of this aluminizing treatment, the specific microstructure, intermetallic phases, and coating thickness can be altered.[68] Early aluminide coatings on steel alloys were investigated in molten nitrate salt by Carling et al. 1983[69] and revealed markedly better corrosion performance when compared to uncoated samples. More recently, iron-aluminide and nickel-aluminide coatings on steel (examples of these are provided in Figure 1.6) have similarly shown significant improvement in corrosion resistance in high temperature nitrate salt.

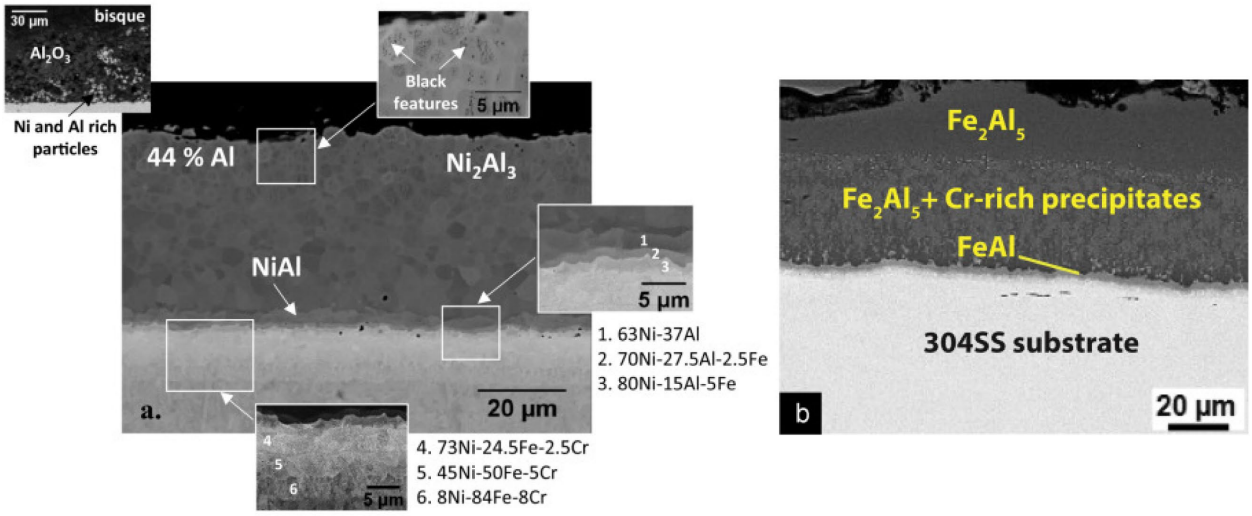

Figure 1.6: Microstructure of a) a nickel-aluminide coating on P91 steel[30] *and b) an iron-aluminide coating on 304SS*[39] *used in high temperature nitrate salt corrosion experiments.*

1.5. Nitrate Salt Decomposition and Elevated Temperature Corrosion in Solar Salt

In using nitrate salt for intermediate loop and/or heat storage systems, the operating temperatures slated will be significantly higher than that of current commercial applications. Similar to advanced nuclear reactor designs, the concentrated solar industry is also aiming for higher temperatures in order to utilize the supercritical carbon dioxide Brayton cycle at temperatures >600°C (compared to the steam-Rankine cycle currently utilized by molten-salt power towers operating at max temperatures around 570°C).[70] The main factor preventing the operation of Solar Salt at higher temperatures has been the significantly increased corrosion rates of materials observed.

At elevated temperatures, nitrate (NO_3^-) salt is known to undergo decomposition into nitrite (NO_2^-) via Equation 1.1. The nitrite can then undergo a second order decomposition resulting in the formation of oxide species (Equations 1.2-1.4). Still other decomposition reactions can occur accounting for peroxides (O_2^{2-}) and superoxides (O_2^-) (Equations 1.5-1.9). Determining dominant reactions, intermediate reactions, and equilibrium concentrations of these various specifics is complex,[33,71–77] though it is widely believed that the formation of these oxygen species is attributable to the increased corrosion rates observed in elevated temperature nitrate salt. These decomposition reactions become significant starting at temperatures ≥570°C, hence the current maximum operating temperature for Solar Salt.

$$NO_3^- \rightleftharpoons NO_2^- + \frac{1}{2}O_2 \quad (1.1)$$

$$2NO_2^- \rightleftharpoons O^{2-} + 2NO + \frac{1}{2}O_2 \quad (1.2)$$

$$2NO_2^- \rightleftharpoons O^{2-} + NO + NO_2 \quad (1.3)$$

$$2NO_2^- \rightleftharpoons O^{2-} + N_2 + \frac{3}{2}O_2 \quad (1.4)$$

$$O^{2-} + NO_3^- \rightleftharpoons NO_2^- + O_2^{2-} \quad (1.5)$$

$$O_2^{2-} + 2NO_3^- \rightleftharpoons 2NO_2^- + 2O_2^- \quad (1.6)$$

$$2NO_2^- \rightleftharpoons 2O_2^- + N_2 \quad (1.7)$$

$$2O_2^- \rightleftharpoons O_2^{2-} + O_2 \quad (1.8)$$

$$2O_2^{2-} \rightleftharpoons 2O^{2-} + O_2 \quad (1.9)$$

Given the presence of several gaseous species among the various decomposition reactions, it becomes evident that the gas space above molten nitrate salt can have a significant impact on its decomposition and thus corrosivity. A N_2 environment (when compared to synthetic air) has been shown to increase corrosion and promote the formation of significantly more Fe_2O_3 on the surface.[34] At temperatures ≥560°C, nitrite concentrations (a measure of decomposition and corrosivity of salt) have been shown to decrease as O_2 partial pressures increase as well as when under a closed system (as opposed to open air).[78] For reference, in concentrated solar receiving towers, Solar Salt is exposed to atmospheric air and experiences consistent thermal cycling following the day/night cycle. For intermediate loop/energy storage applications, the nitrate salt can be sealed and potentially pressurized with various gas compositions. Along these lines, gaseous impurities such as CO_2 and H_2O can also impact salt corrosivity and have been

investigated in several studies.[41,79–82] In these instances, CO_2 and H_2O react with the nitrate salt to form carbonates (CO_3^{2-}) and hydroxides (OH^-).

To account for the phenomenon of decomposition and to minimize confusion with the overall body of high temperature nitrate salt literature, in this dissertation, "elevated temperature" is defined to be at temperatures ≥570°C. The presence of significant numbers of oxidizing species at elevated temperatures as a result of decomposition enables many possible reaction pathways for corrosion. Below are some possible reduction and oxidation half reactions in nitrate salt that may play a role:[83,84]

Possible Reduction Half Reactions		Possible Oxidation Half Reactions	
		Iron	
$NO_3^- + 2e^- \rightleftharpoons NO_2^- + O^{2-}$	(1.10)	$Fe + O^{2-} \rightarrow FeO + 2e^-$	(1.17)
$NO_2^- + e^- \rightleftharpoons NO + O^{2-}$	(1.11)	$3FeO + O^{2-} \rightleftharpoons Fe_3O_4 + 2e^-$	(1.18)
$2NO_2^- + 6e^- \rightleftharpoons N_2 + 4O^{2-}$	(1.12)	$2Fe_3O_4 + O^{2-} \rightleftharpoons 3Fe_2O_3 + 2e^-$	(1.19)
$NO + \frac{1}{2}O_2 + e^- \rightleftharpoons NO_2^-$	(1.13)	*Nickel*	
$NO_2 + e^- \rightleftharpoons NO_2^-$	(1.14)	$Ni + O^{2-} \rightleftharpoons NiO + 2e^-$	(1.20)
$2NO_3^- + e^- \rightleftharpoons 2NO_2^- + O_2^-$	(1.15)	*Chromium*	
$2NO_3^- + 2e^- \rightleftharpoons 2NO_2^- + O_2^{2-}$	(1.16)	$2Cr + 3O^{2-} \rightleftharpoons Cr_2O_3 + 6e^-$	(1.21)

In elevated temperature Solar Salt, sodium-iron-oxide ($NaFeO_2$) has often been detected in the outermost corrosion layer of corroded samples.[30,32,38,47,48,59,60,62,63,69,85–88] Figure 1.7 shows the phase stability diagram for the Na-O-N system at 900K along with the respective oxides of Fe, Cr, and Ni. In an air environment, $NaFeO_2$ and $NaCrO_2$ are thermodynamically stable over their oxide counterparts, while NiO is stable over Na_2NiO_2. The presence of $NaCrO_2$ is not observed, however, due to the preferential formation of sodium chromate (Na_2CrO_4) which is highly soluble.

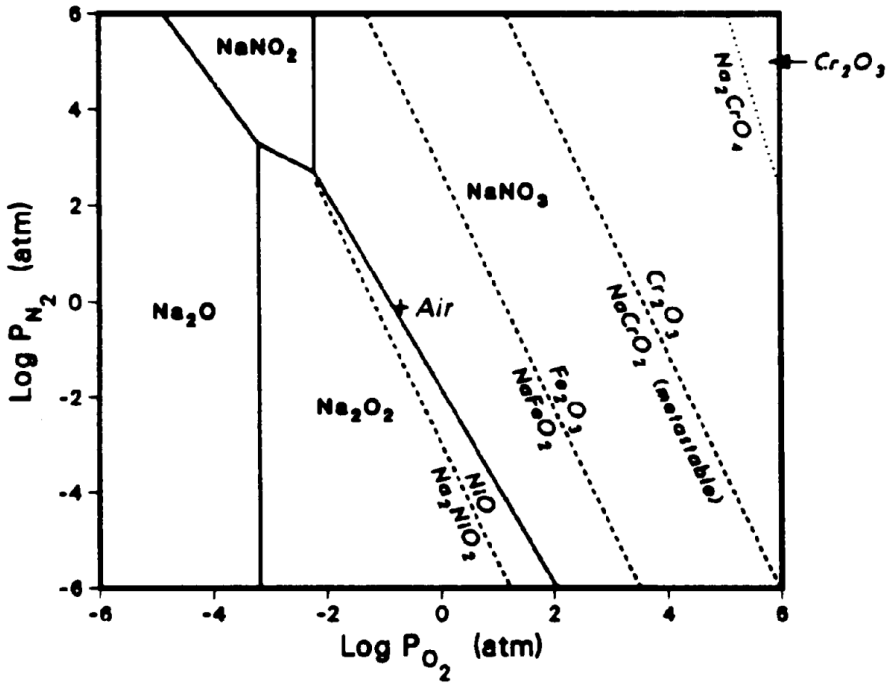

Figure 1.7: Phase stability diagram for the Na-O-N system at 900K (solid) with metal oxide and sodium-metal-oxide stability boundaries for Fe, Cr, and Ni (dotted).[86]

While substantial literature on the corrosion rate of materials exists for high temperature Solar Salt, literature at elevated temperatures (≥570°C) is more limited. Particularly rare are long-term, high temperature corrosion studies with nitrate salt which enable more detailed understanding of the interplay between nitrate salt decomposition and material corrosion behavior. 316SS has been the alloy most examined and as mentioned before is the alloy presently used in high temperature Solar Salt environments. Figure 1.8 shows all corrosion rate data of 316SS at elevated temperatures readily available in literature plotted in a 3D time-temperature vs. corrosion rate plot.[59,60,62,63,69,85–87,89–91] For clarity, Figure 1.8a and Figure 1.8b show the same 3D plot rotated to produce pseudo-2D corrosion rate vs. temperature and corrosion rate vs. time plots. It is clear that corrosion rates significantly increase as temperatures increase beyond 570°C and especially above 600°C. It is also clear that corrosion rates within a given temperature have a noticeable dependence on exposure time indicating that short exposure time experiments are not necessarily representative of corrosion rates for long-term applications. In order to enable use of Solar Salt to higher operating temperatures, further understanding of the corrosion performance of 316SS and other alloys is required.

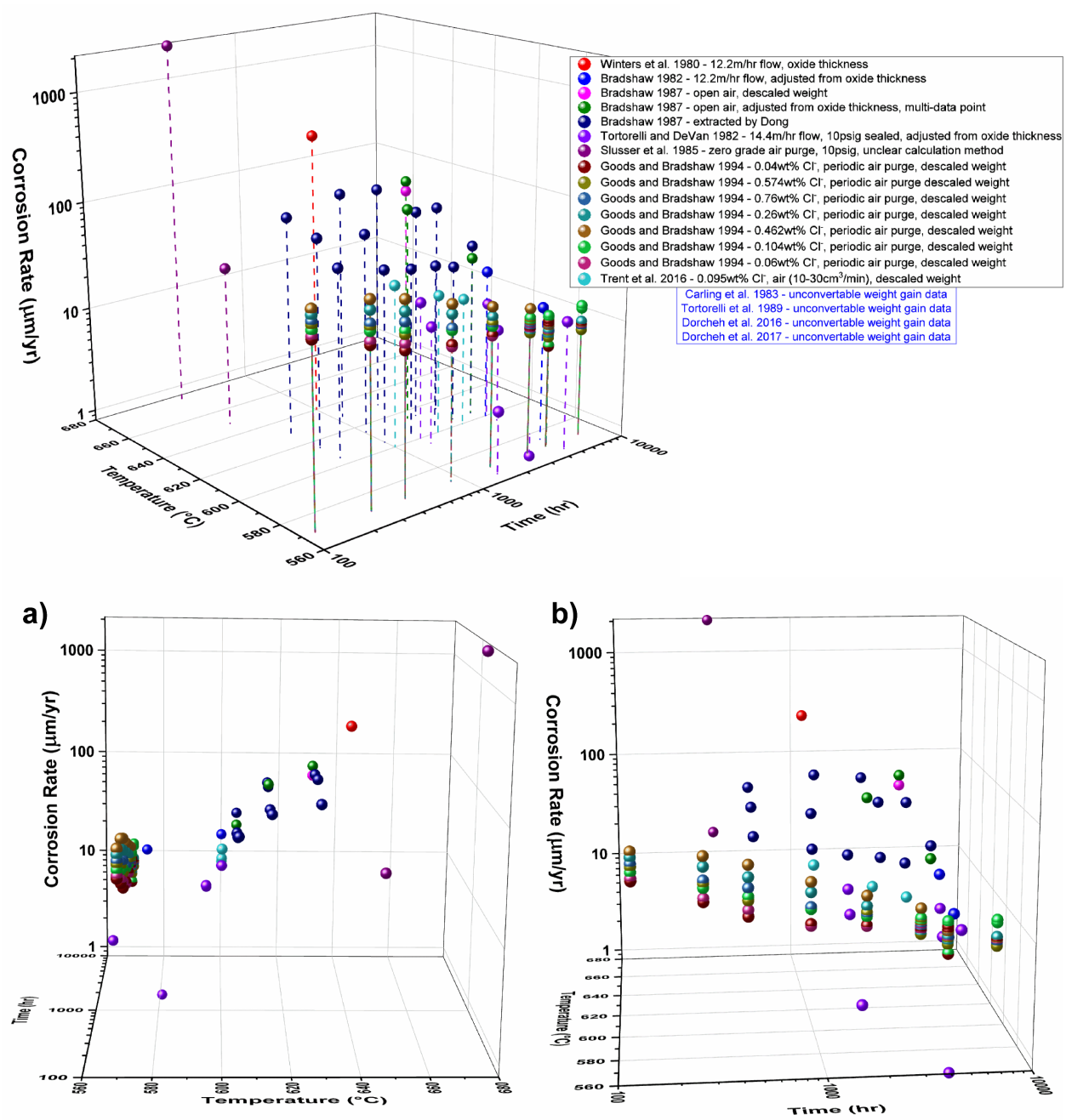

Figure 1.8: 3D plot of 316SS corrosion rate data in elevated temperature Solar Salt available from literature (top). Pseudo-2D corrosion rate vs. temperature (a) and corrosion rate vs. time (b) plots obtained from rotating the overall 3D plot.

Chapter 2 – Dissertation Scope and Research Questions

Given the interest to push the use of molten nitrate salt to higher temperatures, the objective of this dissertation is to expand the understanding of elevated temperature corrosion in nitrate salt. In this dissertation, corrosion experiments in elevated temperature Solar Salt were conducted for a variety of different steel and nickel alloys.

Chapter 3 details the results of a multi-alloy corrosion study in which the corrosion performance of twelve different materials was examined. In Chapter 4, a temperature scoping study was performed on 316SS in which the magnitude of change in corrosion rates as a function of temperature was obtained. The heart of the dissertation revolves around a long-term corrosion study detailed in Chapter 5 in which materials (predominantly 316SS and 601) were exposed to Solar Salt for a range of different temperatures and durations. Data generated includes detailed corrosion rate determination, corrosion scale microscopy, and salt chemistry evolution that expands the Solar Salt corrosion literature base both in terms of the alloys examined, but also in the array of temperatures and salt exposure times scoped.

Through the conduction of a multi-alloy corrosion study, a temperature scoping study, and a long-term corrosion study in elevated temperature Solar Salt, the following guiding questions are tackled:

1. How do alloys of different compositions perform in elevated temperature Solar Salt?
2. What is the magnitude of increase in corrosion rates as temperatures are pushed above current operating temperatures?
3. What is the time and temperature dependence on the corrosion performance of materials in Solar Salt?
4. What is the corrosion scale morphology of steel and nickel alloys and how does it evolve over time?
5. What role does nitrate salt decomposition play in the observed increases in corrosion rates?
6. What are the mechanisms which describe the increase in corrosion rates observed in elevated temperature Solar Salt?

In addressing these questions and many more, greater understanding of elevated temperature corrosion in nitrate salt is obtained for continued materials development in nitrate salt applications.

Chapter 3 – Multi-Alloy Corrosion Study

3.1. Background

As described in the Introduction, a wide range of different materials have been investigated for use in high temperature nitrate salt environments including steels, nickel alloys, AFA alloys, and coatings. However, the parameter space in corrosion experiments is vast, ranging beyond specific material and salt compositions to aspects including temperature, time, impurities, gas space, thermal gradients, and flow. Changes to any of these aspects can result in substantially different corrosion performances for the same material. Furthermore, there are often inconsistencies in reporting methods and priorities amongst the many researchers investigating the topic. Comparison of the corrosion performance of alloys across different studies is therefore precarious, and one must be cautious in trying to draw conclusions from data spanning many experimental methods. This limits both the understanding of results as well as the ability to utilize the greater body of research to predict corrosion behavior of materials in potential applications.

Metrics for describing the corrosion performance of materials include weight loss, the depth of attack through microscopy, surface recession, and changes in material microstructure. Weight change corrosion rate measurements is one of the most widely used methods for quantifying corrosion rates, especially in oxidizing corrosion environments that form oxides. The more precise term is descaled weight loss and involves cleaning off the corroded layers of a material through a series of acid and solvent immersions. While there are errors associated with such a technique,[92] if performed properly it provides a common and reliable metric that enables cross-comparison of corrosion rate data. As was highlighted in Figure 1.8, significant elevated temperature Solar Salt corrosion work used experimental and reporting methods that make it difficult to draw useful comparisons. Some studies, for example, reported weight gain as their metric for corrosion performance, which can be unreliable due to uncontrolled spallation of corrosion oxide layers. Despite confusingly also being a method utilizing weight change, this method does not enable proper calculation of corrosion rates and thus makes it incompatible for corrosion performance comparisons beyond the original study.

In terms of elevated temperature corrosion, the body of literature is significant but sparse compared to the corrosion parameter space especially when considering experimental and reporting differences. A few studies have investigated several alloys simultaneously and thus provide the ability to directly compare corrosion performance of different alloys.[49,62] However, datapoints are limited and significant investigation throughout the corrosion parameter space is still required to ensure confidence in the relative performance of alloys. In this Chapter, the results of a multi-alloy corrosion study will be discussed. Simultaneous investigation of a wide range of different materials was performed enabling direct comparison of the effect of alloy composition on relative corrosion performance in elevated temperature Solar Salt.

3.2. Materials and Methods

3.2.1. Materials

Twelve different materials were examined as part of this overall multi-alloy corrosion study. This included six stainless steel variants (316, 709, N60, AFA-OCB, AFA-OCL, AFA-OCF), five

nickel-based alloys (601, 617, 214, 224, 233), and an aluminide coating. Elemental compositions of the alloys are detailed in Table 3.1. As described in the introduction, 316SS has already been employed in concentrated solar power plants exposed to Solar Salt and acts as the main alloy for comparison throughout this dissertation work. Alloy 617, along with 316SS, are ASME BPVC Section III code certified and can thus be used in significant components of high temperature nuclear reactors. Alloy 709 is currently undergoing code case review for inclusion. N60 is a steel alloy commonly used for components requiring resistance to galling and wear. Alloy 601 is a commonly used nickel alloy and along with -OCB, -OCL, -OCF, and all the other nickel alloys are AFA alloys with varying amounts of aluminum and other alloying elements.

Examination of this slate of materials is performed in the pursuit of enabling direct comparison of corrosion resistance across different classes of alloys (steels, nickel-based alloys, alumina-forming materials) in elevated temperature Solar Salt. The potential differences in corrosion behavior between individual alloys are scoped as a function of their elemental compositions. While the collection of alloys tested here provides a range of different compositions for examining corrosion resistance in nitrate salt, it is to be noted that the individual compositions are tailored for a wide variety of properties (mechanical properties, microstructure, phase stability, manufacturability, cost, etc.). For example, significant amounts of molybdenum and cobalt are present in Alloy 617 and 233 to take advantage of solid solution strengthening for improved mechanical properties.

Table 3.1: Nominal composition of alloys used during the multi-alloy corrosion study.

Alloy	Alloying Element*													
	Fe	C	Cr	Ni	Al	Mn	Mo	Co	Nb	Si	Cu	W	Y	Ta
316SS	Bal.	0.04	17.5	11.5	-	1	2.25	-	-	0.5	-	-	-	-
709	Bal.	0.08	20	25	-	0.9	1.5	-	-	0.4	-	-	-	-
N60	Bal.	0.1	17	8.5	-	8	0.75	-	-	4	-	-	-	-
AFA-OCB	Bal.	0.2	14	25	3	2	2	-	1	-	0.5	1	-	-
AFA-OCF	Bal.	0.2	14	25	4	2	2	-	2.5	-	0.5	1	-	-
AFA-OCL	Bal.	0.2	14	12	2.5	10	-	-	1	-	3	-	-	-
601	12.5	0.1	23	Bal.	1.35	1	-	-	-	0.4	1	-	-	-
617	3	0.1	22	Bal.	1.15	1	9	12.5	-	1	0.5	-	-	-
214	4	0.15	16	Bal.	4.5	1	1	2	-	0.5	-	1	0.02	-
224	27.5	0.05	20	Bal.	3.8	0.5	0.5	2	-	-	-	0.5	-	-
233	1.5	0.1	19	Bal.	3.3	0.4	7.5	19	-	-	-	-	0.03	0.5

*Some minor alloying elements have been omitted.

All alloys were obtained via commercial vendors in sheet form (except for N60 which was obtained in the form of a 1-inch rod) and then machined into individual corrosion coupons. Holes were machined into the coupons to enable hanging into the molten salt. A portion of the machined 316SS samples were sent to a commercial vendor for coating to produce the aluminide coating corrosion coupons. More specific coupon dimensions are detailed in subsequent subsections. The dimensions and weight of all samples were measured prior to exposure to molten salt.

3.2.2. Corrosion Setup

The overall corrosion setup involved five duplicate corrosion vessels that enabled the ability to run five corrosion experiments simultaneously within a study (Figure 3.1). A schematic of an individual corrosion vessel is provided in Figure 3.2. An alumina crucible obtained from AdValue Technology measuring 160mm in length and 84mm in diameter was used to hold the nitrate salt which was in turn placed inside a steel liner to protect the overall steel vessel from potential molten salt spillage. The vessel and liner were made from 316SS and enclosed an internal volume roughly measuring 300mm in length and 95mm in diameter. The furnace heating elements were located outside the steel vessel. The vessel head contained gas inlet and outlet connections as well as a port to feed a thermocouple into the molten salt for in-situ temperature monitoring. The vessels were sealed using a high temperature gasket, and pressure was controlled through utilizing a backpressure regulator. For all the experiments, the corrosion vessels were operated in a semi-sealed gas space. In other words, after setting the backpressure regulator to the target pressure setpoint, inlet gas flow was shut off but any gas generation during the experiments was allowed to vent to prevent additional pressure buildup. Ultra zero grade synthetic air was utilized as the initial gas cover space.

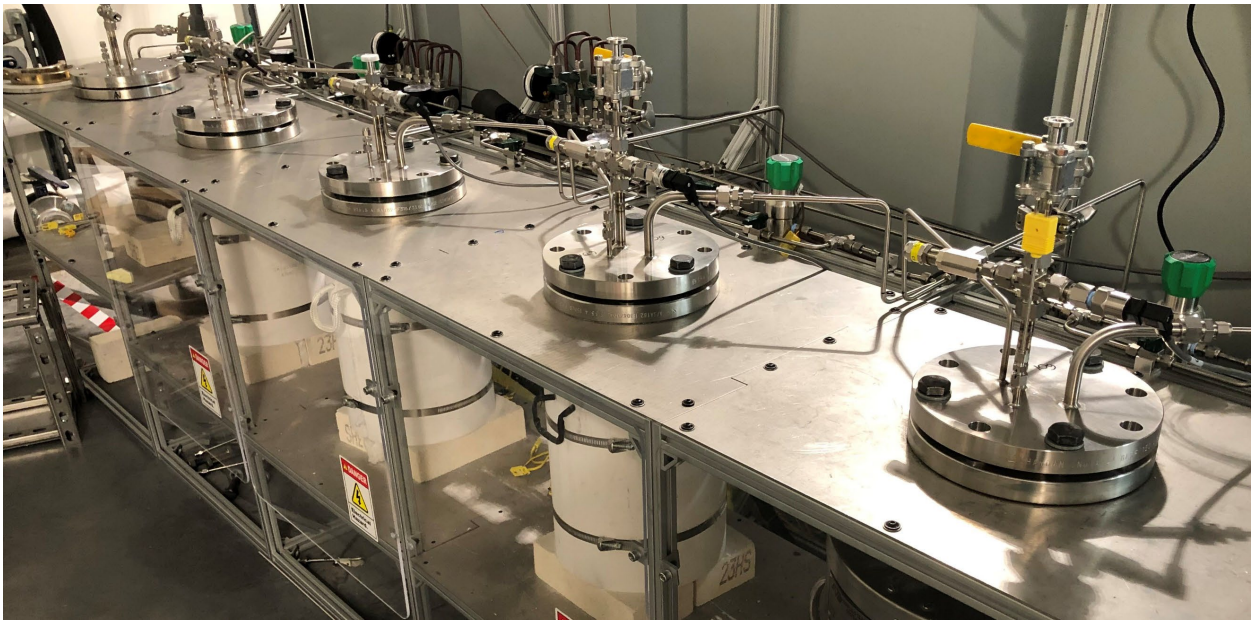

Figure 3.1: Five duplicate corrosion vessels utilized for Solar Salt corrosion experiments.

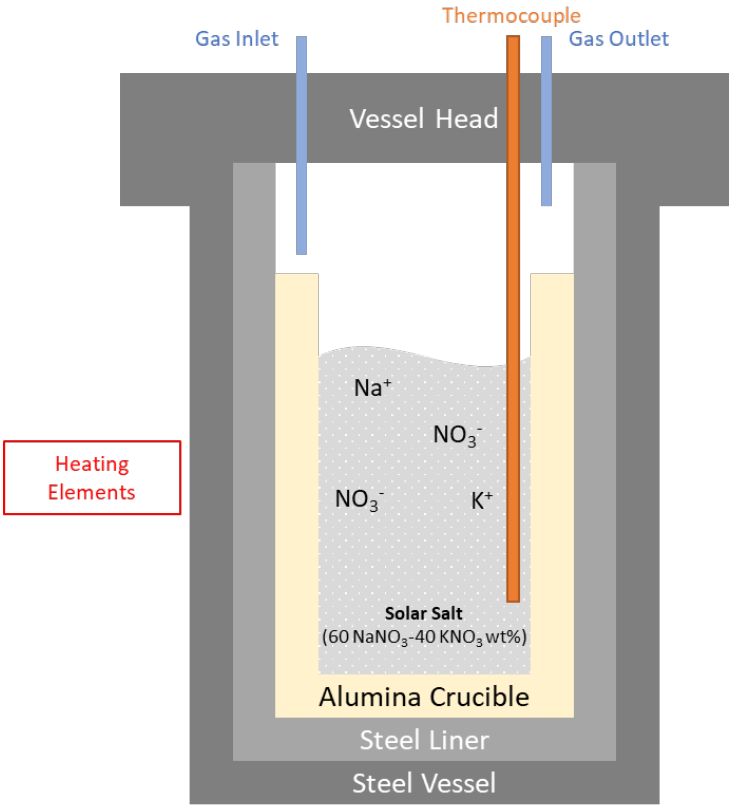

Figure 3.2: Schematic of an individual corrosion vessel used in the corrosion experiments.

An initial ramp to test temperature was performed for each fresh batch of Solar Salt to enable removal of volatile impurities and to adequately melt the salt prior to sample insertion. Nitrate salt at elevated temperatures is known to generate NO_x gas which has significant health risks. Therefore, prior to opening the corrosion vessel after time at temperature, the gas space was flushed with ultra zero synthetic air to purge any accumulated NO_x gases. Similarly for safety reasons, sample insertion and extraction were performed around 350°C to enable sample extraction while the salt was still molten while minimizing the generation and exposure to NO_x gas and other high temperature hazards.

Two distinct rounds of experiments were performed as part of the overall multi-alloy corrosion study due to a combination of space, timing, and practical considerations. As such, significant differences in experimental conditions were imposed between some samples within this study and are detailed in the subsequent sections.

3.2.3. Experiment Set 1

The first set of experiments had conditions summarized as: 630°C, 600hr, 15psig, 0.46wt% Cl^- impurity salt, large hanging samples. 500g of Solar Salt was utilized in each experiment mixed from 60wt% sodium nitrate and 40wt% potassium nitrate procured from a commercial vendor. Table 3.2 shows the impurity specifications for the nitrate salt used in this study with Cl^- impurities for this batch of nitrate salt tested as being 0.46wt%. Of the various impurities typically

found within stock sodium nitrate and potassium nitrate, Cl^- impurities have generally been the most notable in potentially having a significant effect on corrosion performance.

Table 3.2: Impurity specifications for the nitrate salt used in this study.

Impurity	Concentration Specification (wt%)
H_2O	<0.2
Nitrite	<1
Chloride	0.46*
Carbonate	<0.1
Sulfate	<0.75
Hydroxyl	<0.2
Magnesium	<0.05

*Actual concentration tested from batch of salt.

Alloys utilized in this set of experiments were 316SS, 709, N60, 601, 617, 214, 224, 233, and the aluminide coating. Examples of corrosion coupon dimensions are shown in Figure 3.3. Being machined from a rod, the N60 coupons were circular measuring 1-inch in diameter and 3mm in thickness. All the other alloys were machined into rectangular coupons measuring roughly 10cm in length and 1.3cm in width. The 316SS and aluminide 316SS samples had thicknesses of 1.5mm while the other samples had thicknesses of 3mm. 7.5mm diameter holes were machined into the specimens to enable hanging of the samples.

Figure 3.4 shows the corrosion vessel schematic including the sample hanging configuration. Coupons were hung from an alumina tube threaded through two holed-bars attached to the vessel head. Each sample was isolated from the vessel components as well as each other using alumina sleeves and spacers to minimize potential galvanic effects. Around 6-8 samples (depending on coupon and spacer thicknesses) were able to be exposed in a single vessel using this method. Due to the tube itself not being fully inserted into the salt, the coupons were only partially submerged. N60 samples were attached to an alumina tube hung using 316SS wire looped through the tube and were fully submerged. Three coupons of each alloy were split into different duplicate vessels and exposed to molten Solar Salt at 630°C for a target of 600hr and a gas space pressure of 15psig. Two of the coupons of each alloy were used for weight change corrosion measurements while the third was used for microscopy.

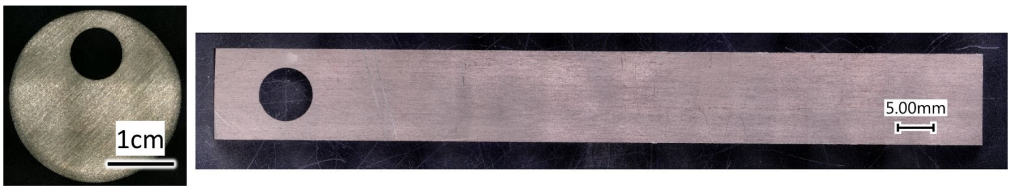

Figure 3.3: Examples of the coupon dimensions for experiment set 1. Left: 1-inch diameter sample machined from N60 rod. Right: 10cm sample machined from sheet.

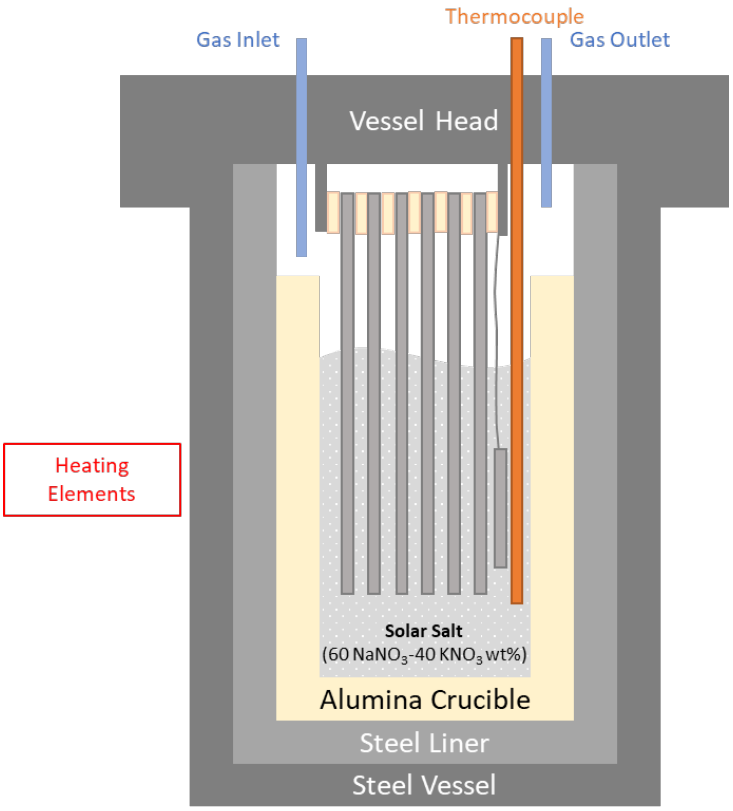

Figure 3.4: Schematic of a corrosion vessel for experiment set 1 with samples hanging from the vessel head.

3.2.4. Experiment Set 2

The second set of experiments had conditions summarized as: 600°C or 630°C, 600hr, <1psig, 0.01wt% Cl^- impurity salt, small/medium submerged samples. Like the first set of experiments, 500g of Solar Salt was utilized in each experiment, however, from a different batch of sodium nitrate and potassium nitrate with Cl^- impurity concentration tested to be 0.01wt%. As will be discussed in the Results and Discussion section, some effects of Cl^- impurity were likely observed when comparing data from the higher Cl^- impurity salt to the lower Cl^- impurity salt. The 0.01wt% Cl^- impurity salt was utilized in this second set and future experiments to minimize Cl^- effects in the data collected.

The cover gas pressure for the second (and future) set of experiments was reduced to essentially atmospheric pressure. Backpressure regulators were set to <1psig to ensure the corrosion vessels were sealed from the environment while preventing gas buildup (semi-sealed). Cover gas pressure is expected to affect the corrosion rate of materials, namely higher pressures reducing corrosion rates,[62] though literature is sparse quantifying the magnitude of these effects. Performing all the experiments at elevated pressure would also enable altering the partial pressure of gas species such as O_2 which as described in the Introduction can significantly impact nitrate salt decomposition and corrosion. However, this line of investigation was not pursued and is thus outside the scope of this study.

Alloys utilized in this set of experiments were 316SS, AFA-OCB, AFA-OCL, and AFA-OCF. Instead of the large hanging samples employed in the first set of experiments, small/medium size samples (Figure 3.5) were utilized. This was due to the testing of a 60-sample holder that would eventually be employed in the long-term corrosion experiments (Chapter 5). Figure 3.6 shows the corrosion vessel schematic including the 60-sample holder that was employed for this set of experiments. The sample holders were made from 316SS and alumina components, and samples were secured on branches using 316SS pins. Each sample was isolated from the vessel components as well as each other using alumina sleeves and spacers to minimize potential galvanic effects.

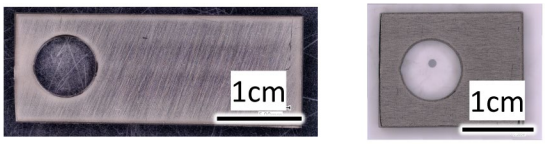

Figure 3.5: Examples of the coupon dimensions for experiment set 2. Left: 3.5cm medium-sized sample. Right: 2cm small-sized sample.

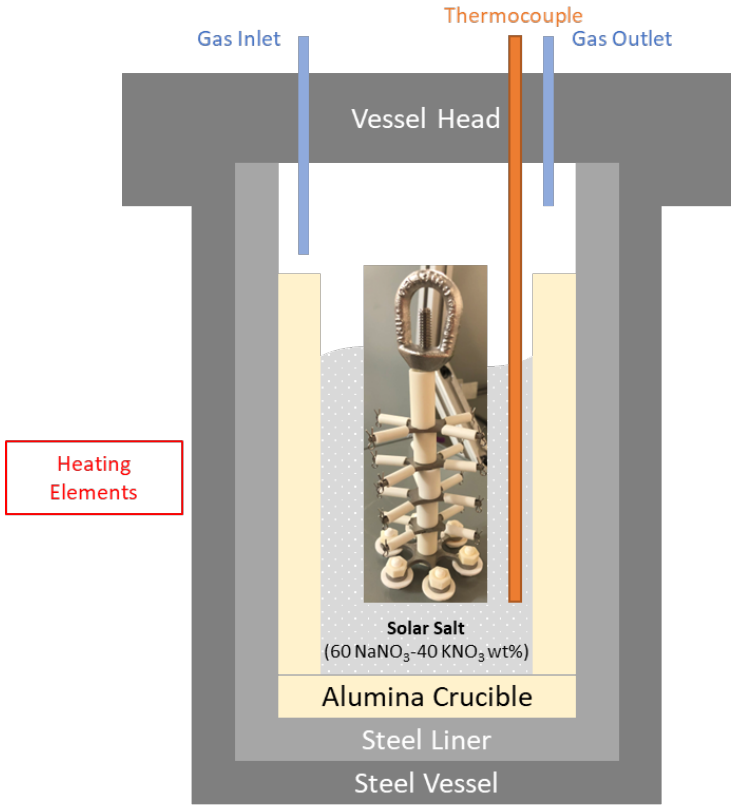

Figure 3.6: Schematic of a corrosion vessel for experiment set 2 with the 60-sample holder used for hanging samples.

Two separate experiments, one at 630°C for 600hr and one at 600°C for 600hr, were performed. In each, three medium-sized coupons of each alloy measuring roughly 3.5cm in length, 1.3cm in width, and 1.5mm in thickness were fully submerged within the salt. An

additional three small-sized 316SS coupons 2cm in length were also placed in the experiments. All of the 316SS samples were used for weight change corrosion measurements, while one of the coupons of each of the other alloys were reserved for microscopy. An additional experiment containing three large hanging 316SS samples was also performed, exposing the large 316SS samples to the 600°C condition for comparison.

3.2.5. Post-Corrosion Examination

Corroded samples set aside for microscopy were cut into smaller cross sections via a precision high speed saw and then mounted in epoxy along with an un-corroded piece. The samples were then polished to a final polishing step using 0.25µm diamond suspension. Microscopy and energy-dispersive X-ray spectroscopy (EDS) was performed utilizing a FEI Quanta scanning electron microscope (SEM).

Weight change corrosion rates were determined following ASTM G1-03 and ISO 8407 guidelines at room temperature using 20% (v/v) nitric acid in 30-minute intervals for the steel alloys and 2M hydrochloric acid in 5-minute intervals for the nickel-based alloys. Between each cleaning step, the samples were weighed on a Mettler Toledo XPR206DR scale with precision of ±0.000005g. For large sample coupons which were not fully submerged into the salt, the height of the salt meniscus line was measured, and two separate corrosion rates were calculated (one using the full surface area and one using the submerged surface area). Exact exposure times at test temperature above 3°C below the target temperature (i.e., >627°C or >597°C) were calculated from thermocouple readings.

3.3. Results

3.3.1. Weight Change Corrosion Rates

Figure 3.7 shows the average obtained weight change corrosion rates for the various alloys in 630°C Solar Salt plotted in relation to one another. For the samples that were fully submerged within the molten salt (316SS Small, 316SS Medium, N60, AFA-OCB, AFA-OCL, and AFA-OCF), the error bars shown are standard deviations. For the partially submerged large samples, the values plotted are the average corrosion rates obtained when using the full sample surface area and the error bars are the average corrosion rates if only the submerged surface area was used. The true corrosion rate for the partially submerged samples is therefore in between the plotted bar and the end of their respective error bar (likely towards the error bar end as will be discussed in Chapter 4). The corrosion rates calculated using only the submerged surface area can therefore be viewed as conservative estimates. The corrosion rate values are also listed in Table 3.3. Figure 3.8 shows the average obtained weight change corrosion rates for the alloys tested in 600°C Solar Salt plotted in relation to one another along with their respective 630°C data counterparts. The 600°C corrosion rate values are also listed in Table 3.4. The error bars shown are akin to Figure 3.7. In these experiments, only the 316SS Large samples were partially submerged. Note that the 630°C 316SS Large samples were tested in a different batch of nitrate salt (0.46wt% Cl^- impurity) than all the others in Figure 3.8 (0.01wt% Cl^- impurity).

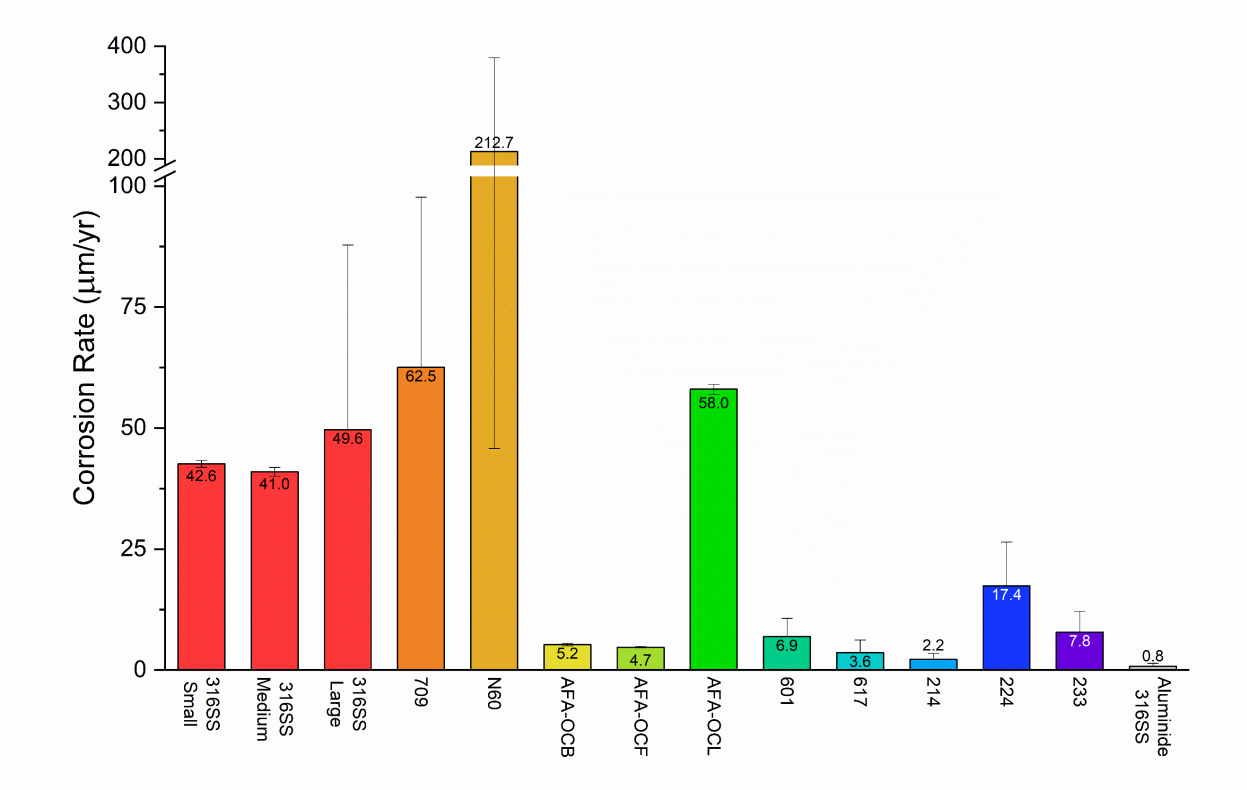

Figure 3.7: Comparison of weight change corrosion rates of the various alloys exposed to 630°C Solar Salt for 600hr.

Table 3.3: Weight change corrosion rates of the various alloys exposed to 630°C Solar Salt for 600hr.

Alloy	Corrosion Rate (µm/yr)
316SS Small	42.6 ± 0.7
316SS Medium	41.0 ± 0.9
316SS Large	49.6 + 38.2
709	62.5 + 35.2
N60	212.7 ± 166.9
AFA-OCB	5.2 ± 0.3
AFA-OCL	58.0 ± 1.0
AFA-OCF	4.7 ± 0.1
601	6.9 + 3.8
617	3.6 + 2.6
214	2.2 + 1.2
224	17.4 + 9.1
233	7.8 + 4.3
Aluminide 316SS	0.8 + 0.6

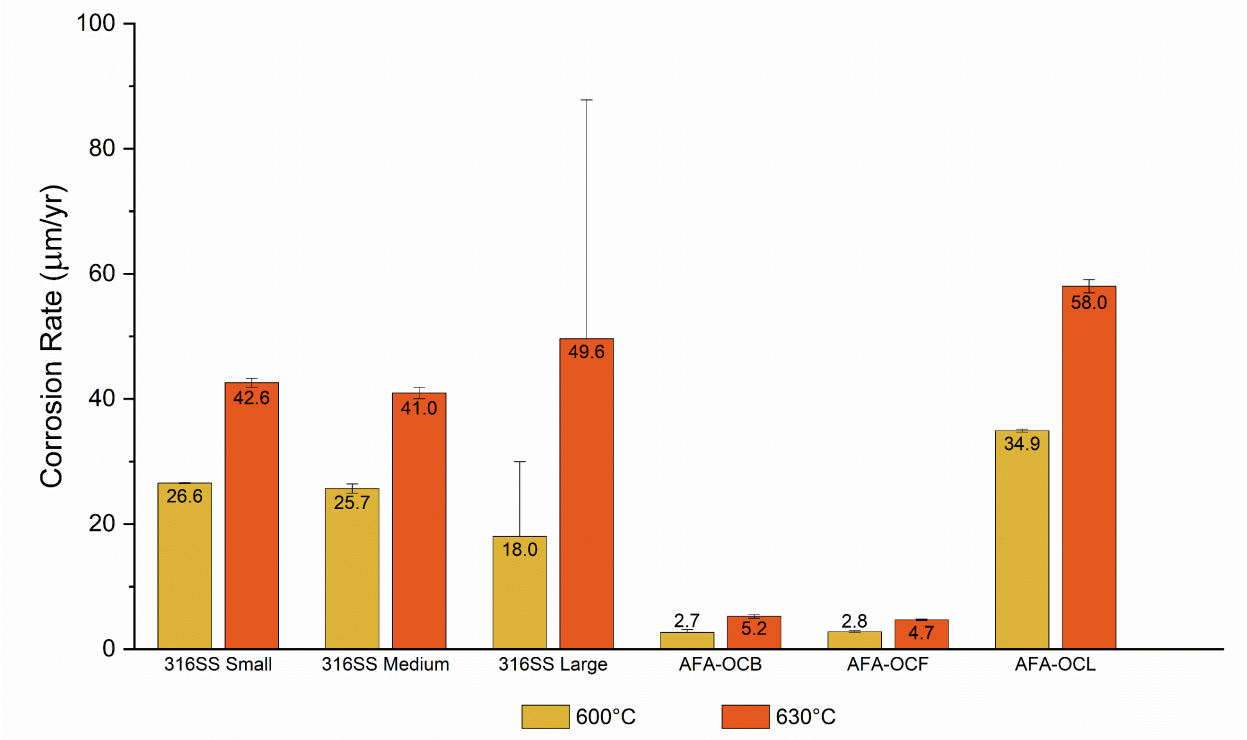

Figure 3.8: Comparison of weight change corrosion rates of the various alloys exposed to 600°C and 630°C Solar Salt for 600hr.

Table 3.4: Weight change corrosion rates of the various alloys exposed to 600°C Solar Salt for 600hr.

Alloy	Corrosion Rate (µm/yr)	
	600°C	630°C
316SS Small	26.6 ± 0.1	42.6 ± 0.7
316SS Medium	25.7 ± 0.7	41.0 ± 0.9
316SS Large	18.0 + 11.9	49.6 + 38.2
AFA-OCB	2.7 ± 0.5	5.2 ± 0.3
AFA-OCL	34.9 ± 0.2	58.0 ± 1.0
AFA-OCF	2.8 ± 0.1	4.7 ± 0.1

Prior to discussing general conclusions from the data obtained, a few specific results need to be noted. Firstly, the two N60 samples used in weight change corrosion rates provided vastly different corrosion rates. One exhibited a corrosion rate of 45.8µm/yr (which is on the order of the other steel alloys) while the other had a corrosion rate of 380µm/yr, causing both the high average and large standard deviation relative to the other alloys. As will be shown in the microscopy section, the third N60 sample utilized for microscopy exhibited a corrosion layer that suggests a corrosion rate on the order of several hundred µm/year. While dissimilar material effects might be present, this effect is likely negligible from analysis of the corrosion rates from samples between pots. All vessels containing N60 samples had similar arrangement of alloy

varieties, and thus dissimilar material effects likely do not explain why one N60 sample performed significantly better than the other two to such a degree. Analyzing the other samples in the vessels with the anomalously high corrosion rate N60 samples, it is evident that a systematic difference that would have resulted in higher corrosion rates across the board (such as undetected temperature excursions, gas flow/leakage, anomalous impurity content, etc.) also cannot explain the data. While vessels appeared to have slight variance in the corrosion environments imposed on the samples, in vessels that had samples exhibiting higher corrosion rates than their counterparts in other vessels, all samples (steel and nickel-based alloys) had higher corrosion rates (further discounting dissimilar material effects), but nowhere near the level of increase observed by the N60 samples.

It is possible that some galvanic effect was at play due to the less controlled hanging of the N60 samples utilizing 316SS wire (compared to the partially submerged samples hung solely from an alumina rod). Despite efforts to minimize/eliminate galvanic concerns using alumina components, it is possible that intimate contact between the N60 and 316SS wire occurred for at least two of the three N60 samples during the experiments. Figure 3.9 shows images of samples that were part of the multi-alloy corrosion study post-extraction. One of the images is from the vessel containing the N60 sample exhibiting 380µm/yr corrosion rate (Figure 3.9a) while the other is from the vessel containing the 45.8µm/yr corrosion rate N60 sample (Figure 3.9b). In these images, both N60 samples appear to be touching the 316SS wire along an end of the alumina tube it was hung from, revealing the possibility for this to have also occurred during the experiment. Note that while the images also suggest that the other hanging samples could have also been in intimate contact with each other, this was likely due to the sample extraction process which required tilting and inversion of the vessel head which caused the samples to touch each other while the salt froze. It was confirmed during mock trials in air, performing weight change cleaning steps, and during extraction with the nitrate salt still molten that the samples hung straight with significant gaps, and the data does not indicate any significant galvanic (or other) effects occurred for any of the partially submerged hanging samples.

If galvanic effects resulting from contact between two of the N60 samples (and not the third) and 316SS wire were to explain the vastly different corrosion rates observed, this would suggest that N60 is less noble than 316SS in elevated temperature nitrate salt, with N60 preferentially corroding and in turn protecting the 316SS wire. Visual inspection during extraction (and as seen in Figure 3.9) of the N60 samples, however, noted no obvious difference in behavior between the N60 samples and 316SS wires, and it was only after commencing the weight change corrosion rate cleaning process that it was evident one of the N60 samples performed significantly worse than the other. Ascertaining whether the cause was galvanic or some other reason in nature is unfortunately unable to be remedied by this study. If it is indeed galvanic, this would place concerns on components in elevated temperature nitrate salt using N60 for galling and wear resistance as they would likely be in intimate contact with other alloys such as 316SS.

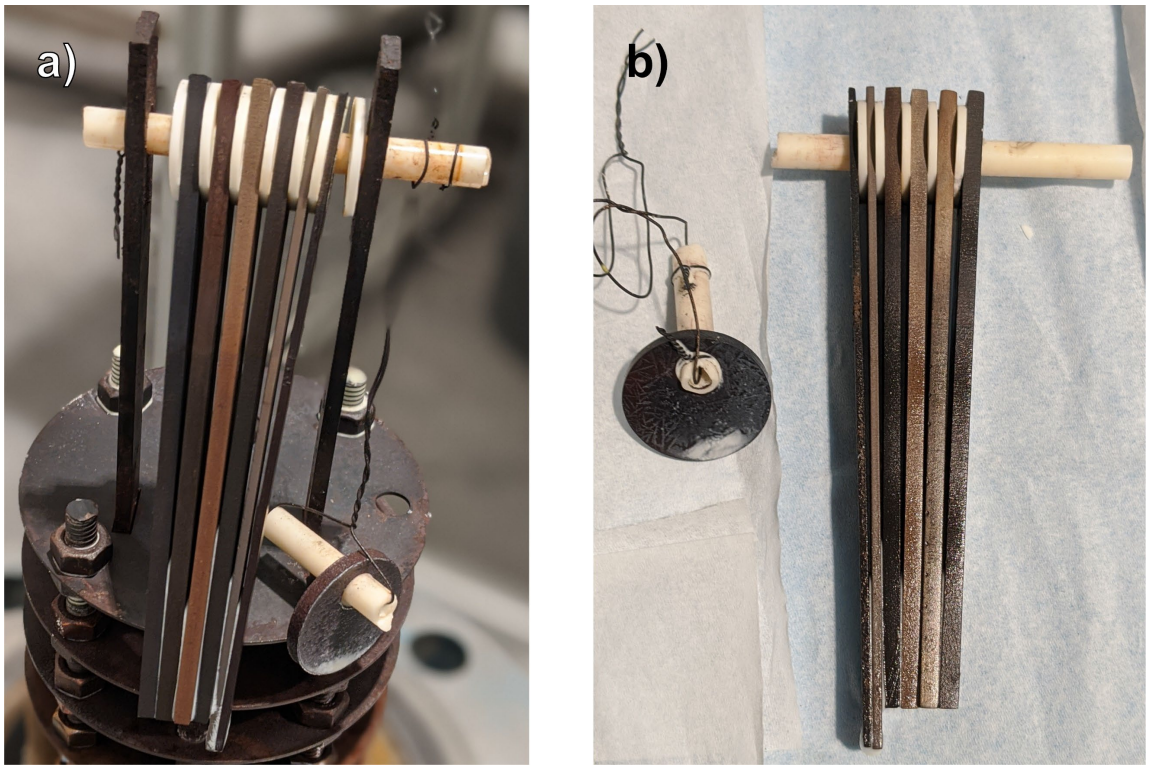

Figure 3.9: Images of samples post-extraction from multi-alloy corrosion experiments. a) From the vessel containing the N60 sample exhibiting 380µm/yr corrosion rate. b) From the vessel containing the N60 sample exhibiting 45.8µm/yr corrosion rate.

A second detail to note from the data is that there was likely an effect from utilizing different batches of salt on the obtained corrosion rates. This is most easily explained using the data from Figure 3.8/Table 3.4. The 630°C 316SS Large samples were corroded in the 0.46wt% Cl^- impurity salt while all the other 316SS data was obtained using the 0.01wt% Cl^- impurity salt. Despite the issues comparing partially submerged corrosion rates vs. fully submerged values, it is evident that the corrosion rate for the 630°C 316SS Large samples is significantly greater than that of the other 630°C 316SS samples. In fact, as will be discussed in Chapter 4, refined estimation of the corrosion rate utilizing air corrosion rate data likely places the corrosion rate for the partially submerged samples towards the end of the error bar. This would mean that the corrosion rate for the 630°C 316SS Large samples is roughly twice that of the 316SS in the lower Cl^- impurity salt. Potential sample size dependence effects will also be further discussed in Chapter 4, but in summary would not explain for the differences in corrosion rates especially when considering that the 316SS Large samples exposed to 600°C Solar Salt would have corrosion rates in line with the other 316SS samples in the same specification salt at the same temperature.

It is therefore likely that different impurity concentrations between the different batches of salt (of which Cl^- being the most obvious) were the cause of the difference in observed 316SS corrosion rates. As discussed in the Introduction, chloride impurities promote de-adherence of the oxide layers, hindering the protectiveness of the corrosion oxide scale and thus increasing corrosion. Of the alloys tested in this study, only 316SS and N60 appeared to have obvious signs of flaking post-corrosion. This means the effects of Cl^- impurities may have only significantly

affected 316SS and N60, and that the results for the other alloys may be less impacted. Flaking from 316SS exposed to 0.46wt% Cl^- salt at 630°C is shown in Figure 3.10. The 316SS samples exposed 0.01wt% Cl^- salt (including at 630°C) did not show as obvious signs of flaking.

Figure 3.10: 316SS sample exposed to 0.46wt% Cl^- specification salt at 630°C for 600hr. Both sides showed obvious signs of flaking post-extraction, examples of which are pointed to by red arrows. Patches of white are solidified nitrate salt.

Considering the various nonidealities between experiments described above, several overall conclusions regarding the relative corrosion performance of the various alloys can still be made. Firstly, the aluminide coating is especially protective in elevated temperature Solar Salt, exhibiting a corrosion rate lower than any non-coated alloy at around 1µm/yr. The AFA steel alloys seem to show significant improvements in corrosion performance when compared to the non-AFA steels except for AFA-OCL, which exhibited a corrosion rate similar to the non-AFA steels. In general, the nickel alloys (also AFA in nature) appear to perform significantly better than the non-AFA steels with Alloy 224 performing the worst of the bunch. Further analysis of the differences in corrosion performance will be performed in the Discussion section.

3.3.2. Corrosion Scale Microscopy

Figure 3.11 shows the various corroded alloy samples in preparation for microscopy. Due to the large size of the samples, they had to be cut into smaller pieces prior to mounting in epoxy for polishing. During the cutting process, significant flaking of the corrosion layer was observed especially for N60 and slightly for 316SS due to the stresses involved and exposure to cooling

water. Significant N60 oxide flakes from the cutting process are shown next to N60 sample in Figure 3.11. While complete corrosion scales were still able to be successfully imaged for these samples, as will be discussed in Chapter 5, exposure to water and cutting prior to mounting in epoxy was avoided in future microscopy to minimize potential loss of entire layers of the corrosion scale.

Visual inspection of the partially submerged samples revealed the presence of meniscus lines on the sample surface corresponding to the salt level. Liquid-Air-Interfaces (LAI) are known to potentially cause localized corrosion as a result of local changes in environment from surface tension, evaporation, and other effects.[93–95] As such, pieces of the corroded samples containing the meniscus were also cut for examination, the results of which will be discussed later in this section. Pieces providing different cross-sectional views (width, thickness, length) were also cut and imaged, but the different cross sections did not reveal any discernable differences in corrosion layer morphology.

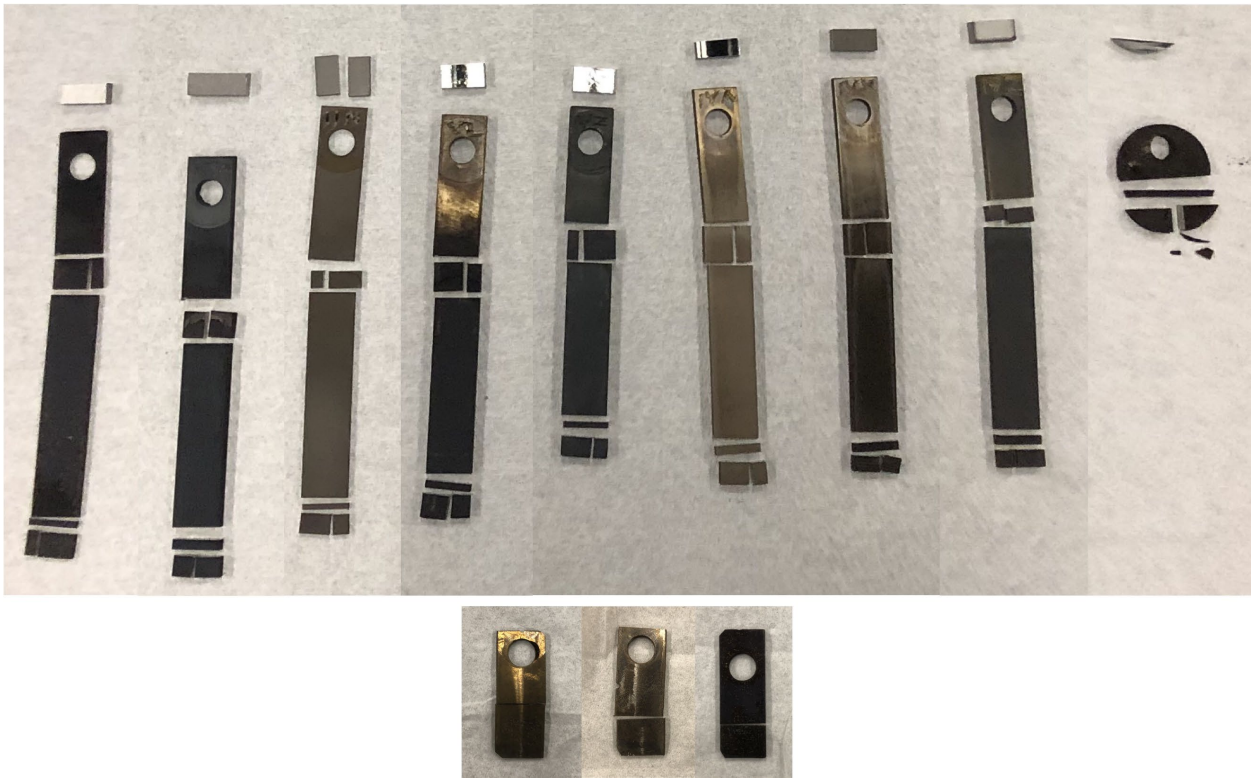

Figure 3.11: Alloys corroded in 630°C Solar Salt for 600hr in preparation for microscopy. Top row from left to right: 316SS, 709, Aluminide 316SS, 601, 617, 214, 224, 233, N60. Bottom row from left to right: AFA-OCB, AFA-OCF, AFA-OCL.

Figures 3.12-3.24 show SEM images and EDS maps of the corrosion oxide layers for the various alloys corroded in 630°C Solar Salt for 600hr. Unless otherwise noted, for all the SEM images and EDS maps provided, the left side corresponds to bulk metal while the darkest region on the right side corresponds to the epoxy the sample was mounted in. The microscopy images provided in this section are from regions that contained some of the most interesting features/behavior observed while looking around the entire sample surface and thus do not

necessarily represent the norm of the corrosion scale for the given sample. Material-specific details revealed from microscopy of individual alloys will be described below. Note that the microscopy provided in this section is a subset of the overall microscopy conducted for these samples. While the images provided here contain most of the described features of interest, a few features detailed are not clearly contained within the images provided. These features will be noted when applicable. A summary of the different layers and features exhibited by the various materials from the overall microscopy conducted will be provided in the Discussion section.

316SS (Figure 3.12): The corrosion oxide scale exhibited by 316SS agrees well with other literature examining corrosion of 316SS in elevated temperature Solar Salt. The outer oxide layer consists of an Fe oxide containing Na ($NaFeO_2$) that then transitions into subsequent layers containing Fe oxides and an inner Cr oxide layer (Cr_2O_3). During weight change corrosion measurements, initial cleaning steps readily saw the removal of brown oxide particles, leaving behind black oxides that were then removed over the course of subsequent cleaning steps. This suggests the presence of both hematite (Fe_2O_3) and magnetite (Fe_3O_4) with hematite towards the surface. Despite the known presence of both iron oxide variants, similar to other studies, clear delineations were not able to be observed through microscopy.[34] The bulk metal immediately beneath the oxide shows clear evidence of Cr and Mn dealloying, resulting in a region enriched in Fe and Ni.

Figure 3.12 also shows an instance of oxide de-adherence from the bulk metal surface. As was noted previously, the corroded 316SS (and N60) samples were susceptible to flaking during sample preparation and handling. Despite the previous discussion regarding likely influence of Cl^- impurities, presence of Cl was not detected in the 316SS corrosion scale (nor in the corrosion scale for any other alloy). This is similar to literature where even if Cl^- impurities were shown to affect corrosion rates, it was difficult to detect in the corrosion layer itself.[38,59,88] Regardless, the stresses induced from the sample preparation process resulted in the ability to observe weak interfaces in the corrosion scale. Throughout microscopy of the 316SS sample, the interface between the innermost Cr_2O_3 layer and the bulk metal surface appeared prone to de-adherence. Other susceptible interfaces included between the Cr_2O_3 and iron oxide layers and within the iron oxide layer. Several instances of these de-adherence interfaces are exhibited in the microscopy shown in Chapter 5.

709 (Figure 3.13): Alloy 709 exhibited a corrosion layer arrangement akin to 316SS, albeit more intact in the case of Figure 3.13. This specific microscopy image more clearly shows the boundaries between layers, again with $NaFeO_2$ on the surface followed by Fe oxides and Cr_2O_3. Interestingly, instead of a distinct layer of Cr_2O_3 right before the bulk metal interface like for 316SS, the Cr_2O_3 layer appears to be interspersed with material that is enriched only in Ni. This region could be viewed as being comprised of "oxide pegs" with a Cr_2O_3 sheath surrounding Ni-rich inclusions (the brighter islands in the SEM image).[96,97] In this case, these pegs are densely packed and are heavily overlapping. Due to the lack of a distinct Cr_2O_3 layer, the Ni-enriched inclusions are likely from the simultaneous dealloying of Cr and Fe (which has less immediate protection from the Cr_2O_3) to form their respective oxides.

N60 (Figures 3.14-3.15): The N60 microscopy sample exhibited a corrosion oxide scale much larger than any other material, hinting at a corrosion rate on the order of several hundred μm/yr. The thick (around 250μm) oxide layer did not have any distinct layer arrangement and was heavily depleted in Cr. Pockets of Na indicate the high probability of salt penetration during the experiment. Figure 3.15 shows higher magnification microscopy along the bulk metal-oxide boundary revealing that the features near this boundary in the bulk surface were instances of nitrate salt penetration and subsequent corrosion. Figure 3.15 also shows an extremely thin layer of enriched Ni exactly at the interface. Interestingly, Figure 3.14 reveals that beyond the nitrate salt penetration region within the bulk surface, distinct features appearing brighter than the bulk metal extend deeper (up to around 50μm beyond the extent of salt penetration) into the bulk metal surface. EDS was not able to distinguish any compositional differences that could explain these features.

AFA-OCB (Figure 3.16): The vast majority of the sample surface was protected by a thin alumina (Al_2O_3) layer at the metal surface and exhibited minimal evidence of corrosion. Some pockets of increased corrosion (such as the one shown in Figure 3.16) existed, but the extent of these pockets was limited both along the surface and into the bulk by the successful formation of Al_2O_3 underneath. Of note, MoNb phases were readily observed near the surface of the metal, though they do not appear to have had any significant effect on the corrosion performance.

AFA-OCF (Figure 3.17): Akin to their near identical weight change corrosion rates, the AFA-OCF material appeared to behave near identically to AFA-OCB. The sample surface was protected by a thin alumina (Al_2O_3) layer at the metal surface and exhibited minimal evidence of corrosion. Pockets of deeper corrosion were not readily detected throughout the surface imaged. Even if these pockets did exist somewhere along the surface area of the material, they likely would have been small and contributed minimally to overall corrosion. MoNb phases were readily observed near the surface of the metal.

AFA-OCL (Figure 3.18): In Figure 3.18, nitrate salt can be observed blooming out from the sample-epoxy interface, obscuring the sample surface and especially the O and Na signals. This was likely due to incomplete cleaning of the samples during the sample preparation process (which included water) and will also be more thoroughly discussed in Chapter 5. The corrosion scale appears to be comprised mainly of an outermost $NaFeO_2$ layer and inner iron oxides. The near surface bulk metal has significant dealloying of Cr and Mn. While some regions of Cr_2O_3 and Al_2O_3 can be discerned, they do not appear to form complete layers to protect against subsequent corrosion. As will be discussed further in the Discussion, this was likely due to the significant amounts of Mn in this alloy. MoNb phases were readily observed near the surface of the metal.

601 (Figure 3.19): Alloy 601 appears to exhibit a corrosion layer arrangement similar to Alloy 709 starting with $NaFeO_2$ as the outermost layer followed by an Fe oxide layer and an oxide peg configuration at the bulk metal interface. Due to having Al as an alloying element, the oxide peg for Alloy 601 appears to have a multi-layered Cr_2O_3 and Al_2O_3 sheath surrounding the Ni-rich inclusions. This indicates that while the addition of Al is indeed protective, the concentration of Al is too low for a complete layer to be formed. It is noted that Chapter 5 contains microscopy of Alloy 601 that reveals changes in the oxide peg morphology as a function of temperature and

time. Figure 3.19 also shows a piece of bulk material on the oxide surface, potentially revealing how relatively large chunks of material could be removed during corrosion.

617 (Figure 3.20): Alloy 617 exhibited a corrosion scale consisting of an Fe oxide region (thin relative to other alloys due to Alloy 617 only containing 3% Fe) followed by a thin Al_2O_3 layer covering a Cr and Mn de-alloyed region in the bulk material. As shown in Figure 3.20, phases containing CoMnNa were sometimes found on the oxide surface. These phases appeared to be loosely adhering to the Fe oxide interface as several were found to be separated from the oxide surface as a result of the sample mounting process. CrMnMo and TiN phases were readily observed near the surface of the metal.

214 (Figure 3.21): Alloy 214 behaved similarly to the similarly well-performing AFA-OCB and AFA-OCF alloys with the sample surface protected by a thin alumina (Al_2O_3) layer at the metal surface. Some pockets of deeper corrosion (like shown in Figure 3.21) were detected though they were limited both along the surface and into the bulk by the successful formation of Al_2O_3 underneath. CrMn phases were readily observed near the surface of the metal (prominent in microscopy beyond Figure 3.21).

224 (Figure 3.22): The corrosion scale of Alloy 224 has the presence of Al_2O_3 within the outermost $NaFeO_2$/Fe oxide layers. The presence of Al_2O_3 in the outer layer appears to be unprotective, however, and another layer of Al_2O_3 can be detected along the metal-oxide interface covering a Cr and Mn de-alloyed region in the bulk material. Interestingly, the Cr-depletion/Ni enrichment region appears to be nonuniform in nature, with lines of depletion/enrichment extending farther in some areas over others. CrMn and TiN phases were readily observed near the surface of the metal.

233 (Figure 3.23): Alloy 233 contained a corrosion scale similar to Alloy 617 though with a less smooth layer arrangement. The outermost layer consisted of an Fe oxide region followed by a sparse Al_2O_3 layer covering a Cr and Mo de-alloyed region in the bulk material. As shown in Figure 3.23, phases containing CoMnFeNa were sometimes found on the oxide surface that were loosely adhering. TiTaSi (in regions beyond Figure 3.23) and CrMo phases were readily observed near the surface of the metal.

Aluminide Coating (Figure 3.24): The aluminide coating appeared to be highly corrosion resistant with the entire sample surface protected by a thin Al_2O_3 layer.

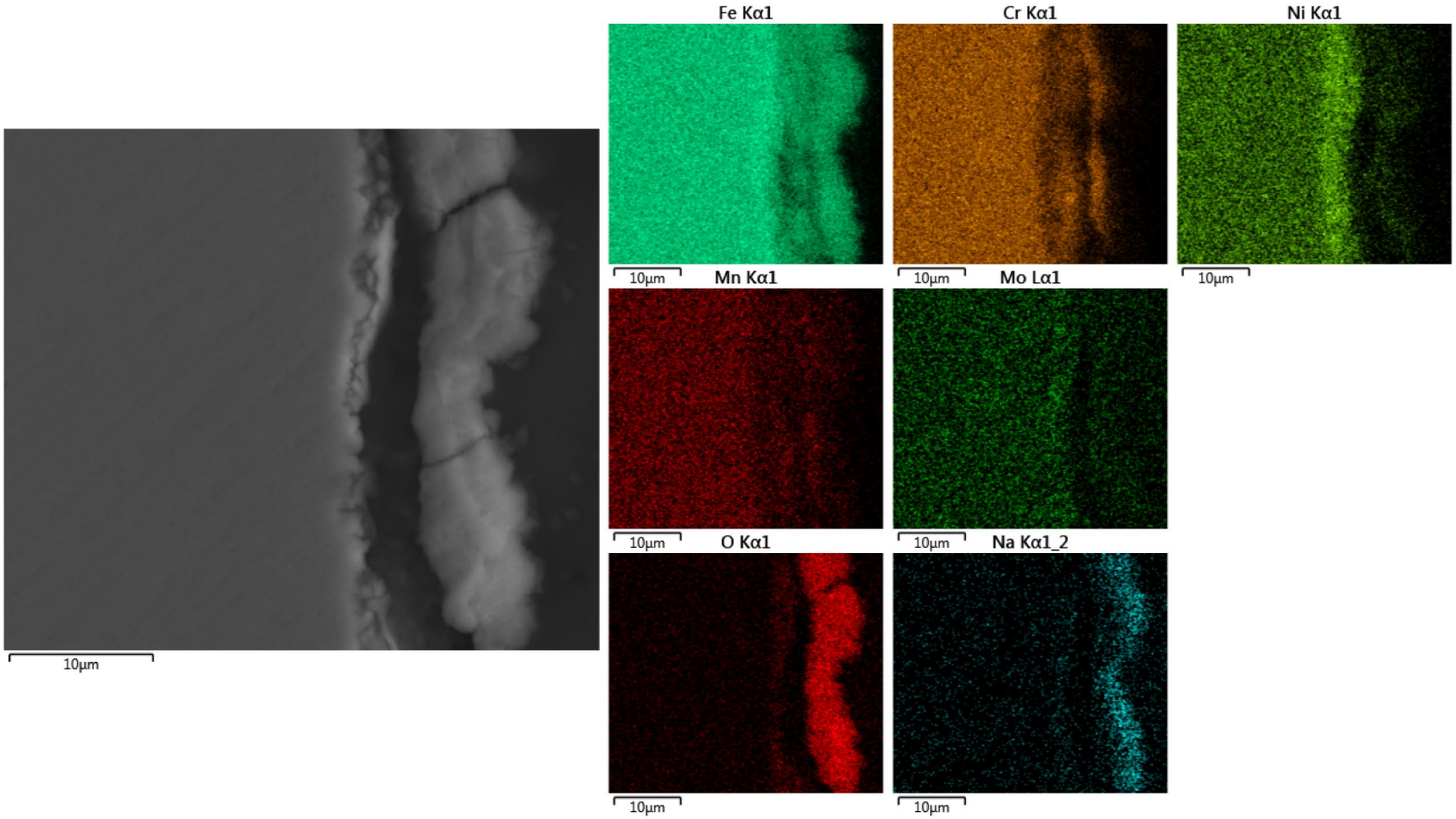

Figure 3.12: SEM image and EDS elemental maps for 316SS exposed to 630°C Solar Salt for 600hr. 4000x magnification.

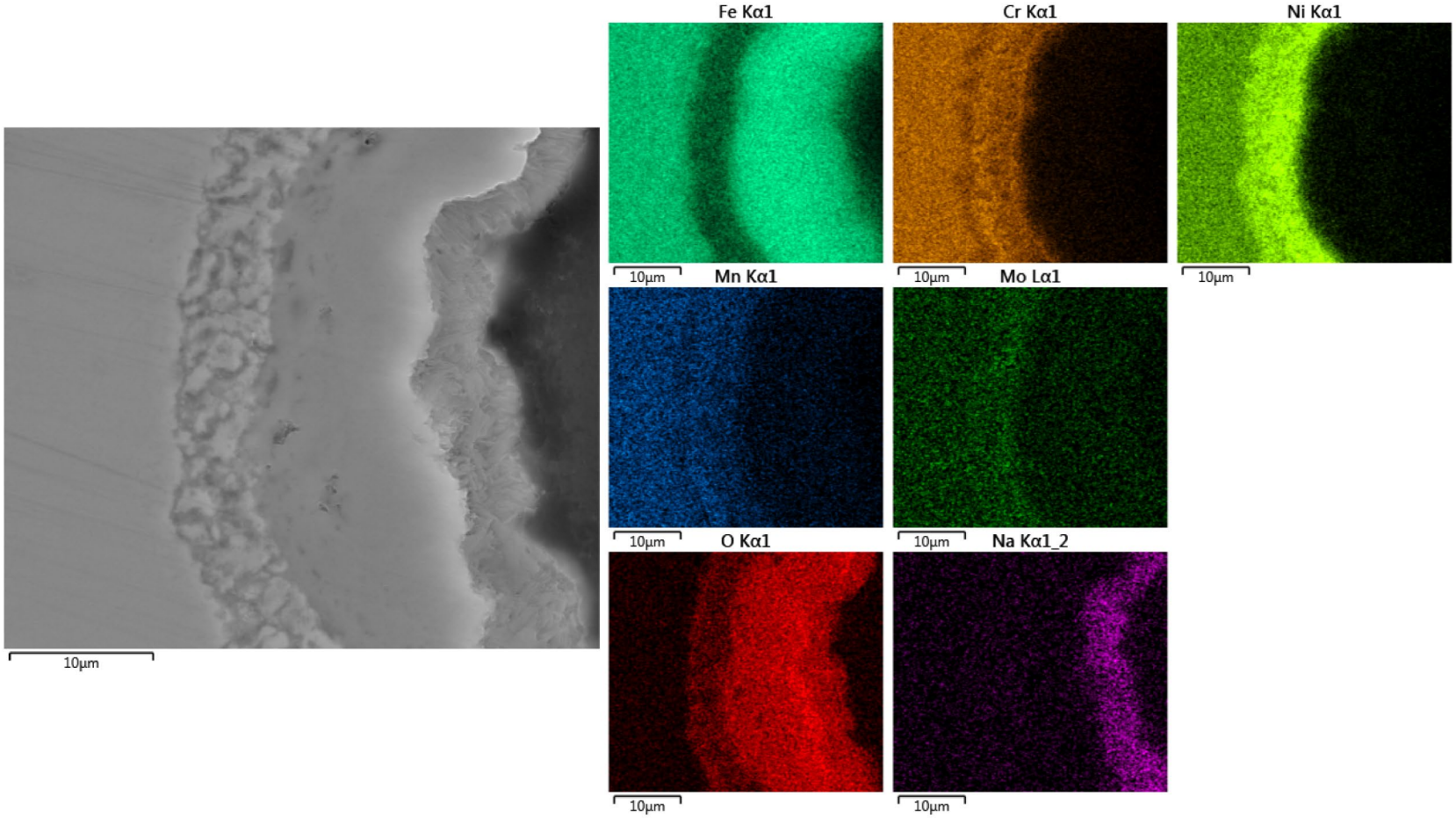

Figure 3.13: SEM image and EDS elemental maps for Alloy 709 exposed to 630°C Solar Salt for 600hr. 4000x magnification.

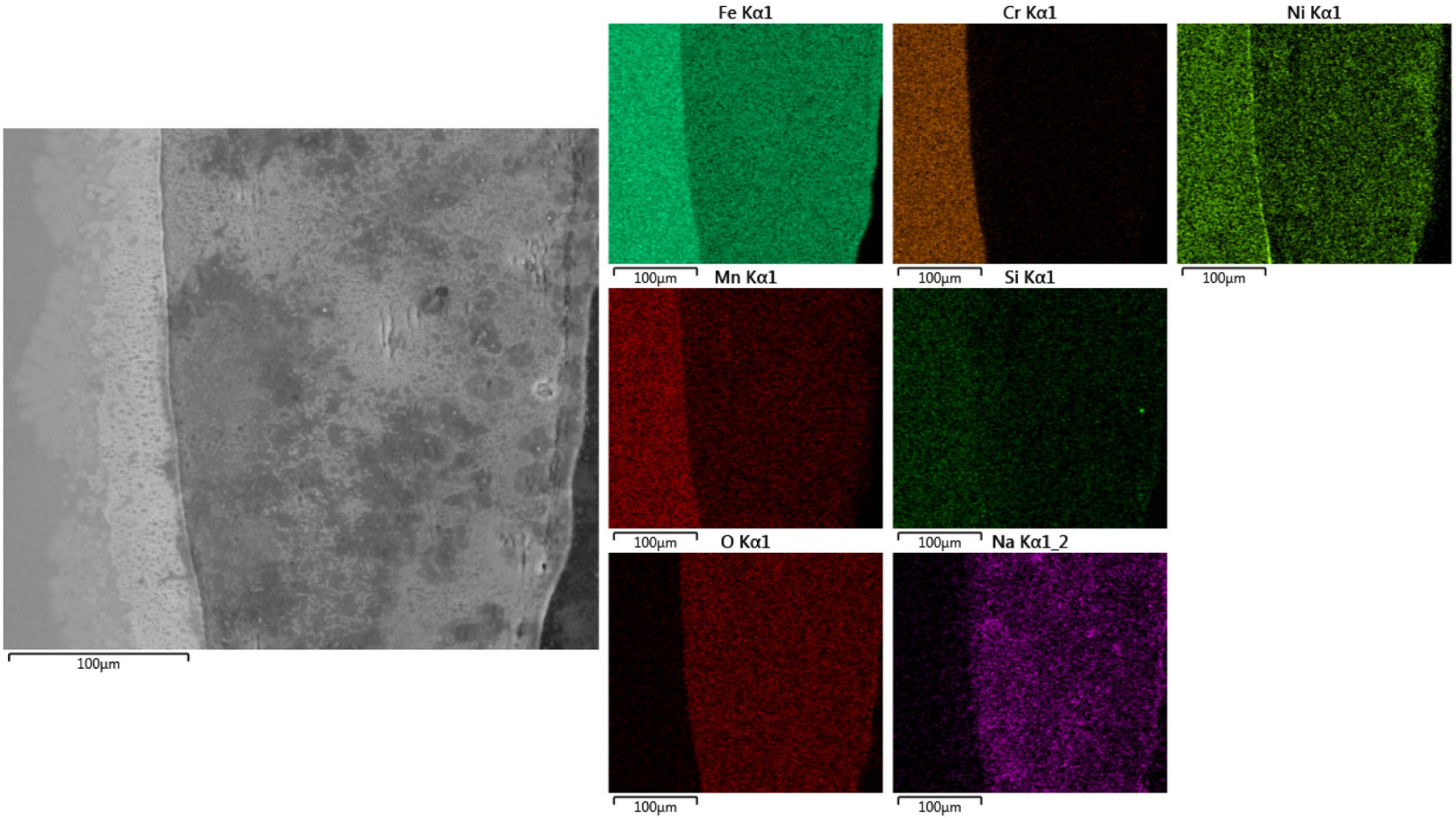

Figure 3.14: SEM image and EDS elemental maps for N60 exposed to 630°C Solar Salt for 600hr. 1000x magnification. Note that the corrosion scale is significantly larger than that of the other alloys and that the magnification is different.

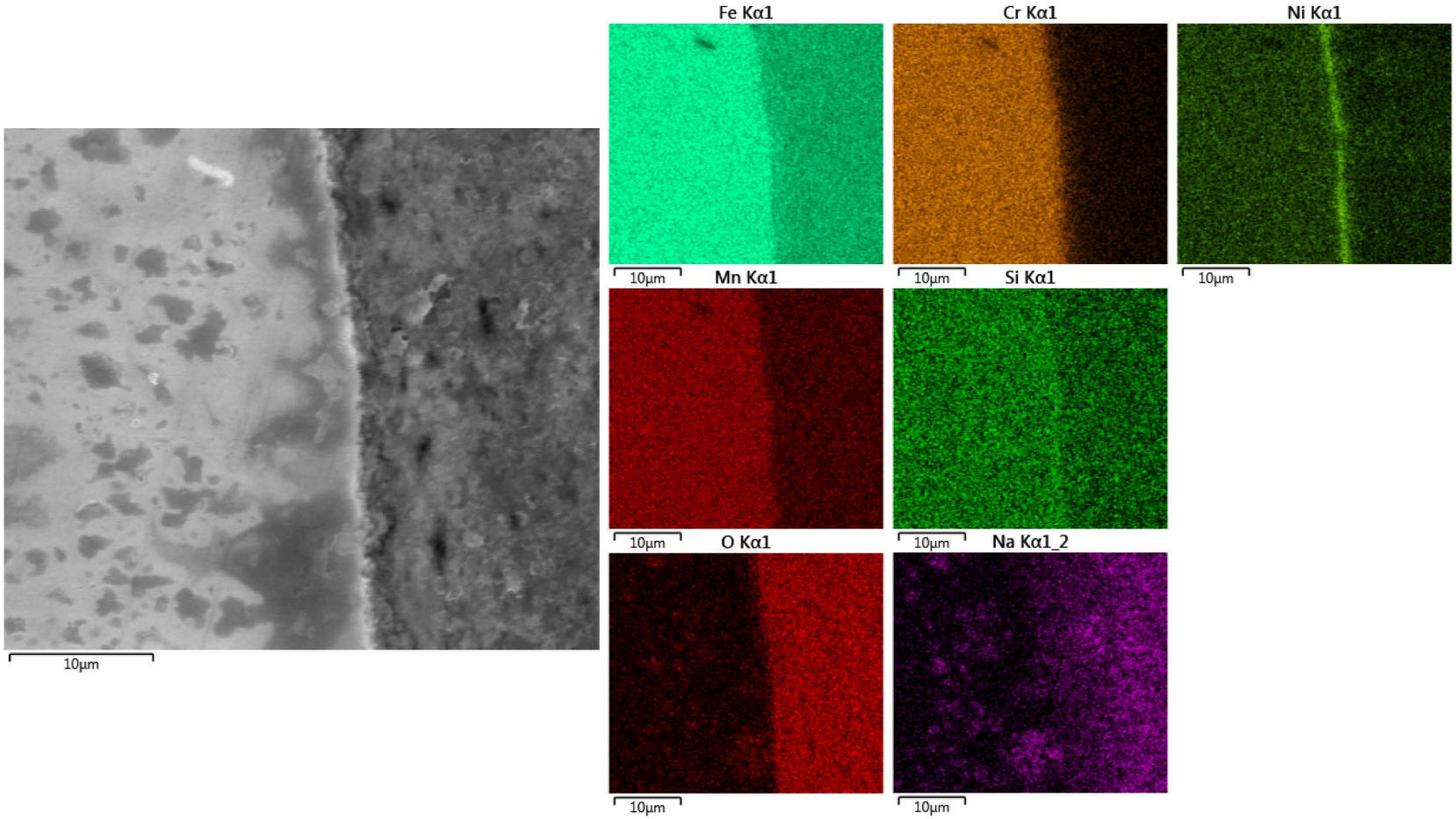

Figure 3.15: SEM image and EDS elemental maps along the metal-oxide boundary for N60 exposed to 630°C Solar Salt for 600hr. 4000x magnification.

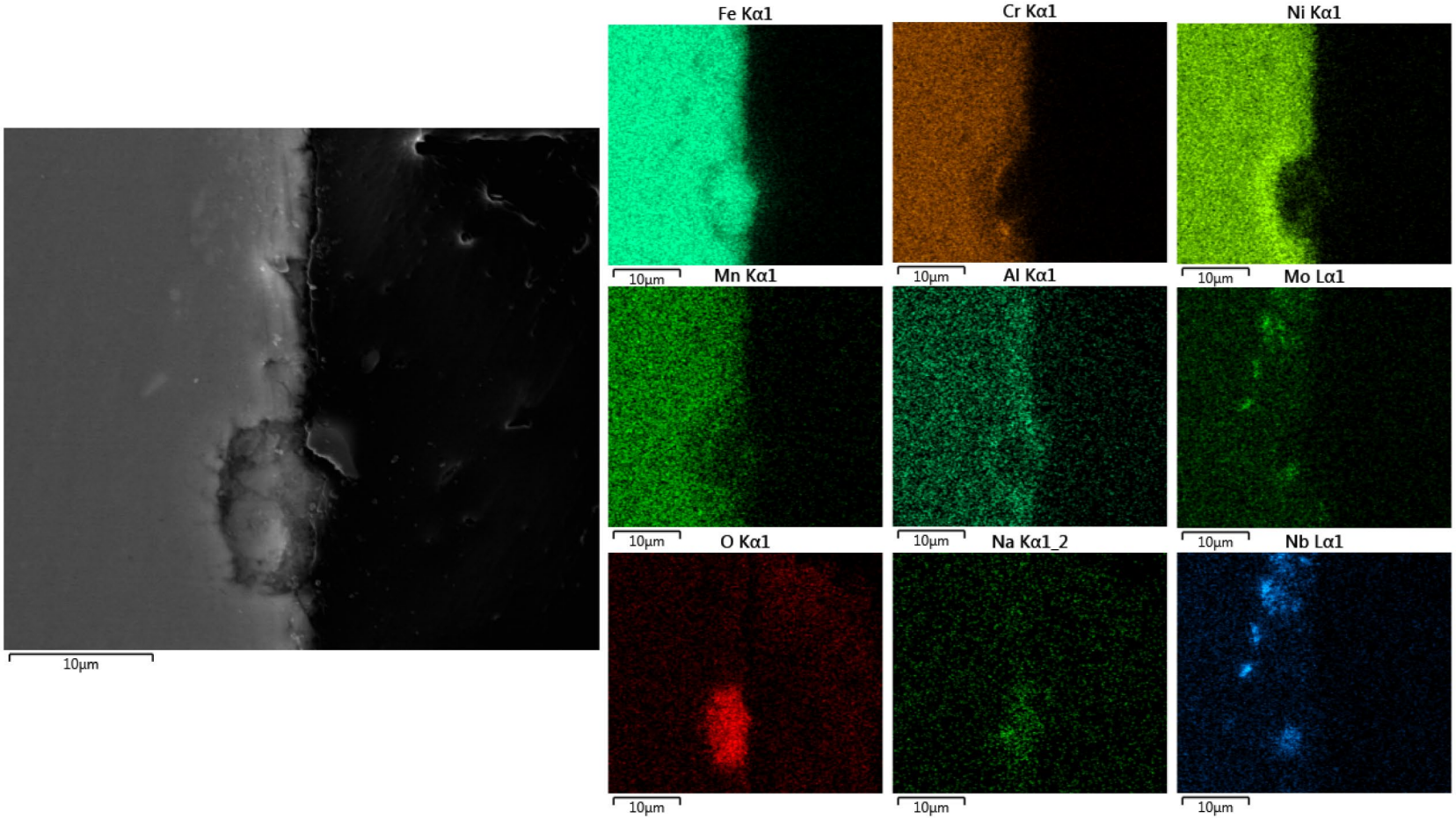

Figure 3.16: SEM image and EDS elemental maps for AFA-OCB exposed to 630°C Solar Salt for 600hr. 4000x magnification.

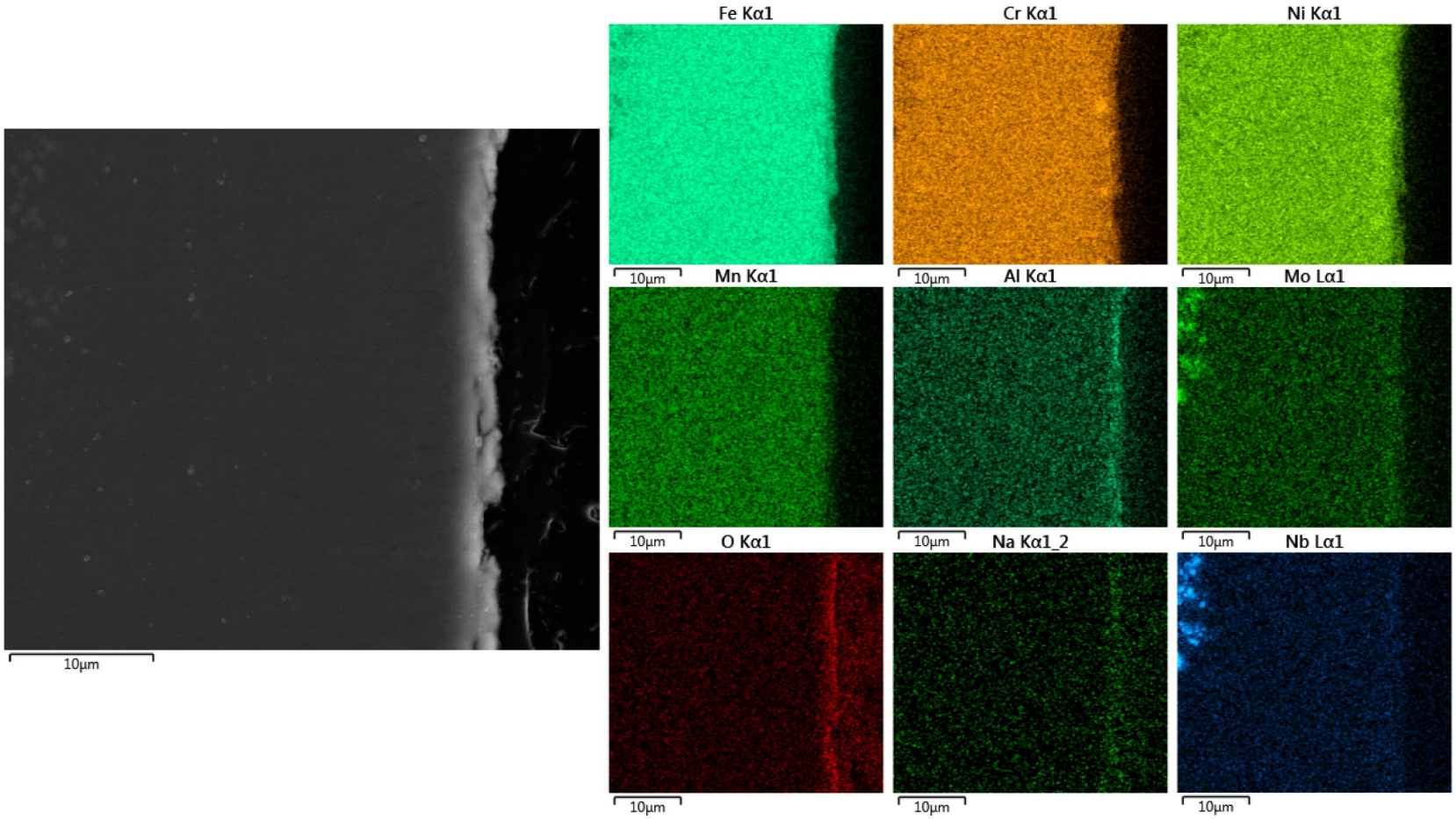

Figure 3.17: SEM image and EDS elemental maps for AFA-OCF exposed to 630°C Solar Salt for 600hr. 4000x magnification.

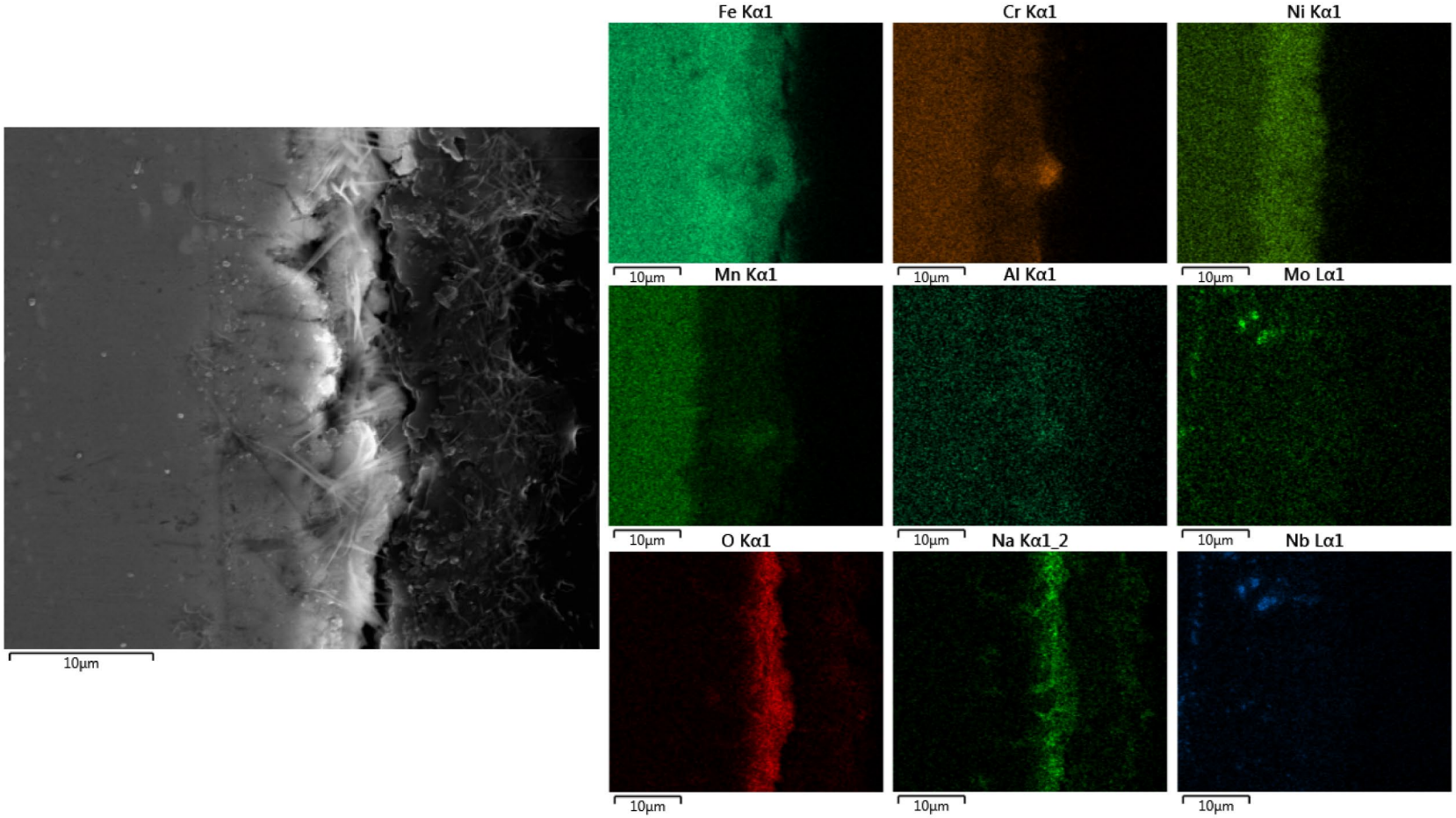

Figure 3.18: SEM image and EDS elemental maps for AFA-OCL exposed to 630°C Solar Salt for 600hr. 4000x magnification.

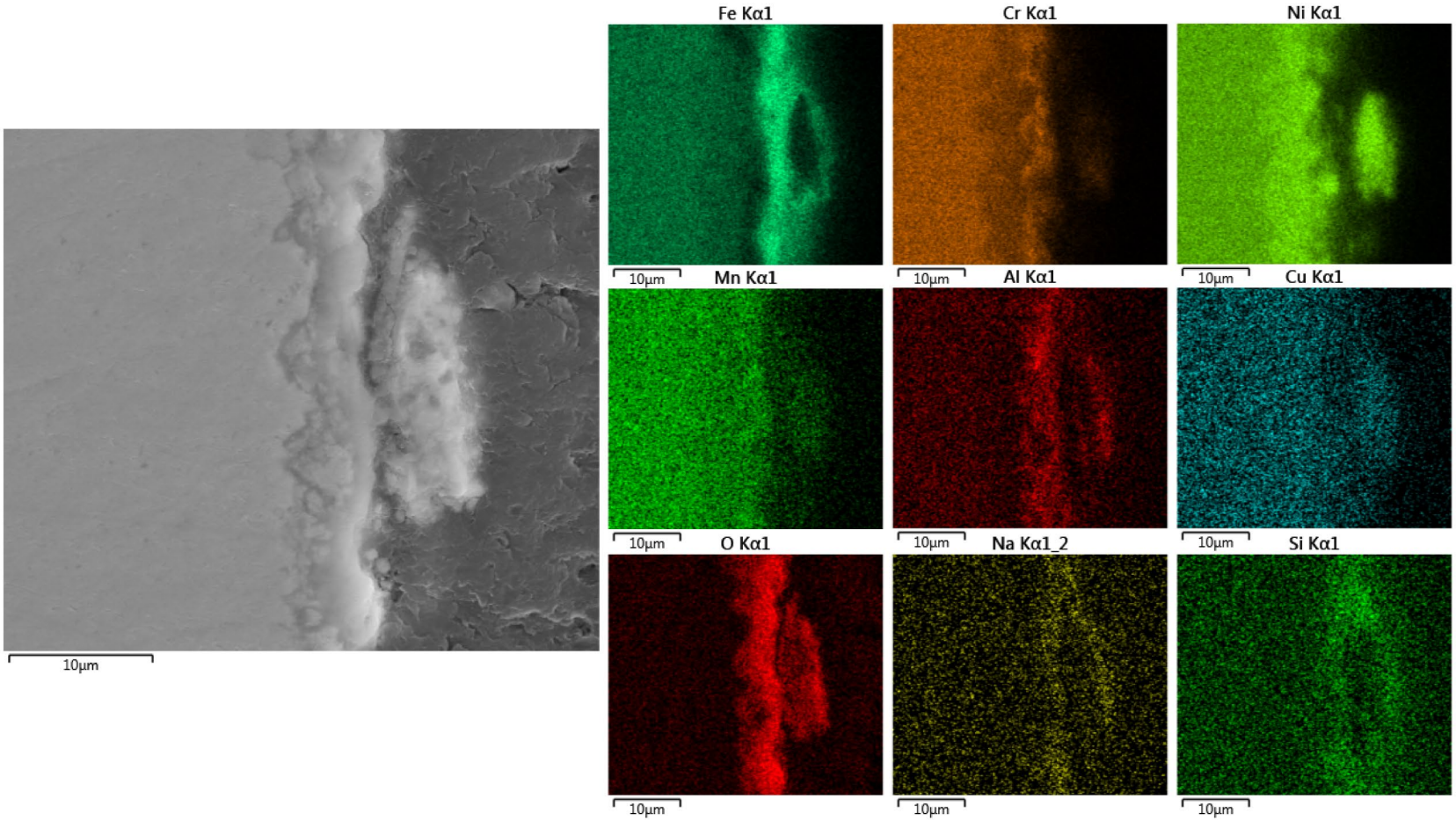

Figure 3.19: SEM image and EDS elemental maps for Alloy 601 exposed to 630°C Solar Salt for 600hr. 4000x magnification.

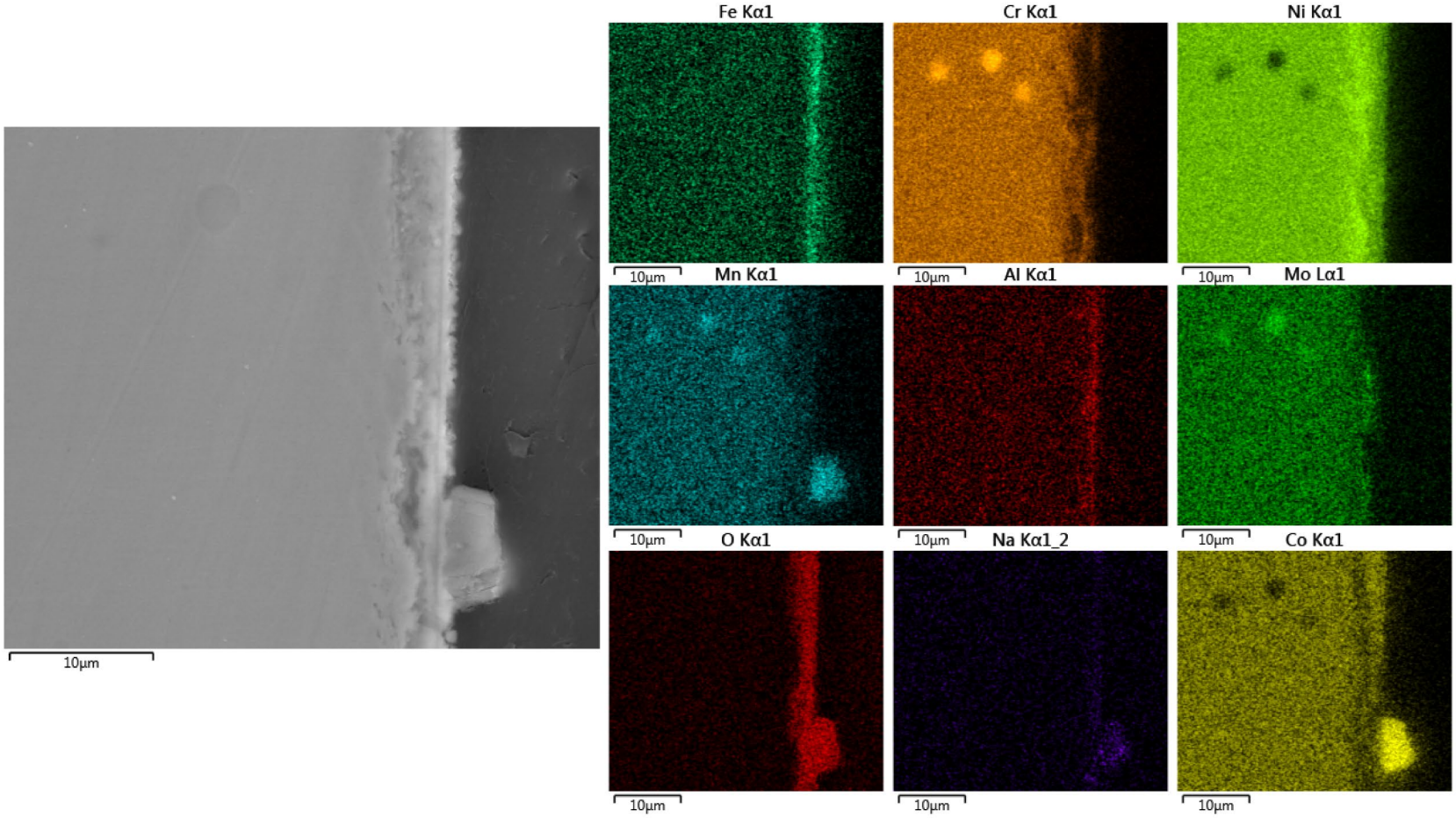

Figure 3.20: SEM image and EDS elemental maps for Alloy 617 exposed to 630°C Solar Salt for 600hr. 4000x magnification.

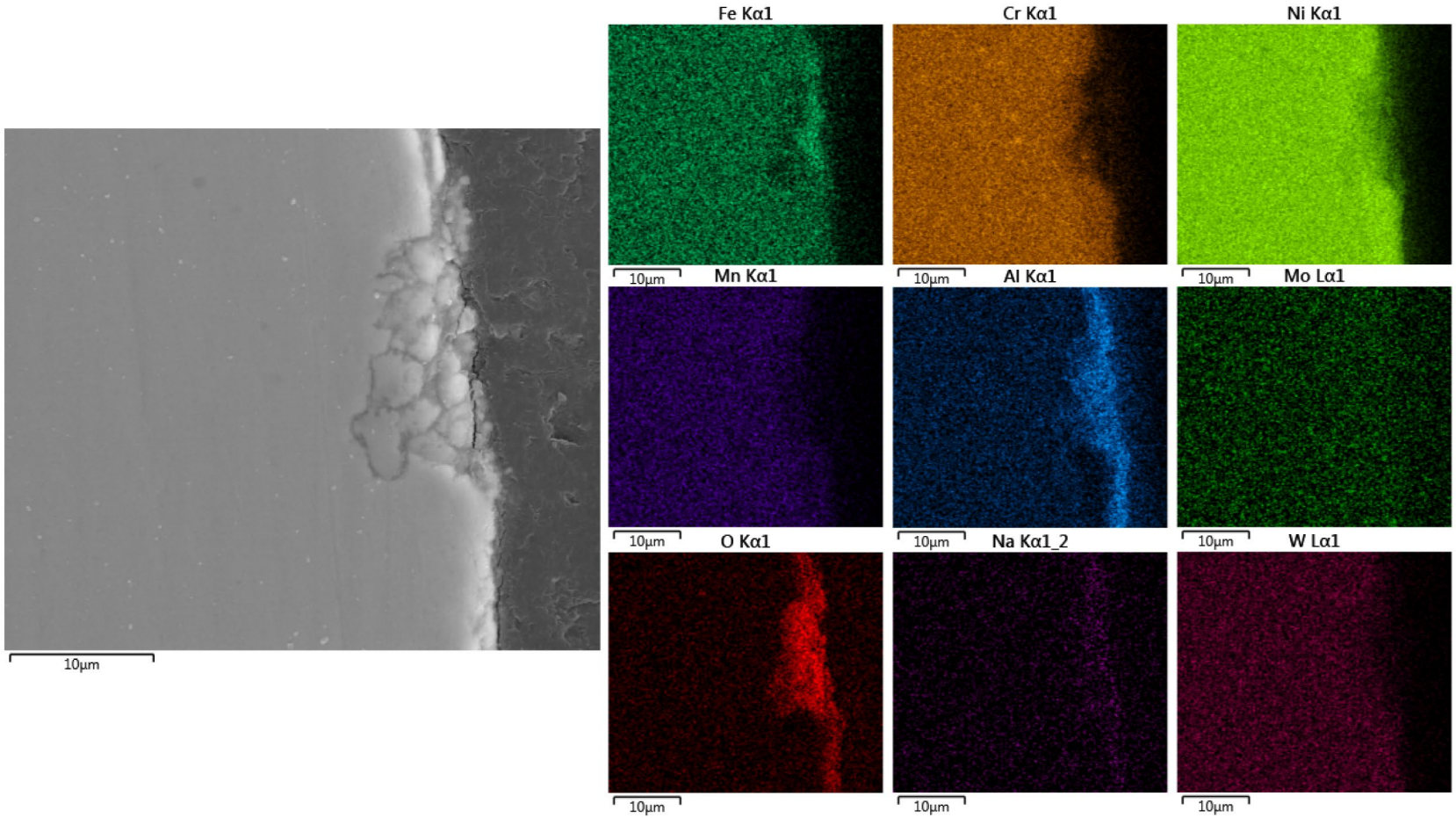

Figure 3.21: SEM image and EDS elemental maps for Alloy 214 exposed to 630°C Solar Salt for 600hr. 4000x magnification.

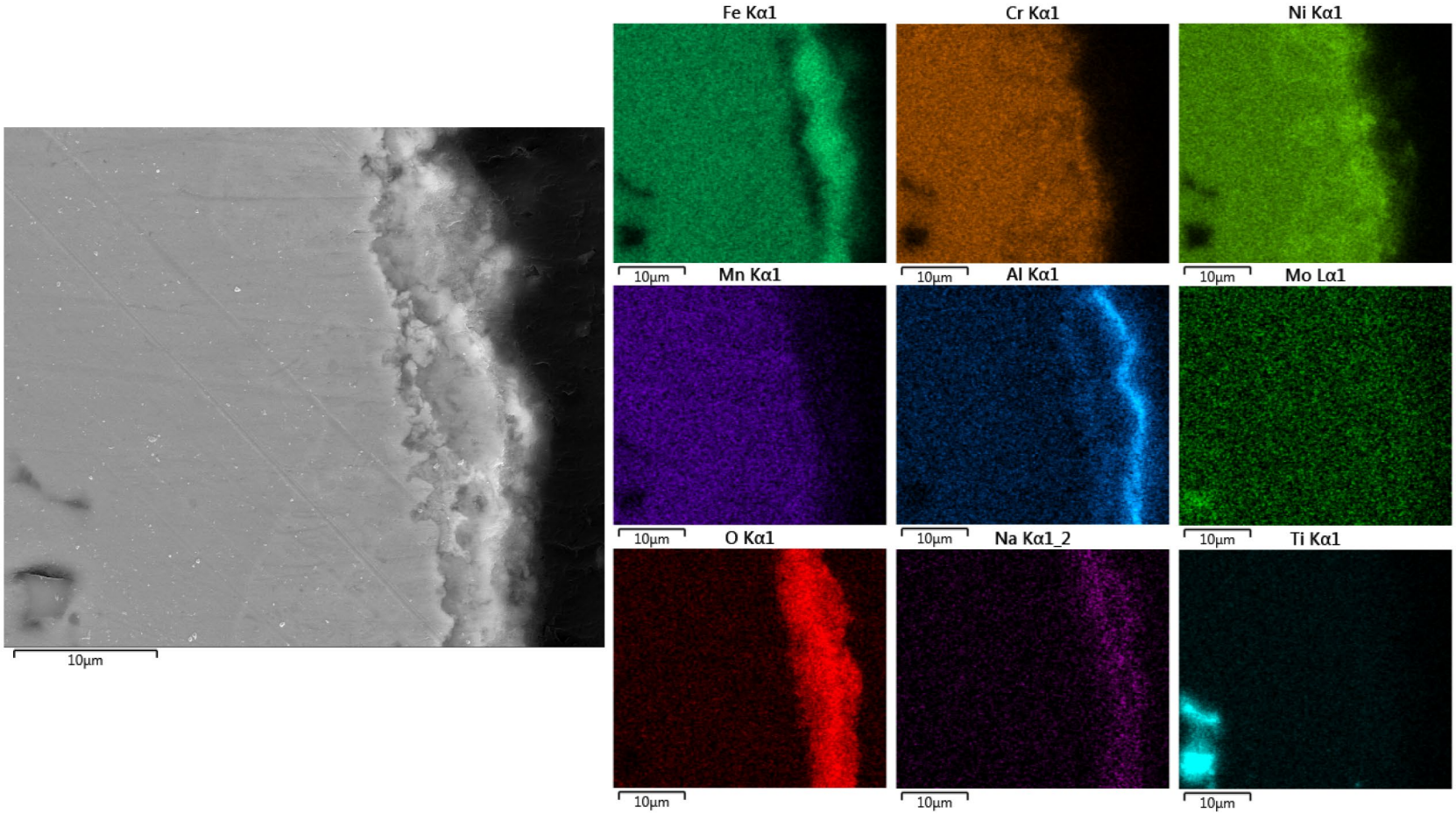

Figure 3.22: SEM image and EDS elemental maps for Alloy 224 exposed to 630°C Solar Salt for 600hr. 4000x magnification.

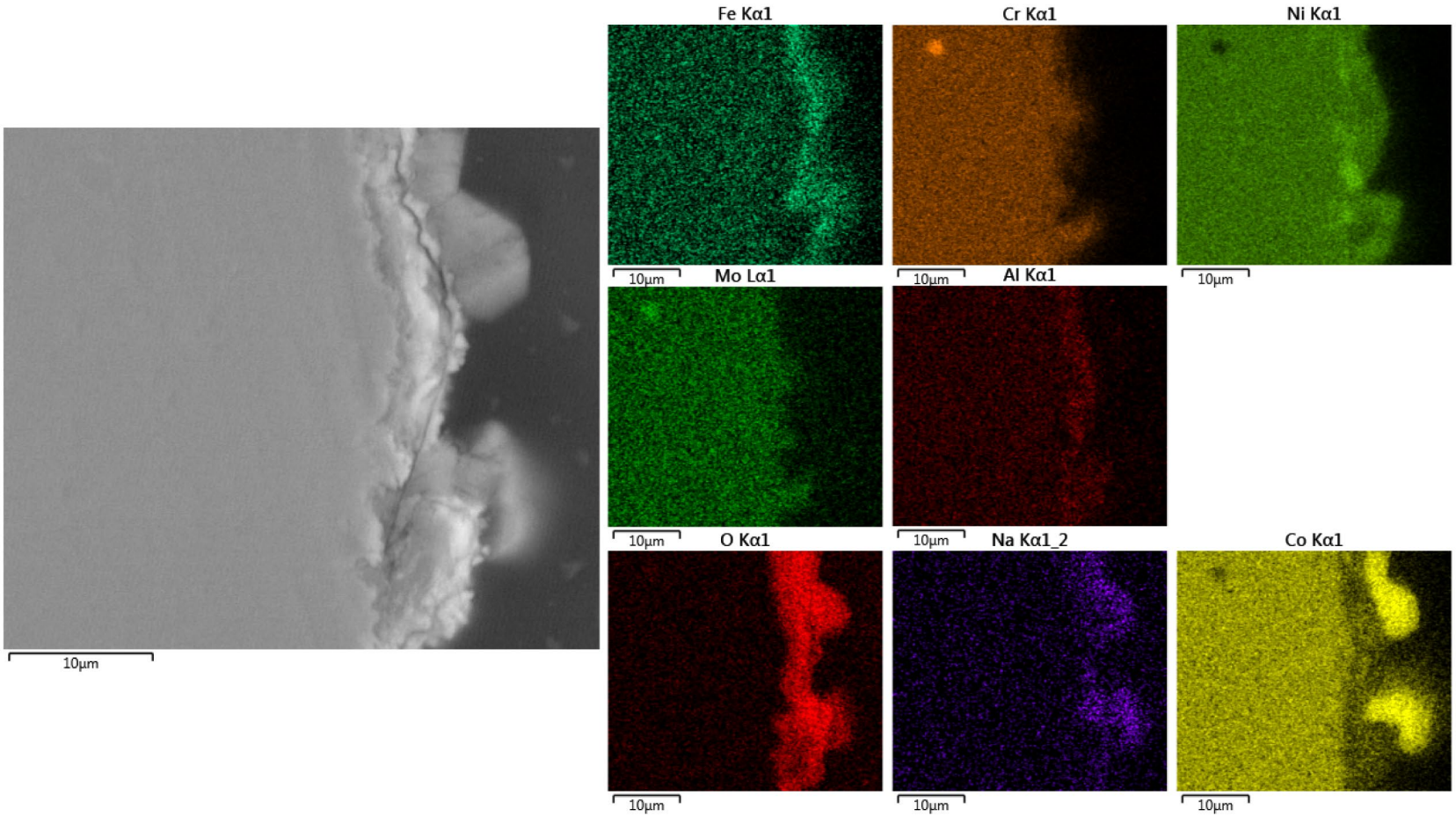

Figure 3.23: SEM image and EDS elemental maps for Alloy 233 exposed to 630°C Solar Salt for 600hr. 4000x magnification.

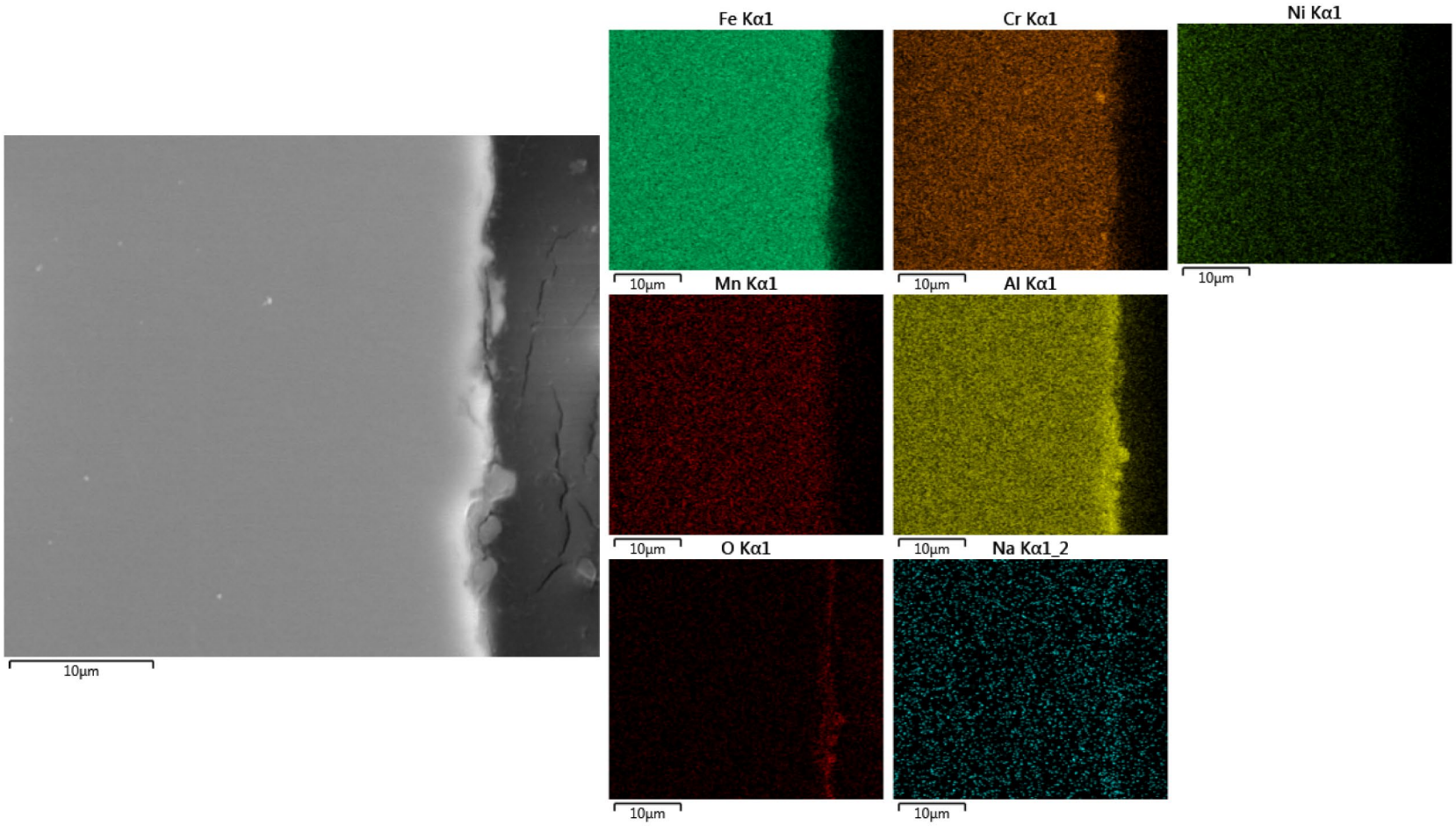

Figure 3.24: SEM image and EDS elemental maps for aluminide coating exposed to 630°C Solar Salt for 600hr. 4000x magnification.

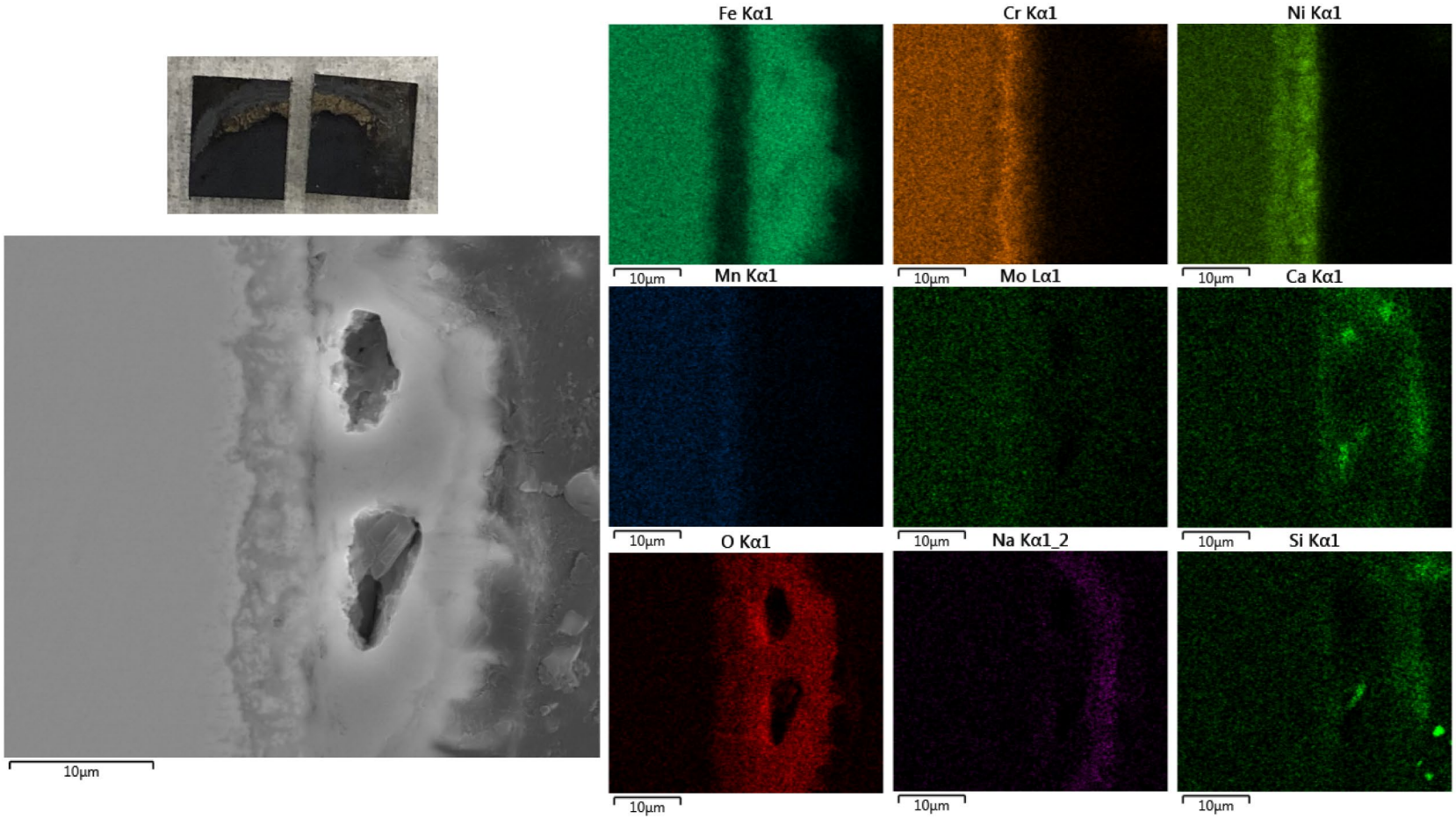

Figure 3.25: SEM image and EDS elemental maps for the meniscus region of Alloy 709 exposed to 630°C Solar Salt for 600hr along with an optical image of the associated area (top left). 4000x magnification.

In addition to the features observed in the corrosion scales of the various materials that were detailed above, there were several other interesting findings from the microscopy. In general, examination of the meniscus regions of the corroded samples did not reveal any significant differences in the corrosion scale. The only meniscus that exhibited features of note was that from Alloy 709 (Figure 3.25). In the Alloy 709 sample meniscus, elevated amounts of Ca and Si particles were observed, some of which were embedded within the corrosion oxide layers. Ca and Si are very common environmental impurities and can be introduced from many avenues during the experiment (sample preparation, salt, crucible, vessel, air, etc.). It is evident that these impurities float on top of molten nitrate salt and collect at the meniscus region. At the end of the day, these impurities do not appear to have a significant effect on the corrosion performance of the material. The embedded particles caused the Alloy 709 oxide layer to protrude but do not appear to have caused preferential corrosion deep into the material. For all the other materials, despite the visually obvious meniscus lines, the corrosion scale at the meniscus regions were indistinguishable than that from the bulk submerged surface in the SEM.

For the aluminide coating, while no pockets of extended corrosion akin to the well performing AFA alloys were observed, cracking of the aluminide coating was readily found along the sample surface (Figure 3.26). EDS mapping of cracked regions did not reveal the presence of oxides or salt species, indicating that these cracks were likely formed as a result of the post-corrosion sample preparation process. However, the presence of these cracks indicates the brittle nature of the aluminide coating with potential implications for long-term applications that may have significant stresses involved (such as thermal stresses and flow stresses). Literature indicates that aluminide coatings may have self-healing properties at elevated temperatures, but it is unknown if this would be the case in a nitrate salt environment.[98,99] Figure 3.26 also shows the complex microstructure formed as a result of the aluminizing process. This will be detailed further in Chapter 5.

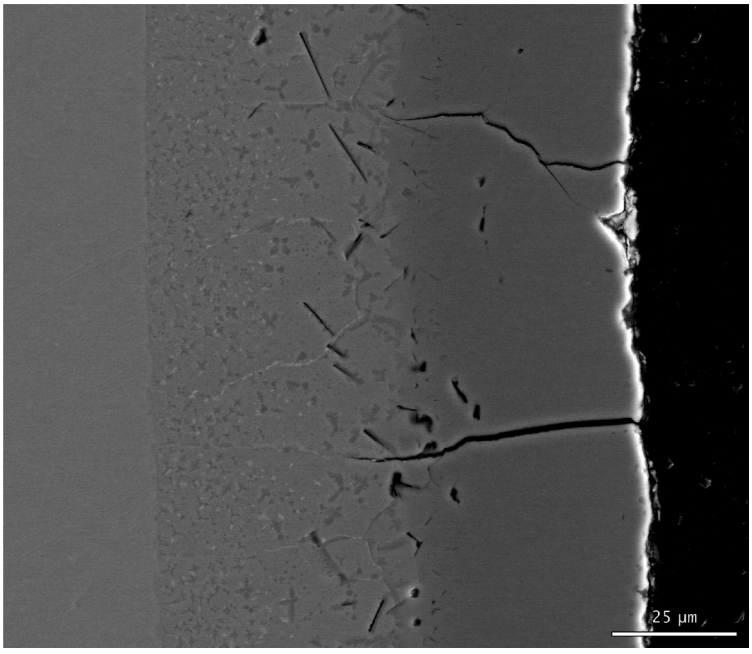

Figure 3.26: Cracking of the aluminide coating observed during microscopy.

3.4. Discussion

3.4.1. Comparison of Weight Change vs. Oxide Depth Corrosion Rates

Utilizing the SEM images, corrosion rates for the various alloys can also be estimated using the length of the corrosion scales observed through the equation:

$$SEM\ Corrosion\ Rate = \frac{Corrosion\ Oxide\ Thickness}{Time\ of\ Exposure}$$

Figure 3.27 shows a comparison of the corrosion rates obtained via SEM imaging vs. the conservative corrosion rate values obtained via weight change. The SEM corrosion rate is found to be consistently higher than that calculated from weight change. This is likely due to combined effects of the oxide scales being less dense than the base metal and contributing extra material/mass (like O) as well as the infiltration and presence of salt species artificially inflating the oxide thicknesses. While the specific corrosion rate values differ greatly between the SEM image and weight change calculations, the relative performance of the materials regarding nitrate salt corrosion is preserved. Other than 601 and 233 which swapped positions, the order from lowest to highest corrosion rate is consistent.

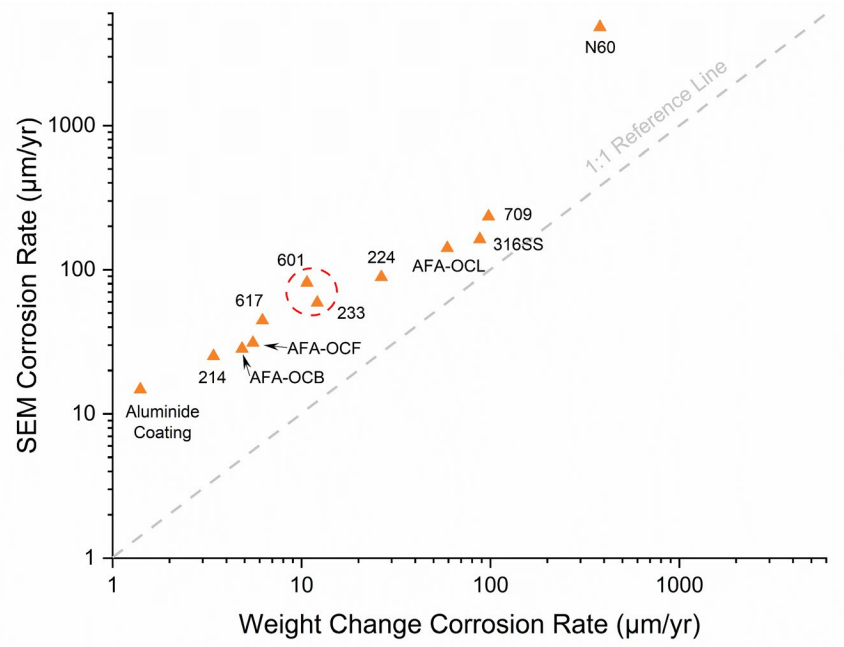

Figure 3.27: Comparison between corrosion rates obtained via SEM images vs. those obtained via weight change.

Note that this method using oxide thicknesses is performed in this discussion for illustrative purposes. While this method has been used in others studies[87,89] it is not a preferred method due to significant errors caused by aspects such as porosity, spallation of oxide layers, nonuniformity of layers, multi-component layers, and dissolution of alloying elements (like Cr in nitrate salt). However, given that corrosion studies are often limited in samples and overall statistics, this analysis shows that crude corrosion rate measurements from microscopy can still provide reliable conclusions regarding the relative performance of materials. This indicates that

the size of the corrosion scale observed through microscopy is useful as a rough guide for overall corrosion performance.

3.4.2. Summary of Corrosion Scale Morphologies

Table 3.5 details the various corrosions layers and their arrangement exhibited by the materials exposed to 630°C Solar Salt for 600hr. Estimations of the various layer sizes are provided from microscopy measurements. A common oxide layer arrangement was generally shared amongst the alloys: starting with $NaFeO_2$ and Fe oxides on the surface, followed by Cr_2O_3 or Al_2O_3 (for AFA alloys), and a Cr (and Mn) de-alloyed region in the near surface bulk material. Variations between alloys were mainly dependent on the presence or absence of a complete or partial Al_2O_3 layer in the corrosion scale. Non-AFA alloys relied solely on the presence of thick Fe oxide layers that enabled the formation of stable Cr_2O_3 underneath. Metal precipitate phases were observed near the metal surface for several alloys, exact identities depending on the alloying elements present. Of note, the alloys with compositions containing significant amounts of Co (617 and 233) exhibited large Co phases on the surface of their corrosion scales.

It was evident during microscopy that separation occurred between some of the corrosion layers likely as a result of the stresses induced during the sample preparation process. Figure 3.28 shows an extreme example from the corrosion scale of N60, in which the oxide layer can be readily observed to have fully separated at the metal-oxide interface. Similar separations were noted during the microscopy of the other corroded materials and are highlighted in Table 3.5. While the corrosion scales analyzed through microscopy in this study appear to be complete and therefore indicate adherence of the oxide layers during the experiment, these separation layers represent interfaces that could be prone to spallation under corrosion applications involving significant stress. Spallation of oxide layers (as well as other phases on the oxide surface like the Co-containing phases for 617 and 233) could have significant implications both in terms of exposing fresh metal surfaces to corrosion as well as fouling in nitrate salt applications.

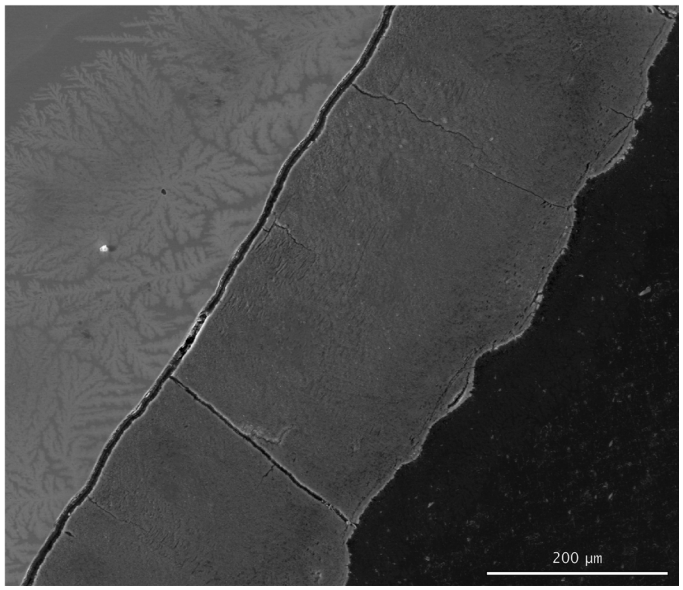

Figure 3.28: Separation of the oxide layer along the metal-oxide interface observed for the corroded N60 sample.

Table 3.5: Summary of corrosion scale morphologies exhibited by materials corroded in 630°C Solar Salt for 600hr. Layers that were observed to separate during microscopy are highlighted in orange.

	Alloy	Innermost Layer	Intermediate Layer	Outermost Layer	Comments (Orange = Separation Layer)
Iron Alloys	316SS	Cr depletion/Ni enrichment (~5µm)	Cr oxide + Fe oxide (~3µm) (~6µm)	Fe+Na oxide (~6µm)	• Corroborates with high temperature nitrate salt 316SS literature
	N60	Ni w/ Na penetration (~1µm)	Cr depleted alloy oxide w/ Na (~250um)	Fe+Na oxide (~10µm)	• Dendritic features in metal (~75µm) • Mn phases on oxide surface • Very thick flaking corrosion scale
	709	Cr oxide/Ni inclusion oxide pegs (~10µm)	Fe oxide (~15µm)	Fe+Na oxide (~10µm)	
	AFA-OCB	Al oxide (~3µm, isolated spots upwards of 10µm)			• Majority of surface with ~3µm Al oxide, but isolated places of greater corrosion • Prominent MoNb phases in bulk
	AFA-OCF	Al oxide (~3µm)			• Prominent MoNb phases in bulk
	AFA-OCL	Cr depletion/Ni enrichment (~10µm)	Fe Oxide (~8µm)	Fe+Na oxide (~6µm)	• Incomplete Cr and Al oxide layers present • Prominent MoNb phases in bulk
Nickel Alloys	601	Cr depletion/Ni enrichment (~7µm)	Cr oxide + Al oxide/Ni inclusion oxide pegs (~7µm)	Fe+Na oxide (~7µm)	
	617	Cr depletion/Ni enrichment (~4µm)	Al oxide (~1µm)	Fe oxide w/ Na (~2µm)	• CoMnNa phases on oxide surface (~7µm) • CrMnMo and TiN phases in bulk
	214	Al oxide (~3µm, isolated spots upwards of 10µm)			• Majority of surface with ~3µm Al oxide, but isolated places of greater corrosion • CrMn phases in bulk
	224	Cr depletion/Ni enrichment (~13µm)	Al oxide (~1µm)	Fe+Na oxide w/ Al oxide (~7µm)	• Outermost Al oxide is likely unprotective • Cr depletion/Ni enrichment region is nonuniform • CrMn and TiN phases in bulk
	233	Cr depletion/Ni enrichment (~5µm)	Al oxide (~2µm)	Fe oxide w/ Na (~2µm)	• CoMnFeNa phases on oxide surface (~7µm) • CrMo and TiTaSi phases in bulk
	Aluminide Coating	Al oxide (~3µm)			• Coating prone to cracking • Diffusion coating layers within bulk metal

Table 3.6: The alloy compositions along with the weight change corrosion rates obtained for the various alloys.

Alloy	Alloying Element*											Corrosion Rate (µm/yr)
	Fe	C	Cr	Ni	Al	Mn	Mo	Co	Nb	Si	Cu	
316SS	Bal.	0.04	17.5	11.5	-	1	2.25	-	-	0.5	-	**49.6 + 38.2**
709	Bal.	0.08	20	25	-	0.9	1.5	-	-	0.4	-	**62.5 + 35.2**
N60	Bal.	0.1	17	8.5	-	8	0.75	-	-	4	-	**212.7 ± 166.9**
AFA-OCB	Bal.	0.2	14	25	3	2	2	-	1	-	0.5	**5.2 ± 0.3**
AFA-OCF	Bal.	0.2	14	25	4	2	2	-	2.5	-	0.5	**4.7 ± 0.1**
AFA-OCL	Bal.	0.2	14	12	2.5	10	-	-	1	-	3	**58.0 ± 1.0**
601	12.5	0.1	23	Bal.	1.35	1	-	-	-	0.4	1	**6.9 + 3.8**
617	3	0.1	22	Bal.	1.15	1	9	12.5	-	1	0.5	**3.6 + 2.6**
214	4	0.15	16	Bal.	4.5	1	1	2	-	0.5	-	**2.2 + 1.2**
224	27.5	0.05	20	Bal.	3.8	0.5	0.5	2	-	-	-	**17.4 + 9.1**
233	1.5	0.1	19	Bal.	3.3	0.4	7.5	19	-	-	-	**7.8 + 4.3**

*Some minor alloying elements have been omitted

3.4.3. General Protectiveness of Major Alloying Elements

Based on the obtained weight change corrosion rates and microscopy, several conclusions regarding the effects of certain alloying elements on corrosion performance in elevated temperature Solar Salt can be made:

- Aluminum is highly beneficial to corrosion performance. The best performing alloys were those able to form a complete Al_2O_3 layer. This alumina layer minimized further corrosion, resulting in thin overall corrosion scales and low corrosion rates. As some of the AFA alloys did not appear to be fully protected, it is likely that a critical concentration of Al (in relation to the identity and amounts of other alloying elements) is needed for complete protection.
- Iron forms thick, but stable oxide layers on the surface of the material. However, the Fe oxide layers are prone to cracking and separation, indicating the porous nature of these layers and limiting their protectiveness. The Fe oxide on the surface tended to react with Na from the nitrate salt to form $NaFeO_2$.
- Nickel appears to be highly stable in nitrate salt. Nickel alloys that did not appear to be fully protected by an alumina layer exhibited lower corrosion rates than steel alloys that were also not protected by alumina. It is unclear whether Ni forms a complete oxide layer (NiO) that protects against further corrosion. If it does, it would likely be especially thin given the lack of significant O signal within the Ni enriched regions and likely not able to significantly prevent other elements from diffusing and reacting (as seen in the N60 microscopy sample).
- Chromium as an alloying element appears detrimental in terms of nitrate salt corrosion. This is due to the high solubility of Cr in nitrate salt and, unlike in many other oxidizing environments, highlights the inability to rely on Cr_2O_3 for corrosion resistance in nitrate salt. However, stable Cr_2O_3 layers were observed under thick Fe oxide layers. This means Cr could potentially offer corrosion protection through a Cr_2O_3 layer but only if Fe oxide of sufficient thickness exists to prevent its contact with the nitrate salt. This also relies on the Fe oxide layers to not spall off and expose the underlying Cr_2O_3 layer.
- Manganese, like chromium, appears highly soluble in nitrate salt. Throughout all the alloys, Mn tended to follow the same composition profiles as Cr. However, unlike Cr which sometimes formed Cr_2O_3, Mn did not form any stable phases that could provide protection from further corrosion. This indicates that Mn is especially detrimental in terms of corrosion resistance.
- Molybdenum similarly is hypothesized to be soluble in nitrate salt. However, the depletion profiles for Mo did not appear to be as prominent as Cr and Mn for the Mo-containing alloys except for 233. This hints at potentially reduced diffusion of Mo compared to Cr and Mn, though regardless, Mo does not appear to provide any significant corrosion resistance in nitrate salt. Sublimation of Mo oxide (MoO_3) is also noted to be important at temperatures above 600°C,[100–104] meaning that Mo likely would not be able to contribute to corrosion resistance in the oxide form in elevated temperature nitrate salt.
- Cobalt as an alloying element appears to result in the formation of Co-containing phases on the surface of the corrosion scale. While several other phases containing various alloying elements were observed amongst the various alloys, these tended to be within the bulk metal rather than on the oxide surface.

Through this alloying element analysis, differences in the observed corrosion rates for the various materials can be explained to a degree. The significant concentration of Mn and reduced amount of Ni in N60 compared to 316SS could explain the substantial increase in corrosion rates observed (though as mentioned in Section 3.3.1. galvanic effects could have also played a significant role). Compared to the amount of highly soluble alloying elements (Cr and Mn), the concentration of Ni in the alloy was insufficient to form a sufficiently stable bulk metal boundary, resulting in runaway corrosion. Similarly, the high amounts of Mn and relatively low amounts of Ni in AFA-OCL compared to the other AFA steel alloys may have prevented the Al from forming a complete Al_2O_3 layer. This resulted in the corrosion rate for AFA-OCL being on the order of the non-AFA 316SS and 709. In terms of the nickel alloys, 224 had significantly higher corrosion rates compared to the other nickel alloys which could be explained by the relatively high amounts of Fe in the alloy that would corrode and form oxide layers. Given the Al content in 224, it is however unclear why a complete alumina layer was unable to be formed like in AFA-OCB and AFA-OCL. Regardless, given that 224 is a nickel-based alloy, its corrosion performance was better than the iron-based steels similarly not protected by alumina.

This elemental analysis for the differences in corrosion rates is summarized in Table 3.6, which shows the alloy compositions along with the weight change corrosion rates obtained for the various alloys. Alloying elements deemed to be beneficial/detrimental to corrosion resistance are noted (relative to Fe). Certain values of alloying elements are highlighted as likely elemental explanations for the significant differences in corrosion performance for some alloys when compared to other similar alloys. The Co content in alloys 617 and 233 are also highlighted given the presence of significant Co phases on the oxide surfaces for these alloys.

3.5. Conclusion

Through simultaneous corrosion of many material varieties coupled with subsequent weight change and microscopy analysis, the effects of alloying elements on corrosion resistance in elevated temperature Solar Salt were examined. Likely effects from Cl^- impurities between different specifications of nitrate salt complicate the comparisons, but general conclusions can still be made in good confidence. Corrosion rates calculated from SEM images are significantly higher than corresponding corrosion rates calculated from weight change, but the relative corrosion performance between alloys is generally preserved.

The best performing materials in 630°C Solar Salt for 600hr were those that were able to form complete and stable alumina layers. This included AFA-OCB, AFA-OCL, 617, 214, and the aluminide coating which all exhibited corrosion rates less than or around 5µm/yr. This indicates the highly beneficial effects of Al as an alloying element with respect to corrosion resistance in nitrate salt. Some other AFA alloys also showed the presence of alumina in their corrosion scales, but the alumina did not appear to be fully protective. This is likely due to their compositions including significant amounts of elements deleterious to corrosion performance. This includes Cr and Mn which are known to be highly soluble in nitrate salt. 601 and 233, two nickel alloys, still managed to exhibit corrosion rates on the order of 10µm/yr. 224, another nickel alloy, exhibited a higher corrosion rate on the order 20µm/yr potentially due to its relatively high Fe content, but this is still well below the corrosion rates exhibited by the Fe-based steels which were above 50µm/yr. Despite being an AFA alloy, AFA-OCL exhibited a corrosion rate similar to the non-AFA

steels, likely due to the significant Mn content in this alloy. The extremely high corrosion rates for N60 could be explained by the relatively high Mn and low Ni content, but potential galvanic effects for the N60 samples complicate confidently ascertaining the representative corrosion behavior for the alloy.

Cr_2O_3 was found to be stable underneath significant thicknesses of Fe oxide. The protection offered by this chromia layer is likely limited, however, due to potential porosity and fragility of the Fe oxide layers. Fe oxide reacted with Na at the corrosion scale surface to form $NaFeO_2$. Co-containing alloys, 617 and 233, revealed the presence of Co phases on the surface of the oxide scale. These phases were found to be loosely adhering and may have significant implications for nitrate salt applications.

Note that much of the above conclusions are from analysis considering only alloy composition and do not include potential microstructural effects on the observed corrosion rates. Discussion on potential microstructural effects in elevated temperature Solar Salt corrosion such as grain boundaries is explored in Chapter 5. For the samples that were only partially submerged in nitrate salt, the meniscus region does not appear to cause elevated corrosion, but the presence of impurities that likely float in the nitrate salt is increased. For the alloys corroded in 600°C Solar Salt, their corrosion rates were almost half that of when corroded in 630°C Solar Salt. Further investigation on the magnitude of change in corrosion rates as a function of temperature will be performed in Chapters 4 and 5.

Chapter 4 – Temperature Range Corrosion Study

4.1. Background

Figure 1.8 in the Introduction highlighted the rapid increase in corrosion rates as temperatures rise above 570°C. While the overall trend is clear across the data, significant jumps in temperature exist within the literature, reducing the confidence in the rate of increase in corrosion as a function of temperature. Combined with the limited data and the previous discussion in Section 3.1 about cross-comparison of data, it becomes prudent to perform systematic studies targeting the effect of temperature changes on corrosion rates in elevated temperature Solar Salt. In this study, 316SS was exposed to elevated temperature Solar Salt ranging from 570°C to 650°C with several intermediate temperature steps.

Furthermore, the results from Chapter 3 highlighted the difficulties in comparing corrosion rates extracted from partially submerged samples to those that were fully submerged. This provided motivation to alter the experimental procedure for this study to ensure full submersion of salt exposed samples in order to remedy this issue. Given that corrosion of the materials in regions above the salt line was readily apparent, corrosion of samples entirely in the gas space above the molten nitrate salt was also investigated as part of this study.

4.2. Materials and Methods

The overall corrosion setup and general experimental details have been described extensively in Chapter 3. In this study, 316SS samples were exposed to Solar Salt at a wide range of elevated temperatures: 570°C, 590°C, 600°C, 610°C, 620°C, 630°C, and 650°C. As explained throughout the dissertation thus far, 316SS is currently employed in concentrated solar power plants exposed to Solar Salt and acts as the main alloy for comparison throughout this dissertation work. The coupons were configured within the corrosion vessels to be either fully submerged within the salt or fully in the gas space (air) above the salt. Figure 4.1 shows the corrosion vessel schematic including the two-way sample hanging configuration. Gas space corrosion coupons were hung from an alumina tube threaded through two holed-bars attached to the vessel head. For the fully submerged samples, 316SS wire was threaded through the tube hanging the gas space samples and another alumina tube that would be submerged in the molten salt. Each sample was isolated from the vessel components, the wire, and each other using alumina sleeves and spacers to minimize potential galvanic effects.

Rectangular coupons were fabricated from a 316SS sheet to a length of 3.7cm, width of 1.4cm, and a thickness of 1.6mm. A portion of the samples were fabricated from leftover 10cm coupons from the Chapter 3 experiments that were cut in half and measured roughly 5cm in length, 1.3cm in width, and 3mm in thickness. The different-dimensioned samples were split amongst the various experiments to detect any potential geometric biases. Based on the data obtained and as will be discussed in Section 4.4.2., the effect of the dimensional differences was deemed negligible. Two gas space coupons and three salt coupons in each condition were used for weight change corrosion rate determination. Samples were exposed for 645hr with a semi-sealed gas space at <1psig. 500g of Solar Salt made from the same 0.01wt% Cl- impurity batch of nitrate salt described in Section 3.2.4 was used in each experiment. As described in Section 3.2.5., exact exposure times at test temperature above 3°C below the target temperature were

calculated and weight change corrosion rates were determined following ASTM G1-03 and ISO 8407 guidelines.

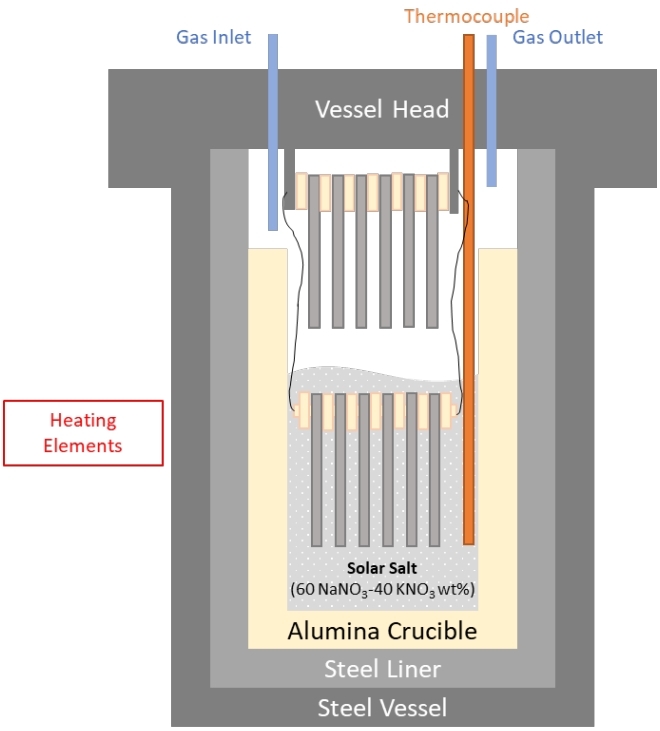

Figure 4.1: Schematic of a corrosion vessel for the temperature range corrosion study with some samples hanging fully submerged within the salt and other samples fully in the gas space.

4.3. Results

Figure 4.2 shows the obtain weight change corrosion rates for Solar Salt submerged and gas space 316SS from 570°C to 650°C for 645hr. For the 600°C experiment, it was discovered after sample extraction that the alumina tube holding the salt-exposed samples had caught on the rim of the alumina crucible, thus only partially submerging the samples and rendering the 600°C salt-exposed sample data unusable. Also included for comparison in Figure 4.2 are the 600°C and 630°C fully submerged 316SS corrosion rates from Chapter 3. While the time of exposure was slightly different (600hr vs. 645hr), the observed corrosion rates for those samples appear in line with those obtained in this study. Table 4.1 details the corrosion rate values as well as the ratio between the salt-exposed and gas space corrosion rates. Error bars listed are standard deviations from the average corrosion rates obtained.

From 570°C to 610°C, the corrosion rate of 316SS appears to increase steadily as a function of temperature from around 20µm/yr to 30µm/yr. Above 610°C, however, the corrosion rate rapidly increases, reaching around 45µm/yr at 630°C and 100µm/yr at 650°C. This rate of increase appears to diverge from the increase in corrosion rates observed in the gas space similarly around 610°C. For example, from 570°C to 610°C the gas space corrosion rate hovered around 25% of the salt exposed corrosion. At 650°C, this ratio drops to around 15%.

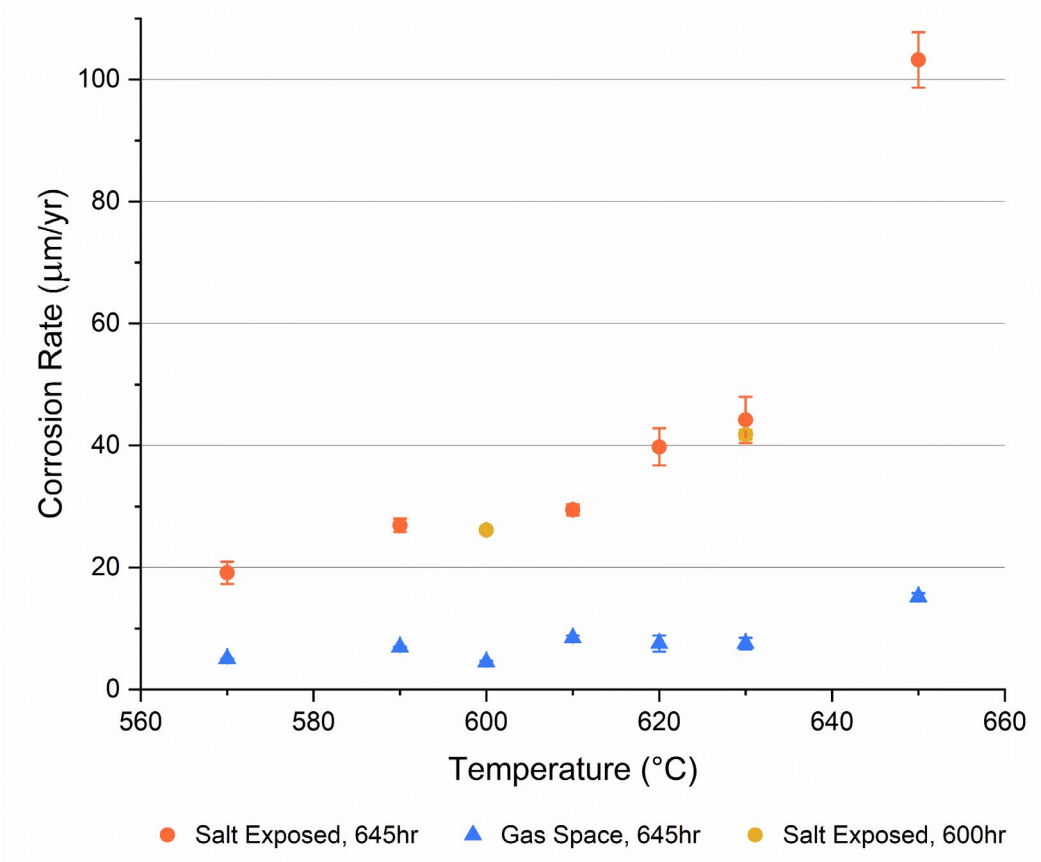

Figure 4.2: Weight change corrosion rates of 316SS in Solar Salt (salt exposed and gas space) vs. temperature.

Table 4.1: Weight change corrosion rates of 316SS in Solar Salt (salt exposed and gas space) vs. temperature.

Temperature (°C)	Corrosion Rate (µm/yr)		Gas/Salt Corrosion (%)
	Salt Exposed	Gas Space	
570	19.1 ± 1.8	5.1 ± 0.0	26.4
590	26.9 ± 1.1	6.9 ± 0.1	25.8
600	26.2 ± 0.5*	4.5 ± 0.2	17.2
610	29.5 ± 0.9	8.5 ± 0.4	28.7
620	39.8 ± 3.0	7.5 ± 1.3	19
630	44.2 ± 3.8	7.5 ± 0.9	17
630*	41.8 ± 0.8	-	-
650	103.2 ± 4.5	15.2 ± 0.6	14.7

*Exposed for 600hr, from Chapter 3 study.

It is of note that significant flaking of the oxide layers was observed during post-extraction storage of the 316SS sample surfaces exposed to 650°C Solar Salt. An extreme example is shown in Figure 4.3 in which large portions of oxide flaked off and exposed bare metal surface prior to any cleanings for weight change corrosion measurements. Some flaking did occur for the lower temperature salt-exposed 316SS samples, but in much reduced amounts as the test temperature decreased.

Figure 4.3: Extreme flaking observed from a 316SS sample exposed to 650°C Solar Salt during post-extraction storage.

4.4. Discussion

4.4.1. Arrhenius Analysis on Temperature

The rapid increase in corrosion rates at temperatures above 600°C indicates a potential change in the processes controlling corrosion in elevated temperature Solar Salt. To investigate this, an Arrhenius plot comparing the obtained corrosion rates for the various temperatures is shown in Figure 4.4. An Arrhenius plot enables extraction of the activation energy of an observed process through the equation:

$$k = Ae^{\frac{-E_a}{RT}}$$

where k is the rate constant of a reaction, A is a pre-exponential factor, R is the gas constant, T is the temperature (in Kelvin), and E_a is the activation energy. In plotting ln(corrosion rate) vs. 1/T, E_a can be calculated from the slope of a linear fit through the data:

$$E_a = -R * Slope$$

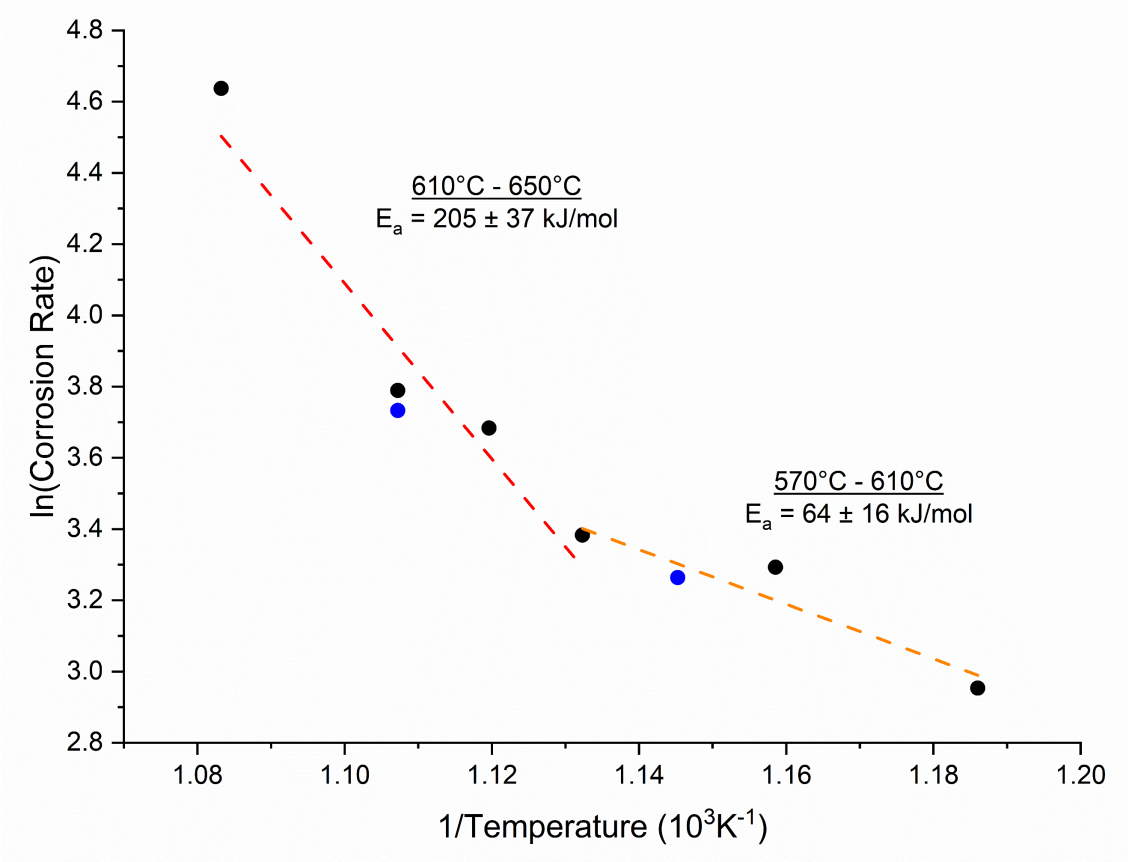

Figure 4.4: Arrhenius plot of the weight change corrosion rates of 316SS in Solar Salt for 645hr. 600hr datapoints from Chapter 3 are highlighted in blue.

The activation energies extracted from the corrosion rate data are 64 kJ/mol for temperatures between 570°C-610°C and 205 kJ/mol for temperatures between 610°C-650°C which is in good agreement with literature values.[85] Curiously, these values appear to be similar to the activation energies obtained for the diffusion of oxygen[105–107] through iron oxide and the diffusion of alloying elements through steel[108,109], respectively. This would suggest that between 570°C-610°C, the corrosion rate of 316SS is rate limited by the diffusion of oxygen species. Given that oxygen species are generated through the decomposition of nitrate salt, this indicates that the amount of decomposition occurring at these temperatures is low enough to bottleneck corrosion. In contrast at the higher temperatures, sufficient decomposition occurs such that the generation of oxide species is likely not the rate limiting step anymore. Corrosion rates rapidly increase and instead appear to be constrained by the diffusion of alloying elements such as Cr to react and corrode away. However, it must be noted that this study is ill-equipped to ascertain the nature of the rate limiting processes associated with the activation energies extracted. Targeted studies are needed to confirm if these processes are indeed diffusion related or potentially completely different.

4.4.2. Refinement of Partially Submerged Corrosion Rates

Using the relative corrosion rates between 316SS samples fully submerged in the nitrate salt and those simultaneously suspended in the gas space, it is possible to obtain more precise

corrosion rates from the partially submerged 316SS samples from Chapter 3. Knowing the surface area submerged compared to the total sample surface area, the contribution from corrosion in air can be extracted out to produce an estimate of the salt-exposed corrosion rate. The results of this analysis are plotted in Figure 4.5 along with the previously reported corrosion rates for 316SS from Chapter 3.

The new corrosion rates enable more confident determination of two conclusions. Firstly, the effect of the sample geometry on the obtained results is likely insignificant. Despite the small and medium samples having salt-exposed surface areas 70% and 45% less than the submerged surface area for the large samples, respectively, the corrosion rates in 600°C were consistently determined to be around 26µm/yr. Secondly and building on this, the 0.46wt% Cl^- impurity salt that was used for the 630°C partially submerged samples was significantly more corrosive than the 0.01wt% Cl^- impurity salt used for the other experiments plotted. The gas space corrected corrosion rate for the 630°C partially submerged 316SS samples was almost twice as high as the other 630°C samples.

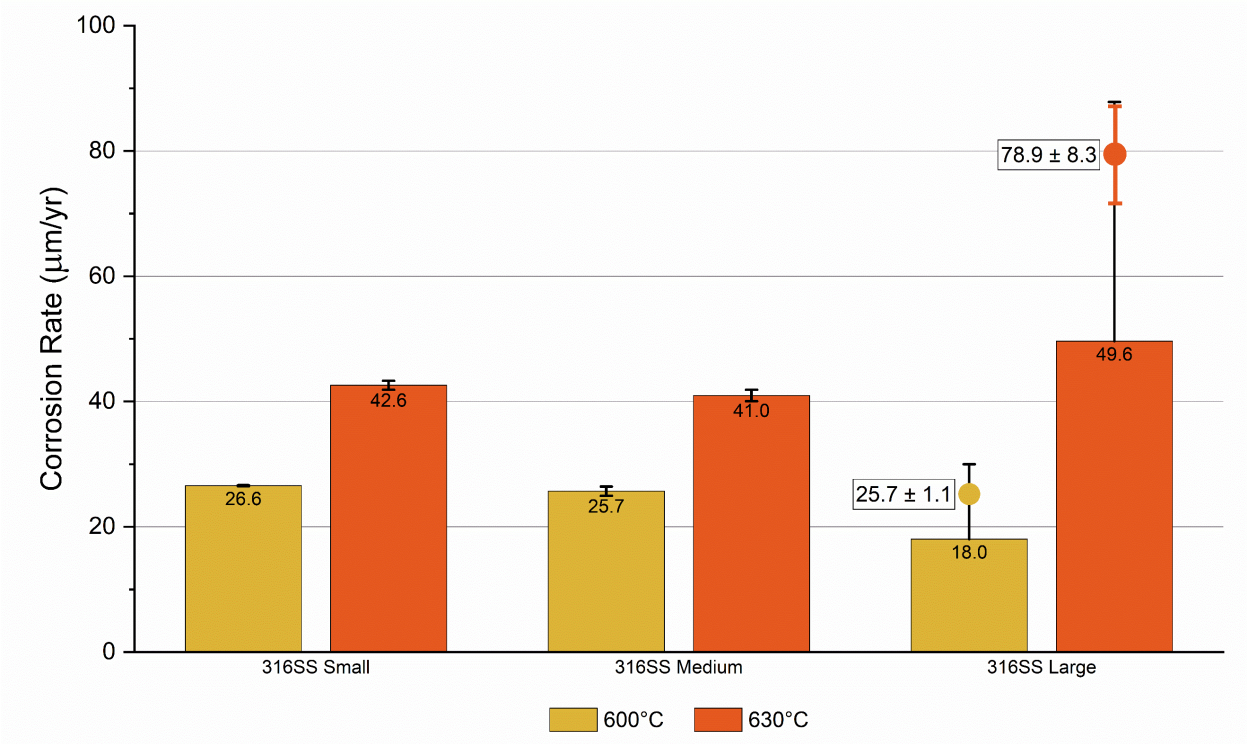

Figure 4.5: Estimated 316SS weight change corrosion rates for partially submerged samples obtained through gas space corrosion correction (dots) compared to previously reported data from Chapter 3 (bars).

4.5. Conclusion

Corrosion rates of 316SS in elevated temperature Solar Salt was shown to significantly increase as a function of temperature and especially for temperatures >610°C. At 570°C, the corrosion rate exhibited by 316SS was around 20µm/yr while this increased to around 100µm/yr at 650°C. Arrhenius analysis revealed the presence of an inflection point around 610°C for which

the rate limiting process in nitrate salt corrosion appeared to change. Activations energies of 64 kJ/mol and 205 kJ/mol were determined for temperatures ranges between 570°C-610°C and 610°C-650°C, respectively. This indicates the possibility for a change from oxygen diffusion control to alloying element diffusion control for corrosion as the exposure temperature in Solar Salt increases. However, further investigation is necessary to determine the processes associated with the activation energies extracted from Arrhenius analysis. Simultaneous collection of gas space and salt-exposed corrosion rates in this study indicated that significant relative increases in corrosion rates occurred for salt submerged samples. This likely correlates to the change in rate limiting process for Solar Salt corrosion described above.

The collection of the gas space corrosion rates also enabled more refined estimates of the corrosion rates for the partially submerged 316SS samples in Chapter 3. As a result, further evidence was obtained for the different degrees of corrosivity imposed by the two different Cl^- impurity batches of salt used within the Chapter 3 study. While this process showed the ability to extract corrosion rate values from partially submerged samples in good agreement with fully submerged samples, having samples partially submerged is very much not ideal. Furthermore, a negligible effect of sample geometry on the observed corrosion rates was discerned indicating that relatively small coupons can be utilized in good confidence for corrosion experiments. Usage of smaller samples sizes enables the ability to examine more samples simultaneously for increased statistics.

Note that this study only investigated the corrosion rates in Solar Salt as a function of temperature at a singular exposure time of 645hr. Further investigation into time-dependent effects, evolution of corrosion scale morphology, and changes in nitrate salt chemistry as a function of temperature will be investigated in Chapter 5.

Chapter 5 – Long-Term Corrosion Study

5.1. Background

Figure 1.8 in the Introduction revealed that corrosion rates for materials in elevated temperature Solar Salt is heavily dependent on the time of exposure to the salt. Specifically, the corrosion rate of 316SS tends to decrease as a function of time. This touches on the time-dependent nature of corrosion which has significant implications when trying to compare corrosion rates across studies. Several models exist within literature attempting to describe the time-dependent corrosion behavior of metals in oxidizing environments. Three commonly discussed time dependencies are discussed below.[110]

First is the Linear Law which essentially holds for metals in environments in which their oxides are extremely unprotective and/or spall off. This is typically the case for metals that form oxides that are extremely porous or are prone to cracking. In this case, corrosion is essentially unrestrained, and the transport of reactant ions is as fast as the rate of reaction. This relation is described by Equation 5.1, where k and C are constants, y is the corrosion thickness, and t is the time of exposure. C is equal to zero if a pristine surface at the beginning is considered.

$$y = kt + C \tag{5.1}$$

The Parabolic Law describes corrosion oxides that are instead highly adherent and protective. The growth of the oxide results in a correspondingly increasing barrier for diffusion which is described as a y^2 thickness dependence (or sometimes referred to as a square root time dependence). This relation is described by Equation 5.2, where again where k and C are constants, y is the corrosion thickness, and t is the time of exposure (C = 0 for a pristine surface at t = 0). It is of note that depending on which reactants diffuse faster, the oxide may tend to exhibit inward growth or outward growth.

$$y^2 = kt + C \tag{5.2}$$

Finally, the Logarithmic Law was proposed (as well as other more complicated laws) as a result of long-term corrosion data tending to not nicely fit with the simplistic laws described previously. The Logarithmic Law describes the situation in which an oxide layer grows to a critical thickness such that the diffusion of ions is too slow compared to their generation. This results in charge buildup at the metal and oxide surfaces and results in a combination of electronic and diffusion considerations. This relation is described by Equation 5.3, where k, A, and C are constants, y is the corrosion thickness, and t is the time of exposure (C = 0 for a pristine surface at t = 0).

$$y = klog(At + C) \tag{5.3}$$

A diagram of the three corrosion time dependence models is shown in Figure 5.1. Figure 5.2 shows a schematic that describes how hypothetical corrosion data might look with the y-axis plotting a parameter such as corrosion thickness, weight gain, or weight loss as a function of time. Note that corrosion rate is defined as the corrosion thickness divided by time. Thus, under a Linear Law condition, obtained corrosion rates would be independent of time:

$$CR = \frac{y}{t} = k = constant \tag{5.4}$$

Put another way, if the corrosion time dependence of a material is not linear, then the determined corrosion rate of a material depends on the time of exposure.

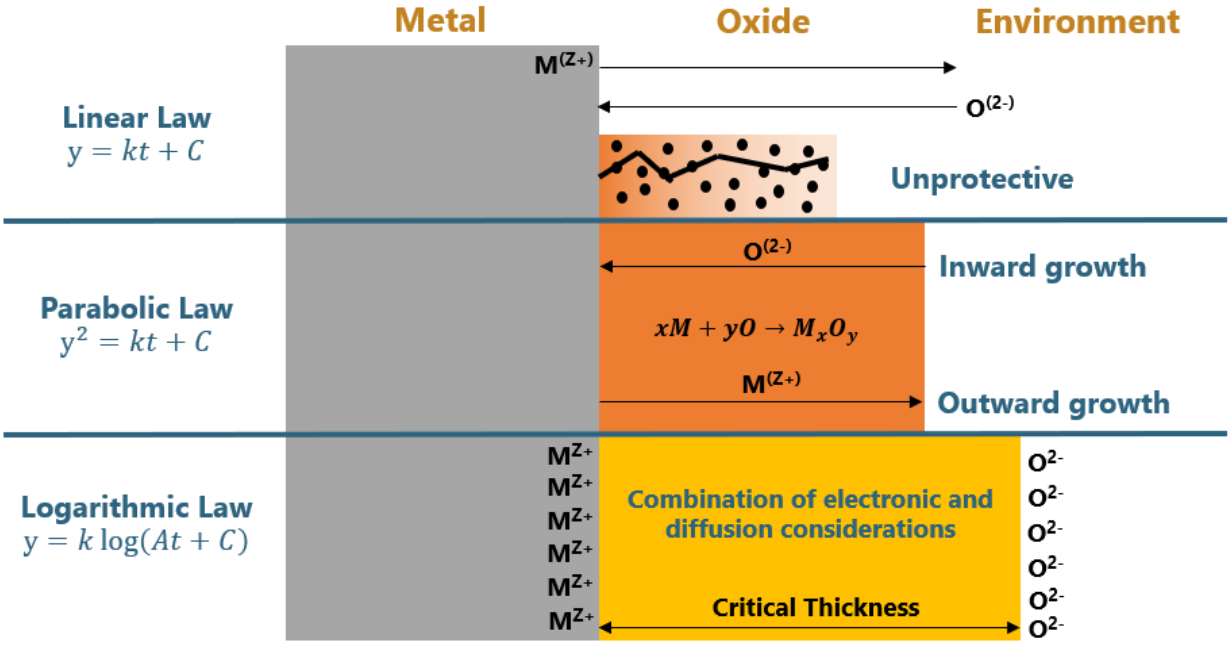

Figure 5.1: Diagram describing corrosion layer behavior under the Linear, Parabolic, and Logarithmic Laws.

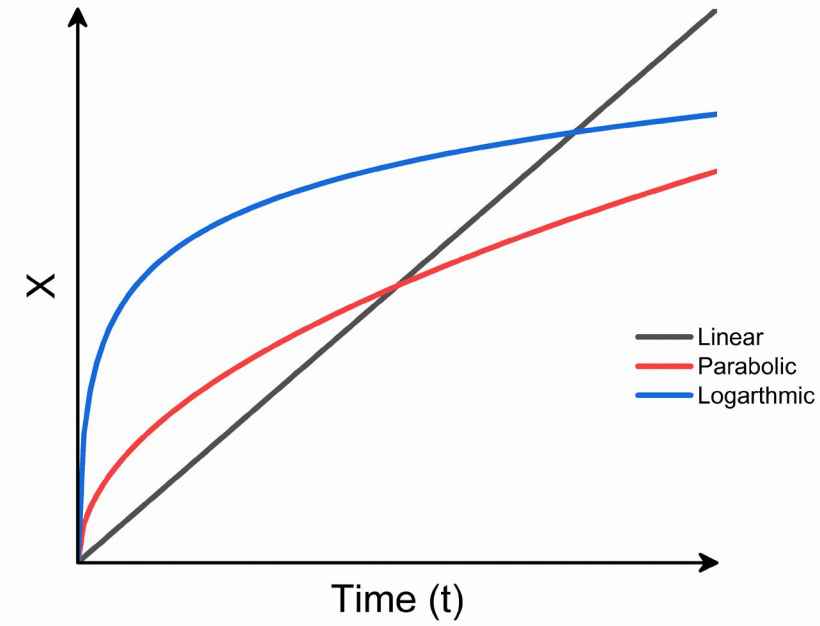

Figure 5.2: Schematic of hypothetical corrosion data following Linear, Parabolic, or Logarithmic corrosion time dependencies. X is a parameter such as corrosion thickness, weight gain, or weight loss.

Using the literature 316SS corrosion data in elevated temperature Solar Salt previously plotted in Figure 1.8, preliminary corrosion time dependency information can be extracted. Figure 5.3 plots the corrosion depth vs. time plots of 316SS literature data for a variety of temperatures. Included in this plot are temperatures with at least three datapoints. For each temperature, a power law fit of $y = Ax^B$ was applied, and data was forced to fit through the origin (representing zero corrosion at time equal zero). In this case, having a B parameter around 1 indicates a likely linear time dependence in corrosion rate, while a B value significantly less than 1 would indicate a parabolic or other time dependence. A perfect parabolic time dependence would have B = 0.5. Note that these datapoints come from studies with significant variance in experimental and reporting methodologies. Thus, as discussed in Section 3.1, caution is advised in trying to draw concrete conclusions. While the cross comparison of literature data is not ideal, this simple fit still hints that there may be a transition in time dependence in the corrosion at higher temperatures. Specifically, the data at temperatures ≤600°C seem to have B values much less than 1 while the data at temperatures ≥605°C have B values extremely close to 1. Several additional studies of 316SS in elevated temperature Solar Salt have been performed in literature, however the data reported was either not conducive for inclusion or did not contain enough datapoints to extract time-dependent data.

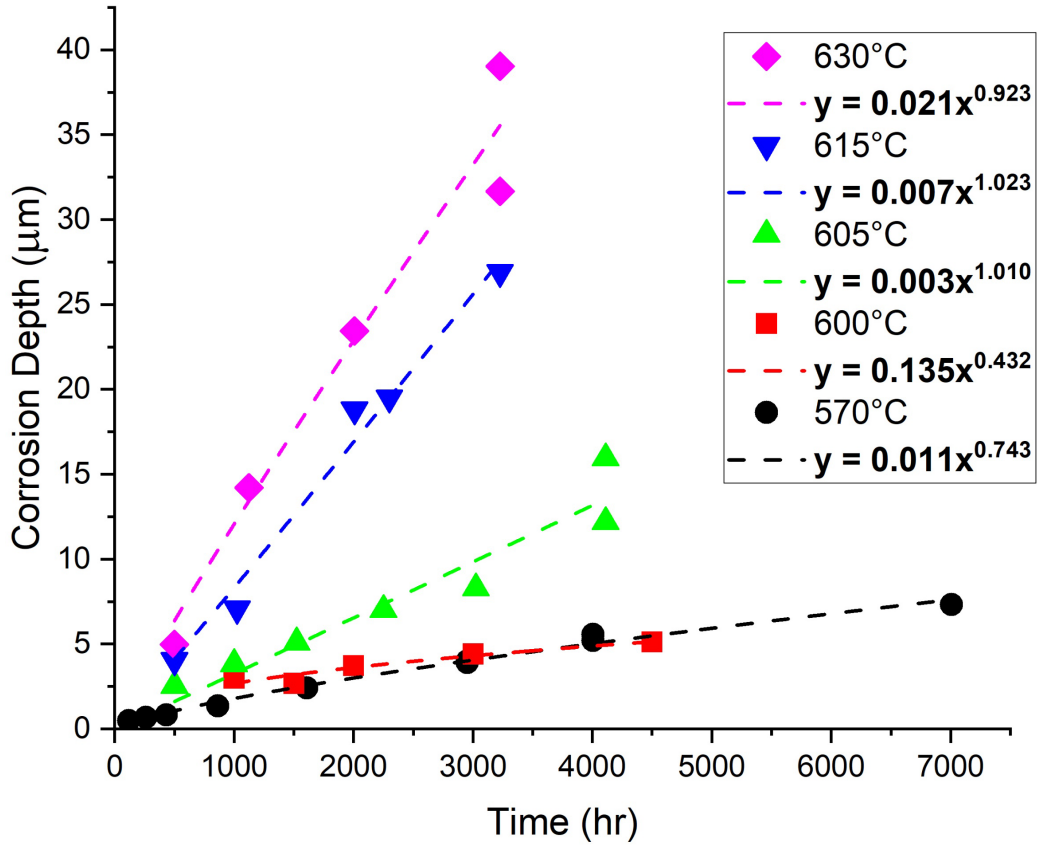

Figure 5.3: Corrosion depth vs. time plots of 316SS corrosion in elevated temperature Solar Salt. Datapoints extracted by Dong from literature data in [86,88–90].

In summary, assuming a material obtains at least some degree of protectiveness from its exhibited corroded surface, corrosion rates from short-term corrosion rates are expected to be artificially high when compared to corrosion rates extracted from long-term corrosion experiments. Understanding the time-dependence in corrosion rates is therefore critically important in the design of components aimed to have lifetimes that are typically much longer than the duration of experiments. In this study, materials were exposed to Solar Salt at a range of elevated temperatures up to a duration of 5000hr. Samples were extracted at intermediate time intervals to investigate nitrate salt corrosion time dependencies.

5.2. Materials and Methods

5.2.1. Materials

Compared to the multi-alloy corrosion study (Chapter 3), only a limited number of alloys were able to be investigated as part of this long-term corrosion study due to space constraints within the corrosion vessels. Two alloys were the primary materials for investigation: 316H and 601. As described previously, 316SS has already been employed in nitrate salt environments and acts as the base alloy for comparison throughout this dissertation. The high carbon variant 316H is often used in high temperature environments due to superior high temperature mechanical properties compared to the base and low carbon (316L) variants. 601 is a commonly used nickel alloy and was included to act as a nickel-based (as well as AFA) comparison to 316H in lieu of being able to fit additional alloy varieties. The 316H material was obtained via a singular slab measuring tens of cm in length and width and several meters in length that individual samples were machined from. The 601 samples were machined from a sheet obtained from commercial vendor.

Other materials examined in this study include 316SS material used for reference, weld materials, and aluminide coatings. As will be described in Section 5.2.2., non-H variant 316SS samples machined from a sheet were inserted into the corrosion experiments at specific intervals to monitor the corrosivity of the Solar Salt over time. These samples are hereafter referred to as 316-REF. Weld material in two variants were also examined. First were samples machined from a 16-8-2 weld pad. 16-8-2 is the weld filler material for welding 316SS components, and its inclusion was to investigate potential susceptibility of weld material to Solar Salt corrosion. 16-8-2 metal was welded into a weld pad spanning several centimeters in length, width, and thickness. Individual samples were fabricated from the weld pad along the welding direction such that the corrosion coupons were comprised completely of weld metal (WM). More explicitly, samples henceforth labelled WM are samples machined from a weld pad of 16-8-2 material such that they only contained weld metal. A second variety of welds examined were autogenous 316SS welds (AutWeld). These samples were fabricated containing an autogenous weld track made on the same stock material used for the 316-REF samples. Roughly one-sixth of the total AutWeld sample surface area was covered by the weld track. The final materials investigated in this study were aluminide coating samples fabricated from 316H and WM samples that underwent an aluminizing treatment (henceforth to be referred to as AL316H and ALWM, respectively).

Coupon dimensions for all materials were around 1.8cm in length, 1.4cm in width, and 1.6mm in thickness with 7mm diameter holes machined for hanging purposes. The dimensions and weight of all samples were measured prior to exposure to molten salt. Images of the different

material coupons are provided in Figure 5.4. Elemental compositions of the alloys are described in Table 5.1.

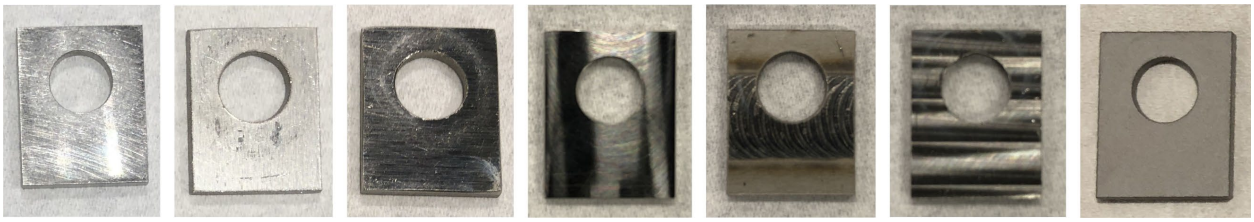

Figure 5.4: Examples of the 1.8cm length corrosion coupons used in the long-term corrosion study. From left to right: 316H, 316-REF, 601, WM, AutWeld front, AutWeld back, and aluminide coating.

Table 5.1: Nominal composition of alloys used during the long-term corrosion study.

Alloy	Alloying Element*								
	Fe	C	Cr	Ni	Al	Mn	Mo	Si	Cu
316-REF	Bal.	0.04	17.5	11.5	-	1	2.25	0.5	-
316H	Bal.	0.06	17.4	11.5	-	1.4	2.4	0.4	-
16-8-2	Bal.	0.1	15.5	8.5	-	1.5	1.5	0.5	0.75
601	12.5	0.1	23	Bal.	1.35	1	-	0.4	1

*Some minor alloying elements have been omitted

Electron backscatter diffraction images of the uncorroded alloys and weld materials are provided in Figures 5.5-5.9. Of note, the two different 316SS variants had significantly different grain sizes with 316H and 316-REF having average grain sizes of 66.7µm and 9.3µm, respectively when disregarding twin boundaries. Both had essentially 100% austenite (FCC) phase fraction. Though the polishing was not ideal for the 601 sample, the average grain size of the material was still able to be determined as 72.3µm which is similar to that of the 316H. The two weld materials contained different weld microstructures and phase fractions of ferrite (BCC) vs. austenite (FCC). The 16-8-2 WM material had 26.4% area fraction being ferrite compared to just 1.4% area fraction ferrite for the 316SS AutWeld.

Figures 5.10 and 5.11 show SEM images and EDS maps of the aluminide coating microstructure. The first 40µm or so of the aluminide coating surface is comprised mainly of Fe and Al with diffuse amounts of other steel alloying elements. The next 50µm or so before the bulk steel material shows a complex intermetallic diffusion region exhibiting distinct NiAl, CrMn, and Mo phases throughout. No significant differences were noted within the aluminide coating regions between AL316H and ALWM.

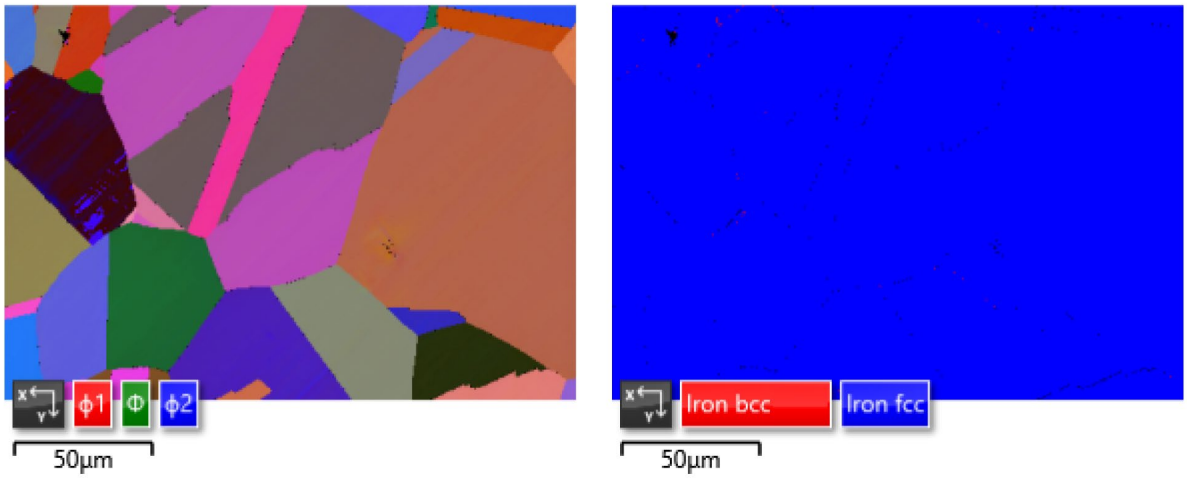

Figure 5.5: EBSD Euler (left) and phase (right) maps obtained for 316H. 1000x magnification.

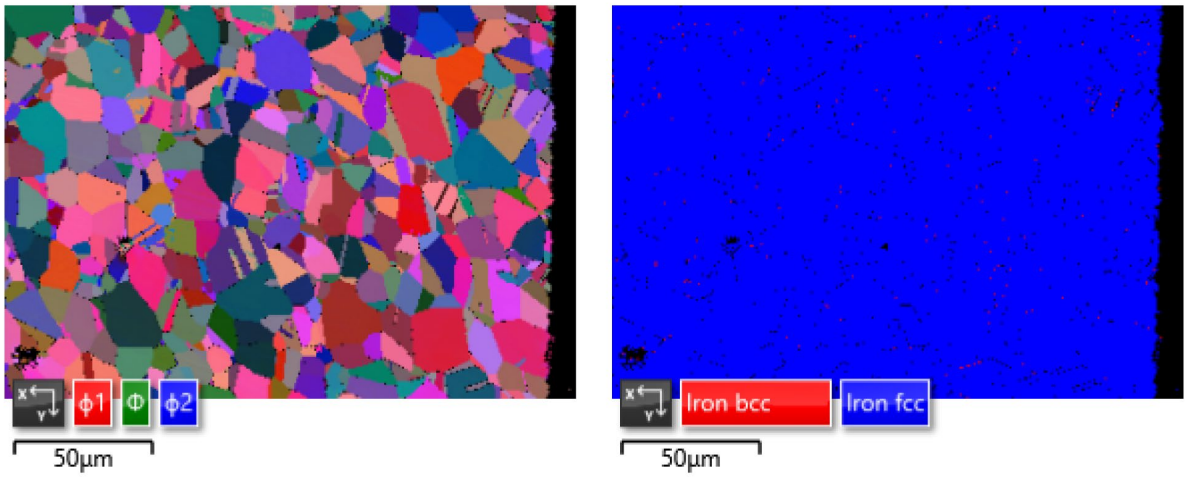

Figure 5.6: EBSD Euler (left) and phase (right) maps obtained for 316-REF. 1000x magnification.

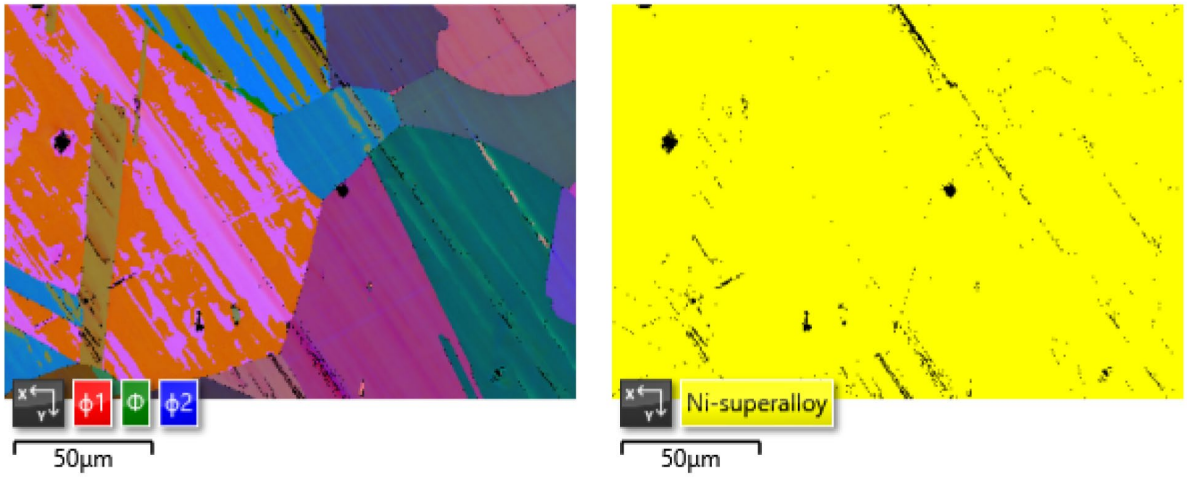

Figure 5.7: EBSD Euler (left) and phase (right) maps obtained for 601. 1000x magnification.

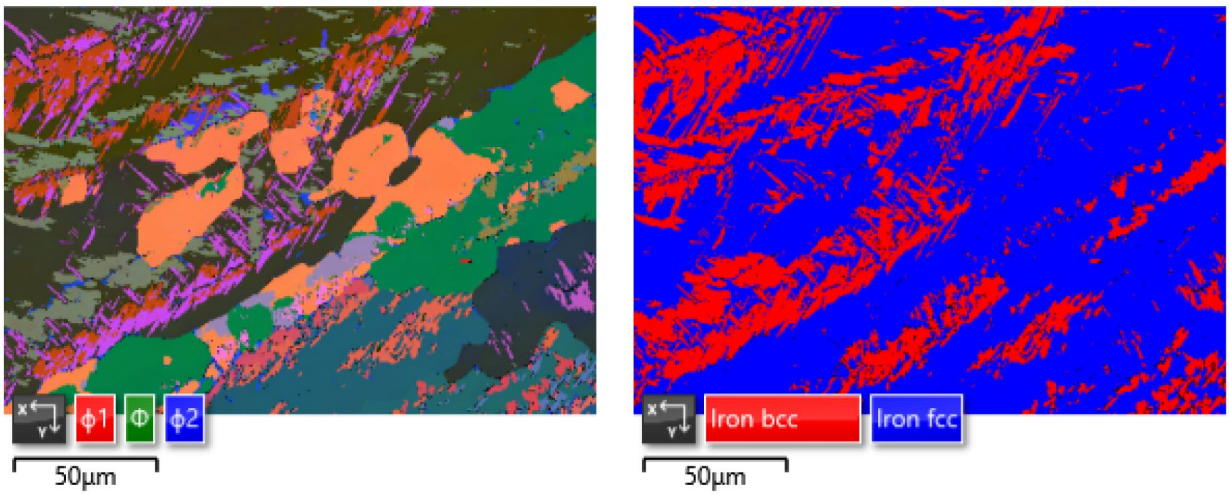

Figure 5.8: EBSD Euler (left) and phase (right) maps obtained for WM. 1000x magnification.

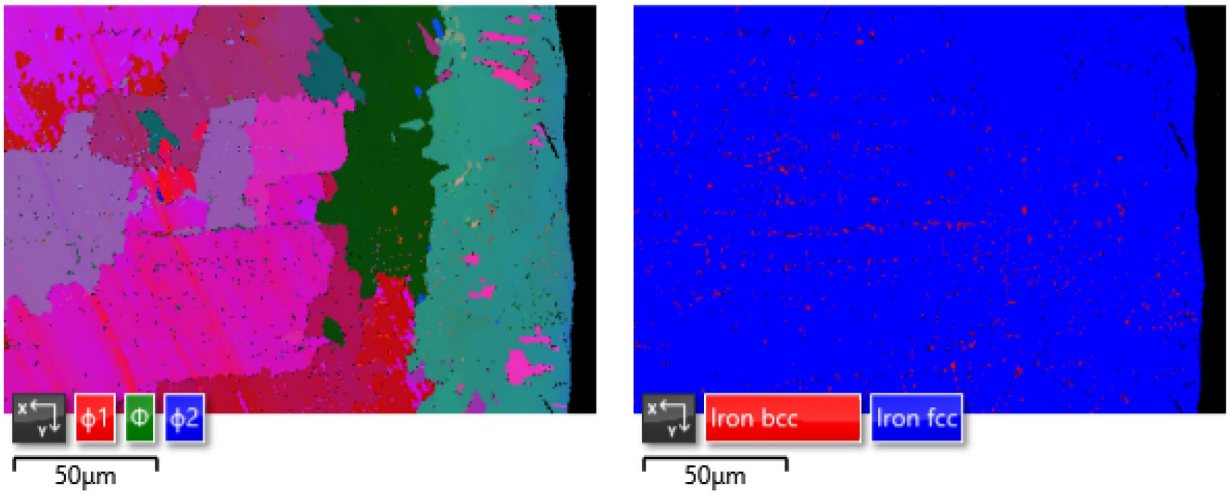

Figure 5.9: EBSD Euler (left) and phase (right) maps obtained for AutWeld. 1000x magnification.

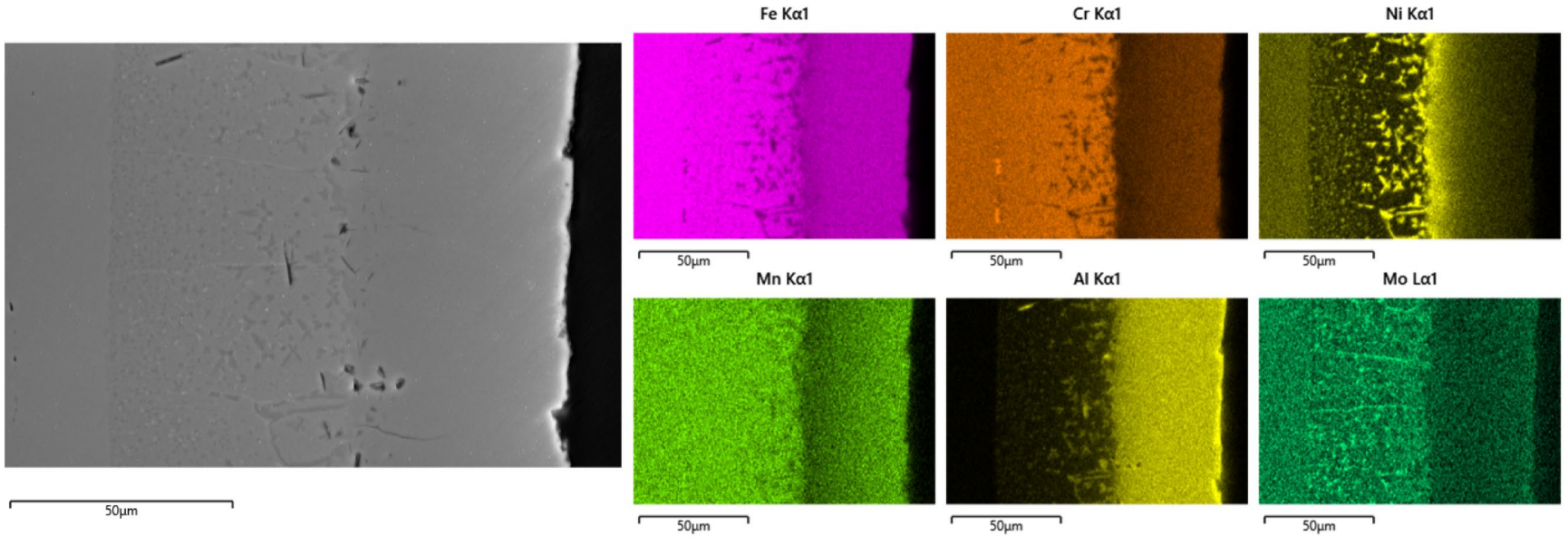

Figure 5.10: SEM image and EDS elemental maps of as-received aluminide coating on 316H. 1500x magnification.

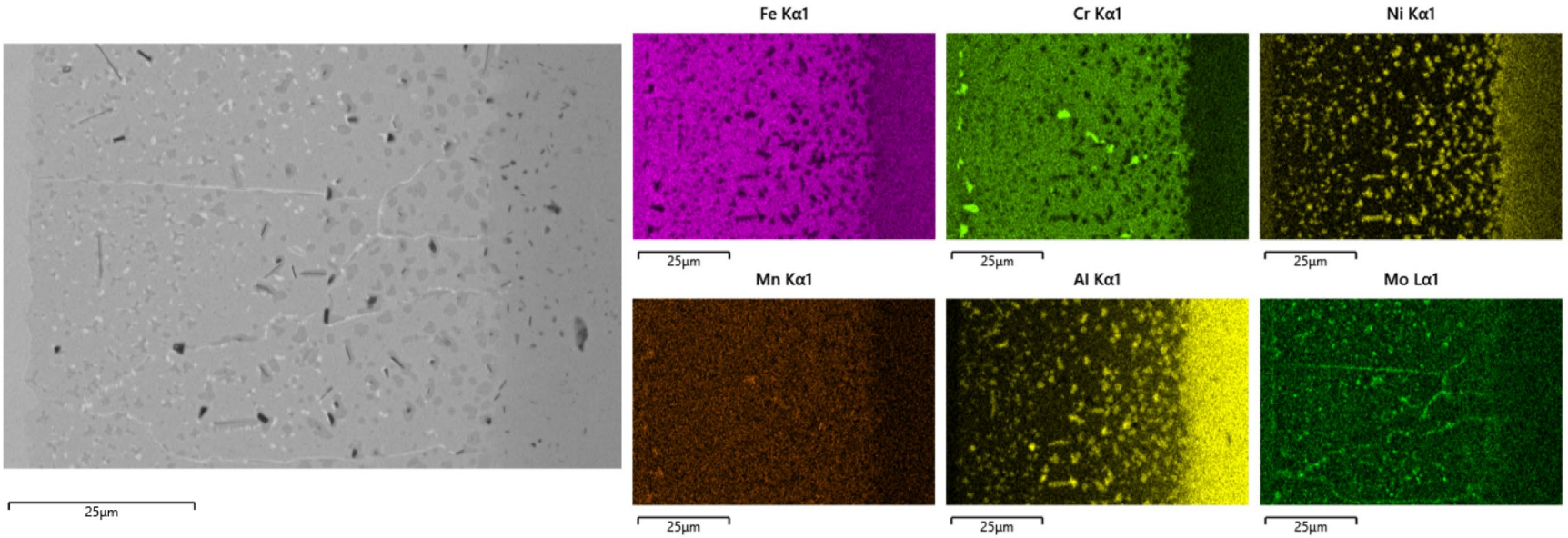

Figure 5.11: SEM image and EDS elemental maps of the intermetallic region in as-received aluminide coating on 316H. 2500x magnification.

5.2.2. Corrosion Setup

The overall corrosion setup and general experimental details have been described extensively in Chapter 3. In this study, samples were exposed to Solar Salt for durations up to 5000hr depending on the material and sample. Five simultaneous experiments were performed at a range of elevated temperatures: 590°C, 600°C, 620°C, 630°C, and 650°C. For this study, a 60-sample holder made of 316SS and alumina components was used in each experiment. Figure 5.12 shows the corrosion vessel schematic including the 60-sample holder that was employed for this set of experiments. Samples were secured on the holder branches using 316SS pins. Each sample was isolated from the vessel components as well as each other using alumina sleeves and spacers to minimize potential galvanic effects.

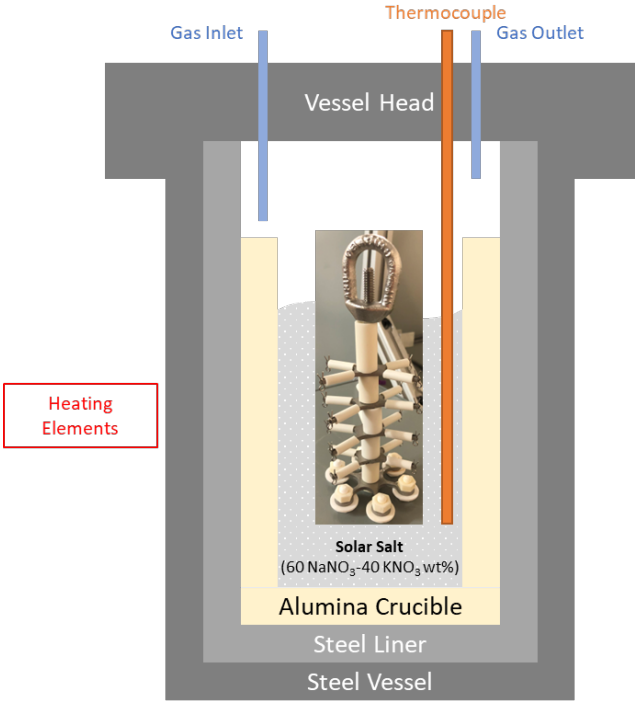

Figure 5.12: Schematic of a corrosion vessel for the long-term corrosion study with the 60-sample holder used for hanging samples.

Sample extractions were performed at 500hr, 1000hr, 2000hr, 3000hr, 4000hr, and 5000hr. As described in Section 3.2.2., temperatures were reduced to 350°C and the gas space was flushed with ultra zero synthetic air prior to opening the corrosion vessels for safety considerations. Removing individual corrosion coupons required extraction of the entire sample tree. Samples that were aimed for longer exposure times were left on the sample holder and reinserted into the corrosion vessel. This process meant that corrosion coupons with target exposure times spanning multiple extractions were subjected to a freeze cycle (visually evident by the solidification of nitrate salt wetted on the coupon surfaces). For example, 5000hr corrosion coupons were subjected to five freeze cycles beyond their planned final extraction at 5000hr as a result of the intermediate extractions.

Due to the holder being limited to hanging 60 samples at a given time, some samples had to be initially inserted at intermediate extractions. 3-4 samples were generated for each material and nitrate salt exposure condition. Due to the limited number of coated samples, only the 620°C and 650°C experiments contained aluminide samples and only two samples for each temperature/time condition examined. The other three experiments contained extra 601 samples for datapoints at additional exposure times. At each 1000hr exposure interval, three 316-REF samples were extracted and three fresh 316-REF samples were inserted. Other than the 316-REF samples, a corroded sample of each material and condition was reserved for microscopy. All other samples were used for weight change corrosion rate determinations.

At the same time as the corrosion coupon extractions, nitrate salt samples were taken for subsequent chemical analysis using a 316SS rod as a cold finger. Both solid (frozen nitrate salt) and aqueous (nitrate salt dissolved in 5g of DI water) salt samples were collected. The height of the salt collected by the cold finger was also measured to monitor the remaining molten salt level over time. Depending on the remaining salt level, roughly 1-2g of nitrate salt was collected for each salt sample. 800g of Solar Salt made from the same 0.01wt% Cl^- impurity specification batch of nitrate salt described in Section 3.2.4 was initially used in each experiment. The semi-sealed gas space pressure was set to <1psig using ultra zero synthetic air prior to each ramp to test temperature.

5.2.3. Mid-Experiment Changes

During the 1000hr extraction, while the samples on the top branches were still submerged at testing temperatures, it became evident that the amount of salt in the crucibles was not enough to ensure full submersion of the samples all the way to 5000hr. There were several avenues of salt loss during the experiments, both intentional and unintentional. Firstly, each salt sample taken from the experiments for chemical analysis removed 1-2g of salt. Second, depending on the wetting of the nitrate salt on the corrosion coupons, at least 0.2g of nitrate salt was lost per extracted corroded sample (that was not reinserted) during sample extractions. Finally, unknown and differing amounts of salt would naturally be lost as a result of nitrate salt decomposition into gaseous species and/or collected as nitrate salt “snow” along interior surfaces of the corrosion vessel (and thus outside the melt). Beyond salt loss, the total number of samples remaining to be reinserted decreased as samples were fully extracted, and thus the salt level would drop due to reduced displacement.

To remedy this issue, an additional 200g of fresh Solar Salt was added to the 590°C, 600°C, and 650°C experiments, and an additional 235g was added to the 620°C and 630°C. The difference in added amounts was due to slight variations in alumina crucible diameters and in measured heights of remaining molten salt at the time. A fresh salt bakeout was performed and additional nitrate salt samples for chemical analysis were taken prior to re-insertion of the corrosion coupons. As an additional precaution, long exposure time samples to be reinserted were moved to lower branches on the sample trees as space became available. During the subsequent remaining extractions, it was confirmed that the salt level remained high enough to submerge any remaining corrosion coupons.

Another experimental addition was performed as a side effect of the 1000hr extraction salt addition. Due to the salt addition, subsequent salt bakeout, and time needed to resume the

experiments, corrosion coupons to be reinserted into the salt were exposed to room temperature air for around one week. During this time, significant flaking of the oxide layers from some of the samples was observed likely related to hydration of the nitrate salt solidified on the sample surfaces by the atmosphere. The amount of flaking was most severe for the 650°C samples while the 590°C and 600°C samples had minimal/no flaking.

To be able to explore potential impacts of prolonged and numerous freeze cycles, two additional samples of both 316H and 601 were added to the 620°C, 630°C, and 650°C experiments during the 2000hr extraction. These samples were submerged separately from the 60-sample holder and were to remain submerged within the molten salt during extractions until the 5000hr extraction (3000hr total time of exposure). Figure 5.13 shows a schematic of how these continuously submerged samples were hung inside the corrosion vessel. These samples were hung from an alumina tube that was secured by threaded wired 316SS hooked on the alumina crucible rim. The corrosion coupons were isolated from each other, the 60-sample holder, and 316SS wire using alumina components.

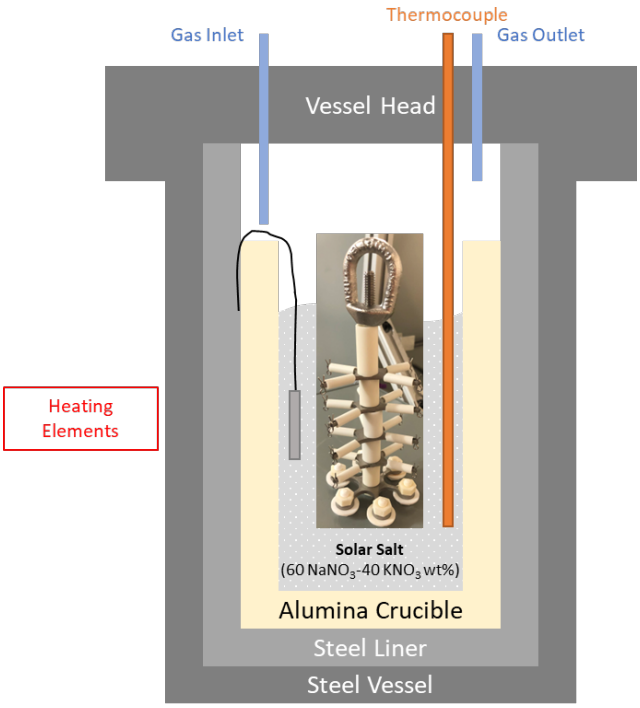

Figure 5.13: Schematic of a corrosion vessel for the long-term corrosion study with the addition of continuously submerged samples in the 620°C, 630°C, and 650°C experiments.

5.2.4. Mid-Experiment Temperature Excursions

Salt temperatures were measured in-situ during the experiments using a thermocouple inserted into the molten salt. Three notable temperature excursions occurred over the course of operating the 5000hr corrosion experiments. First, between the 500hr and 1000hr extractions (around 200hr in), a major temperature excursion occurred as a result of an unplanned sitewide power outage. The time between the start of the power outage and heating back to test

temperatures was around 17.6 hours. In this case, the salt froze with the samples inside and likely reached back down to room temperature before the furnaces were able to be restarted.

Second, between the 1000hr and 2000hr extractions, a significant temperature excursion occurred as a result of a planned outage for electrical maintenance. This resulted in salt temperatures dropping below 3°C of the target temperature for about 1.2 to 1.5 hours. Temperature data collection was also halted as a result of the power outage, though the salt is expected to not have frozen during this time. The salt in all experiments likely stayed well above 500°C by the time heating was able to recommence with minimum temperatures reached calculated to range from around 540°C for the 590°C vessel to 610°C for the 650°C vessel.

A final major temperature excursion occurred between the 4000hr and 5000hr extractions as a result of another unplanned sitewide power outage (just one hour after the corrosion vessels had reached test temperatures). The time between the start of the power outage and heating back to test temperatures was around 8.5 hours. While the salt did not cool back to room temperature, it likely reached an estimated minimum temperature of around 150°C, well below the freezing temperature of the salt. As a result, the salt likely froze with the samples inside (including the hanging samples inserted at 2000hr).

Due to the short duration and lack of salt freezing, the second temperature excursion is not expected to have caused significant effects to the overall data. However, the two more severe excursions in which the salt froze with the samples inside likely did affect the data obtained and will be discussed throughout the Results section.

5.2.5. Post Corrosion Examination

In total, 459 corrosion coupons across 7 material variants were exposed to Solar Salt for analysis. As described in Section 3.2.5., exact exposure times at test temperature above 3°C below the target temperature were calculated and weight change corrosion rates were determined following ASTM G1-03 and ISO 8407 guidelines.

For microscopy, unlike in Chapter 3 with the larger corrosion coupons, the smaller long-term corrosion experiment samples were small enough to not require cutting in order to mount and image. There was significant consideration between cleaning the samples of any frozen nitrate salt prior to mounting in epoxy vs. mounting in epoxy directly. In the end it was decided to mount the samples directly in epoxy without cleaning. This resulted in non-ideal microscopy due to blooming of nitrate salt from hydration by the atmosphere and polishing steps that often obstructed the corroded sample edges when imaging. Examples of this are highlighted in the Results and evident in essentially all the microscopy performed. However, this was preferable to the alternative of cleaning the corrosion coupons prior to mounting due to the risk this process would have in irreversibly losing the oxide layers prior to imaging. During sample cleanings for weight change corrosion rate determinations, it was observed that significant amounts of oxide layers were removed during the initial cleaning step removing any frozen nitrate salt. While inner oxide layers would have still remained, cleaning the samples would have likely removed the outermost oxide layers from the entire sample surface. The corrosion samples were polished to a final polishing step using 0.25μm diamond suspension.

Microscopy, energy-dispersive X-ray spectroscopy (EDS), and electron backscatter diffraction (EBSD) was performed utilizing a Thermo Scientific Scios 2 DualBeam FIB-SEM. Samples examined with EBSD had a final polishing step of 0.06μm alumina suspension. While all the 316-REF samples were used for weight change corrosion rate measurements leaving none for microscopy, through microscopy it was determined that the edges of the AutWeld samples far away from the weld bead were unaffected by the welding process and thus were used as surrogates for 316-REF material microscopy.

Additional transmission electron microscopy (TEM) was performed on a portion of the 316H and 601 sample using an FEI TitanX TEM at the National Center for Electron Microscopy at Lawrence Berkeley National Laboratory. This enabled collection of higher resolution images, EDS maps, and 4D-STEM data. 4D-STEM is a technique in which 2D diffraction patterns are collected as the electron beam is rastered along a 2D sample (hence 4D).[111] In this study, 4D-STEM was utilized as a way to obtain diffraction patterns throughout the corrosion oxide layers for potential identification of phases. TEM lamellas were fabricated spanning the depth of the corrosion oxide scale using a Ga focused ion beam (FIB). For samples with thick oxide scales, several TEM lamellas were fabricated to encompass the entire thickness.

Prior to irreversibly using all the generated samples for weight change corrosion measurements and microscopy, X-ray diffraction (XRD) was performed on a 316H and 601 sample in each condition utilizing a Rigaku Miniflex II benchtop XRD using a Cu K_α source. Samples were analyzed from angles 3-90° in 0.01° steps at a rate of 10°/min.

In total, 80 nitrate salt samples were collected from the molten salt during sample extractions: 40 solid and 40 aqueous. Chemical analysis was performed by McCampbell Analytical, Inc. Solid nitrate salt samples were analyzed for nitrate (NO_3^-) and nitrite (NO_2^-) content using ion chromatography and metal content (Cr, Fe, Ni) using inductively coupled plasma mass spectrometry (ICP-MS). Aqueous samples were analyzed for alkalinity using titration.

5.3. Results

5.3.1. Weight Change Corrosion Rates

Figure 5.14 shows the corrosion rates obtained for the 316-REF samples during the long-term corrosion study. Note that these samples were all exposed to 1000hr but inserted at different times during the experiments and therefore provide information on the corrosivity of the Solar Salt as a function of time. There is an especially pronounced increase in corrosion rates for the 316-REF over time for the 630°C and 650°C experiments with a less clear effect for the lower temperatures. This indicates that salt aging at higher elevated temperatures is significant enough to substantially change its corrosivity to previously unexposed materials.

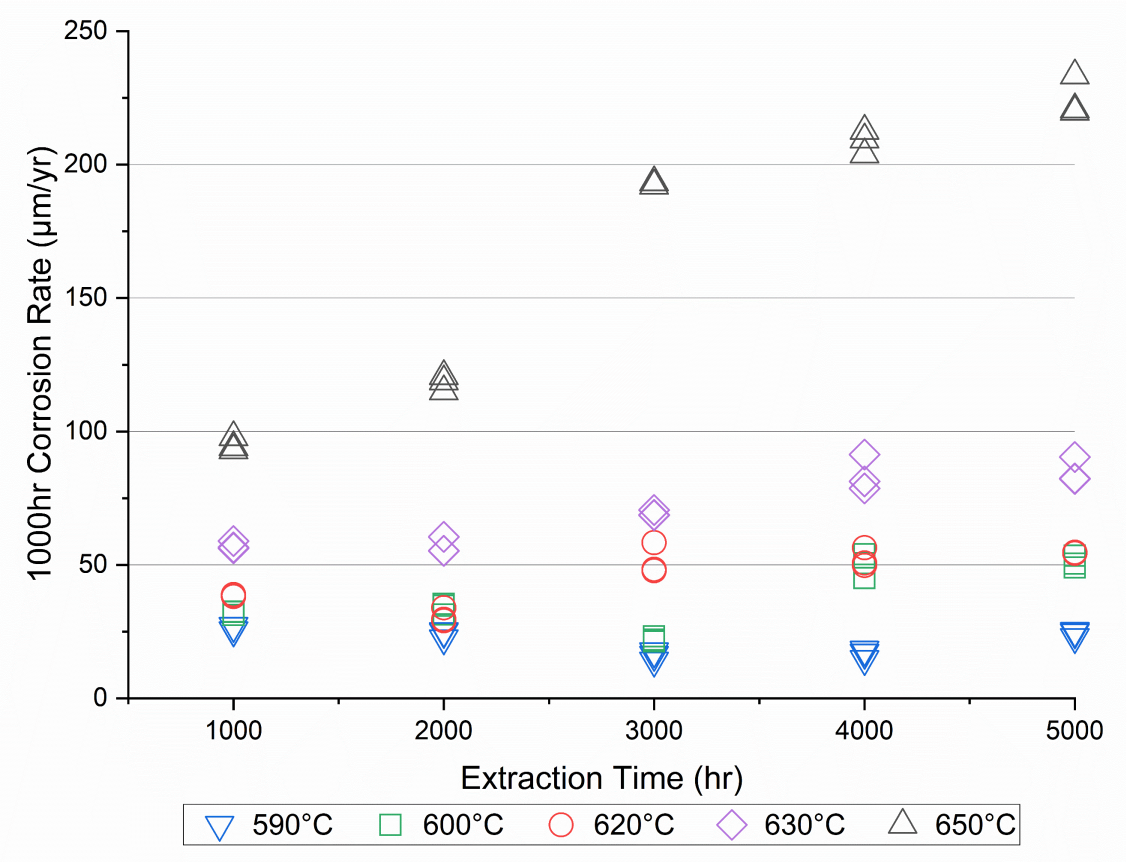

Figure 5.14: 1000hr weight change corrosion rates vs. extraction time for the 316-REF samples.

The corrosion rates obtained for 316H samples are provided in Figure 5.15. For all temperatures, the corrosion rates follow a downward trend as a function of exposure time indicating the existence of protective corrosion scales to some degree. Of note, there appears to be a significant dip in the corrosion rates at 4000hr for 630°C and 650°C. This is likely due to the major temperature excursion that occurred between the 4000hr and 5000hr extractions, as described in Section 5.2.4, that resulted in the salt freezing with the samples inside. As has been noted in previous chapters and likewise observed during this study, the oxide scales of 316SS corroded in Solar Salt were extremely fragile and prone to flaking, especially at higher elevated temperatures. Therefore, it is likely that significant portions of the corrosion scale for 316H flaked off during the freeze excursion for the 630°C and 650°C experiments, exposing fresh material to corrode and resulting in the increase in corrosion rates observed. It is also of note that between the 3000hr and 4000hr extractions was a period of exceptionally smooth operation of the furnaces with no temperature excursions, likely enabling the corrosion oxide layer to remain adherent and protective, thus significantly decreasing the corrosion rates.

It appears that while a similar major temperature excursion occurred between the 500hr and 1000hr extractions, the freezing of the salt with the samples inside in this instance did not noticeably result in increased corrosion rates. This indicates that there may be a thickness dependence of the oxide scale in terms of its friability which can also explain why there does not appear to be as significant effect from the 4000-5000hr excursion for the experiments at

temperatures ≤620°C. Similarly, while flaking was observed for the higher temperature exposed samples during the extended hold in atmosphere after the 1000hr extraction, the total thickness of oxide layer removed / fresh surface exposed at the time may not have been significant enough to substantially increase obtained corrosion rates.

Also plotted in Figure 5.15 are the corrosion rates obtained from the 3000hr exposed 316H hanging samples. These were initially inserted at the 2000hr extraction with the aim to minimize exposure to thermal cycling effects. Their corrosion rates appear to be around the same order as the regular 3000hr samples, but with no clear trend. The 650°C hanging samples exhibited lower corrosion rates, the 630°C samples roughly the same corrosion rates, and the 620°C samples higher corrosion rates. Considering the discussion above surrounding oxide thickness/flaking susceptibility, temperature excursions, and increasing salt corrosivity (from the 316-REF results), it is unclear what may be the cause of these differing relations.

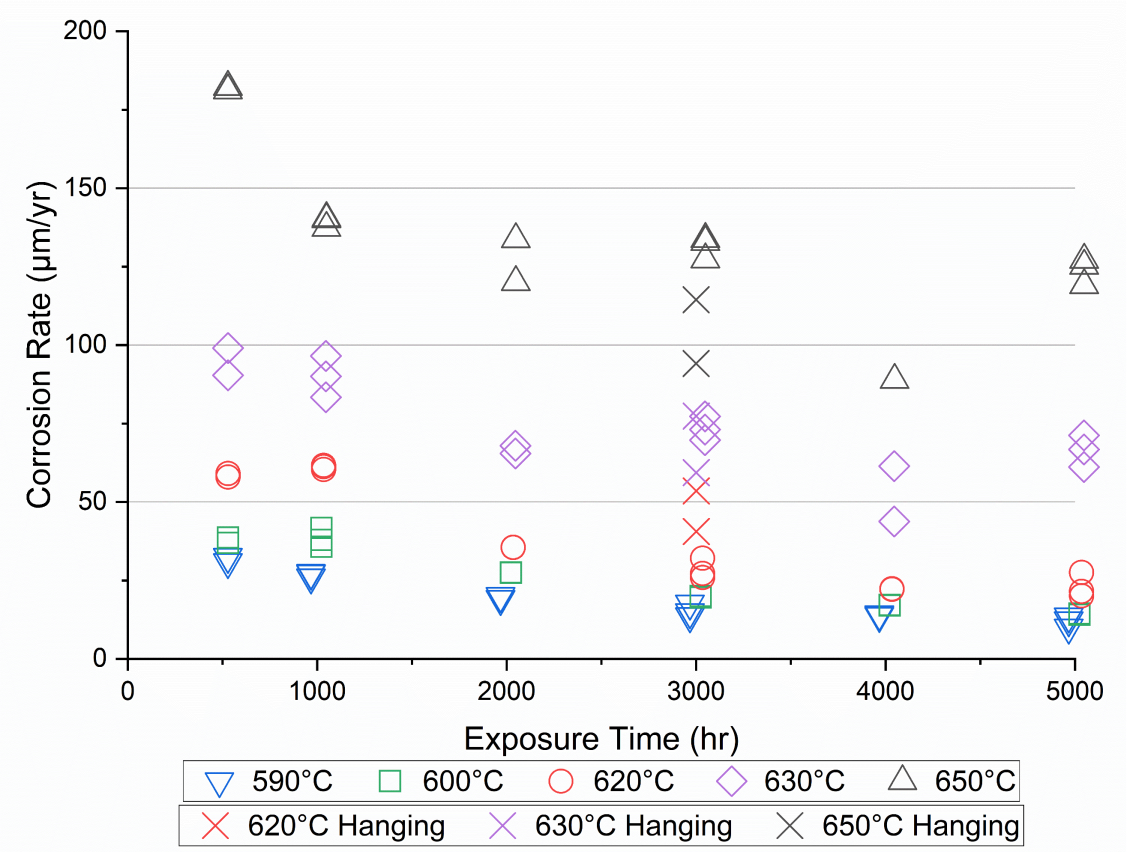

Figure 5.15: Weight change corrosion rates of 316H vs. temperature and exposure time.

Figure 5.16 shows the corrosion rates obtained from the 601 samples and indicates that 601 has significantly greater corrosion resistance compared to 316H. For illustration, 601 at 630°C performed better than 316H at the lowest temperature investigated (590°C), and the corrosion rates for 601 at 650°C were more than 3x less than those for 316H. Like 316H, a general downward trend in corrosion rates can be observed as a function of exposure time indicating a protective nature of the oxide scale. It is noted that little to no flaking was observed for the 601

samples including the 650°C samples. The 650°C data appears to have an uptick in corrosion rate at 5000hr similar to 316H likely due to same explanation regarding the temperature excursion described above. While full flaking may not have occurred, the excursion likely caused cracking in the corrosion oxide layers which would have enabled increased salt penetration to the bulk material surface. Of note, the 650°C 500hr corrosion rates appear to be anomalously low relative to the overall trends across temperatures. There are no 2000hr and 4000hr datapoints for 620°C and 650°C due to the space constraints in including aluminide coating samples in these experiments.

Unlike the 316H hanging samples, the 601 hanging samples exhibited a consistent trend with all exhibiting higher (or in the case of 650°C significantly higher) corrosion rates than the regular 3000hr samples. This would make sense considering the temperature excursion and increased corrosivity of the salt experienced by the hanging samples. However, due to the inconclusive 316H hanging samples data, this effect is hard to claim for certain.

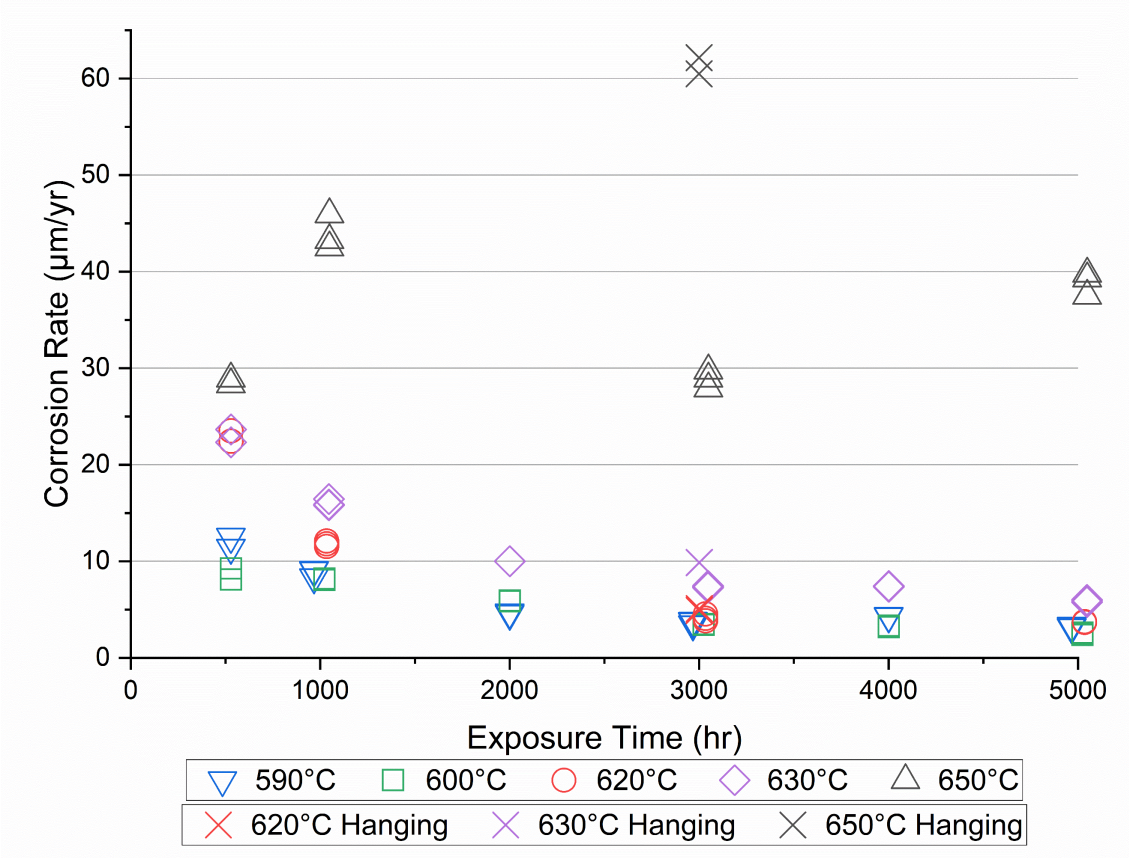

Figure 5.16: Weight change corrosion rates of 601 vs. temperature and exposure time.

Figure 5.17 shows the corrosion rates obtained from the WM samples. For temperatures ≤620°C, the corrosion rates for WM appear to be slightly higher than their respective 316H counterparts. For example, at 600°C, the WM corrosion rates start with an average of 50.6µm/yr at 500hr and drops to 18.5µm/yr at 5000hr, while the 316H corrosion rates average 37.8µm/yr at 500hr and 14.3µm/yr at 5000hr. At 630°C and 650°C, the WM corrosion rates appear

significantly lower than 316H, though the data appears noisier and trends less clear. While all the samples were machined containing solely weld pad material along the same path, unknown variance in weld microstructure across samples could be the root cause of the variance observed. Despite these potential differences, there is no indication that WM corrosion performance is substantially worse than 316H. It is of note that the appearance and flaking of WM samples appeared similar to the 316H samples.

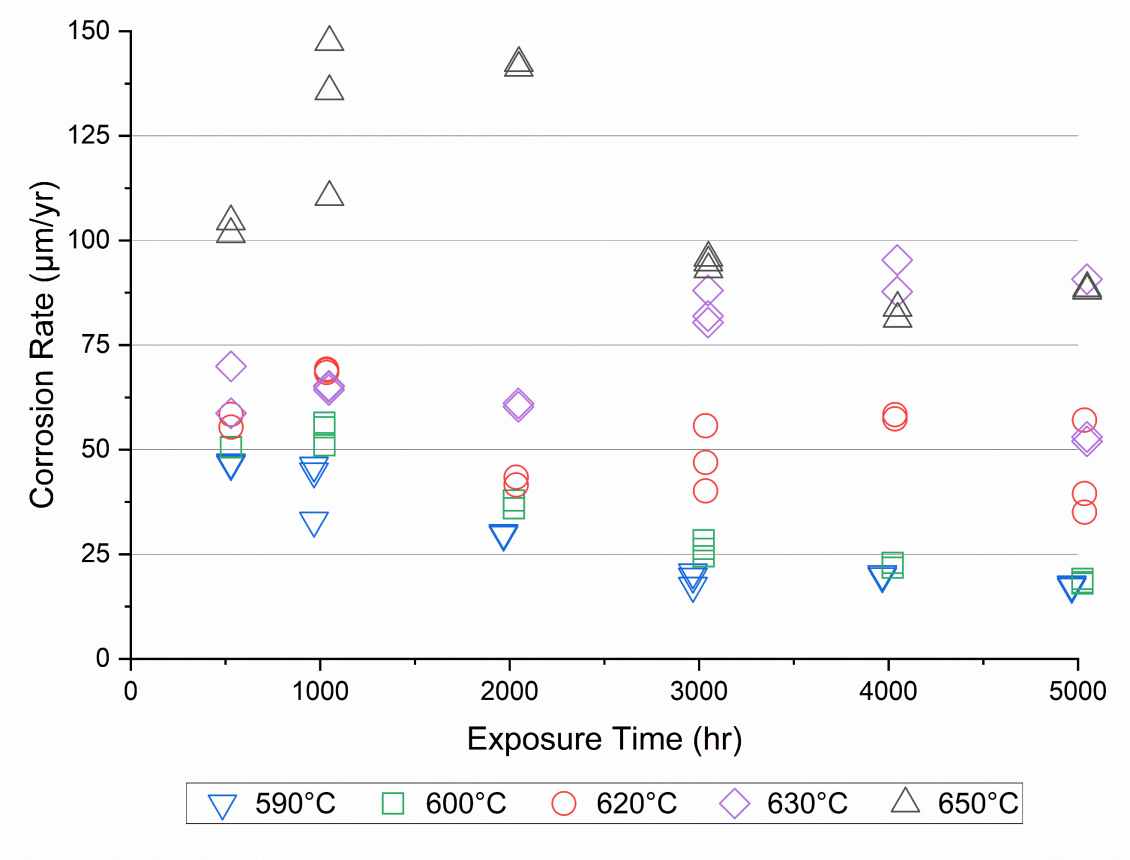

Figure 5.17: Weight change corrosion rates of WM vs. temperature and exposure time.

Figure 5.18 shows the obtained corrosion rates for the AutWeld samples. The corrosion rates were similar to 316H across all exposure temperatures and times and displayed a similar general downward trend. The flaking and general visual appearance of the AutWeld samples was also akin to the 316H and WM samples. Note that the AutWeld were 316-REF samples with roughly 1/6 of surface area covered by weld track and thus these data points cannot be considered full autogenous weld datapoints. The effect of the weld region can be extracted, however, through comparison with the base 316-REF weight change corrosion rates. The AutWeld samples were initially inserted into the vessels at the 1000hr extraction and thus the 1000hr exposed AutWeld samples could be directly compared to the 316-REF samples corroded between 1000hr to 2000hr. The results of this are shown in Table 5.2. While the relative difference in corrosion rates between 316-REF and AutWeld samples was not consistent across all temperatures, it does however indicate that at the highest temperatures, the presence of the weld track likely caused increased corrosion of the AutWeld samples.

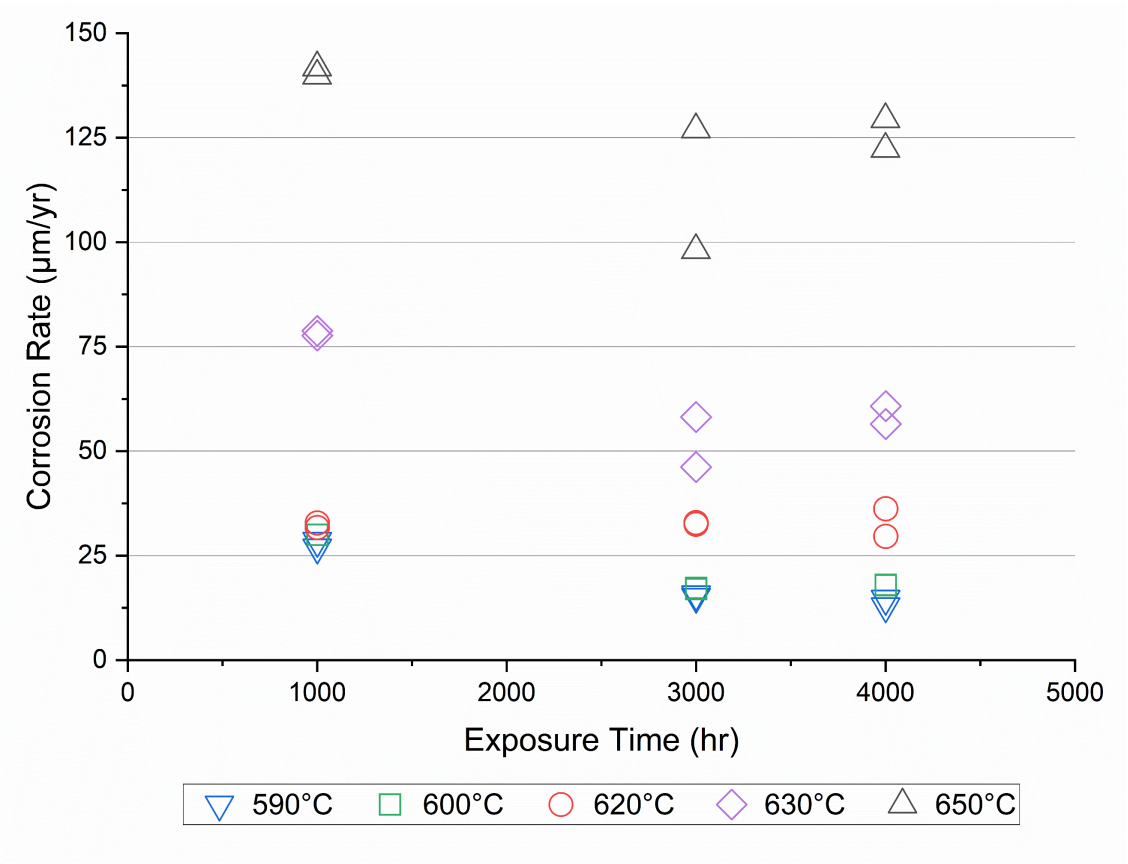

Figure 5.18: Weight change corrosion rates of AutWeld vs. temperature and exposure time.

Table 5.2: Comparison between 316-REF and AutWeld weight change corrosion rates.

Temperature	**Corrosion Rate (µm/yr)**		
(°C)	316-REF (1000hr-2000hr)	AutWeld	AutWeld/316-REF Ratio
650	118.1 ± 2.4	140.8 ± 1.0	1.19
630	57.0 ± 2.5	78.2 ± 0.6	1.37
620	30.9 ± 2.2	32.2 ± 0.5	1.04
600	33.8 ± 1.7	30.0 ± 0.0	0.89
590	24.2 ± 1.2	27.8 ± 0.8	1.15

Figure 5.19 shows the corrosion rates obtained from the aluminide-coated samples. The aluminide coating appears to be extremely protective including at 650°C with corrosion rates starting below 4µm/yr at 1000hr and dropping to around or below 1µm/yr after 4500hr. It appears that the aluminide coated on WM material performed slightly worse than when coated on 316H. This difference could indicate slightly different surfaces as a result of different substrate materials but could also just be variance between different batches. Regardless, this difference is negligible in context with the much larger corrosion rates exhibited by the non-coated materials.

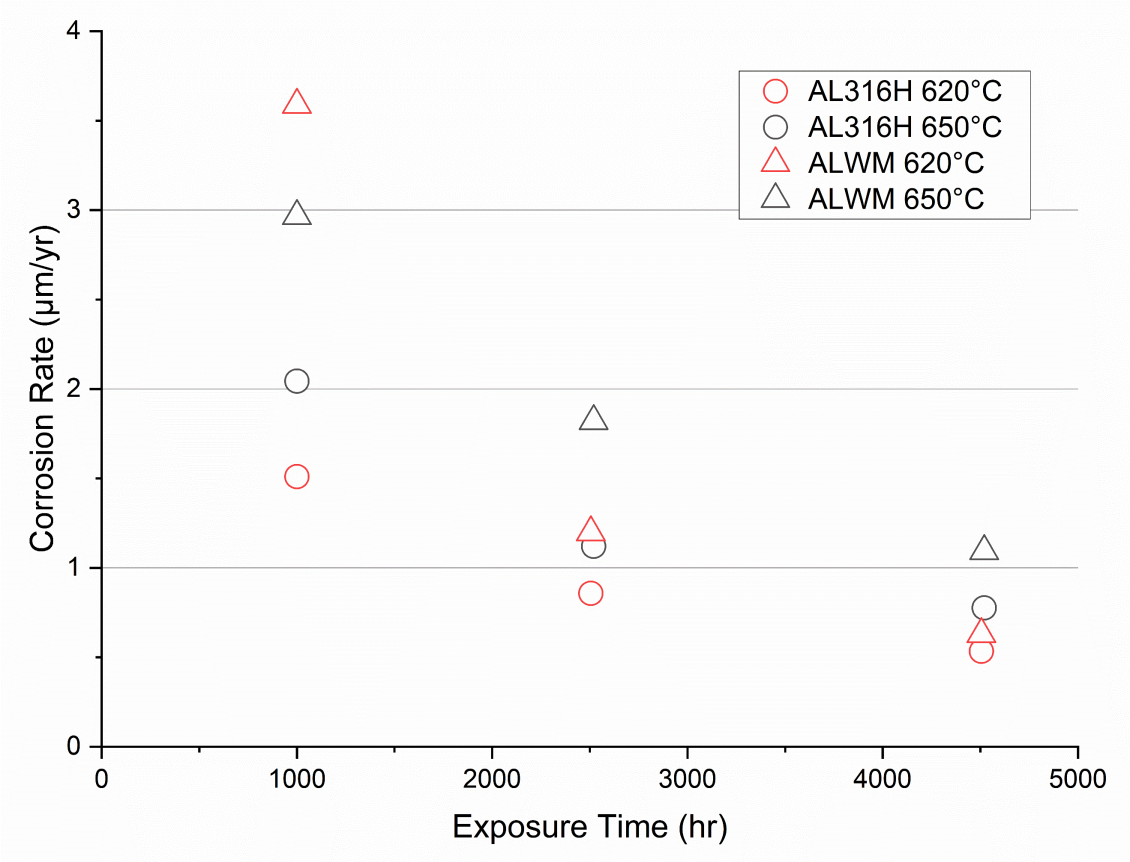

Figure 5.19: Weight change corrosion rates of aluminide coating vs. temperature and exposure time.

5.3.2. Post-Extraction Sample Surfaces

Figures 5.20-5.22 show the appearance of the samples post-extraction from the nitrate salt for 316H, 601, and AL316H, respectively. For 316H, poorly adherent oxide flakes are visibly apparent at the highest temperatures and exposure times. White/yellow cloudy features are residual nitrate salt that solidified on the sample surfaces. The appearance of the WM and AutWeld samples looked essentially identical to the 316H samples. The 601 and aluminide samples did not exhibit obvious signs of flaking including those exposed to the highest temperature and duration.

After cleaning off the salt during weight change corrosion measurements, different coloration was noticed amongst the aluminide samples of various exposure conditions. Figure 5.23 shows the AL316H samples post-salt cleaning with surfaces exhibiting colors ranging from blue to yellow. This change in coloration appears similar to the bluing of steels in which steel surfaces are exposed to corrosive solutions and/or heating to form thin oxides often for aesthetic purposes. The ALWM appeared identical to the AL316H samples both post-extraction and after cleaning.

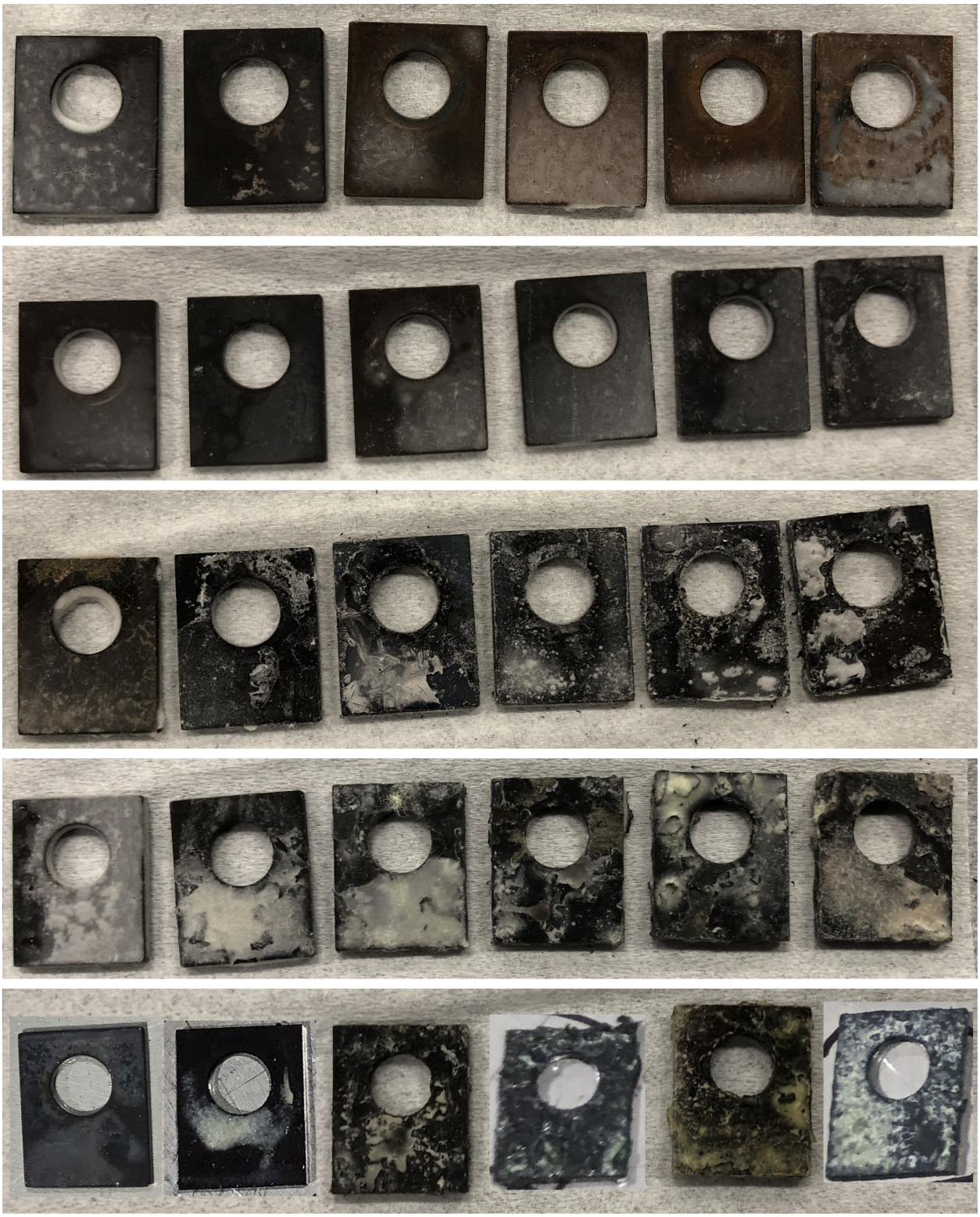

Figure 5.20: 316H samples post-exposure to Solar Salt. Temperatures from top to bottom: 590°C, 600°C, 620°C, 630°C, 650°C. Exposure times from left to right: 500hr, 1000hr, 2000hr, 3000hr, 4000hr, 5000hr.

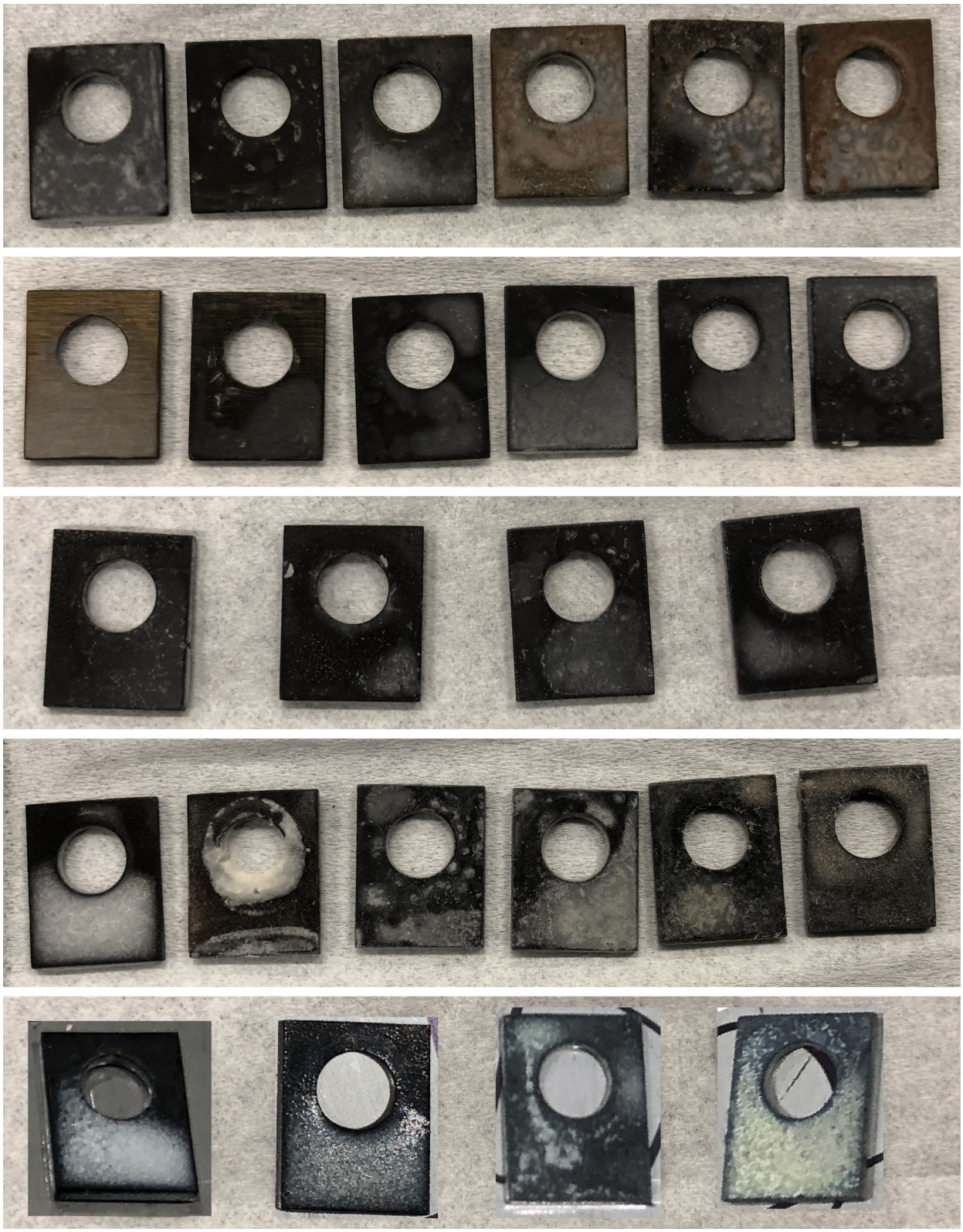

Figure 5.21: 601 samples post-exposure to Solar Salt. Temperatures from top to bottom: 590°C, 600°C, 620°C, 630°C, 650°C. Exposure times from left to right: 500hr, 1000hr, 2000hr, 3000hr, 4000hr, 5000hr. No 2000hr or 4000hr samples were generated for 620°C and 650°C.

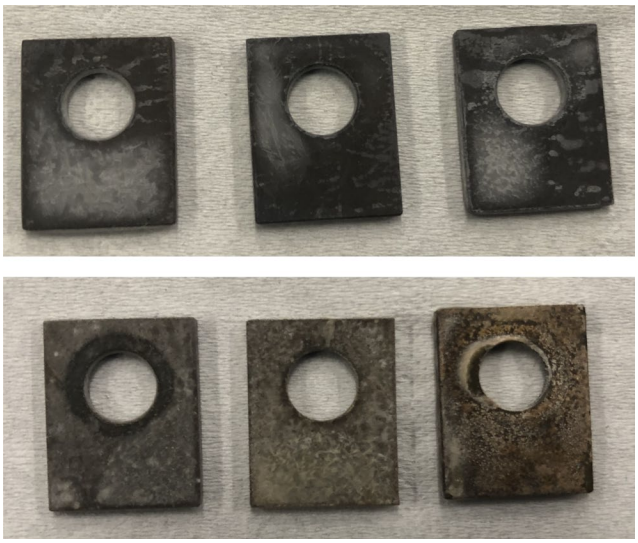

Figure 5.22: AL316H samples post-exposure to Solar Salt. Temperatures from top to bottom: 620°C, 650°C. Exposure times from left to right: 1000hr, 2500hr, 4500hr.

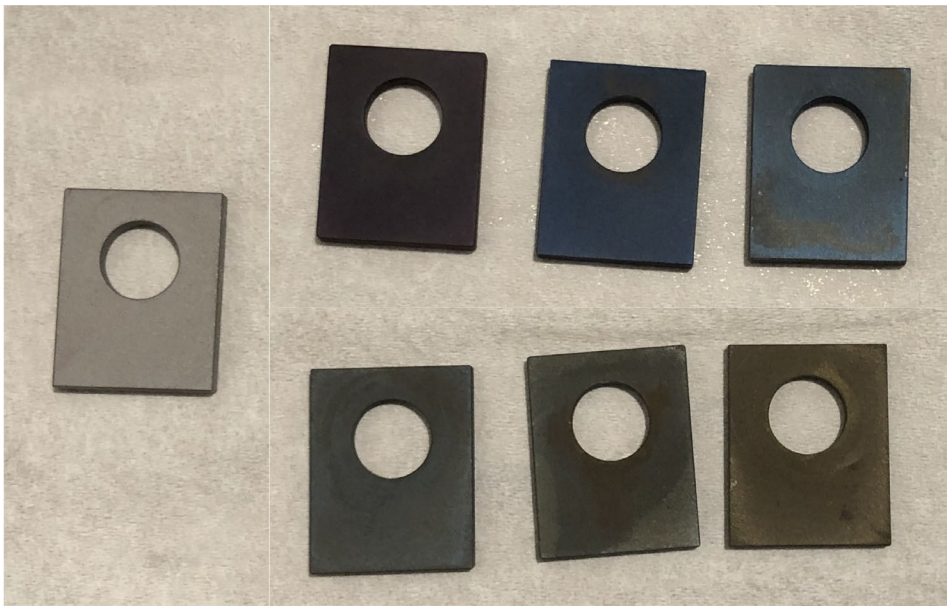

Figure 5.23: AL316H samples after salt was cleaned off revealing coloration as a function of temperature and time. An unexposed aluminide sample is shown on the left. Temperatures from top to bottom: 620°C, 650°C. Exposure times from left to right: 1000hr, 2500hr, 4500hr.

5.3.3. Scanning Electron Microscopy

This section provides a summary of the range of different corrosion scales exhibited by the materials as a function of exposure temperature and time. For all images provided, the images are oriented such that the left side is towards the bulk material while the right side is towards the corrosion scale surface. As explained in Section 5.2.5., corroded samples were mounted without cleaning off the residual nitrate salt in order to prevent loss of the entire oxide scale. As a tradeoff, nitrate salt readily "bloomed" over time over the sample surfaces and

obstructed microscopy of the corrosion scales. Figure 5.24 shows an extreme example for a sample that was left for significant time between microscopy sessions. Microscopy provided in this section are from regions that contained minimal blooming to provide full imaging of the corrosion oxide scale, though it is also evident that in some instances portions of the corrosion scales were fully lost. This is also to note that features appearing to protrude from the polished sample surface are nitrate salt solidification and blooming rather than explicit features of the corrosion layers.

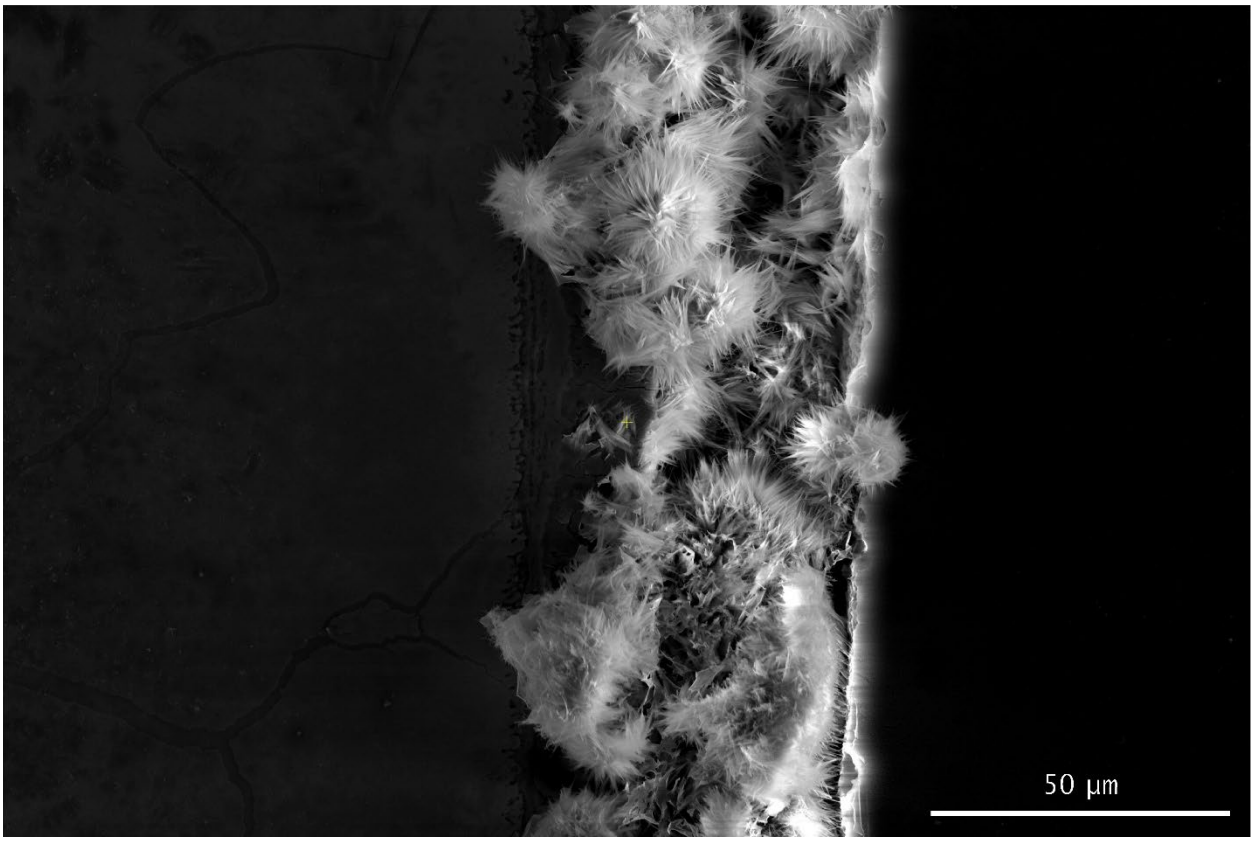

Figure 5.24: Corroded sample exhibiting significant nitrate salt blooming that obstructs microscopy of the corrosion scale.

Figure 5.25 shows a matrix of the corrosion scales observed on 316H containing images from 1000hr, 3000hr, and 5000hr exposure times and 600°C, 630°C, and 650°C exposure temperatures. From this, it is evident that there is a significant increase in corrosion scale thickness as a function of temperature and time. At 600°C for 5000hr (Figure 5.26), the 316H corrosion scale arrangement consists of an outermost $NaFeO_2$ layer followed by iron oxides, Cr_2O_3, and a Cr depletion/Ni enrichment region in the bulk. This arrangement matches well with the arrangement observed in Chapter 3 (316SS at 630°C for 600hr) and in general with other literature data at these temperatures and/or with relatively short exposure times. Also similar to as described in Chapter 3, during weight change corrosion measurements, initial cleaning steps saw the removal of brown oxide particles, while black oxides were removed over the course of subsequent cleaning steps. This indicates the presence of both Fe_2O_3 and Fe_3O_4 within the iron oxide layer, with Fe_2O_3 towards the surface.

At the higher temperatures, the corrosion scale appears to significantly change over time. The 650°C 5000hr corrosion scale (Figure 5.27) exhibits strips of Ni-enriched regions and $NaFeO_2$ throughout the iron oxide region. This could be due to corrosion layer interfaces separating to a degree in which oxide layer uplifting and salt penetration occurs, but not fully detaching to expose the bulk surface. Furthermore, there does not appear to be a clear Cr depletion/Ni enrichment in the bulk surface. Instead, the near surface bulk exhibits a region that is mainly Cr_2O_3 with Ni-enriched inclusions. Across all the microscopy of the 316H samples, clear instances of separation were observed at several interfaces: a) between the inner Cr_2O_3 region and the bulk metal surface, b) between the Cr_2O_3 layer and iron oxide (likely Fe_3O_4) layer, and c) between the Ni-enriched strips and internal $NaFeO_2$ (likely separated as Ni-enriched strips and iron oxide that then formed $NaFeO_2$ due to salt penetration).

Figure 5.28 shows a matrix of the corrosion scales observed on 601 akin to the one previously provided for 316H. It is immediately apparent that the corrosion scales on 601 are significantly smaller than that for 316H (note the 5000x magnification for the 601 images vs. 2500x for 316H). Furthermore, the 601 appears to exhibit non-uniform corrosion, with the formation of oxide pegs that extend various depths within the material. As revealed in Figure 5.29, these oxide pegs are primarily comprised of a Cr_2O_3 sheath surrounding Ni-rich inclusions. Though grain boundaries may have an effect, the prevalence of oxide pegs is much too frequent and spacing much too small to be explained by the 72.3µm average grain size for the 601 material. Cr depletion/Ni enrichment regions can be observed within the bulk metal surface, and iron oxides appear to form on the surface of the corrosion scale.

As exposure temperatures and times increase for 601 (such as in Figure 5.30), rather than appearing to corrode significantly deeper, corrosion appears to proceed predominantly from the Ni-rich inclusions near the surface which results in the corrosion appearing more uniform. Across all temperatures and times, strips of Al_2O_3 can be observed in the corrosion layer. While Al_2O_3 has been shown to be highly protective in elevated temperature Solar Salt, it does not appear to be able to form a complete layer in 601. This indicates that unlike several of the other AFA alloys investigated in Chapter 3, there is likely not enough Al in 601 relative to the other alloying elements to form a complete Al_2O_3 passivation layer. 601 therefore relies on the combination Al_2O_3 and the relatively noble nature of Ni for its corrosion resistance.

Figure 5.31 shows a matrix of the corrosion scales observed on WM (note 2500x magnification in this instance). Corrosion scales appear to be smaller than those for 316H, though it is likely that many of the outer layers flaked off (such as for the 630°C 5000hr sample). In general (such as in Figure 5.32), the corrosion scale morphology on WM is extremely similar to 316H with common oxide layer arrangements, separation layers, and the existence of Ni-enriched strips at higher temperatures and exposure times. The oxide layer thickness also increases as a function of temperature and time. At higher temperatures and exposure times, however, the WM samples show the existence of distinct Cr and Mo phases extending into the bulk material (see Figure 5.33). At the bulk surface, these phases connect to areas of slightly deeper corrosion penetration and likely corresponds to the weld microstructure in the material.

Figure 5.34 shows a matrix of the corrosion scales observed on the AutWeld samples at the weld region (note for 1000hr, 3000hr, and 4000hr exposure times as there were no 5000hr

samples generated) and Figures 5.35 and 5.36 for the weld region at with 600°C 4000hr and 650°C 4000hr exposures, respectively. Figures 5.37-5.39 provides the corresponding microscopy for the AutWeld samples but in a region unaffected by the weld process representing 316-REF. Like the WM samples, the corrosion scales for both the AutWeld and 316-REF appear to be smaller than for 316H, though it is very likely that many of the outer layers flaked off in the samples imaged due to flaking. It is of note, however, that the weld region for the AutWeld samples appeared to be more prone to complete flaking of the oxide layer than the 316-REF region unaffected by the welding process. Regardless, the corrosion scales that were captured again appear similar to 316H in terms of morphology and evolution as a function of exposure temperature and time.

Like the WM samples, distinct Cr and Mo phases were discernable along the grain boundaries. Further investigation of this at higher magnification revealed also the presence of acicular features within the bulk grain volume (Figure 5.40). As will be revealed through TEM in Section 5.3.4., these acicular features, along with the Cr phases along the grain boundaries, are CrN. Revisiting the microscopy of the other alloys, these features were also observed to exist in the near surface bulk but were not as readily apparent as in Figure 5.40 or through TEM. The presence of these features was more pronounced as exposure temperatures and times increased.

Figure 5.41 shows the SEM image and EDS elemental maps for AL316H exposed to the most extreme condition (650°C Solar Salt for 4500hr). Like the weight change corrosion rates suggest, the aluminide coating is extremely resistant to Solar Salt corrosion, and microscopy reveals the presence of a very thin Al_2O_3 layer protecting the underlying material. Also noticeable is the presence of CrMn precipitates near the coating surface. Given that both Cr and Mn are both highly soluble in nitrate salt, this indicates that even the thin Al_2O_3 layer is sufficient to prevent their reaction with the salt.

Similar to in Chapter 3, significant cracking and surface flaking of the aluminide coating was found occasionally (see Figures 5.42 and 5.43). No signs of corrosion were detected along the cracks indicating that they were from the sample preparation process rather than during experiments. However, this again highlights concerns regarding how this brittle aluminide layer would hold up in applications with significant stresses. No discernable change was evident in the intermetallic region of the coating samples, including in areas with significant cracking.

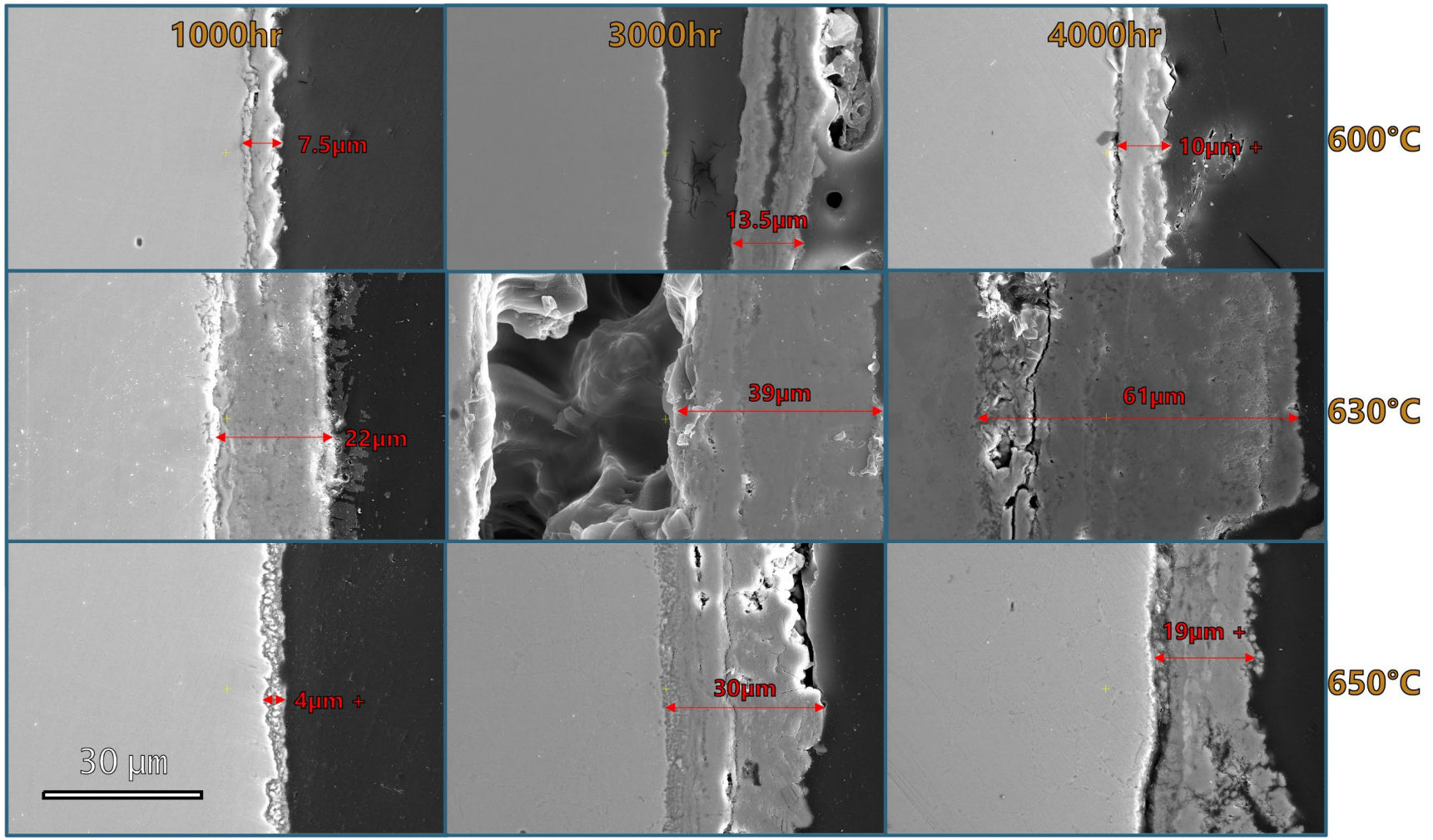

Figure 5.25: Matrix of corrosion scales observed on 316H as a function of temperature and exposure time. 2500x magnification.

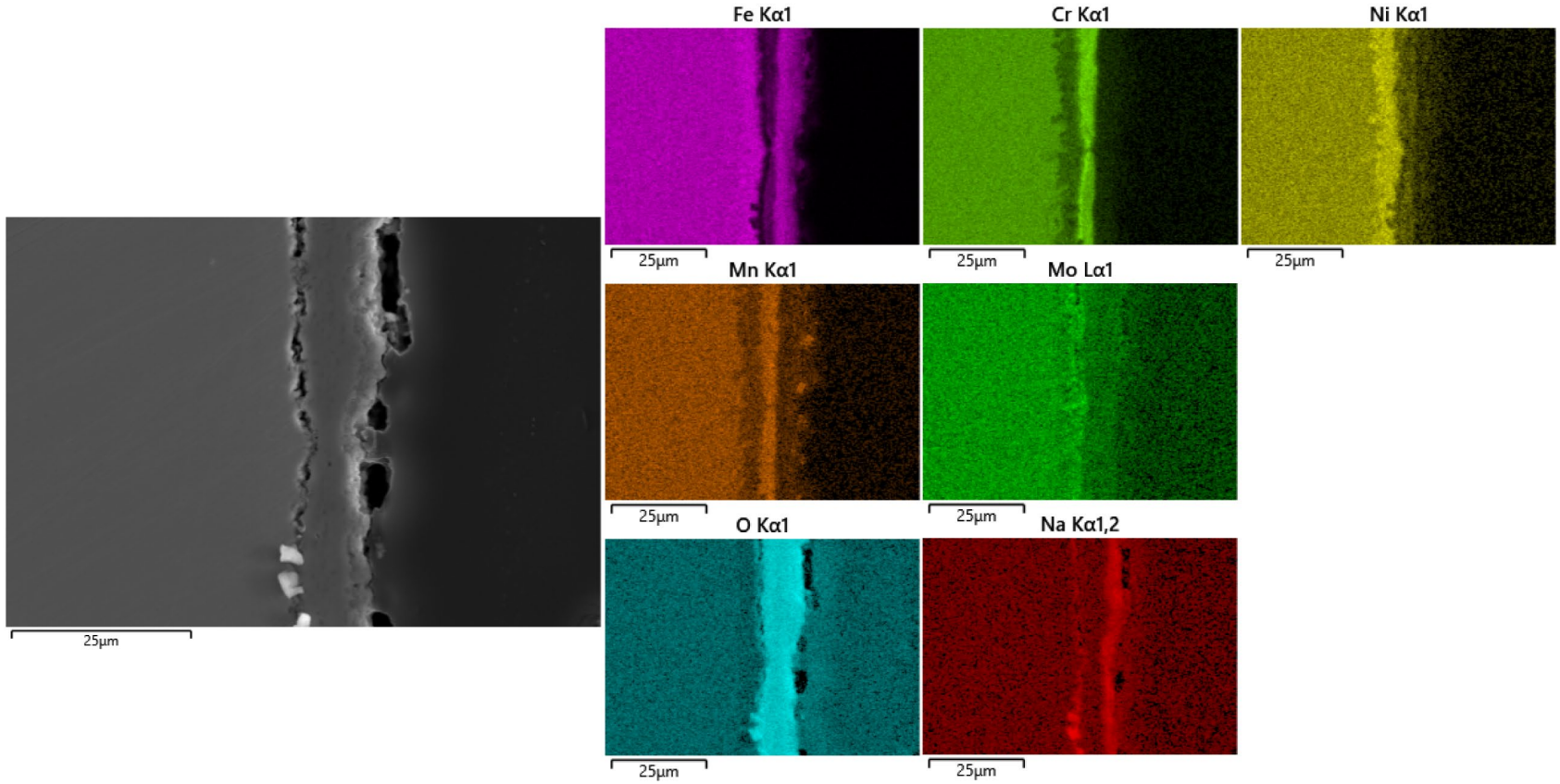

Figure 5.26: SEM image and EDS elemental maps for 316H exposed to 600°C Solar Salt for 5000hr. 2500x magnification.

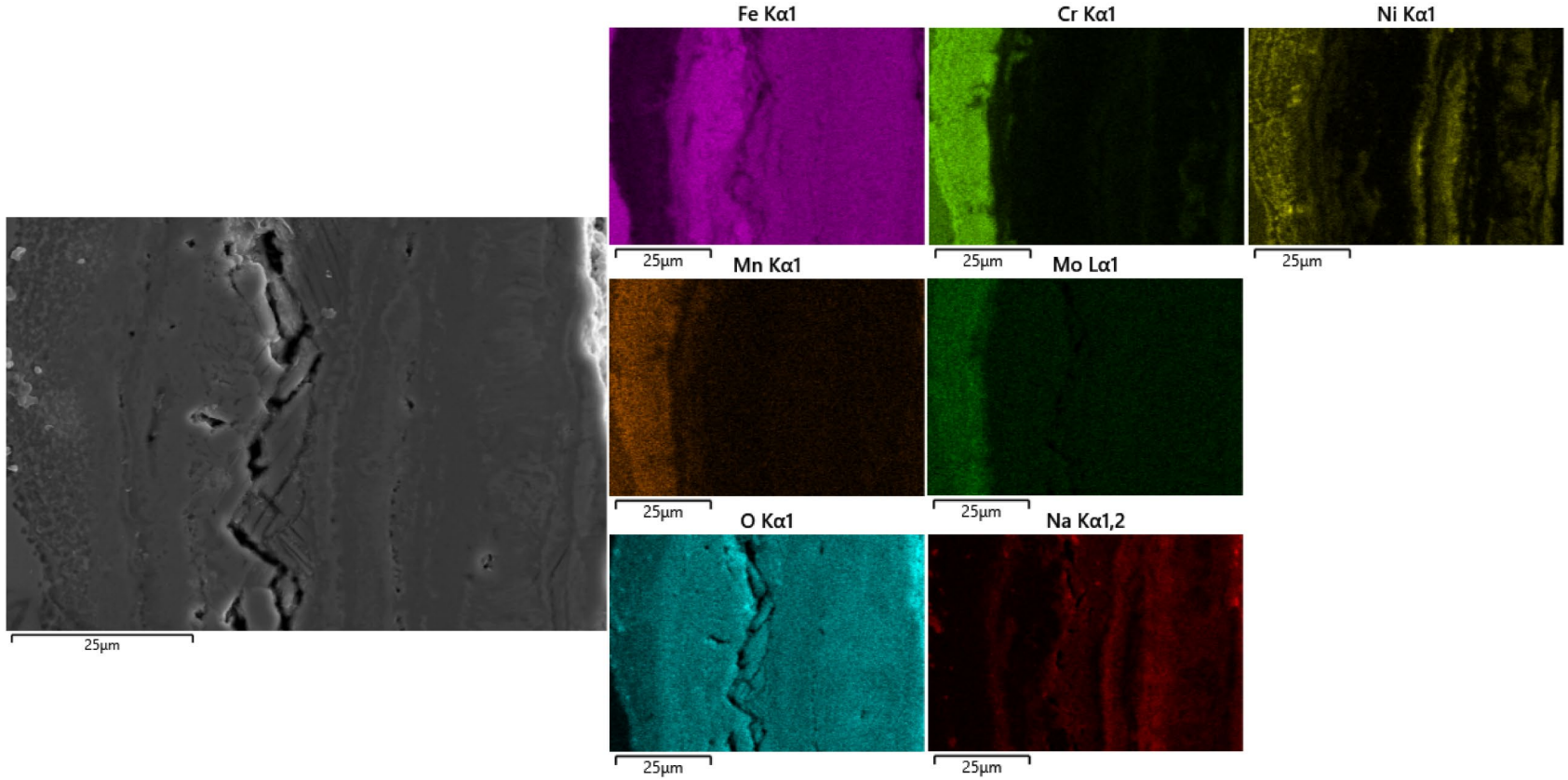

Figure 5.27: SEM image and EDS elemental maps for 316H exposed to 650°C Solar Salt for 5000hr. 2500x magnification.

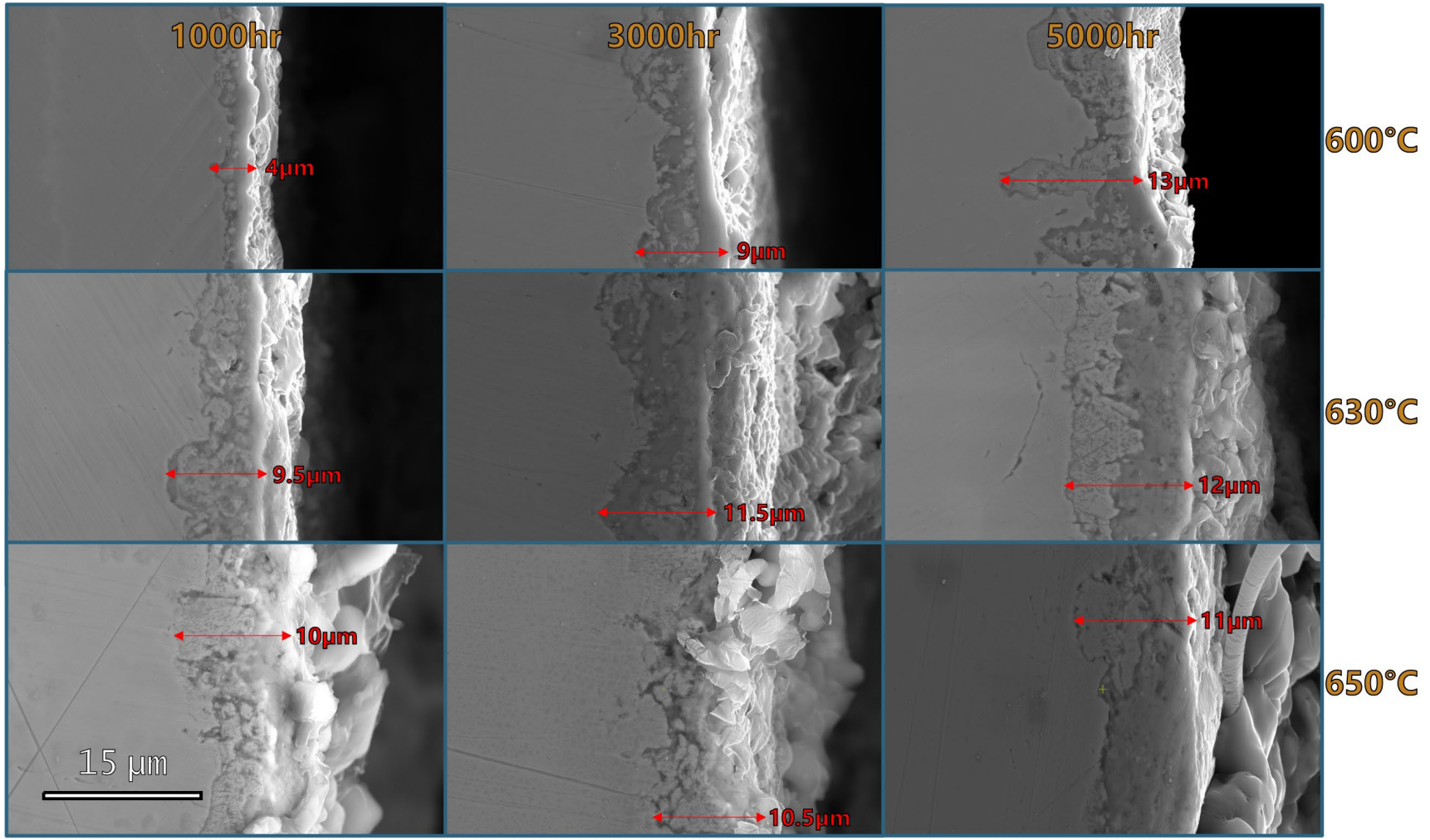

Figure 5.28: Matrix of corrosion scales observed on 601 as a function of temperature and exposure time. 5000x magnification.

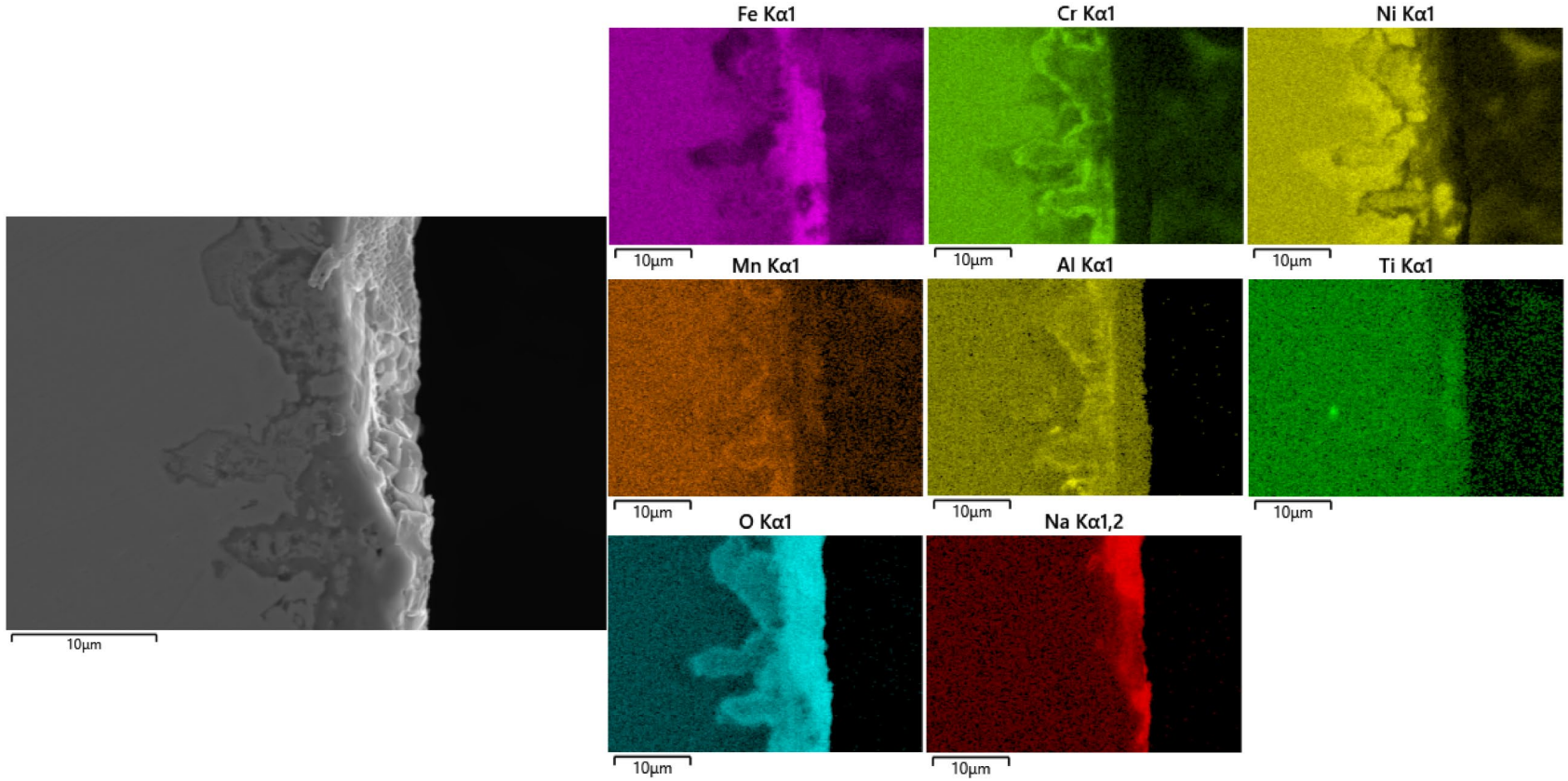

Figure 5.29: SEM image and EDS elemental maps for 601 exposed to 600°C Solar Salt for 5000hr. 5000x magnification.

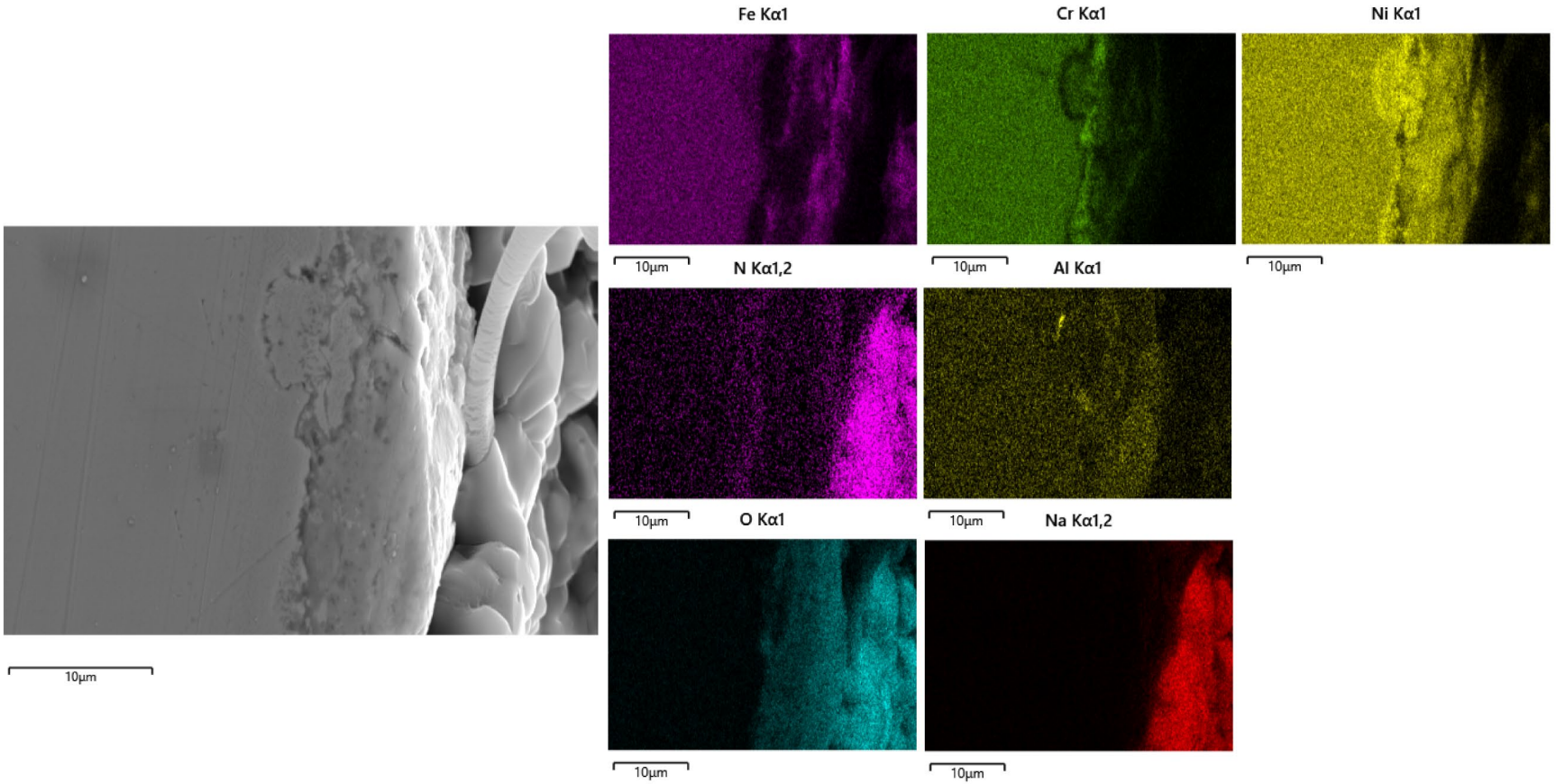

Figure 5.30: SEM image and EDS elemental maps for 601 exposed to 650°C Solar Salt for 5000hr. 5000x magnification.

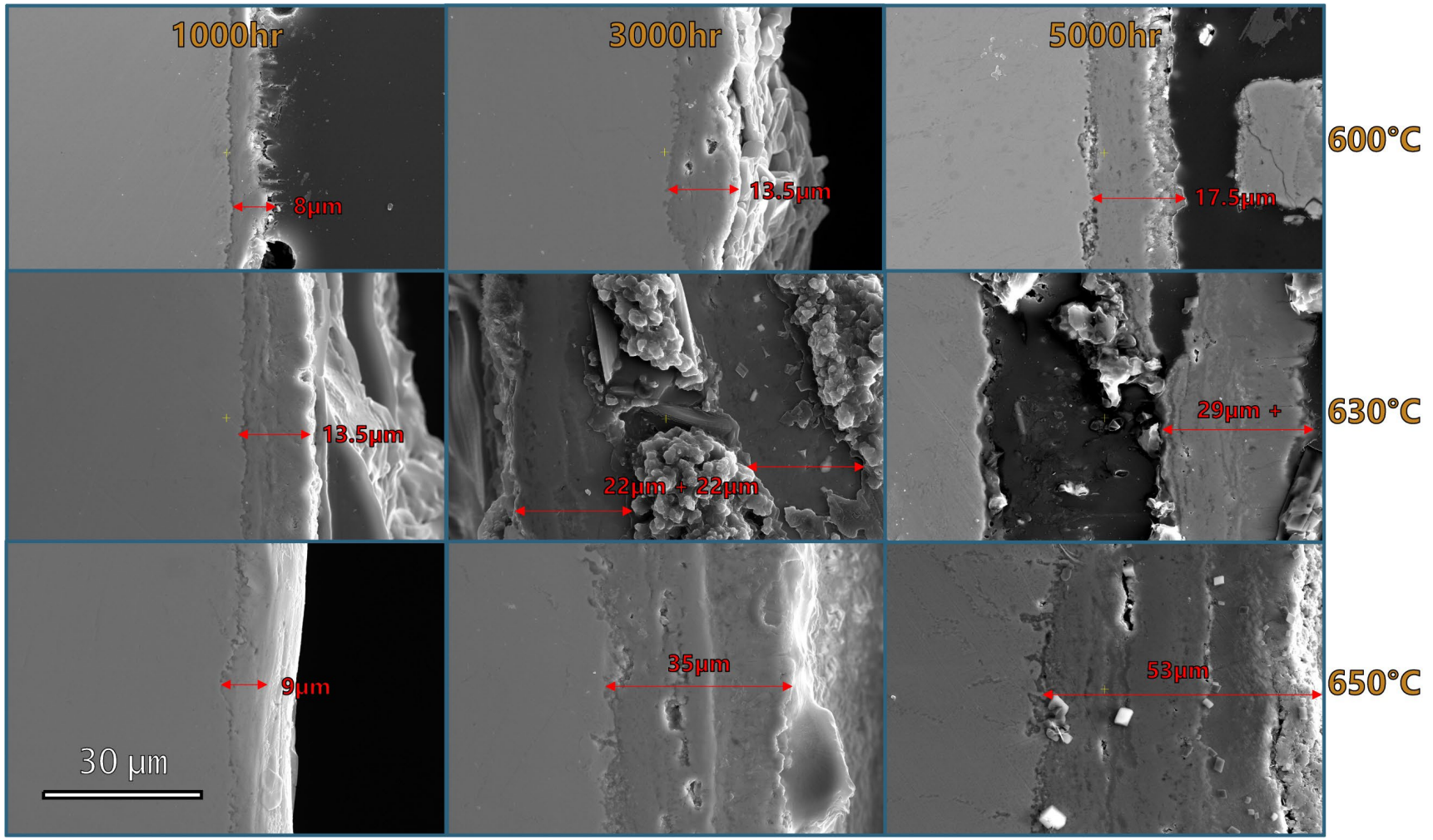

Figure 5.31: Matrix of corrosion scales observed on WM as a function of temperature and exposure time. 2500x magnification.

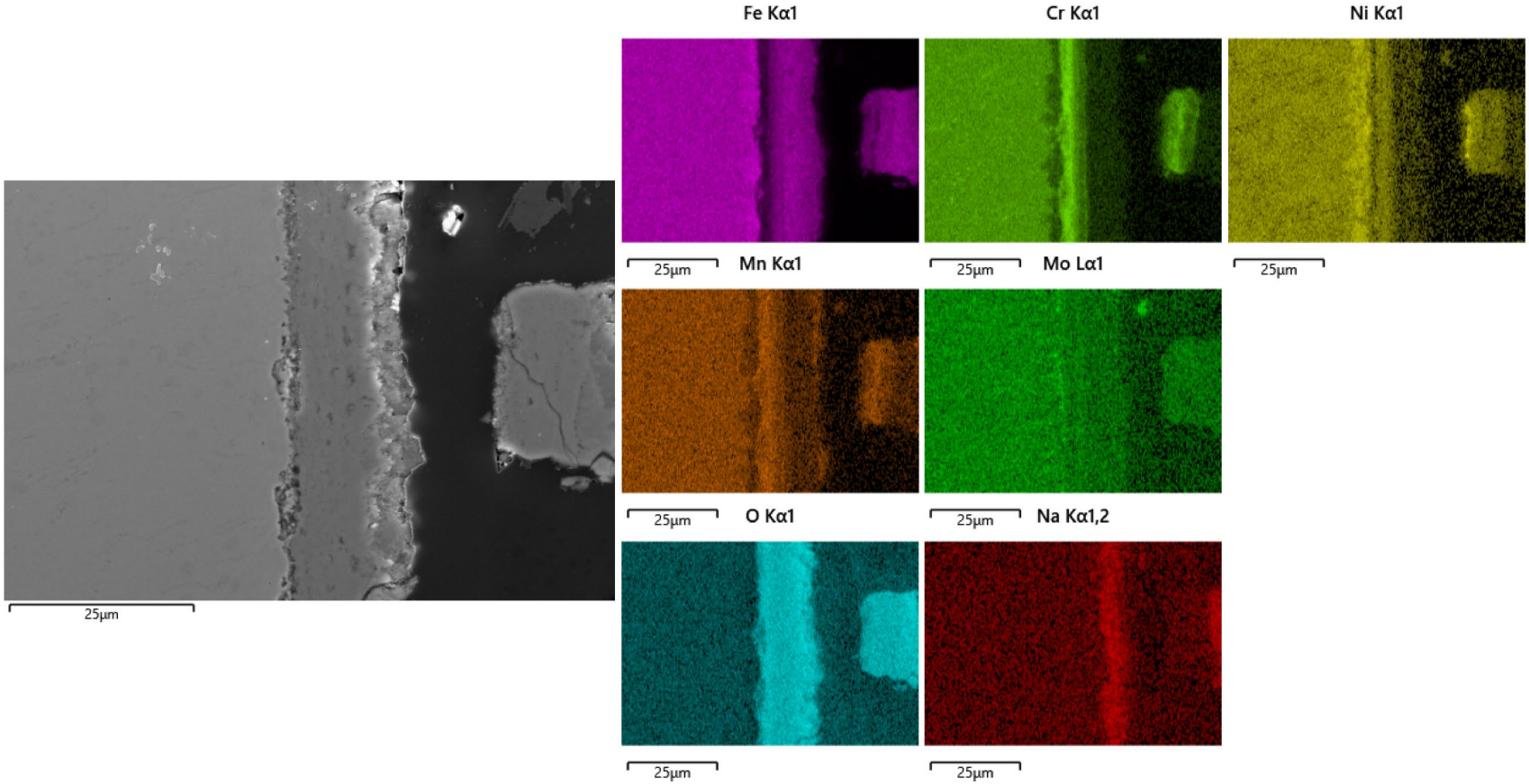

Figure 5.32: SEM image and EDS elemental maps for WM exposed to 600°C Solar Salt for 5000hr. 2500x magnification. A piece of completely de-adhered oxide layer can be observed on the right side of the image.

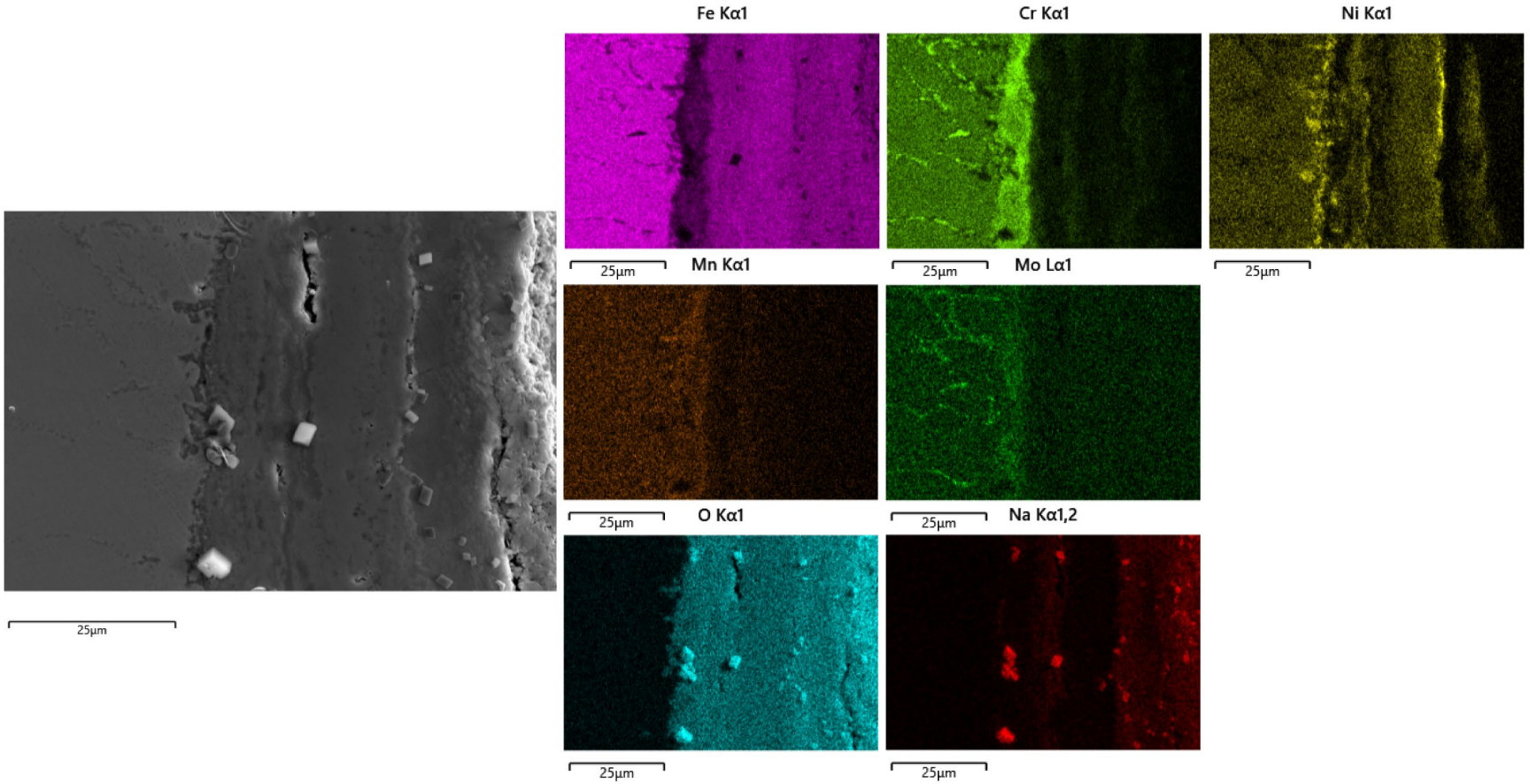

Figure 5.33: SEM image and EDS elemental maps for WM exposed to 650°C Solar Salt for 5000hr. 2500x magnification.

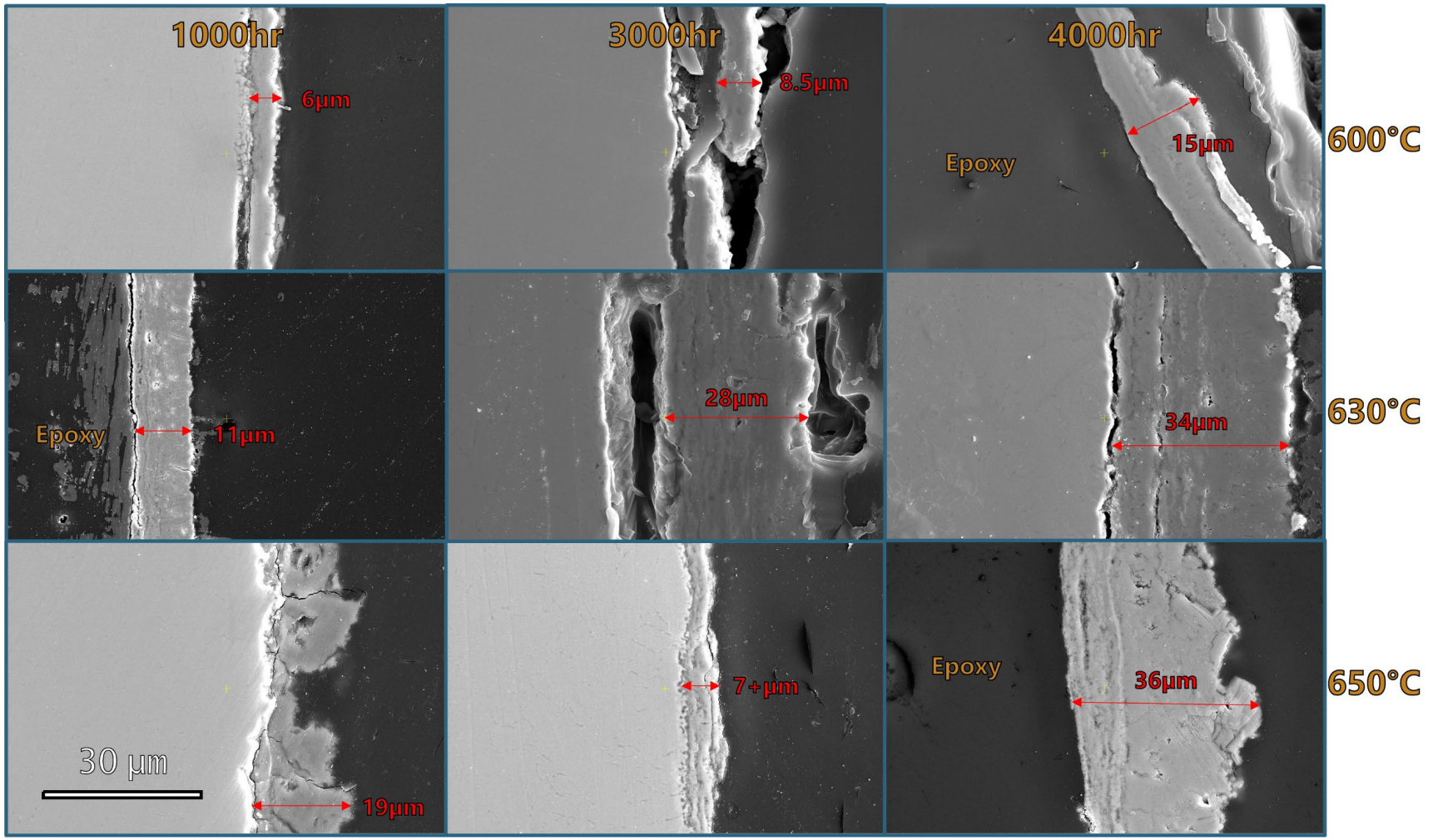

Figure 5.34: Matrix of corrosion scales observed on AutWeld as a function of temperature and exposure time. 2500x magnification.

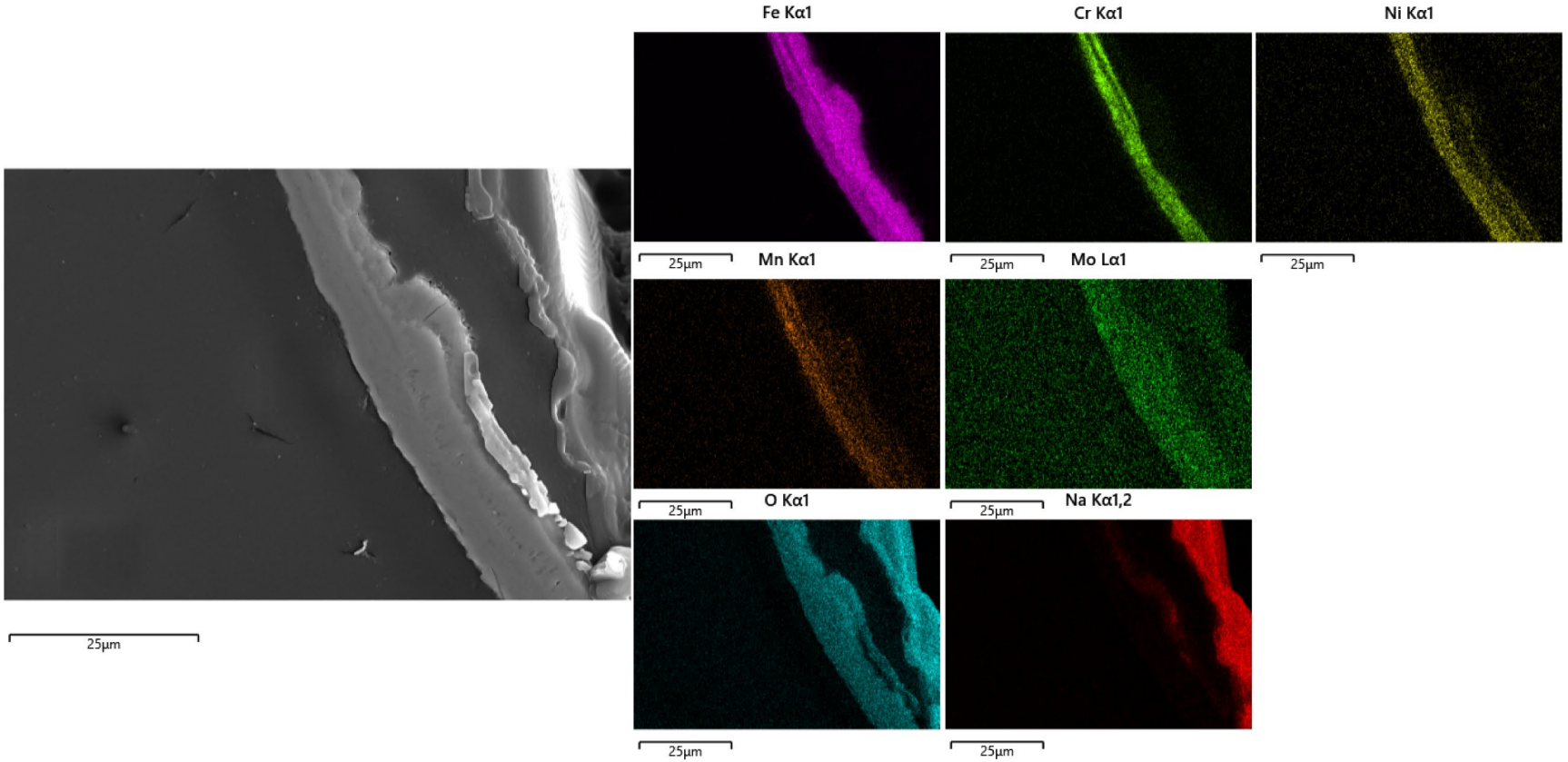

Figure 5.35: SEM image and EDS elemental maps for a spalled off oxide region of AutWeld exposed to 600°C Solar Salt for 4000hr. 2500x magnification.

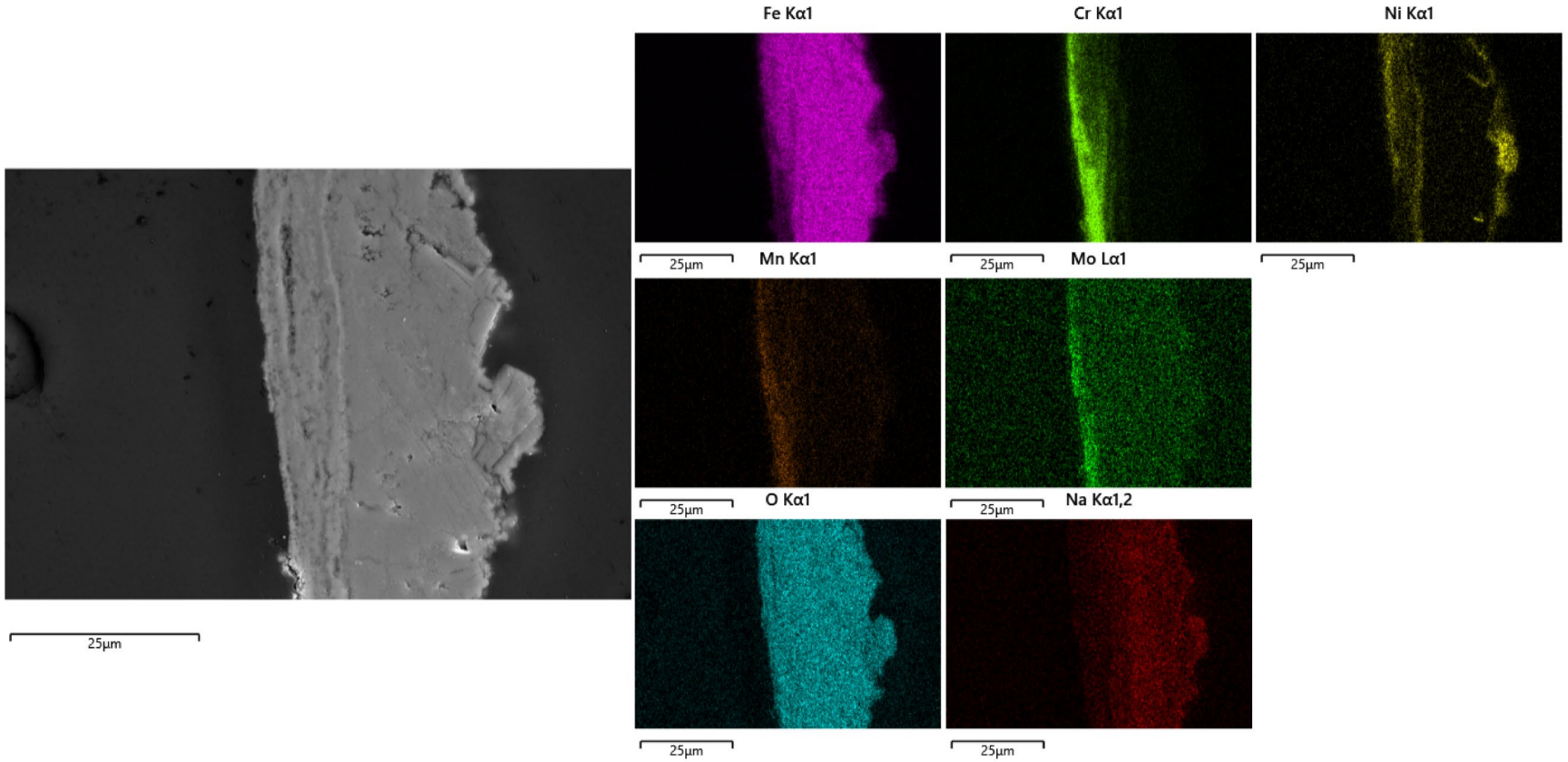

Figure 5.36: SEM image and EDS elemental maps for a spalled off oxide region of AutWeld exposed to 650°C Solar Salt for 4000hr. 2500x magnification.

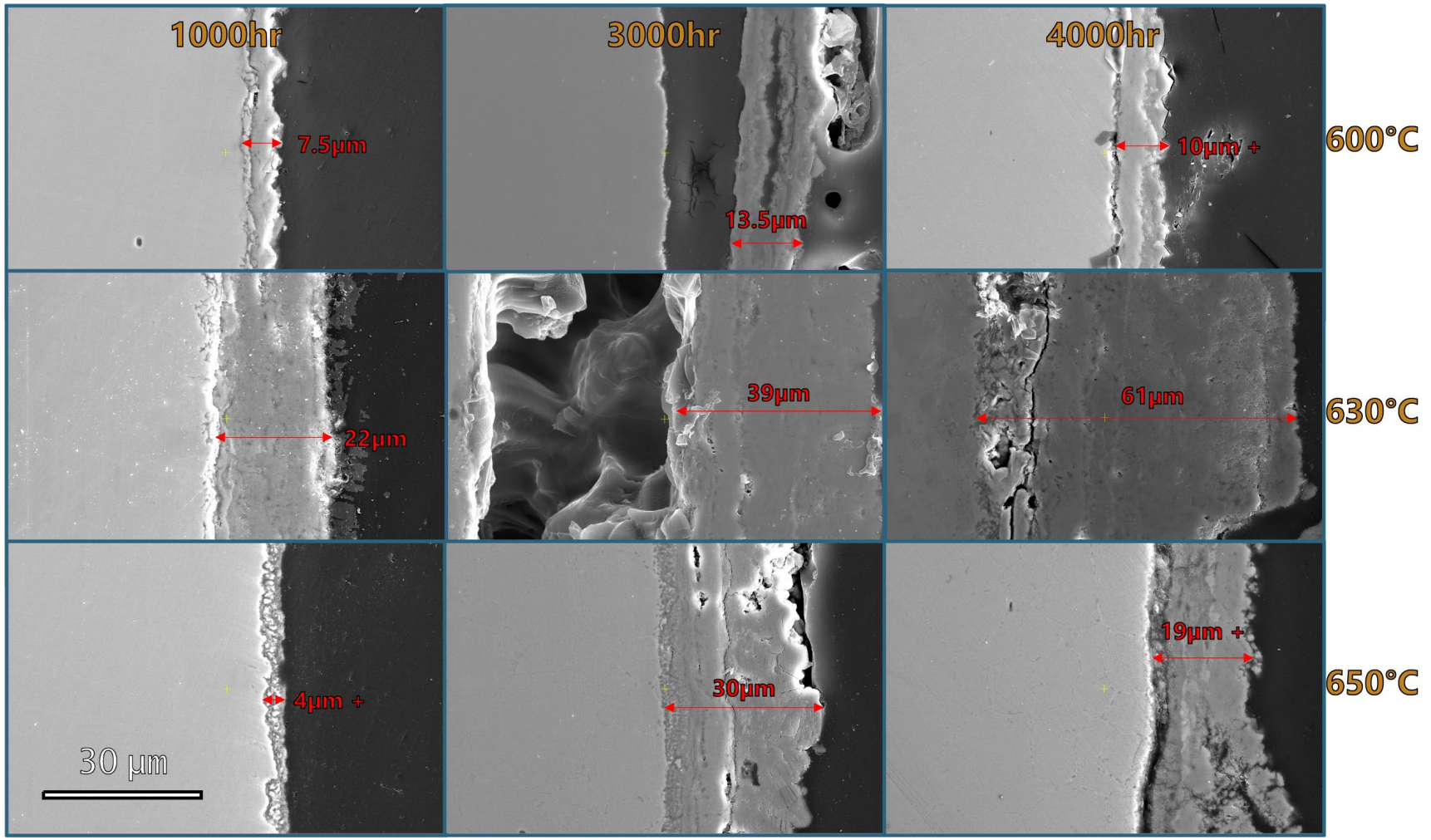

Figure 5.37: Matrix of corrosion scales observed on 316-REF as a function of temperature and exposure time. 2500x magnification.

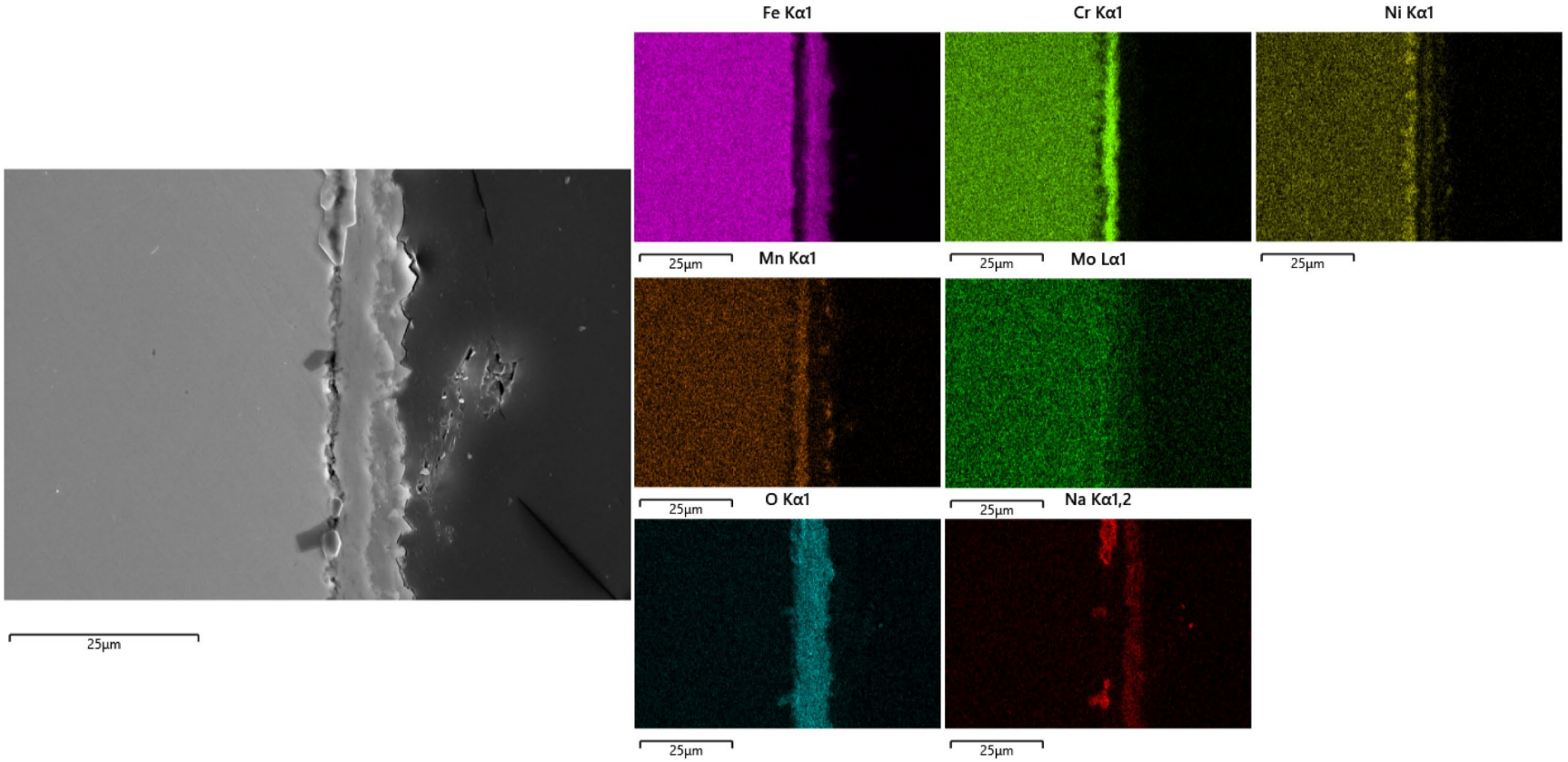

Figure 5.38: SEM image and EDS elemental maps for 316-REF exposed to 600°C Solar Salt for 4000hr. 2500x magnification.

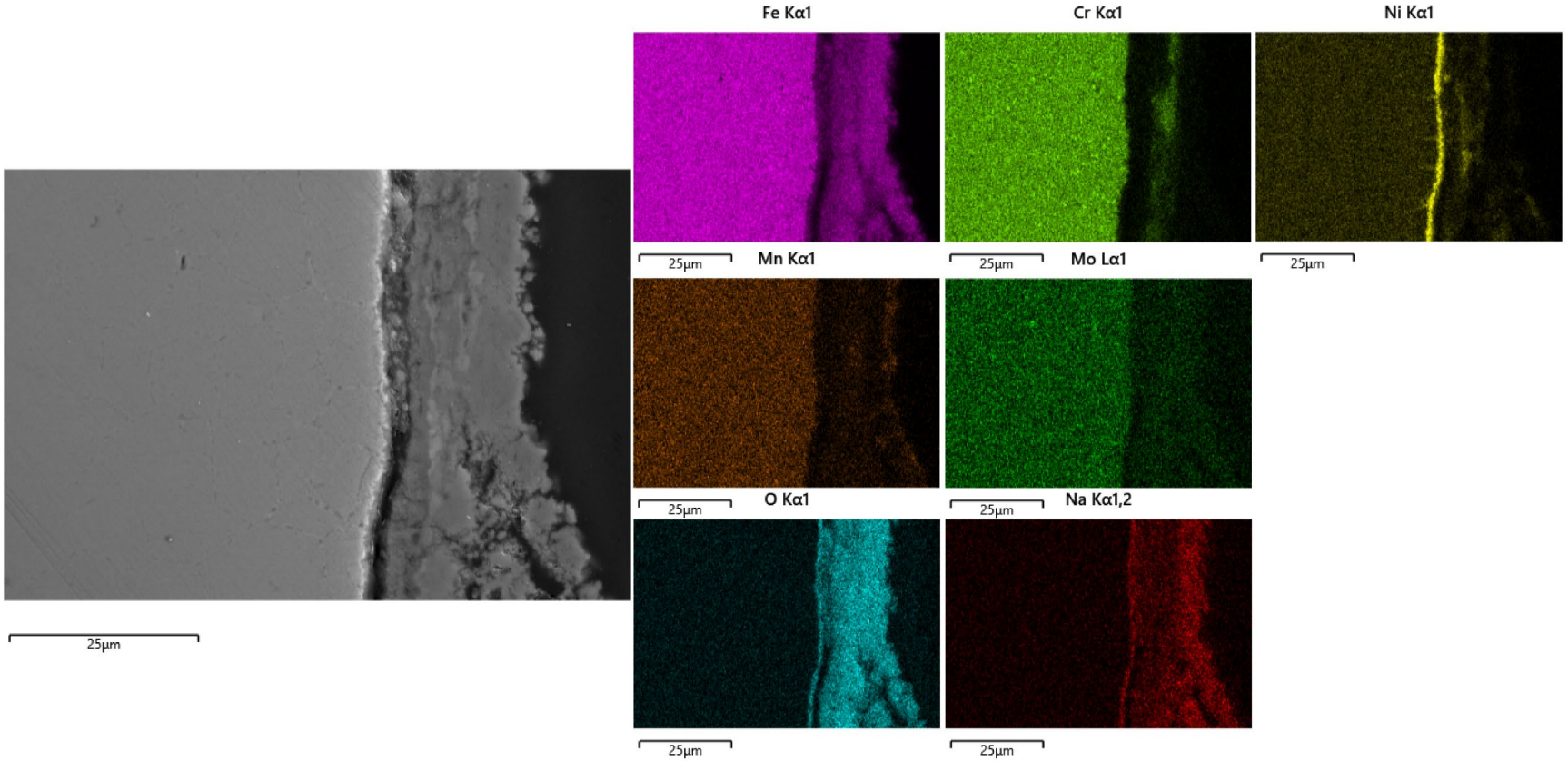

Figure 5.39: SEM image and EDS elemental maps for 316-REF exposed to 650°C Solar Salt for 4000hr. 2500x magnification.

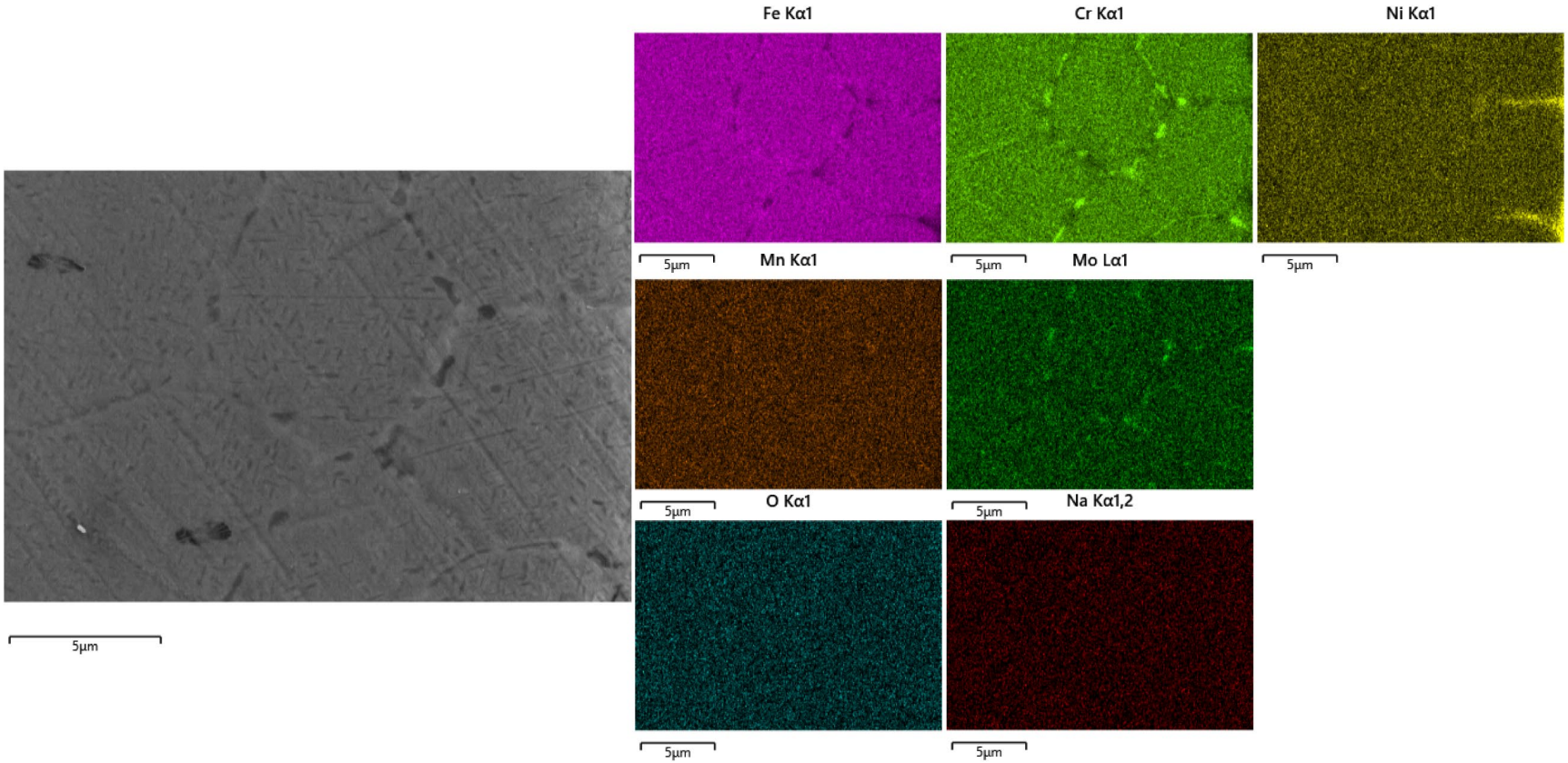

Figure 5.40: SEM image and EDS elemental maps for the near surface bulk metal region of 316-REF exposed to 650°C Solar Salt for 4000hr. 10000x magnification.

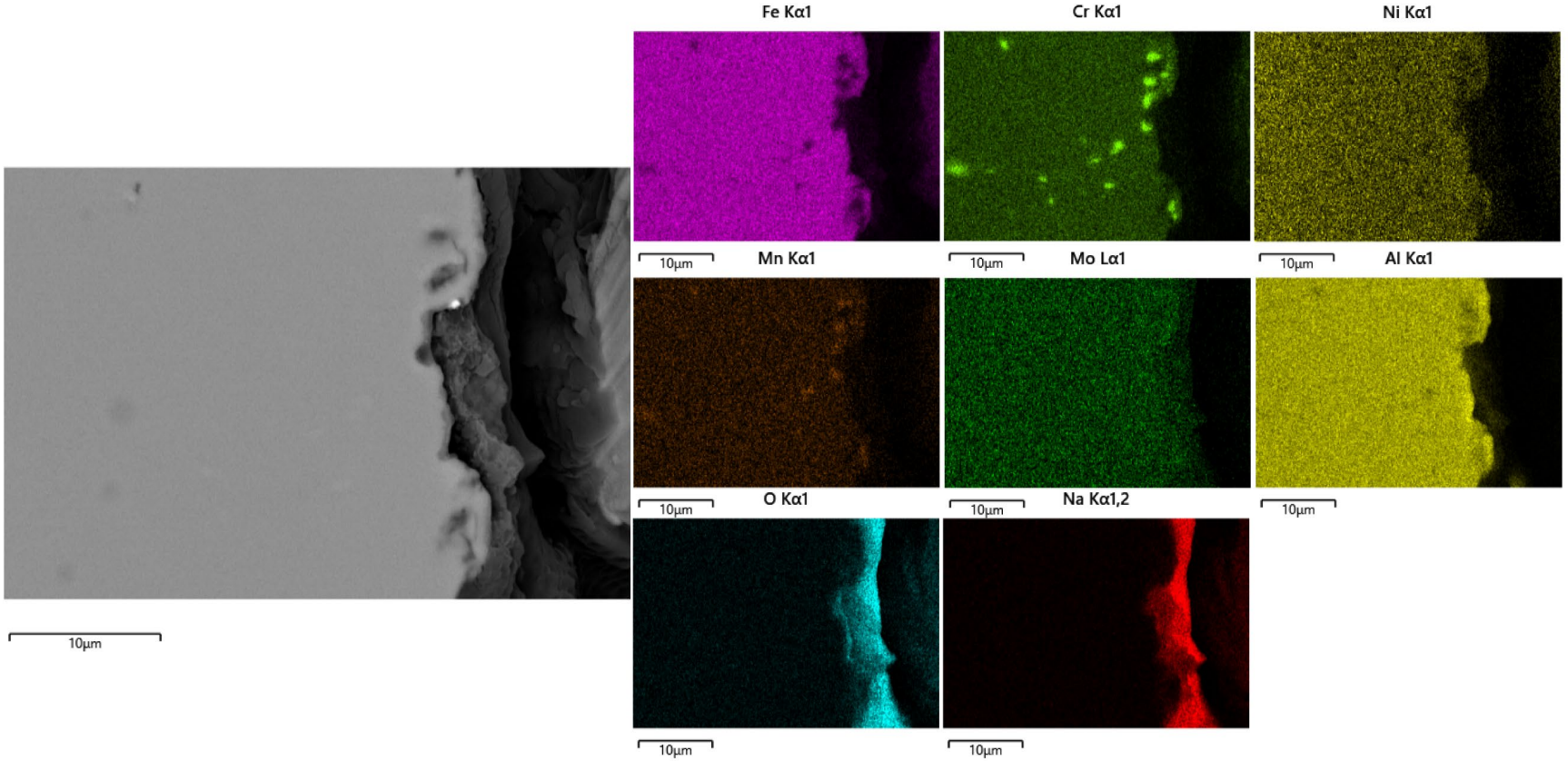

Figure 5.41: SEM image and EDS elemental maps for AL316H exposed to 650°C Solar Salt for 4500hr. 2500x magnification.

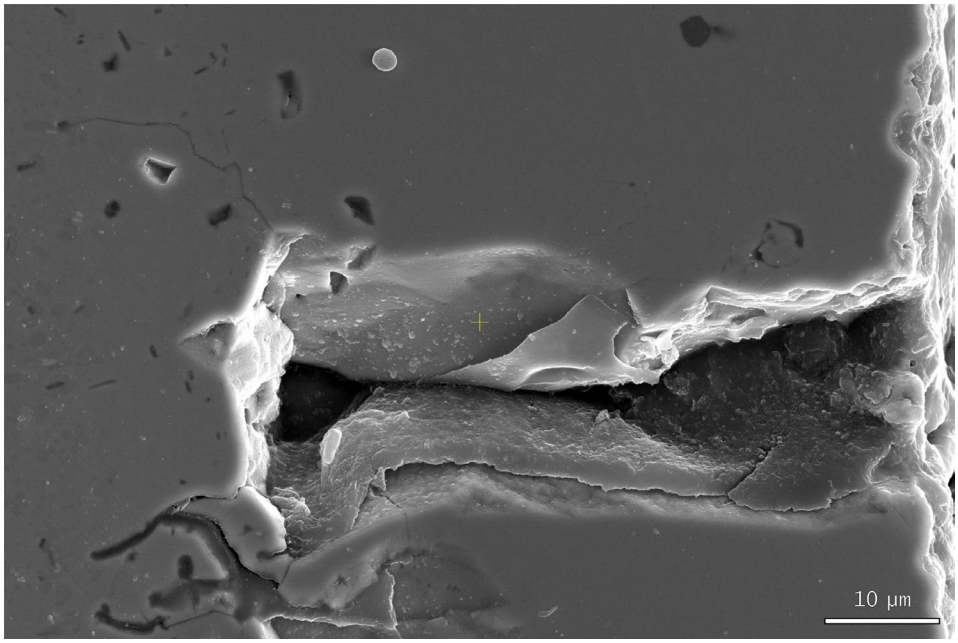

Figure 5.42: Aluminide coating sample exhibiting significant cracking. 2500x magnification.

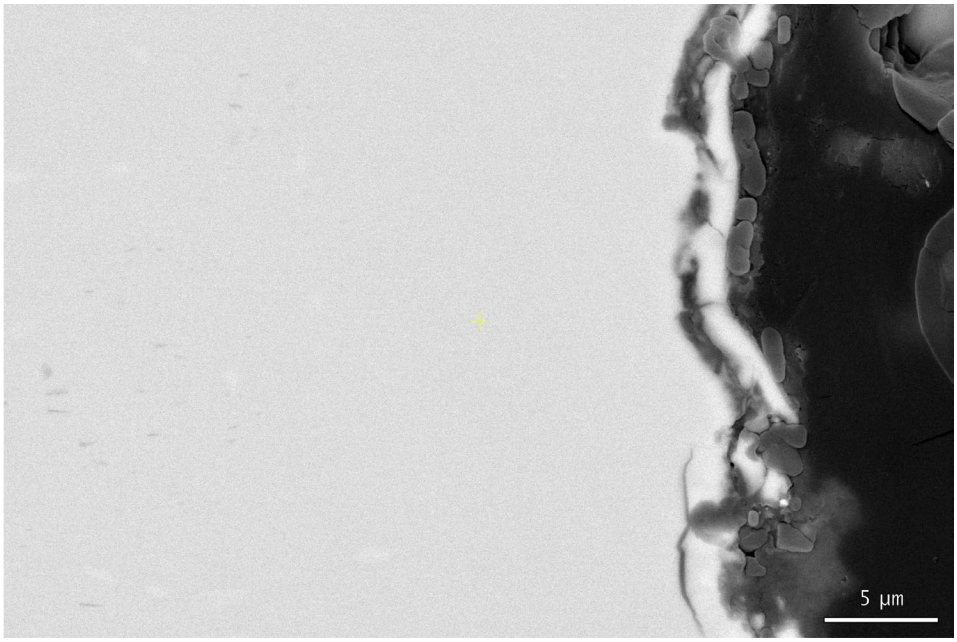

Figure 5.43: Aluminide coating sample exhibiting surface flaking. 5000x magnification.

5.3.4. Transmission Electron Microscopy

Figure 5.44 shows the TEM image and EDS maps of the entire corrosion scale for 316H exposed to 600°C Solar Salt for 5000hr and further details the ordered oxide layer arrangement observed at exposure temperatures where flaking of the oxide layers does not readily occur. The outermost $NaFeO_2$ layer appears faceted in nature and visibly distinguishable from the inner oxide layers. Underneath is a complete iron oxide region and a relatively nonuniform Cr_2O_3/iron oxide spinel layer with Mn enrichment. Hints of Ni phases within the oxide layer can also be

discerned, though not as prevalent as in the higher temperatures as will be described later. Signs of nitrate salt penetration deep within the oxide layer and to the bulk metal surface can be observed by the elevated Na signal around the top left of the images. In the bulk metal surface, there are instances of Mo phases scattered throughout. Figure 5.45 shows the same sample but deeper into the bulk metal region. It is evident that near the surface is a Cr (and Mn) denuded zone resulting in elevated Ni/Fe content. This Cr denuded zone was also present in areas along the bulk metal surface for the 601 samples, an example of which is provided in Figure 5.46.

Figure 5.47 shows the innermost oxide region for 316H exposed to 650°C Solar Salt for 5000hr. Ni phases can be readily observed scattered throughout the Cr_2O_3 region. As will be shown later through 4D-STEM analysis, these phases were confirmed to be metallic in nature. Acicular features are also apparent within the bulk metal surface. Higher magnification microscopy of the bulk metal surface (Figure 5.48) reveals that the acicular features are CrN phases as well as the presence of an extremely thin (few hundred nm) elevated Ni region at the metal-oxide interface. Nitriding of the bulk metal surface was also observed for 601 samples (Figures 5.49 and 5.50) and were more prevalent as sample exposure temperature and duration increased. The presence of Fe oxides on the very surface was also confirmed for 601 samples. Figure 5.51 shows an example of a TEM foil containing a grain boundary that exhibited distinct formation of CrN and Mo phases that correlates with the grain boundary nitriding observed through SEM (Figure 5.40 in Section 5.3.3.).

Continuing with near surface bulk features, Figure 5.52 shows the bulk surface region for a 601 sample indicating a complex arrangement and presence of phases such as AlN, Al_2O_3, Cr_2O_3, and iron oxide. Cr diffusion and associated formation of Cr_2O_3 can also be observed as channels through the bulk metal volume. It is likely through this process that over time, Ni-rich phases get broken up into smaller pieces and embedded within the oxide layers (Figure 5.53). Figure 5.54 shows the distinct transition between CrN and Cr_2O_3 along the bulk metal interface and their highly related geometry. This indicates the formation of CrN phases within the bulk metal as precursors to Cr_2O_3, with the bulk metal interface being the maximum extent of oxygen diffusion through the corrosion scale.

Moving to the oxide layers and particularly the oxide surface, Figure 5.55 shows the outermost oxide region for 316H exposed to 650°C Solar Salt for 1000hr and reveals the presence of significant voids and through-thickness cracking within the oxide layer. Significant cracks and porosity were observed throughout the various oxide layers and corroborate with the occasionally observed evidence of salt penetration deep within the corrosion scale.

Figure 5.56 shows a TEM foil for 601 that contained a significant Ni surface phase as well as the presence of distinct Mo and Cu phases within the oxide. Higher magnification microscopy of the surface phase is provided in Figure 5.57. This Ni surface phase appears similar in morphology to the more readily observed Co surface phases for Co-containing alloys in Chapter 3. Using 4D-STEM, diffraction patterns of the various features were collected, and the Ni phases in the oxide and on the surface as well as the Mo and Cu phases observed in the oxide were all determined to be metallic in nature (Figures 5.58-5.61). The presence of stable metallic Mo is curious given its hypothesized solubility in nitrate salt. This indicates that Mo is at the very least not as soluble as Mn and Cr and/or diffuses slower.

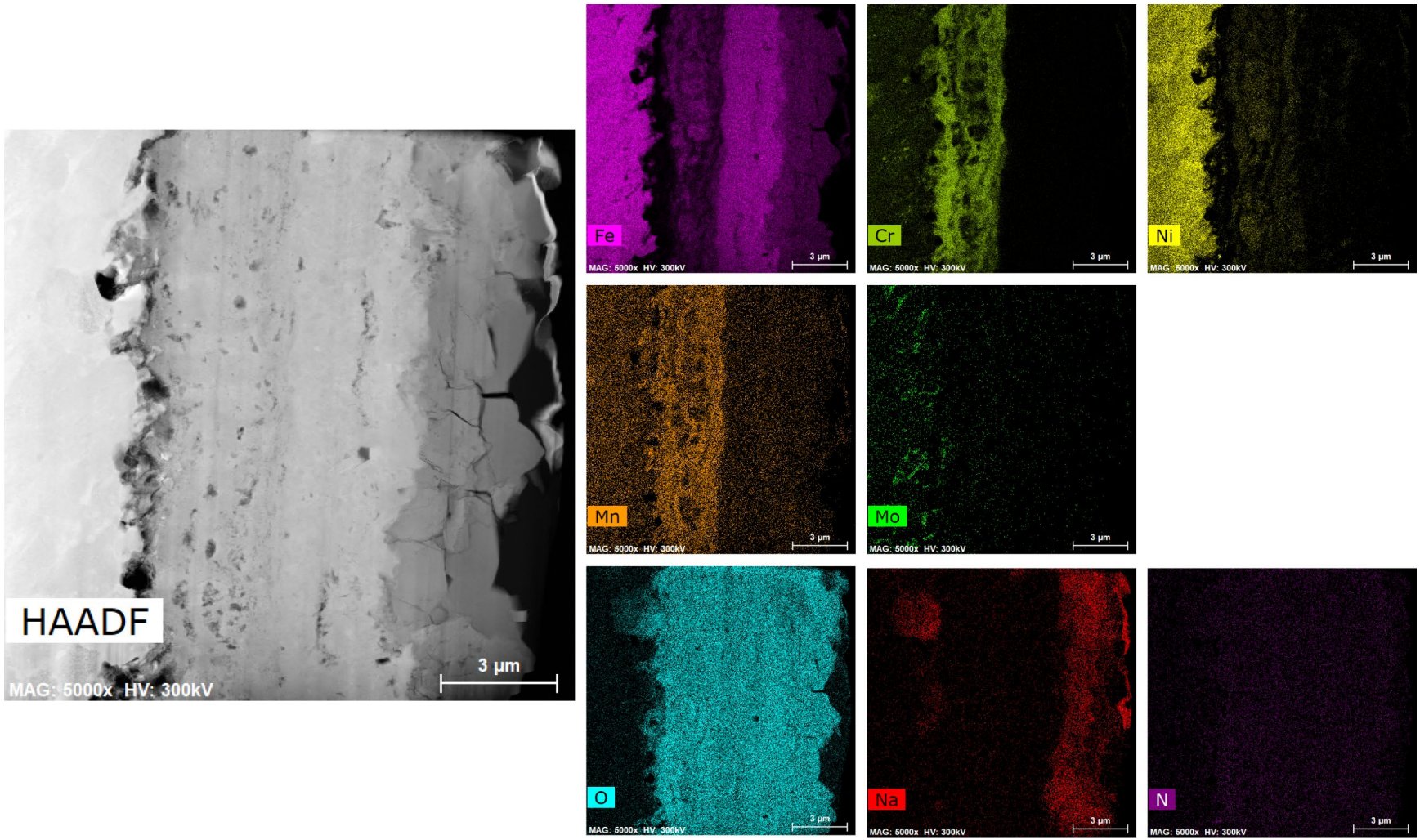

Figure 5.44: TEM image and EDS elemental maps of the corrosion scale for 316H exposed to 600°C Solar Salt for 5000hr. 5000x magnification.

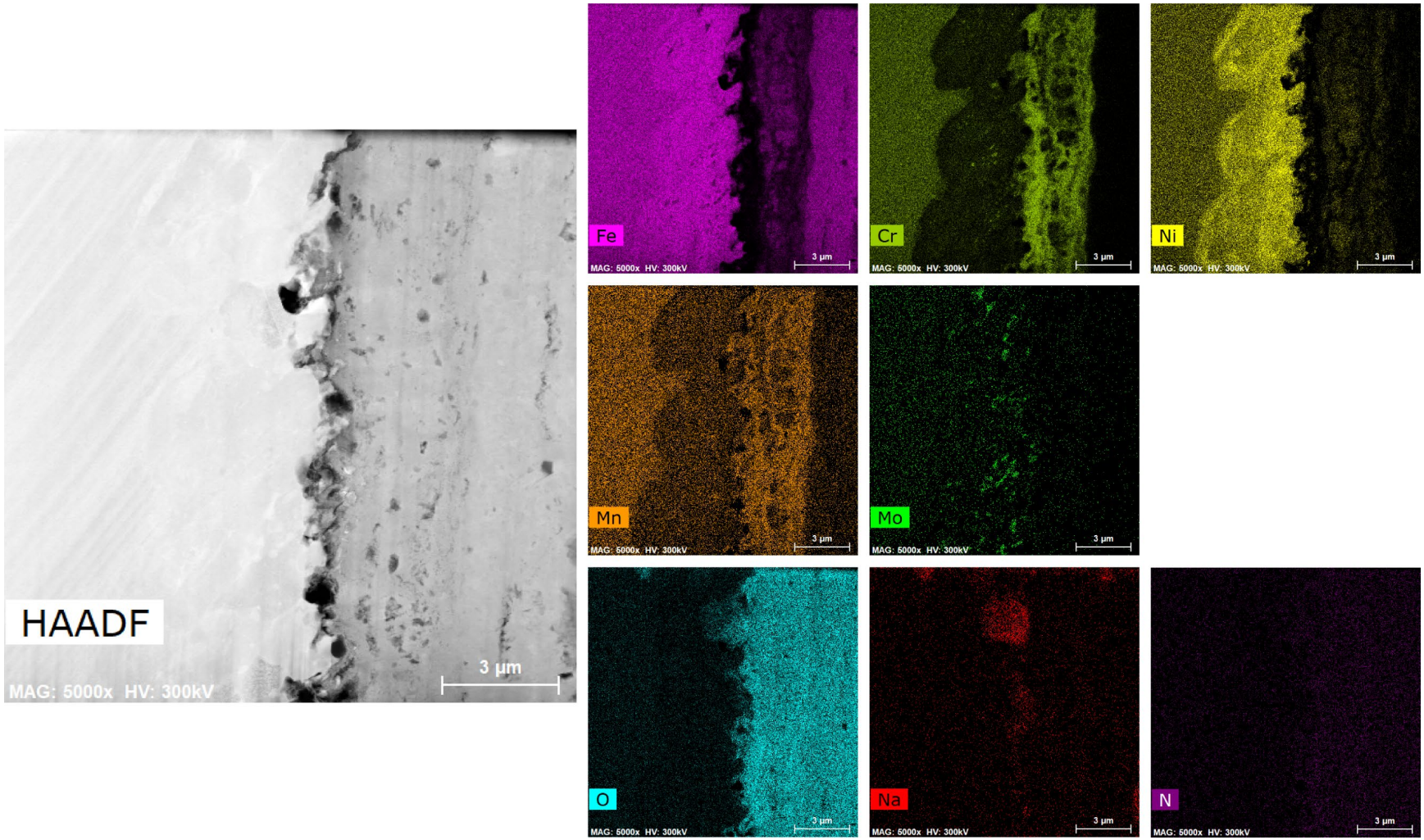

Figure 5.45: TEM image and EDS elemental maps of the bulk surface region for 316H exposed to 600°C Solar Salt for 5000hr revealing the presence of significant Cr (and Mn) denuded regions within the near surface metal. 5000x magnification.

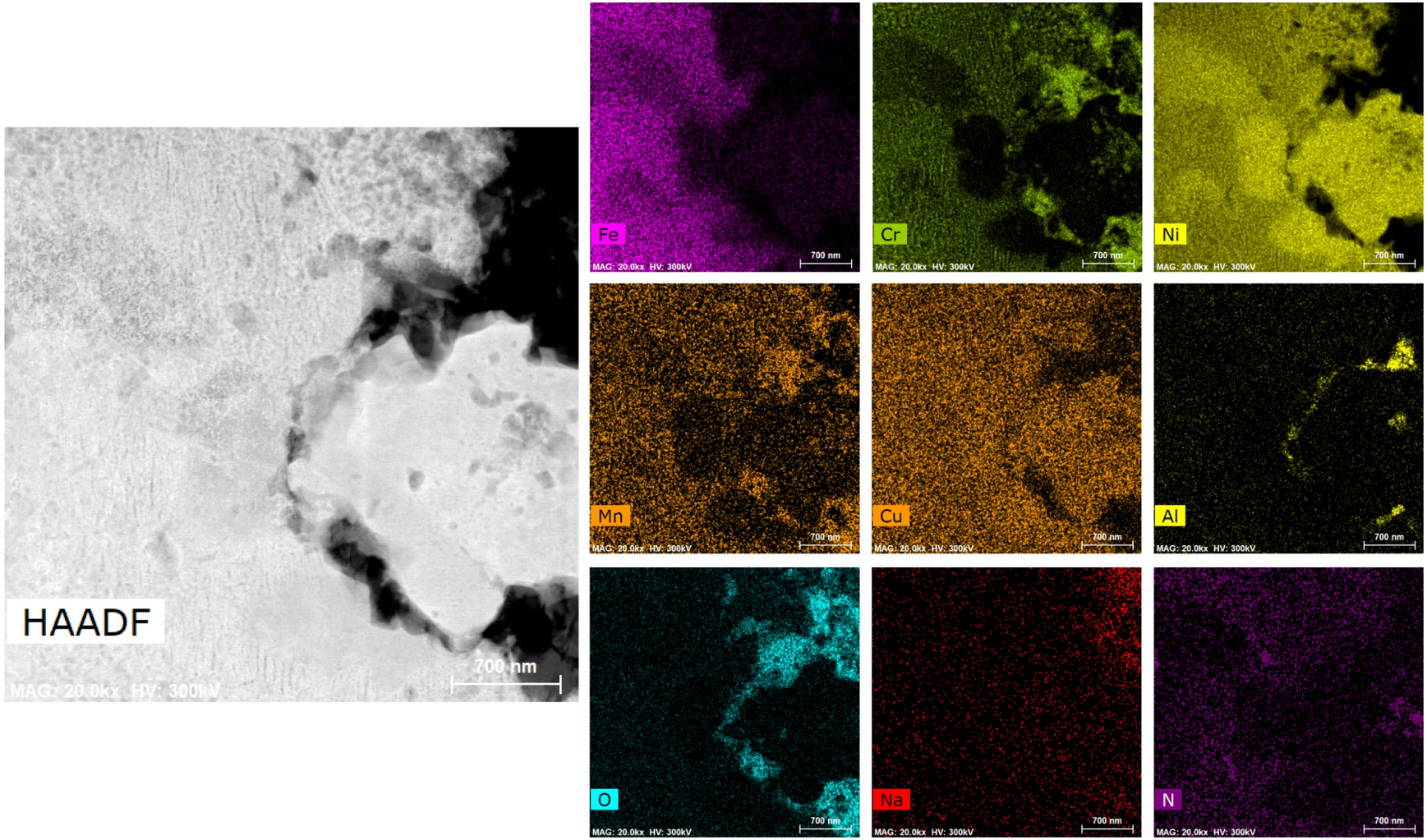

Figure 5.46: TEM image and EDS elemental maps of the bulk surface region for 601 exposed to 650°C Solar Salt for 3000hr revealing the presence of significant Cr (and Mn) denuded regions within the near surface metal. 20000x magnification.

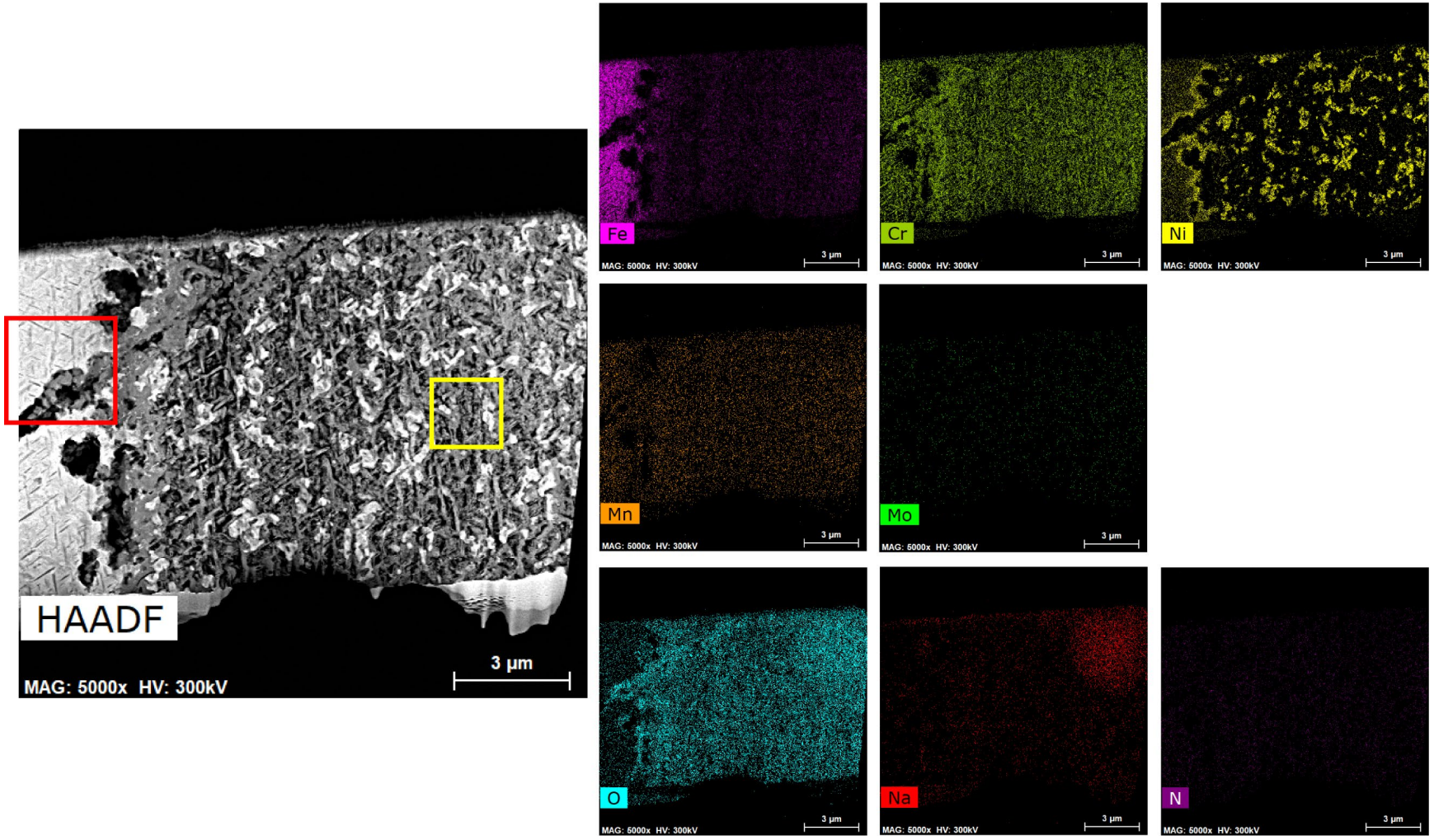

Figure 5.47: TEM image and EDS elemental maps of the innermost oxide region for 316H exposed to 650°C Solar Salt for 5000hr. 5000x magnification. The red box indicates the region imaged in Figure 5.48. Yellow box indicates the region where the Ni-rich phase diffraction pattern was taken in Figure 5.58.

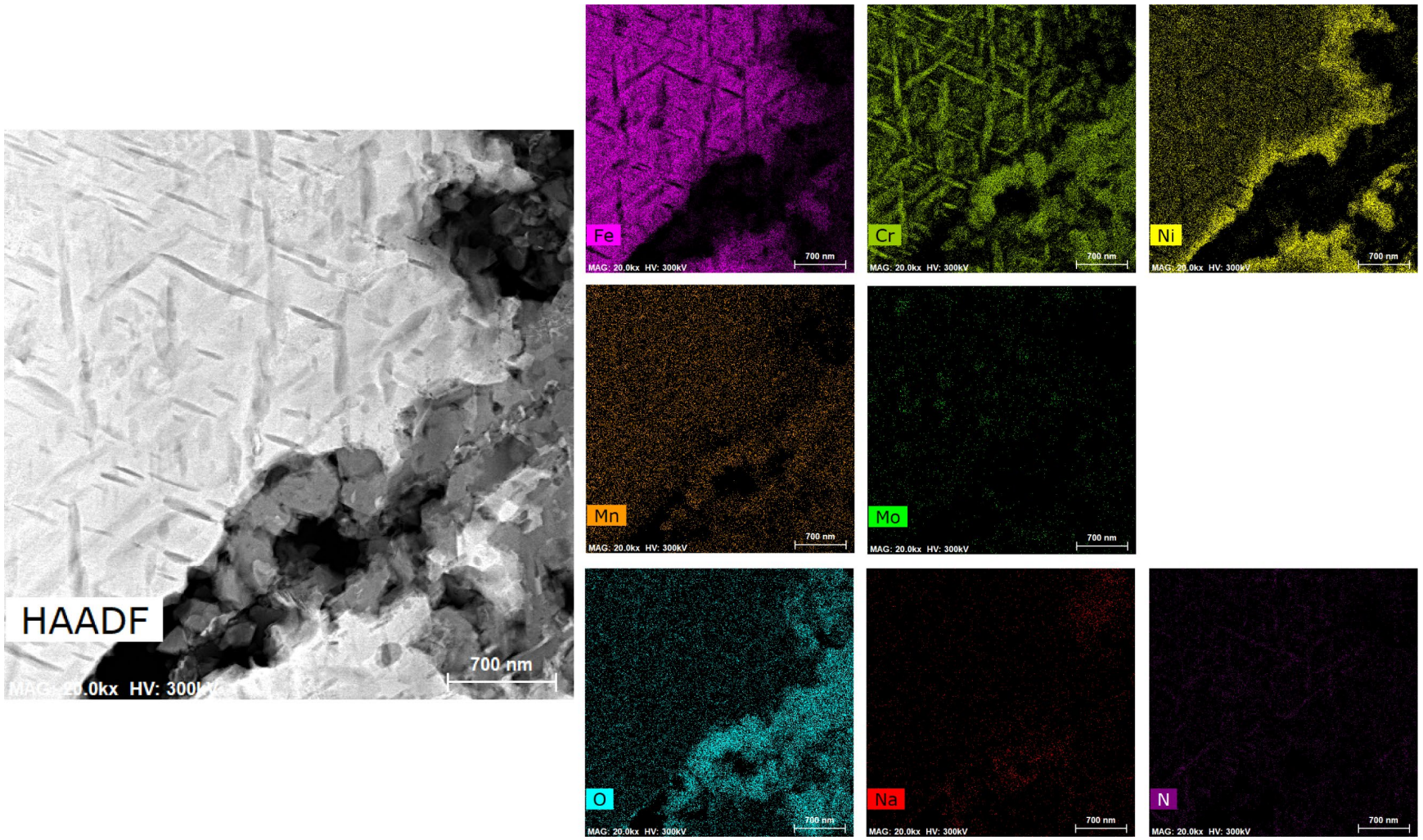

Figure 5.48: TEM image and EDS elemental maps of the bulk surface region for 316H exposed to 650°C Solar Salt for 5000hr indicating the presence of acicular CrN phases. 20000x magnification.

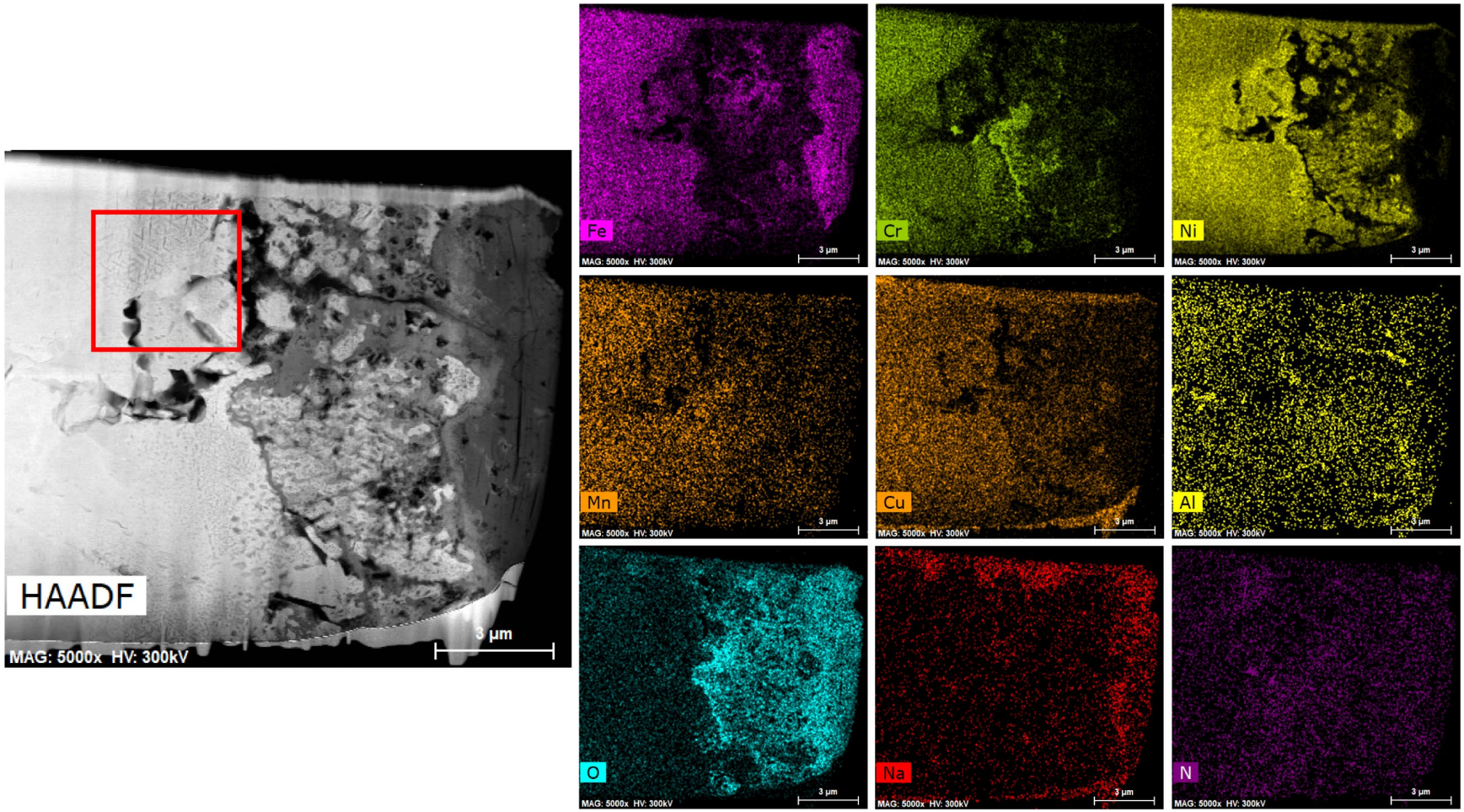

Figure 5.49: TEM image and EDS elemental maps of the corrosion scale for 601 exposed to 650°C Solar Salt for 1000hr. 5000x magnification. The red box indicates the region imaged in Figure 5.50.

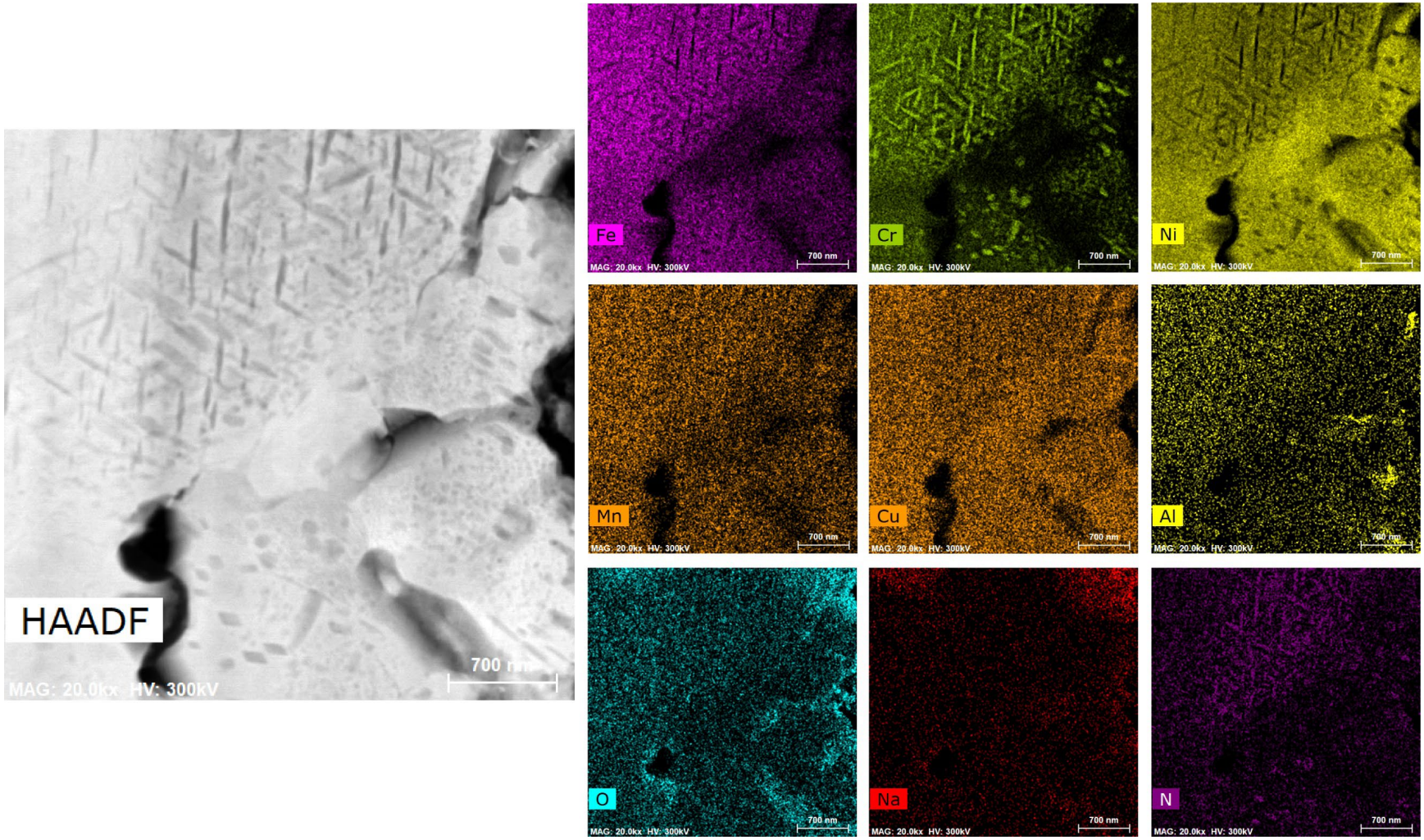

Figure 5.50: TEM image and EDS elemental maps of the bulk surface region for 601 exposed to 650°C Solar Salt for 1000hr indicating the presence of acicular CrN phases. 20000x magnification.

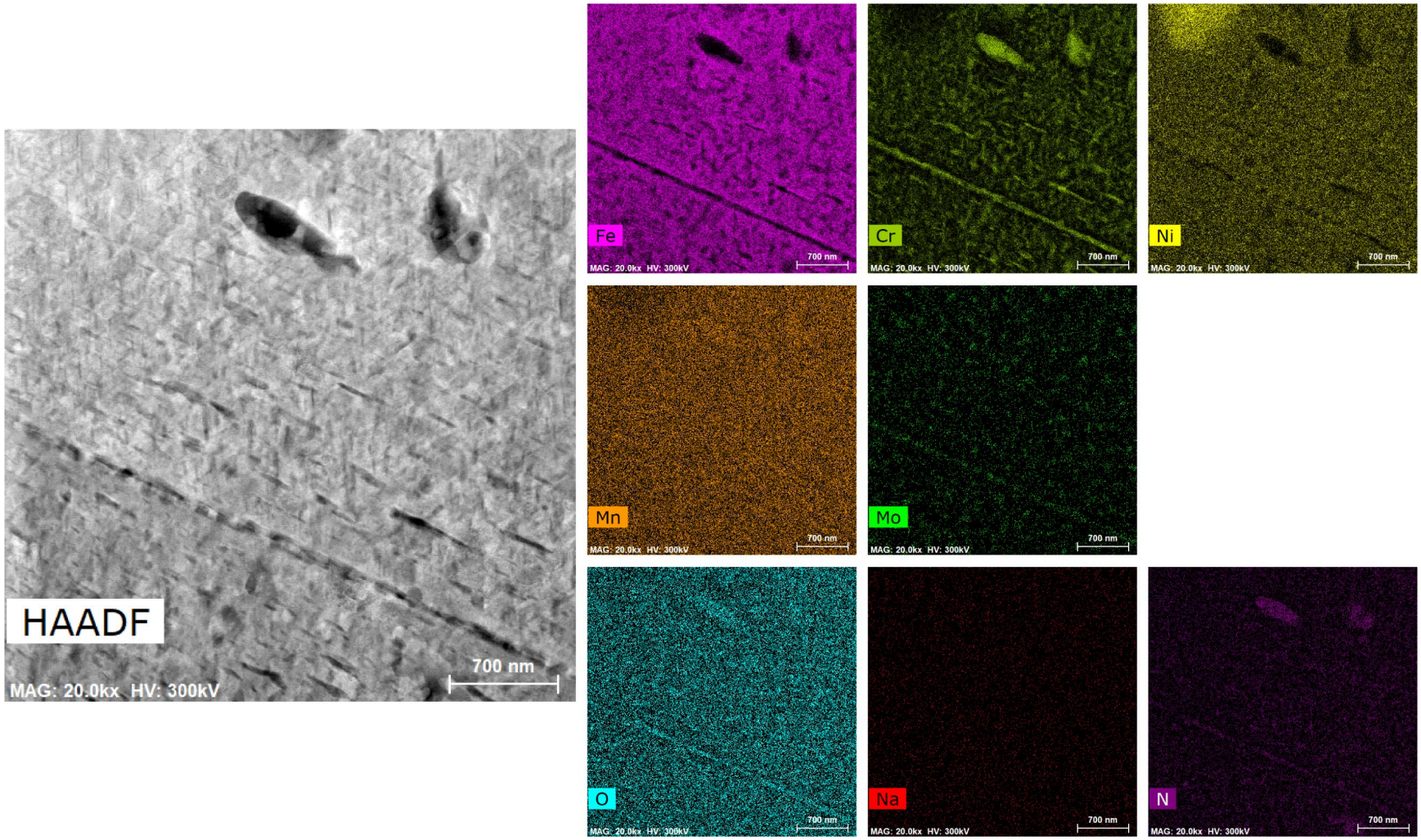

Figure 5.51: TEM image and EDS elemental maps of the bulk surface region containing a grain boundary for 316H exposed to 630°C Solar Salt for 5000hr indicating the presence of CrN, Mo, and oxide phases. 20000x magnification.

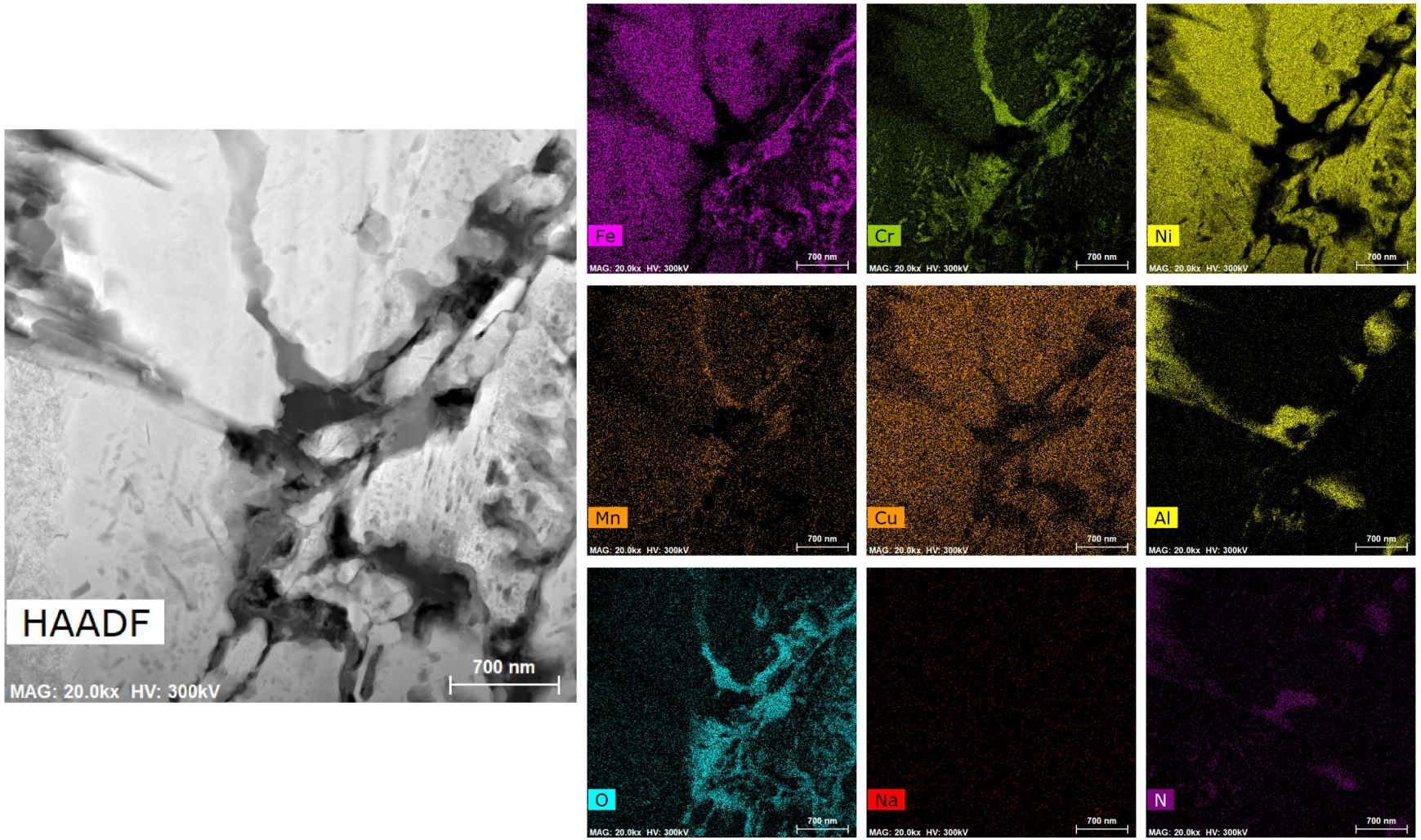

Figure 5.52: TEM image and EDS elemental maps of the bulk surface region for 601 exposed to 600°C Solar Salt for 5000hr indicating the presence of AlN and Al_2O_3 as well as Cr diffusion and Cr_2O_3 formation through bulk volume channels. 20000x magnification.

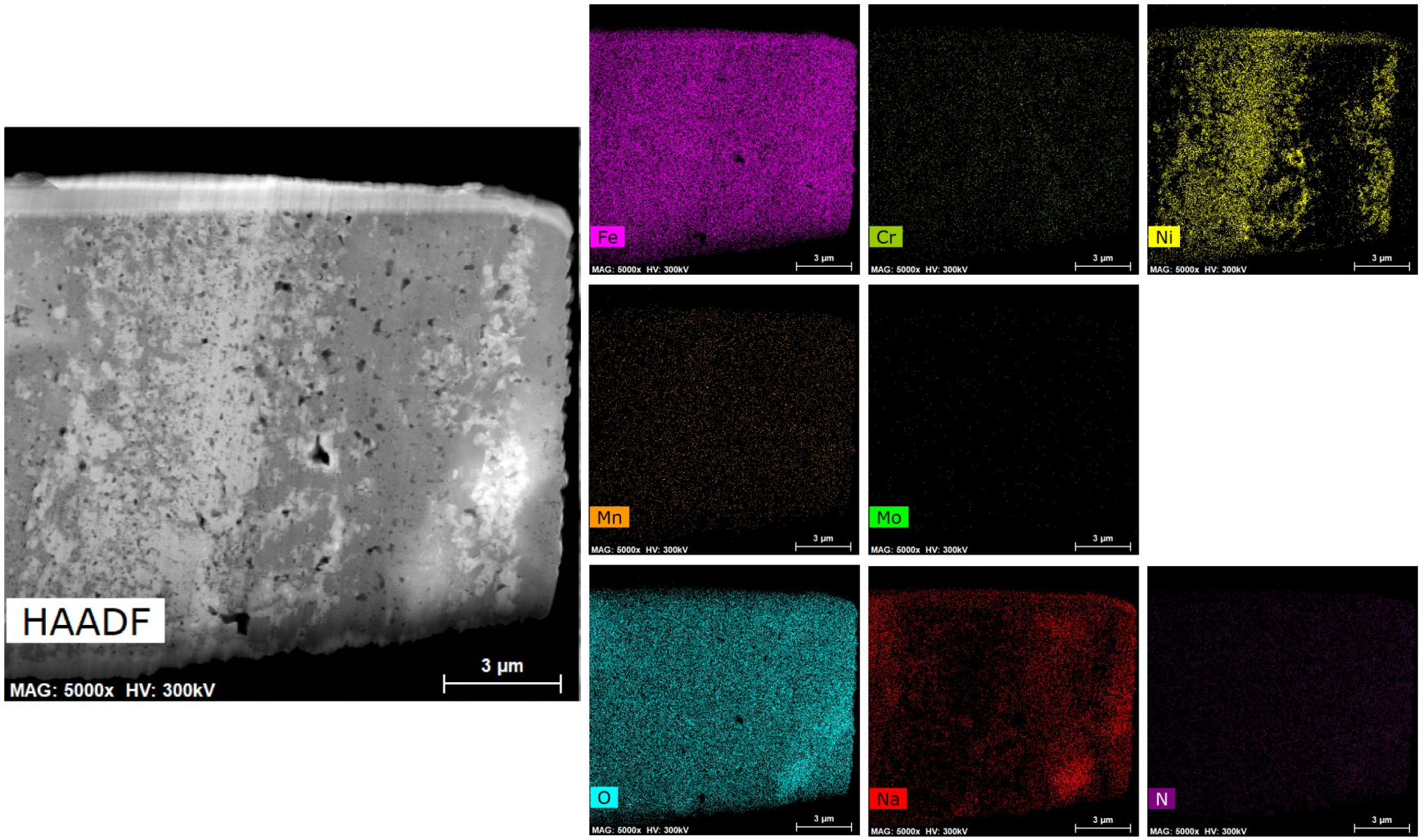

Figure 5.53: TEM image and EDS elemental maps of the intermediate iron oxide region for 316H exposed to 650°C Solar Salt for 5000hr revealing the presence of significant clusters of Ni-rich phases. 5000x magnification.

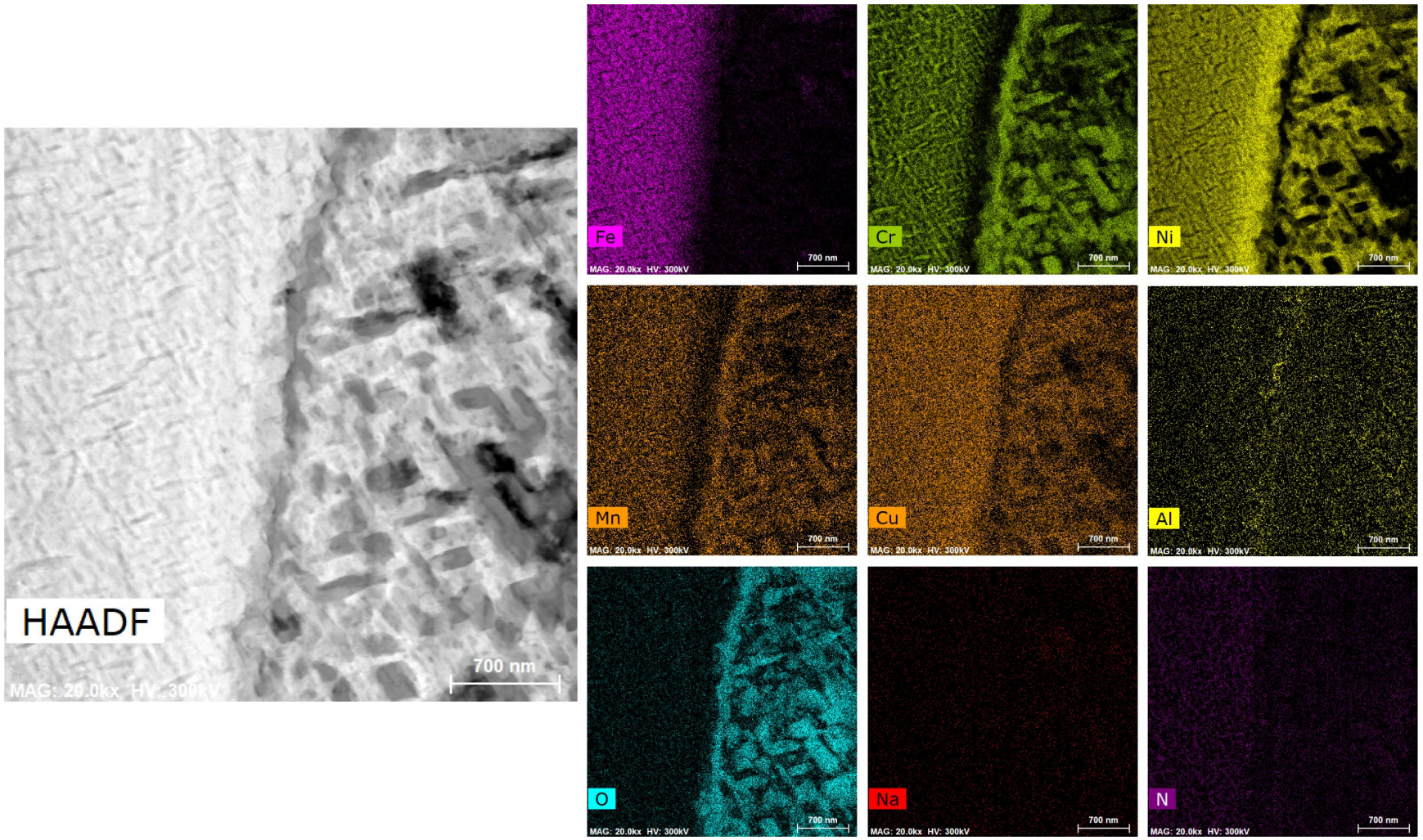

Figure 5.54: TEM image and EDS elemental maps of the bulk surface region for 601 exposed to 650°C Solar Salt for 5000hr detailing the transition from CrN within the bulk metal into Cr_2O_3 in the inner oxide layers. 20000x magnification.

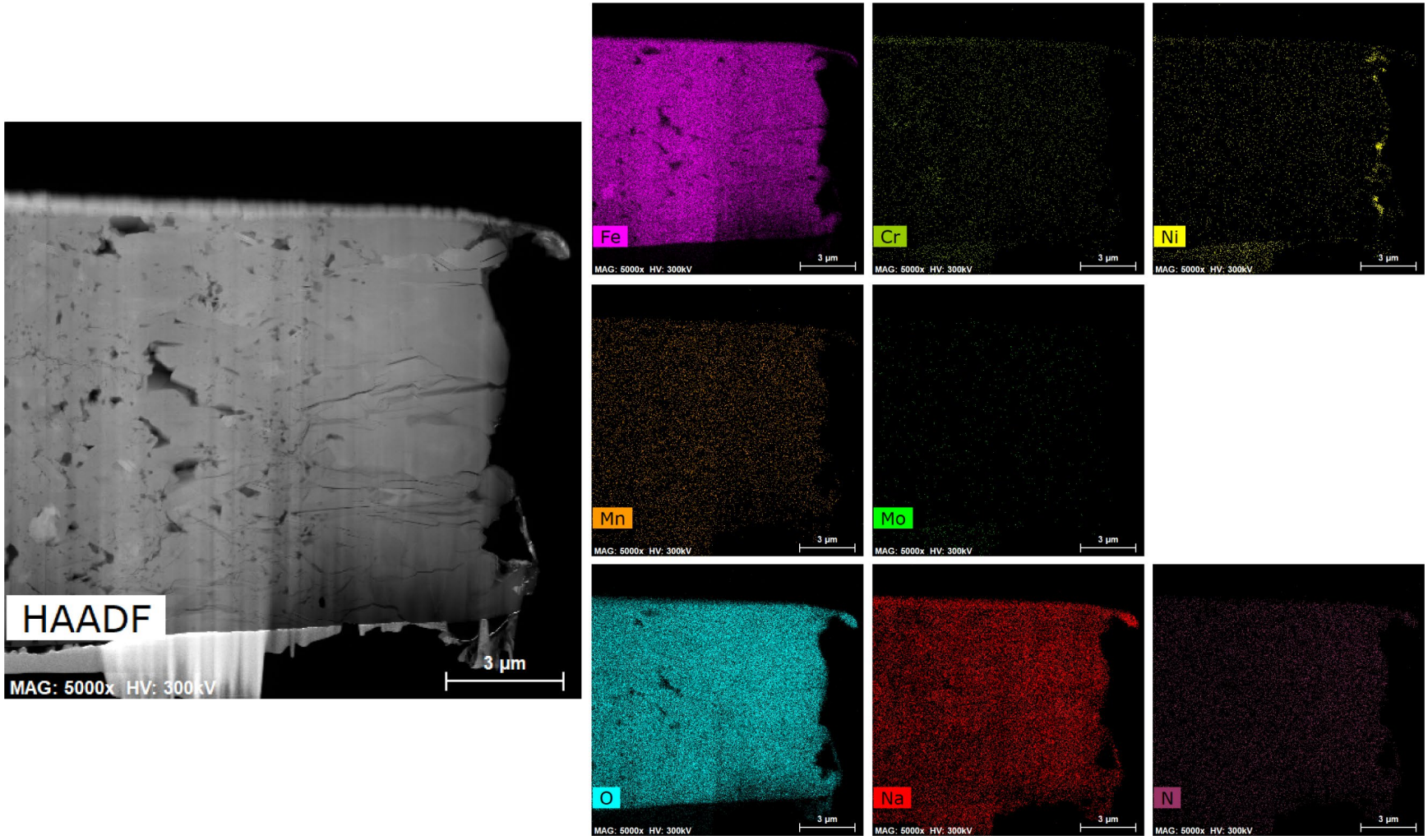

Figure 5.55: TEM image and EDS elemental maps of the outermost oxide region for 316H exposed to 650°C Solar Salt for 1000hr and revealing the presence of significant voids and through-thickness cracking within the oxide layer. 5000x magnification.

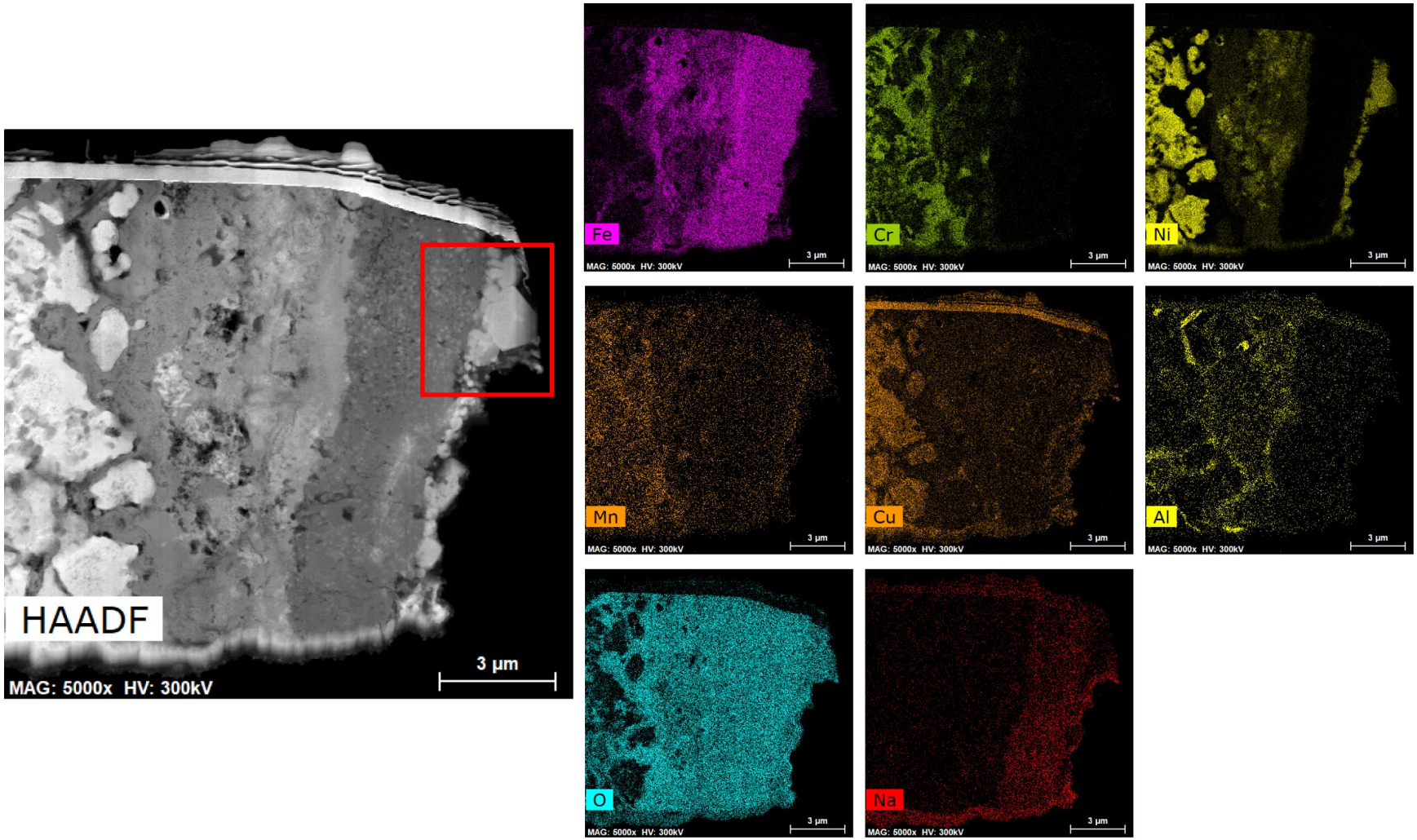

Figure 5.56: TEM image and EDS elemental maps of the corrosion scale for 601 exposed to 630°C Solar Salt for 5000hr revealing the presence of a significant Ni surface phase. 5000x magnification. The red box indicates the region imaged in Figure 5.57.

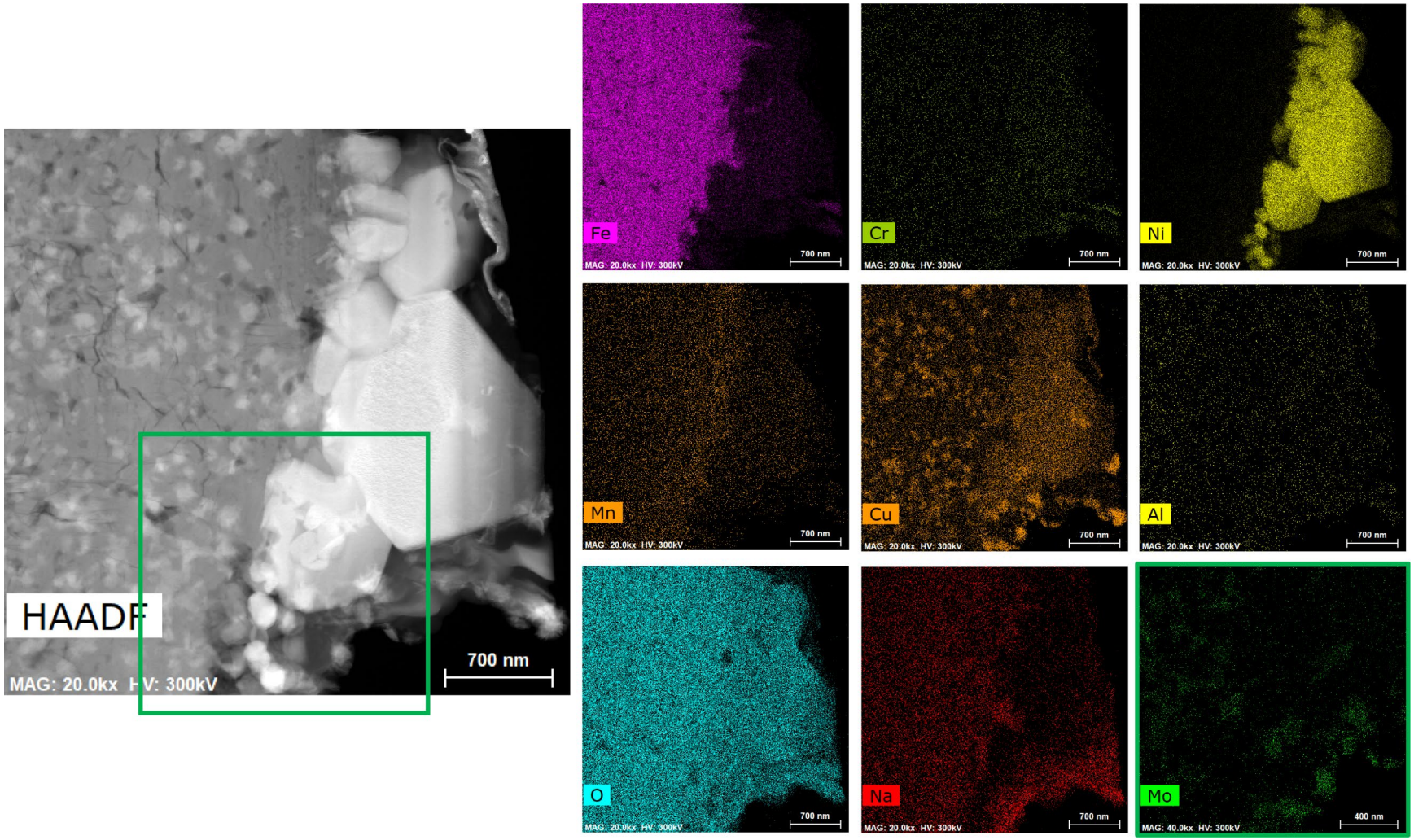

Figure 5.57: TEM image and EDS elemental maps of the Ni surface phase on 601 exposed to 630°C Solar Salt for 5000hr additionally revealing the presence of Mo and Cu phases. 20000x magnification. The Mo EDS map was taken in the region surrounding the green box on the TEM image.

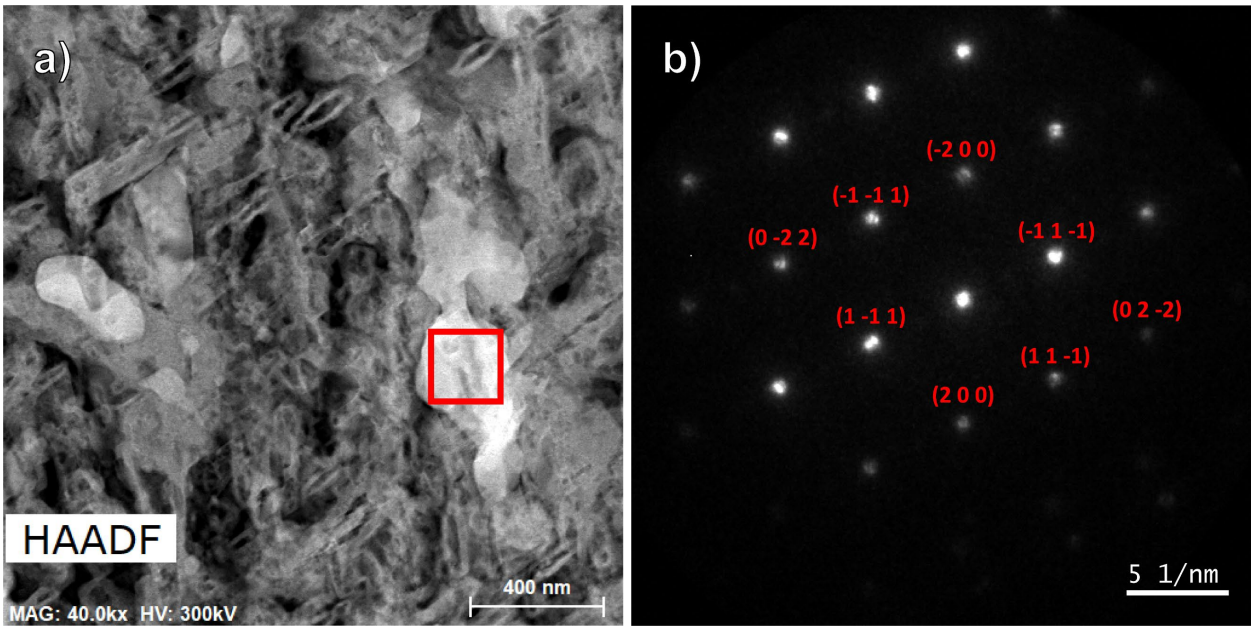

Figure 5.58: a) TEM image of inner oxide region of 316H exposed to 650°C Solar Salt for 5000hr. 40000x magnification (higher magnification of same region in Figure 5.47). The red box indicates the area where diffraction pattern b) was taken. b) Ni FCC diffraction pattern from the Ni phase in the oxide layer revealing its metallic nature. [011] zone axis.

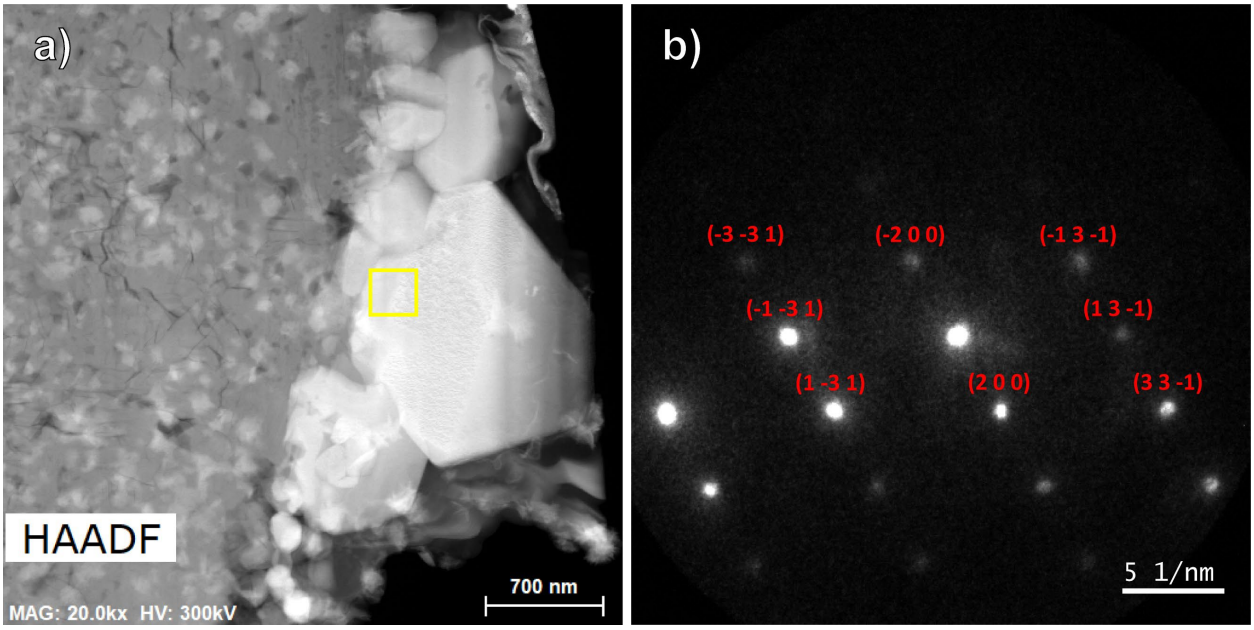

Figure 5.59: a) TEM image of Ni surface phase on 601 exposed to 630°C Solar Salt for 5000hr (from Figure 5.57). 20000x magnification. The yellow box indicates the area where diffraction pattern b) was taken. b) Ni FCC diffraction pattern from the Ni surface phase revealing its metallic nature. [013] zone axis.

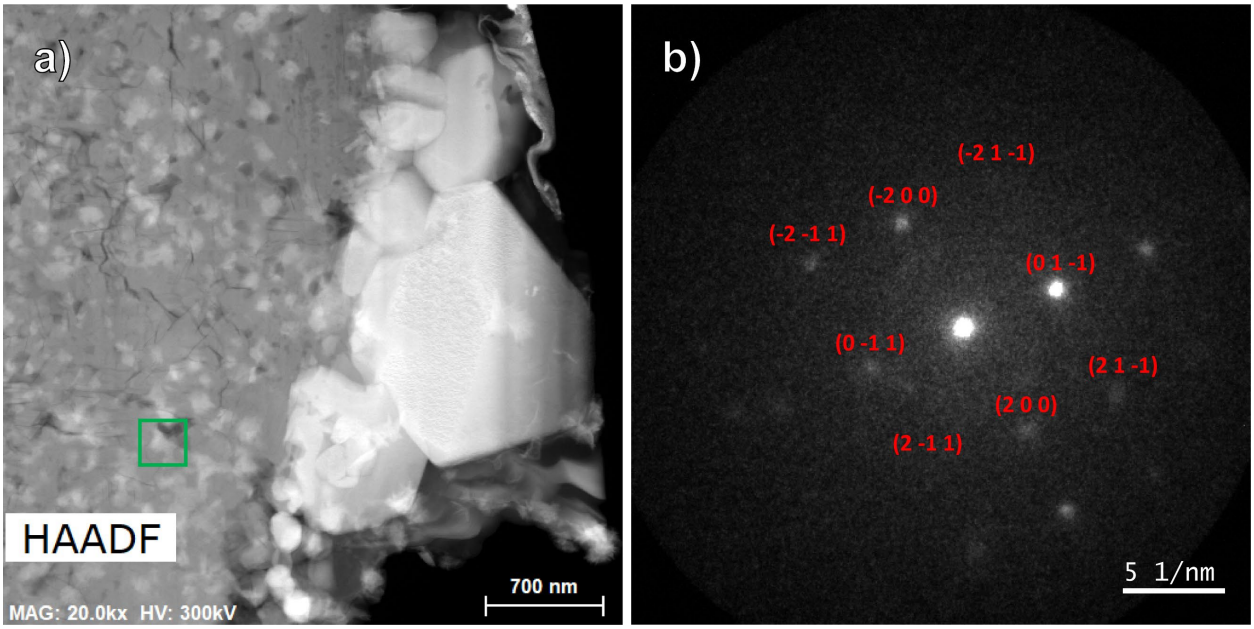

Figure 5.60: a) TEM image of Ni surface phase on 601 exposed to 630°C Solar Salt for 5000hr (from Figure 5.57). 20000x magnification. The yellow box indicates the area where diffraction pattern b) was taken. b) Mo BCC diffraction pattern from the Mo phase in the oxide layer revealing its metallic nature. [011] zone axis.

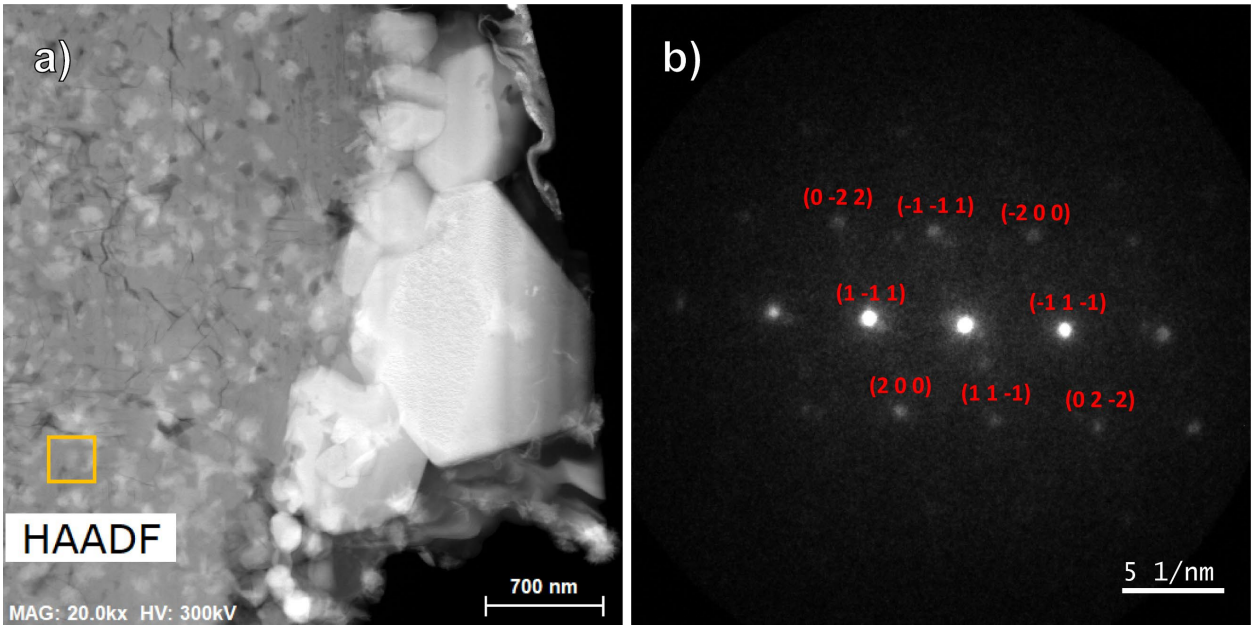

Figure 5.61: a) TEM image of Ni surface phase on 601 exposed to 630°C Solar Salt for 5000hr (from Figure 5.57). 20000x magnification. The yellow box indicates the area where diffraction pattern b) was taken. b) Cu FCC diffraction pattern from the Cu phase in the oxide layer revealing its metallic nature. [011] zone axis.

5.3.5. Electron Backscatter Diffraction

Nothing of note was observed via EBSD of the corroded surface for 601 samples. On the other hand, the steel samples (both welded and unwelded material) exhibited phase transformation of austenite into ferrite at the near surface bulk metal. The extent of the transformation increased as a function of exposure temperature and time with limited to no phase transformation into ferrite observed at the lower temperatures and exposure times (Figure 5.62). Figure 5.63 shows the EBSD maps for 316-REF material exposed to 650°C for 4000hr showing ferrite transformation over 20µm deep within the bulk metal surface along with 25µm+ additional depth of grain boundary ferrite transformation. The ferrite phase was confirmed via 4D-STEM diffraction patterns from 316H in the near surface bulk metal region (Figure 5.64).

The presence of the ferrite phase appears to be co-located with regions of CrN formation, with the uniform ferrite transformation regions containing bulk volume CrN. Beyond this region, only grain boundary formation of CrN is readily present. At the highest temperatures and exposure times, CrN phases were visible along grain boundaries upwards of 80µm within the bulk metal surface.

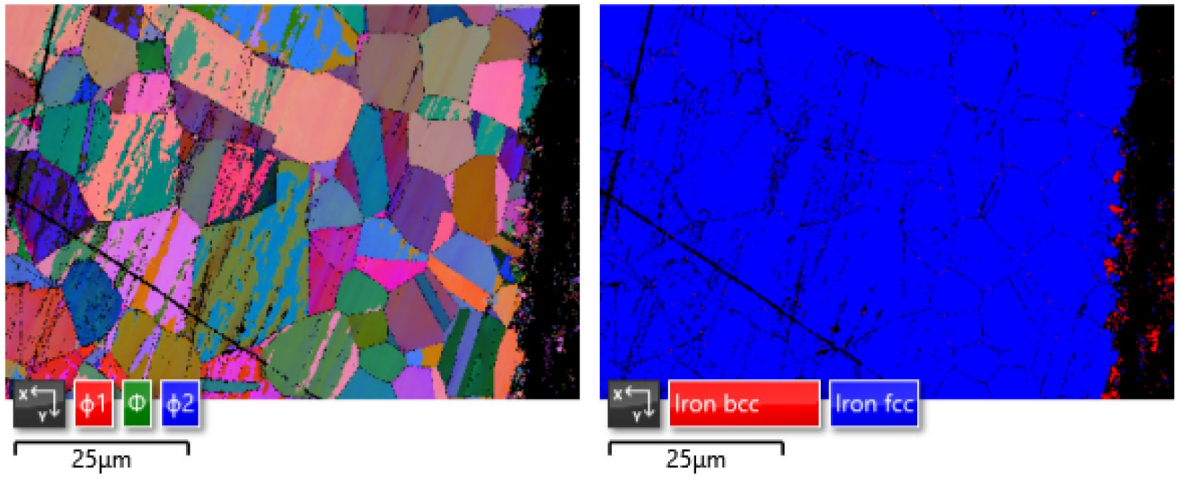

Figure 5.62: EBSD Euler (left) and phase (right) maps obtained for 316-REF exposed to 600°C Solar Salt for 1000hr. 2500x magnification.

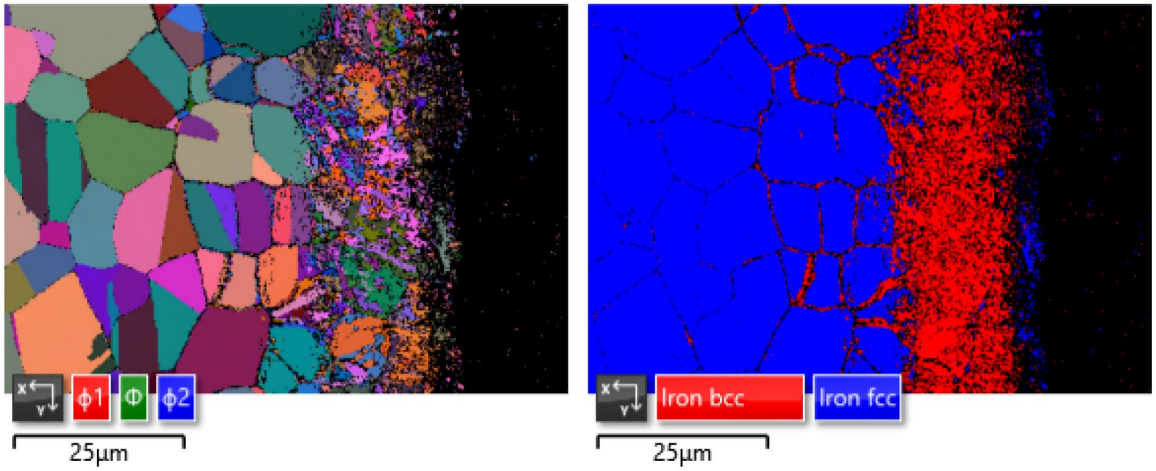

Figure 5.63: EBSD Euler (left) and phase (right) maps obtained for 316-REF exposed to 650°C Solar Salt for 4000hr. 2500x magnification.

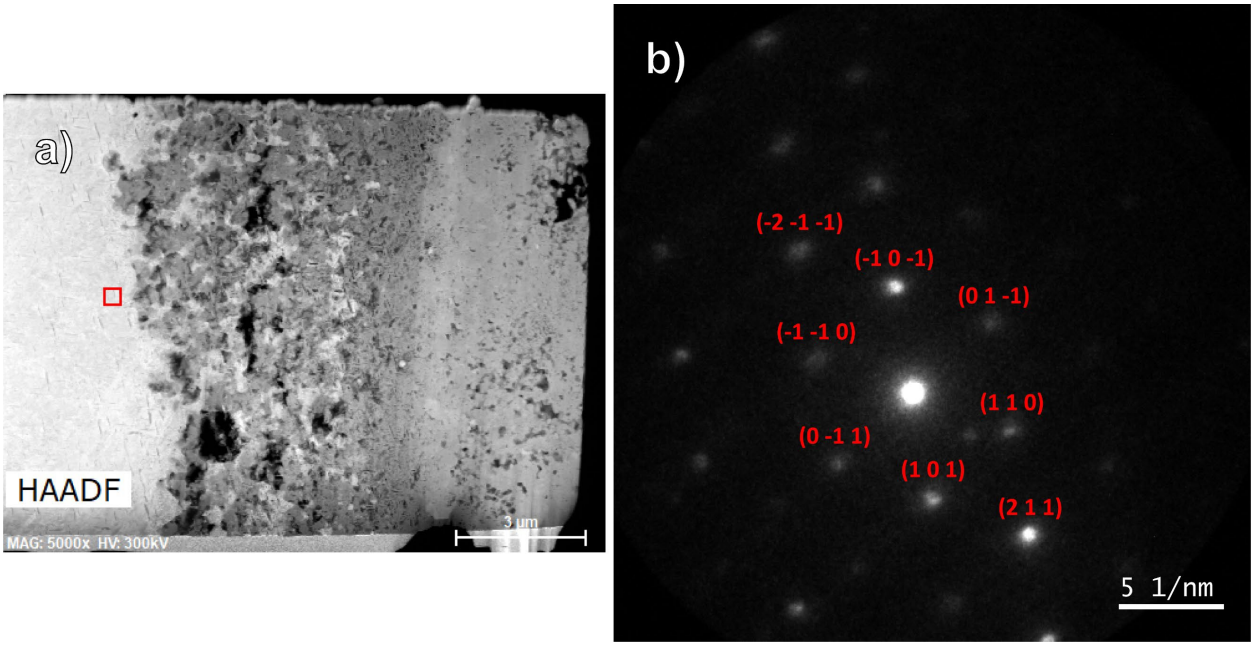

Figure 5.64: a) TEM image of 316H exposed to 650°C Solar Salt for 3000hr. 5000x magnification. The red box indicates the area where diffraction pattern b) was taken. b) Fe BCC diffraction pattern from the near surface bulk metal region revealing its transformation into ferrite. [-111] zone axis.

5.3.6. XRD of Corroded Sample Surfaces

XRD of 316H and 601 samples confirmed $NaFeO_2$ as the outermost oxide layer for samples that exhibited it. The defining feature of $NaFeO_2$ is the presence of a peak at around 19° in the XRD spectra (Figure 5.65). Table 5.3 summarizes the presence of $NaFeO_2$ as detected via XRD as a function of exposure temperature and time. No $NaFeO_2$ was detected for any 590°C samples. For 600°C, $NaFeO_2$ was detected for the 4000hr and 5000hr 316H sample surface. At ≥630°C,

$NaFeO_2$ was readily detected on all 316H and most 601 samples. Note that the samples were not cleaned of nitrate salt prior to XRD meaning uncontrolled thicknesses of nitrate salt were on the sample surface. Therefore, samples which did not have $NaFeO_2$ detected do not mean that it was not present, but rather that the nitrate salt could have been too thick and/or the $NaFeO_2$ layer too thin to detect. Fe_3O_4, Fe_2O_3, NiO, Cr_2O_3, and base alloy peaks corresponding to deeper regions of the corrosion scale were also detected, but inconsistent again because of the residual nitrate salt on the sample surfaces.

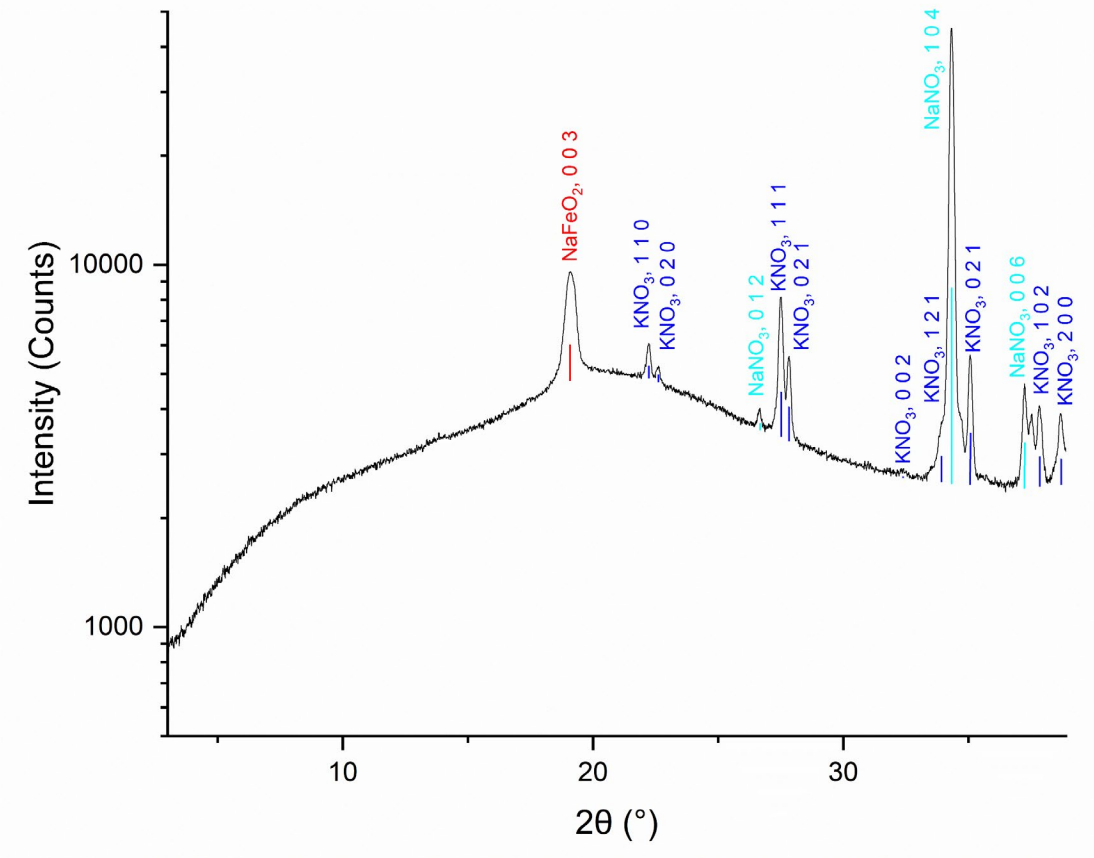

Figure 5.65: XRD of a 601 sample exposed to 650°C Solar Salt for 5000hr exhibiting $NaFeO_2$ on its surface.

Table 5.3: Presence of $NaFeO_2$ revealed via XRD on 316H and 601 samples corroded in elevated temperature Solar Salt as a function of temperature and time.

Temperature (°C)	Alloy	Exposure Time (hr)					
		500hr	1000hr	2000hr	3000hr	4000hr	5000hr
590	316H	N	N	N	N	N	N
	601	N	N	N	N	N	N
600	316H	N	N	N	N	Y	Y
	601	N	N	N	N	N	N
620	316H	N	Y	Y	Y	Y	Y
	601*	N	N	-	Y	-	Y
630	316H	Y	Y	Y	Y	Y	Y
	601	N	Y	Y	Y	Y	Y
650	316H	Y	Y	Y	Y	Y	Y
	601*	N	Y	-	Y	-	Y

*No 2000hr or 4000hr 601 samples were generated at 620°C and 650°C.

5.3.7. Nitrate Salt Analysis

Figures 5.66-5.70 show the solid nitrate salt samples taken during the long-term corrosion study. Prior to any corrosion, the nitrate salt appears white and then yellows as exposure temperature and time increases. The yellow coloration is readily observed throughout literature and attributed to the presence of soluble chromate, Cr(6+), within the nitrate salt. However, for the 650°C 3000hr and 4000hr samples, the salt samples are unmistakably green in coloration. This was also observed in Dorcheh et al. 2016 and Kruigenda et al. 2013 in elevated temperature Solar Salt corrosion studies,[48,87] though no detailed explanation or understanding for this green coloration is readily available within literature. Keiser et al. 1979 asserted that only 5% of the dissolved Cr in 550°C HITEC nitrate salt was Cr(6+), concluding the rest must be Cr(2+) or Cr(3+).[112] Cr(3+) is known to exhibit green coloration within nitrate salt, however, other studies showed that Cr(3+) and its green color are relatively short lived and form yellow chromate starting at temperatures as low as 175°C.[113,114] While salt samples in this study were not extracted at test temperatures, sample extractions were performed at 350°C and thus at a temperature still well above this transition point. Hexanitrato complexes (such as $K_3[Cr(NO_3)_6]$) are also claimed to have green coloration and therefore could be the culprit, but literature on these complexes especially in the context of nitrate salt corrosion is sparse.[114] Unfortunately, this study is ill-equipped to fully ascertain the cause for the transition from yellow to green coloration in the 650°C Solar Salt experiment. It is noted that this occurred during a period of no temperature excursions, and the 5000hr salt sample appearing yellow again was likely due to the major temperature excursion between the 4000hr and 5000hr extractions.

Figures 5.71-5.75 show the aqueous samples taken during the long-term corrosion study. Prior to any corrosion, the nitrate salt dissolves clear within water. As temperature and time increases, the coloration becomes increasingly yellow. Solid oxide particles from flaking oxide layers of corroded samples and sample tree material can be seen in many of the salt samples

collected. Interestingly, the green solid samples for 3000hr and 4000hr at 650°C did not produce distinctly green aqueous solutions. This hints that the species is not stable and/or does not fluoresce green in aqueous solutions. Green-yellow melts were found in Kerridge and Tariq 1969 to become yellow in aqueous solutions with precipitation of green Cr(3+) oxide particles.[113] Precipitation of green particles was not observed when dissolving the salts in DI water and thus lend credence to complexation or other impurities as the cause of the green color rather than Cr(3+).

Figure 5.66: Solid nitrate salt samples taken from 590°C experiment from left to right: after initial bakeout, 500hr, 1000hr, 1000hr fresh salt bakeout, 2000hr, 3000hr, 4000hr, and 5000hr.

Figure 5.67: Solid nitrate salt samples taken from 600°C experiment from left to right: after initial bakeout, 500hr, 1000hr, 1000hr fresh salt bakeout, 2000hr, 3000hr, 4000hr, and 5000hr.

Figure 5.68: Solid nitrate salt samples taken from 620°C experiment from left to right: after initial bakeout, 500hr, 1000hr, 1000hr fresh salt bakeout, 2000hr, 3000hr, 4000hr, and 5000hr.

Figure 5.69: Solid nitrate salt samples taken from 630°C experiment from left to right: after initial bakeout, 500hr, 1000hr, 1000hr fresh salt bakeout, 2000hr, 3000hr, 4000hr, and 5000hr.

Figure 5.70: Solid nitrate salt samples taken from 650°C experiment from left to right: after initial bakeout, 500hr, 1000hr, 1000hr fresh salt bakeout, 2000hr, 3000hr, 4000hr, and 5000hr.

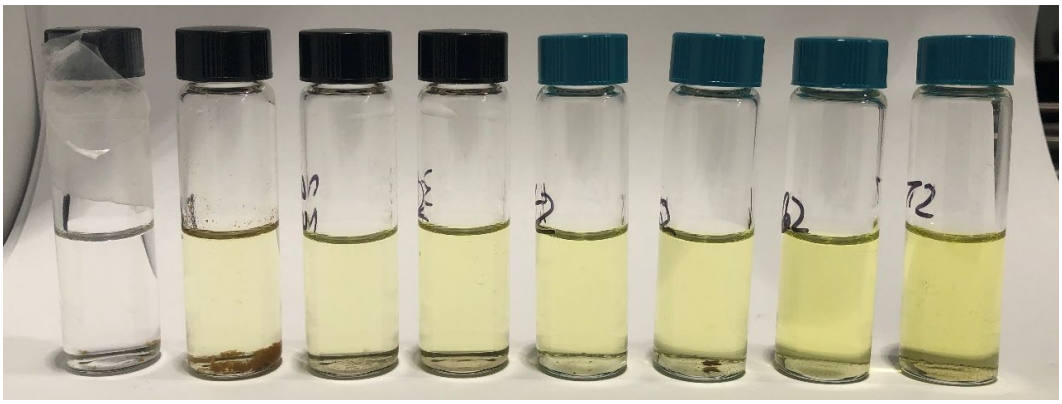

Figure 5.71: Aqueous nitrate salt samples taken from 590°C experiment from left to right: after initial bakeout, 500hr, 1000hr, 1000hr fresh salt bakeout, 2000hr, 3000hr, 4000hr, and 5000hr.

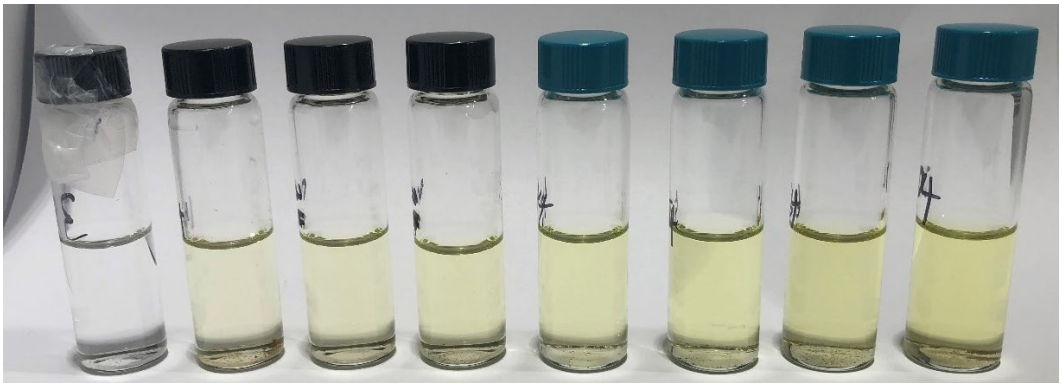

Figure 5.72: Aqueous nitrate salt samples taken from 600°C experiment from left to right: after initial bakeout, 500hr, 1000hr, 1000hr fresh salt bakeout, 2000hr, 3000hr, 4000hr, and 5000hr.

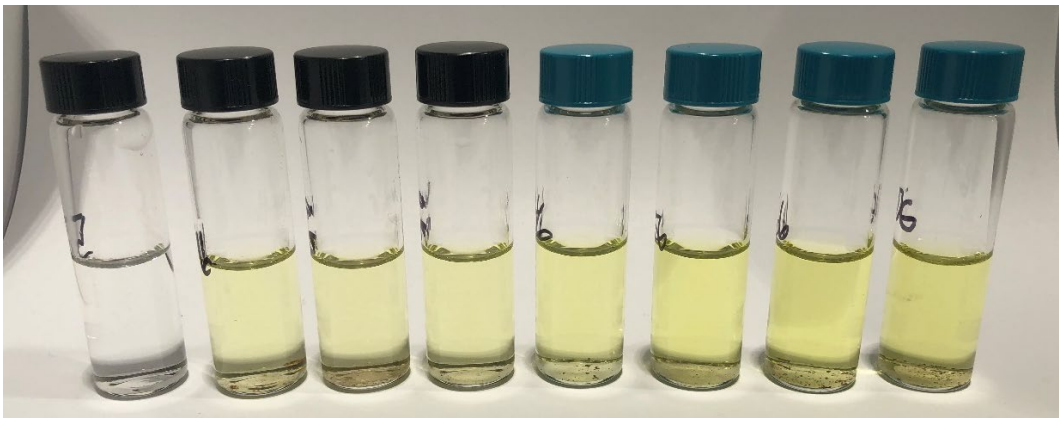

Figure 5.73: Aqueous nitrate salt samples taken from 620°C experiment from left to right: after initial bakeout, 500hr, 1000hr, 1000hr fresh salt bakeout, 2000hr, 3000hr, 4000hr, and 5000hr.

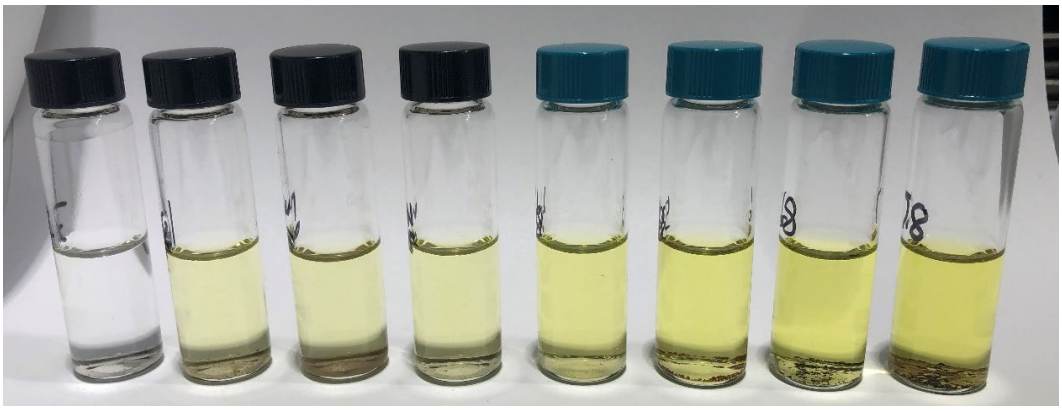

Figure 5.74: Aqueous nitrate salt samples taken from 630°C experiment from left to right: after initial bakeout, 500hr, 1000hr, 1000hr fresh salt bakeout, 2000hr, 3000hr, 4000hr, and 5000hr.

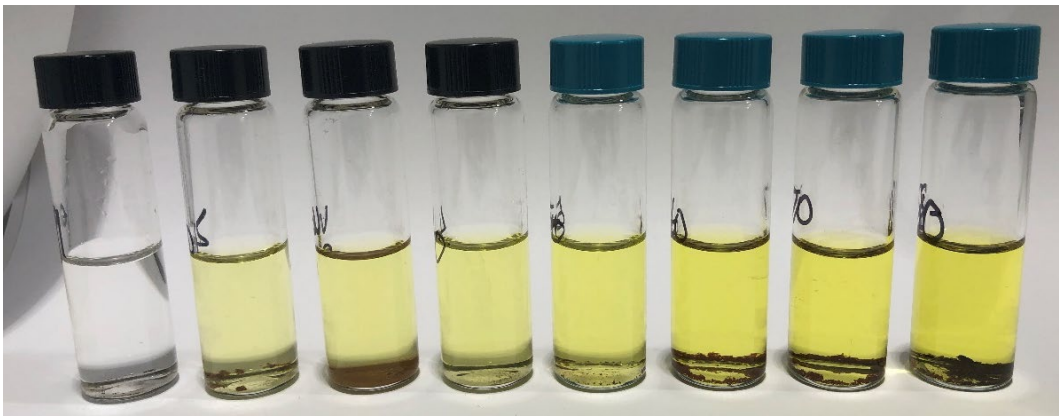

Figure 5.75: Aqueous nitrate salt samples taken from 650°C experiment from left to right: after initial bakeout, 500hr, 1000hr, 1000hr fresh salt bakeout, 2000hr, 3000hr, 4000hr, and 5000hr.

Figure 5.76 shows the nitrite concentration (rest nitrate) in the salt samples as a function of exposure temperature and time. Despite not collecting samples in-situ at test temperature, a clear increase in nitrite concentration is still observed as temperature and time increase. This provides confidence that the relative salt aging dynamics across temperatures have been preserved. The concentration values plotted are likely not representative of equilibrium values due to the lower temperature sampling as well as the semi-sealed nature of the experiments in which gas products of decomposition were able to leave the system. A drop in nitrite concentration was observed for the second 1000hr salt sample that is consistent with the fresh salt addition performed at that time. It is of note that the nitrite concentration appears to struggle to reach back to the peak prior to the 1000hr salt addition. This indicates that the process of corroding metal fosters decomposition of the Solar Salt.

In dissolving nitrate salt samples in DI water quickly after extraction, oxide species react with water and dissolved/atmospheric carbon dioxide to form hydroxides and carbonate species. Alkalinity tests measuring the hydroxide and carbonate species in aqueous samples therefore enable indirect measurement of the oxide concentration in the salt. Figure 5.77 shows the alkalinity of the nitrate salt samples and reveals a clear increase in oxide concentration as

temperature and time increases. The drop for the second 1000hr salt samples is consistent with the fresh salt addition. Again, the absolute values plotted are likely not representative of equilibrium values at test temperatures, however, the data indicates that oxide concentrations could be on the order of 2.4% in the 650°C experiment at 5000hr without any signs of saturation. This helps explain the increased corrosivity of the salt over time as revealed by the corrosion rates of the 316-REF samples. Of note, unlike the nitrite concentration, the oxide concentration appears to quickly surpass the 1000hr pre-salt addition peak. This further elucidates the contribution of metallic corrosion in affecting the kinetics of nitrate salt decomposition. Corrosion of the metallic material consumes oxide (as well as nitrogen species as revealed through nitriding). These species are products of nitrate salt decomposition. Thus, as corrosion rates reduced and samples were removed over time, less total corrosion occurred and correspondingly less nitrate salt decomposition occurred to maintain levels of oxide species.

Nitrate salt samples were also analyzed for dissolved metal content. No Fe or Ni was detected above the detection limits (500ppm for Fe, 5ppm for Ni) except for a few clear outliers likely caused by metal oxide particulates in the salt samples. Cr was however detected in significant concentrations, increasing as a function of temperature and time (Figure 5.78). At 650°C, the dissolved Cr concentration reached 4000ppm at 5000hr and does not appear to show signs of saturation. This confirms extremely high solubility of Cr within nitrate salt and has significant implications regarding mass transport in long term applications utilizing nitrate salt with Cr-containing materials. Similar to the other salt analyses, the drop for the second 1000hr salt samples is consistent with the fresh salt addition.

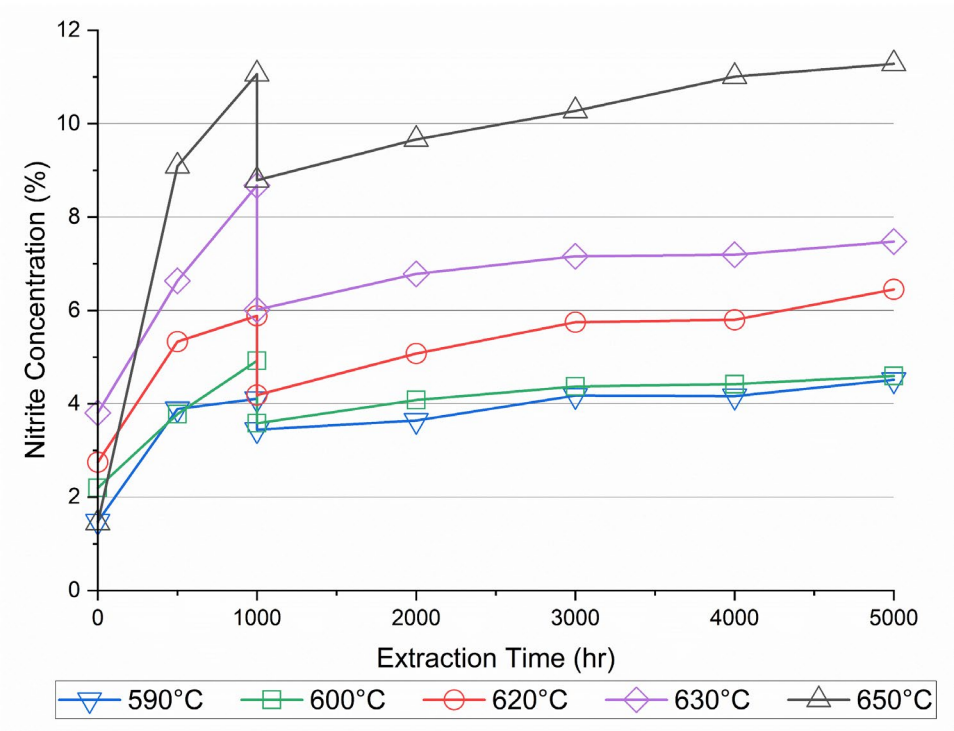

Figure 5.76: Nitrite concentration (rest nitrate) in salt as a function of temperature and time.

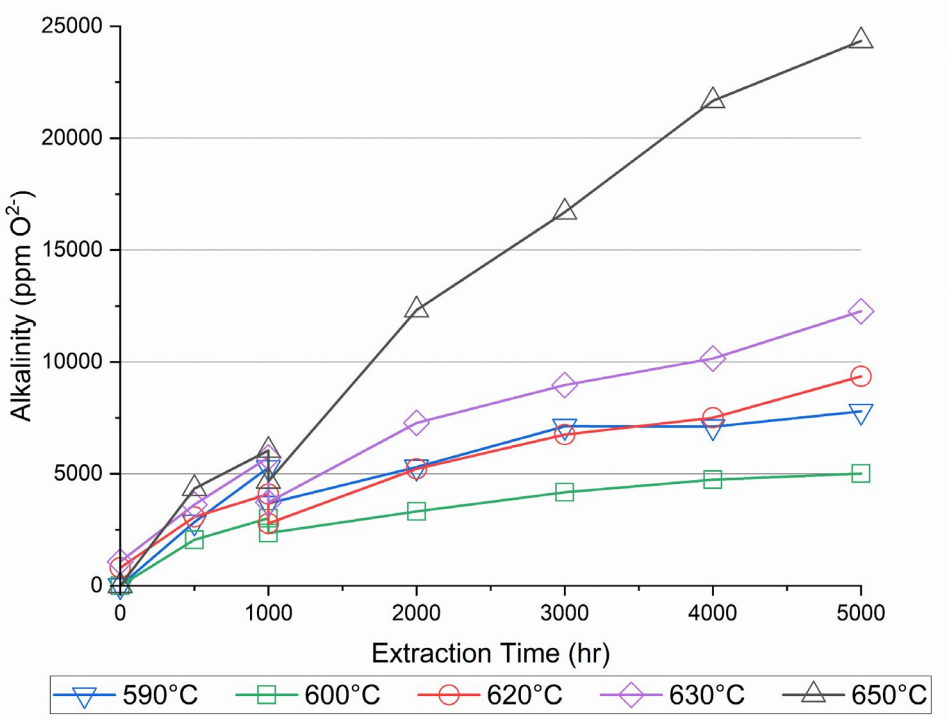

Figure 5.77: Alkalinity of salt as a function of temperature and time.

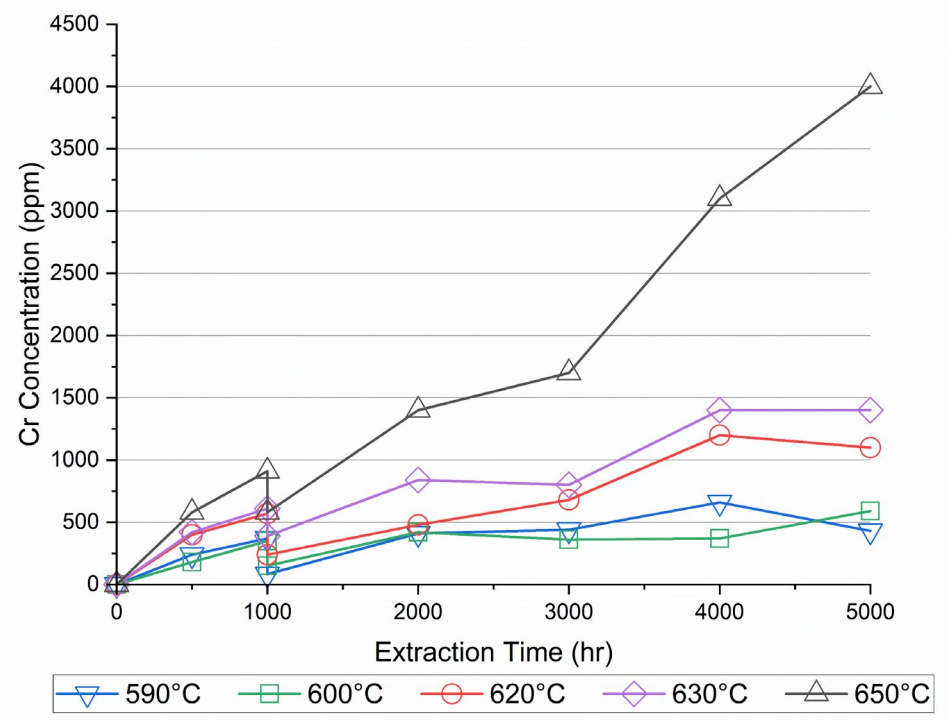

Figure 5.78: Dissolved chromium in nitrate salt as a function of temperature and time. Resolution limit 5ppm.

5.4. Discussion

5.4.1. Corrosion Rate Time Dependencies

Figures 5.79 and 5.80 show the corrosion depth vs. exposure time plots for 316H and 601, respectively, from which corrosion time dependences were obtained. For each temperature, a power law fit of $y = Ax^B$ was applied. Starting with 316H, at temperatures ≤620°C, the exponent values, B, were around 0.5 indicating a near parabolic time dependence for the corrosion rates. This would indicate relatively well-adherent stable corrosion oxide layers that result in diffusion-controlled corrosion. At temperatures ≥630°C, B values were around 0.8. The B values rising to 0.8 could be explained by the significant flaking of the oxide layers observed at these temperatures that exposes fresh metal to the nitrate salt to corrode. Though specific processes are unable to be definitively attributed to the activation energies extracted from the Arrhenius analysis in Chapter 4, the corrosion rate time dependencies examined here lend credence to the diffusion of species as potentially the rate-controlling processes.

For 601, the exponent values at temperatures ≤630°C were significantly below 0.5, indicating a highly protective corrosion scale and a time dependence better than pure diffusion control. This is likely due to the combined protective but nonuniform combination of iron oxides, Cr_2O_3, Al_2O_3, and Ni that resulted in oxide peg formation rather than general uniform corrosion. At 650°C, the corrosion time dependence obtained appears to be linear. Despite this, 601 at this temperature is relatively slow corroding compared to 316H, and the existence of significant outliers at 500hr and 3000hr and the lack of 2000hr and 4000hr datapoints heavily skews the power law fit. For example, assuming the 500hr datapoints were in line with the general downward trend in corrosion rates over time akin to the other temperatures could change the exponent value, B, to around 0.5.

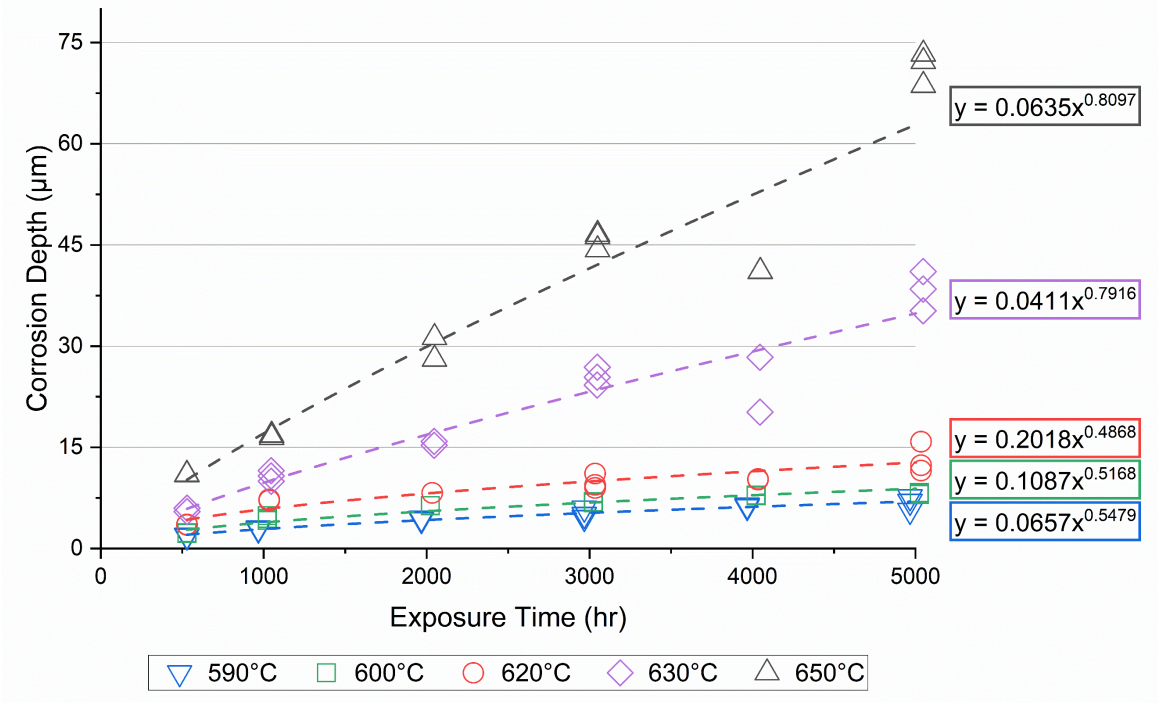

Figure 5.79: Solar Salt corrosion time dependencies obtained for 316H from 590°C to 650°C.

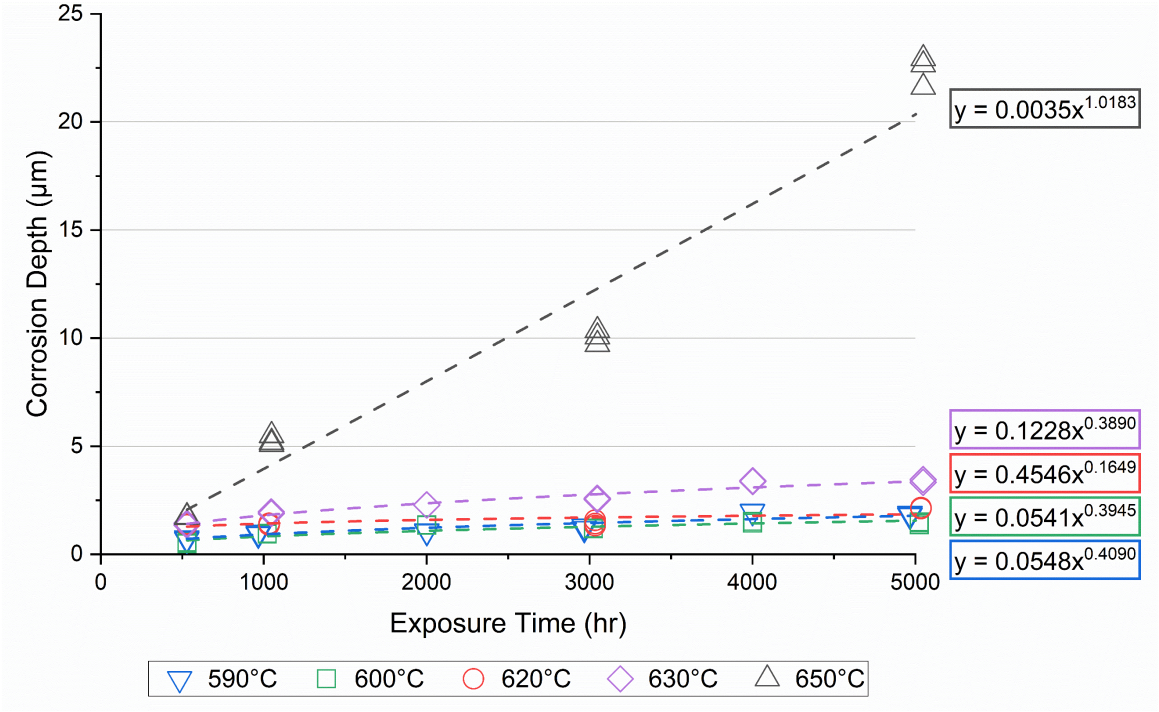

Figure 5.80: Solar Salt corrosion time dependencies obtained for 601 from 590°C to 650°C.

5.4.2. Corrosion Scale Morphology and Evolution

Microscopy has revealed the complex nature of the corrosion scales exhibited by these samples as well as their evolution. In general, the corrosion layer arrangement was consistent between exposure temperature and time conditions just with varying degrees of growth and stability. The outermost layer was $NaFeO_2$, likely formed via reaction of Fe_2O_3 with Na in the nitrate salt. Continuing with the overall layer arrangement, underneath the $NaFeO_2$ layer was an iron oxide layer that significantly grew in thickness as a function of temperature and time. Observations during weight change corrosion measurements and XRD indicate that both Fe_2O_3 and Fe_3O_4 are present in the iron oxide layer, with Fe_2O_3 being towards the surface. However, no clear delineation between the different iron oxide regions is readily apparent through microscopy. The final oxide layer before the bulk metal surface was Cr_2O_3, and Cr denuded / Ni-enriched regions extended within the bulk material. Significant nitriding was observed in the near surface bulk and will be further discussed in Section 5.4.3. For 601, the metal/oxide interface also contained the presence of highly protective Al_2O_3, but not in a complete layer likely due to limited amounts of Al in the alloy relative to other alloying elements.

Beyond the general layer arrangement, significant features were present within the oxide layers. Through-thickness cracks and porosity were common throughout the $NaFeO_2$ and iron oxide layers highlighting the fragility of the corrosion scale. This was made apparent by the significant flaking observed especially for the highest exposure temperature and duration steel samples. Metallic Ni phases were scattered throughout the oxide layers. TEM revealed evidence of intragranular diffusion of Cr and formation of Cr_2O_3 in the near surface Ni-enriched region. This indicates that the metallic Ni phases were likely from the breakdown of the Ni-enriched regions over time, resulting in smaller fragments that become embedded within the oxide layers.

Other metallic phases observed within the oxide layers included Cu and Mo. A metallic Ni-rich phase was also observed on the oxide surface.

Given the high solubility of Cr in nitrate salt, formation of a stable chromia layer indicates inward diffusion of oxygen species at least through the iron oxide layers. The Cr_2O_3 layer generally appears nonporous and likely acts as a significant passivating layer, reducing corrosion rates over time akin to alloys in other oxidizing environments relying on chromia. However, this Cr_2O_3 layer does not offer complete protection due to its precarious relationship with the nitrate salt and the porous nature of the iron oxide layers. As evident in the TEM microscopy, nitrate salt is readily able to find pathways through the iron oxide layers and reach the Cr_2O_3 layer, if not the bulk metal surface. The extent of reaction with and degradation of the Cr_2O_3 layer is likely dependent on the ability of the penetrating nitrate salt to mix with the bulk molten salt. More extreme instances of spallation of the iron oxides would result in unabated contact of the Cr_2O_3 layer with the nitrate salt. It is therefore if and only if the iron oxide layers remain well adherent and limited in porosity that the passivity offered by the chromia layer is able to be taken advantage of. The moment the iron oxide layers spall off, the chromia layer is exposed and quickly reacts to form chromate which subsequently dissolves. Corrosion of the material is then able to continue on fresh metal surface.

This discussion on flaking is also relevant to the aluminide coating samples. Owing to the formation of a complete Al_2O_3 on the coating surface, the aluminide performed exceptionally well when exposed to elevated temperature Solar Salt. Some limited surface flaking was observed on the aluminide samples, but relatively insignificant with respect to the thickness of the coating. However, the stresses involved with sample preparation for microscopy was enough to cause significant cracking of the coating to expose the intermetallic region. Thus, similar to the flaking of the oxide layers exhibited by the steel samples, there is a possibility for significant mechanical degradation of the aluminide coating depending on the application. For example, the materials utilized in nitrate salt applications will likely experience some stresses such as through thermal cycling, molten salt flow, and general maintenance. These brittle and fragile layers can easily be damaged, exposing underlying material and removing their protective nature.

5.4.3. Over-Nitriding of the Bulk Material Surface

The presence of CrN phases in Solar Salt corrosion has been noted in some studies, but it has not been elucidated to such a degree like in this investigation.[30,32,36,86,87] In this study, formation of CrN was observed up to tens of µm within the bulk material surface, and upwards of 80µm along grain boundaries for the highest exposure temperatures and durations. While nitriding is a relatively common treatment to improve the properties of a metal surface, formation of CrN is indicative of over-nitriding which in turn produces a brittle surface layer that reduces mechanical properties.[115,116]

Furthermore, in the steel materials examined in this study, despite the formation of CrN dealloying a ferrite stabilizer, it is evident through EBSD and 4D-STEM that the supersaturation of nitrogen and subsequent formation of CrN caused transformation of the austenite into ferrite. This is likely the result of the strains induced by the formation of CrN within the grain necessitating transformation of the tightly packed FCC arrangement into a more spacious BCC structure. Outside of nitrate salt literature, this has been reported historically through terms such

as “expanded ferrite” or “expanded martensite”, though these terms have been used to describe other microstructures more recently.[117–119] The acicular geometry of the CrN phases indicates it is likely to be specifically the Cr_2N phase. Cr_2N tends to form acicular features oriented with the grain (such as those observed in this study) whereas CrN tends to form more circular clusters.[120]

The over-nitriding of the bulk metal surface indicates that significant diffusion of nitrogen occurs during exposure to elevated temperature nitrate salt which in turn indicates significant generation of nitrogen as a result of nitrate salt decomposition. During lower temperature corrosion in nitrate salt, the amount of nitrogen generated is likely too low and diffusion too slow such that the saturation limit of N in the bulk material is not exceeded to form CrN. As will be discussed in Section 5.4.4., this can have significant implications regarding the mechanism of Solar Salt corrosion at elevated temperatures.

5.4.4. Corrosion Mechanism for 316SS and 601 in Elevated Temperature Solar Salt

The morphology and evolution of the corrosion scales observed in this study indicate significant additions to the corrosion mechanism at these elevated temperatures when compared to lower temperatures. For reference, a simplified schematic for high temperature (≲570°C) corrosion of 316SS in Solar Salt is provided in Figure 5.81 (a more detailed schematic can be found in Figure 1.5 in the Introduction). Incorporating the results from this study, Figure 5.82 shows a schematic describing the corrosion mechanism of 316SS in elevated temperature Solar Salt.

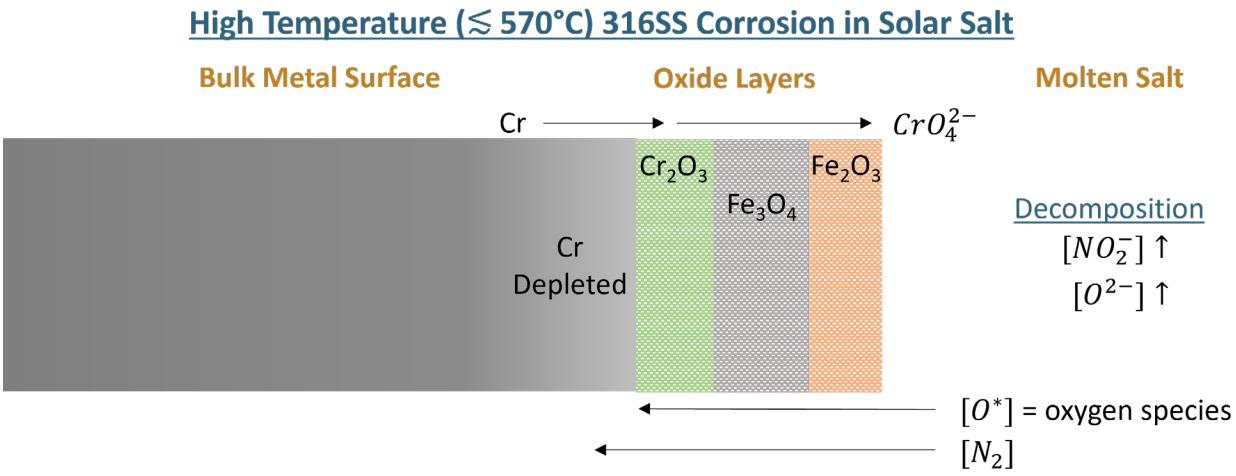

Figure 5.81: Simplified schematic of the corrosion mechanism for 316SS in high temperature (≲570°C) Solar Salt.

A significant addition at these elevated temperatures is the reaction of Fe_2O_3 with Na to form NaFeO2 at the surface of the oxide scale. In general, this and the other oxide layers exhibited significant porosity and through-thickness cracking that limits their ability to impede salt penetration and inward diffusion of corrosive species such as oxygen. Extreme examples of oxide layer flaking would therefore result in unbated access of the nitrate salt to corrode fresh metal surfaces. Similar with the considerations regarding inward diffusion of oxygen, cracking and flaking of the oxide layer would expose the Cr_2O_3 or Cr metal to react with the nitrate salt and form soluble chromate. In cases where the oxide layers remain somewhat protective, it is

evident that inward diffusion of oxygen species reaches at least to the stable Cr_2O_3 layer. Corrosion limiting processes are therefore likely related to the diffusion of alloying elements such as Cr from the bulk material as well as oxygen species to the metal surface/oxide interface.[121]

The increased diffusion of nitrogen relative to oxygen enabled nitriding of the bulk metal surface beyond the oxide layers and especially along grain boundaries with their associated fast diffusion pathways.[122–125] As a result, the formation of CrN and general over-nitriding of the bulk metal surface resulted in the phase transformation of austenite into ferrite. Given the relatively higher diffusivities of elements through ferrite compared to austenite, this phase change enables greater diffusion of species such as Cr to the metal surface/oxide interface to subsequently corrode.[126] In other words, the potentially corrosion-limiting diffusion of alloying elements is able to occur at increased rates beyond that resulting from higher temperatures alone. While significant over-nitriding did occur for the 601 samples, there was no associated phase transformation. In addition to elemental composition considerations, this could explain why the corrosion rates of 316H and the other related 316SS materials were substantially greater than that of 601.

Figure 5.83 shows a schematic describing the corrosion mechanism of 601 in elevated temperature Solar Salt. In general, the corrosion oxide scales for 601 were thin and well-adherent compared to those observed in 316SS. TEM revealed intragranular formation of Cr_2O_3 within the bulk Ni material. Oxide pegs are formed as a result, and corrosion continues over time by carving the Ni-rich inclusions into smaller pieces that embed within the oxide layers. The diffusion of oxygen through these layers result in energetically favorable reaction of the CrN contained within the inclusions to form Cr_2O_3 which in turn further breaks apart the inclusions.[127] This is likely the same mechanism that resulted in the metallic Ni phases observed within the 316H oxide layers.

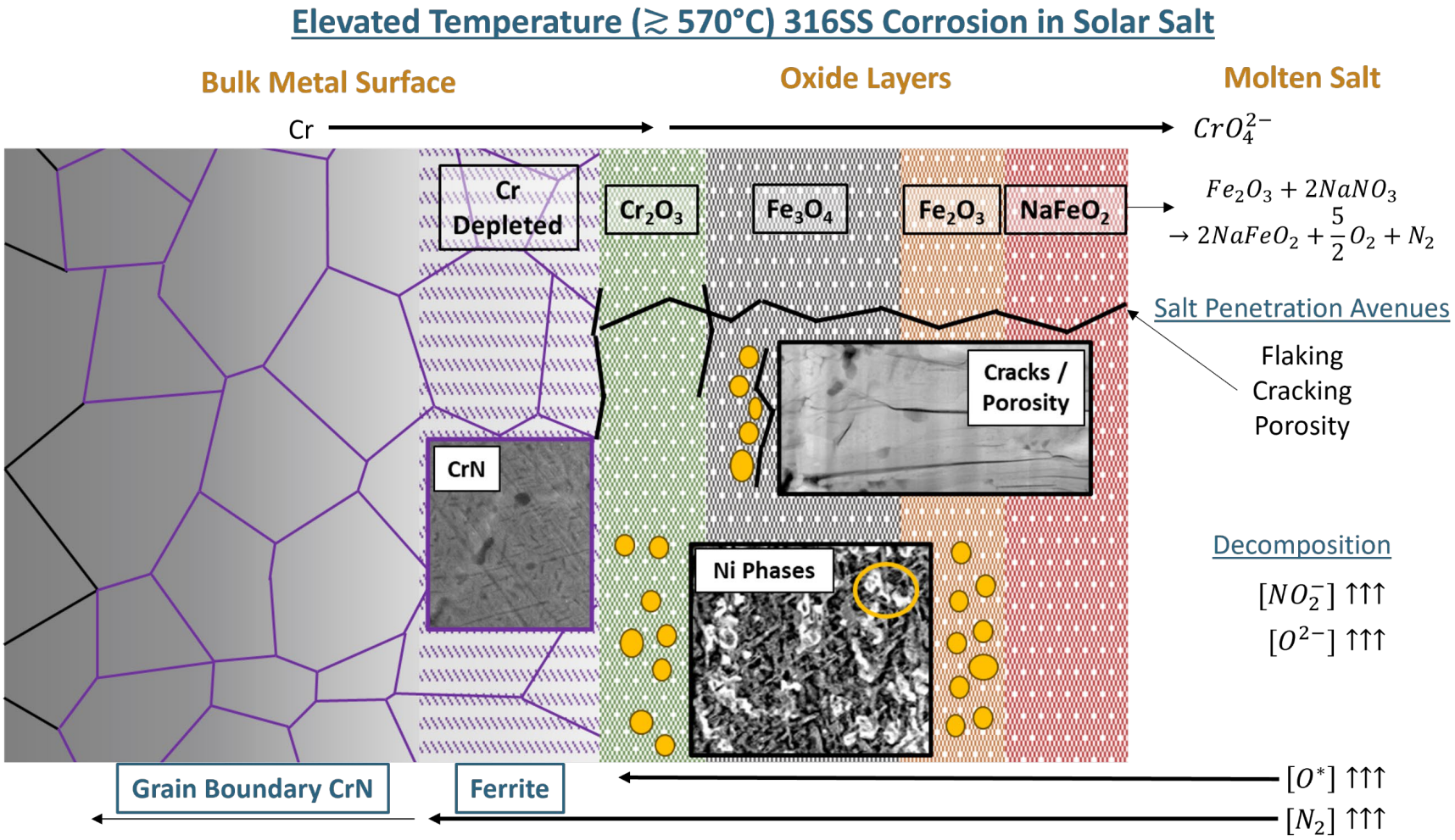

Figure 5.82: Schematic of the corrosion mechanism of 316SS in elevated temperature Solar Salt.

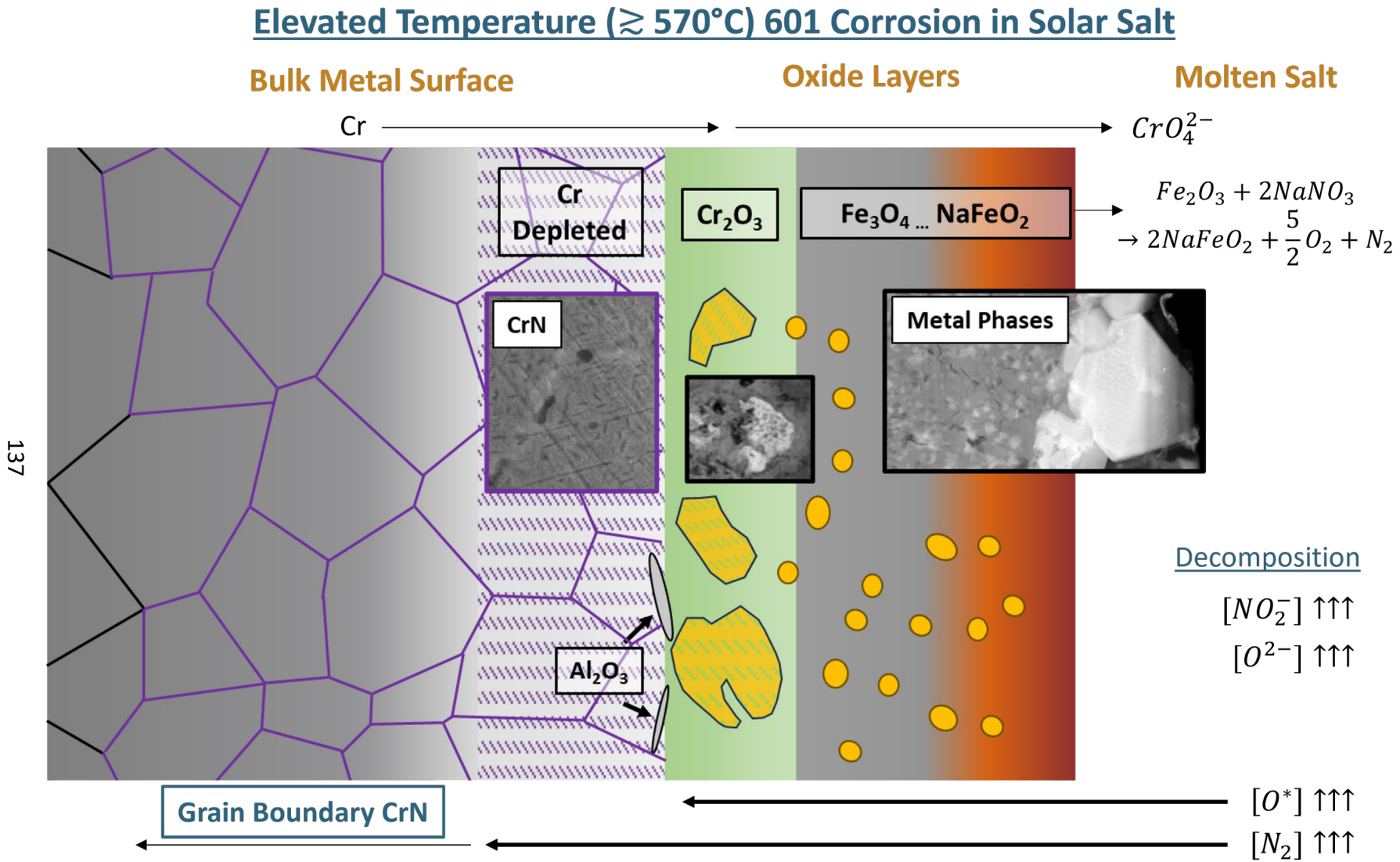

Figure 5.83: Schematic of the corrosion mechanism of 601 in elevated temperature Solar Salt.

5.5. Conclusion

In this study, materials were corroded in elevated temperature Solar Salt ranging from 590°C to 650°C and with exposure times from 500hr up to 5000hr. Corrosion rates were observed to significantly increase as exposure temperatures increased. For instance, the 5000hr corrosion rate for 316H increased an order of magnitude from 12µm/yr at 590°C to 124µm/yr at 650°C. 16-8-2 weld pad material and 316SS autogenous welds were also investigated, revealing corrosion rates on a similar order to the unwelded 316H though with slight differences. 601 exhibited significantly better corrosion performance than the steel samples, with corrosion rates three to eight times lower than 316H across all temperatures and exposure times. 601 at ≤630°C performed better than 316H at 590°C (the lowest temperature examined).

Corrosion rates were observed to decrease as exposure duration increased, suggesting the presence of protective corrosion oxide layers at least to some degree. Corrosion time dependencies for 316H and 601 were extracted from the data and in general revealed power law time dependency exponents significantly less than 1. For 316H at temperatures ≤620°C, the exponent values were around 0.5 indicating a near parabolic time dependence for the corrosion rates. This indicates relatively well-adherent stable corrosion oxide layers that result in diffusion-controlled corrosion. At temperatures ≥630°C, values were around 0.8, indicating reduced protectiveness of the oxide layers which agrees with the significant flaking observed at these temperatures. For 601, the exponent values at temperatures ≤630°C were significantly below 0.5, representing a highly protective corrosion scale likely due to the combined protective nature of iron oxides, Cr_2O_3, Al_2O_3, and Ni that resulted in oxide peg formation rather than general uniform corrosion. The 650°C 601 corrosion data indicated a near linear time dependence, though the confidence in this determination is low due to the relatively significant outliers and limited data at this temperature. Regardless, the corrosion rate of 601 was more than three times lower than 316H at 650°C.

Aluminide coating was also examined and observed to be extremely protective due to the presence of a complete alumina layer, with corrosion rates ≤1µm/yr at 650°C for 5000hr. Significant post-exposure cracking of the coating was observed, however, and like the flaking of the oxide layers observed for the steel samples this could affect the effectiveness of aluminide coatings in long-term applications involving significant stresses.

316SS reference samples exposed for 1000hr during different time intervals revealed increasing corrosivity of the nitrate salt as it aged. This result has significant implications for long-term applications utilizing elevated temperature nitrate salt that may introduce fresh material into the system such as through replacing components. Salt sample analysis corroborated this finding with nitrite and oxide concentrations increasing within the salt over time. Of note, the nitrite concentration (in contrast to the oxide concentration) appeared to struggle to surpass the concentration peak at 1000hr prior to fresh salt addition. This suggests that the process of corroding material drives additional decomposition of the nitrate salt. Cr concentrations were also observed to increase as a function of temperature and time with no signs of plateauing.

Microstructural characterization of the corrosion scales revealed oxide layer arrangements consistent with previous studies, with $NaFeO_2$ on the oxide surface followed by

iron oxides, Cr_2O_3, and Cr (and Mn) depleted regions in the near surface bulk. Metallic phases such as Ni were readily present within the oxide layer, likely remnants of bulk metal material that became embedded over time. 601 also exhibited protective Al_2O_3 phases, but not in complete layers likely due to insufficient Al content relative to other alloying elements. Significant porosity and cracking were observed in the oxide layers especially for the steel samples, enabling the potential for salt penetration deep within the corrosion scale. Complete flaking of oxide layers was also common for the corrosion scale on steels at the highest exposure temperatures and durations, representing the potential for unabated access of the salt to corrode with fresh metal surfaces.

Microscopy also revealed significant over-nitriding within the bulk material surface, with CrN formation occurring to significant depths within the bulk metal surface as well as substantially further into the material along grain boundaries. The extent of the over-nitriding region increased as exposure temperature and time increased. For the steel materials, the formation of CrN phases was associated with transformation of FCC austenite into BCC ferrite. Given the higher diffusivities in ferrite compared to austenite, the phase transformation into ferrite enables increased diffusion of alloying elements such as Cr to the metal-oxide interface which is likely a rate-limiting process for corrosion. Phase transformation did not occur in 601 and along with elemental composition considerations could explain the significantly higher corrosion rates for 316SS compared to 601. In light of these findings, a proposed corrosion mechanism was synthesized for 316SS and 601 in elevated temperature Solar Salt.

Chapter 6 – Overall Dissertation Conclusion

In efforts to use nitrate salts in elevated temperature applications, significant efforts are needed to quantify and understand the increased corrosion rates observed for materials. This dissertation presented a compilation of findings regarding the corrosion performance of steel and nickel alloys in elevated temperature Solar Salt, promoting greater understanding of the underlying corrosion mechanisms involved. The multi-alloy corrosion study in Chapter 3 revealed the widely different corrosion performances in elevated temperature Solar Salt possible for alloys based on their elemental composition. Alloys that were able to form complete alumina layers had the lowest corrosion rates. Despite containing Al and exhibiting Al_2O_3 phases, some AFA alloys failed to produce complete alumina layers which resulted in having corrosion rates on the order of the non-AFA alloys. This indicates that the concentration of Al as an alloying element in an AFA alloy is important relative to the concentration and identity of other alloying elements.

Examining patterns regarding the corrosion rates as well as microscopy of the corrosion scale morphology, the contribution of various alloying elements to corrosion resistance in nitrate salt was assessed. Fe forms the main oxide layers observed across corrosion of the various steel and nickel alloys and likely provides some protection from continued corrosion of the bulk material via reducing the diffusion of corrosive species and alloying elements. However, iron oxide layers were observed throughout the dissertation studies to be relatively thick and exhibit cracking and porosity (if not fully flake off) especially at the highest temperatures investigated. This indicates a limited degree of protectiveness provided by the iron oxide layers.

Cr and Mn content in alloys were deemed to be deleterious to corrosion performance in Solar Salt, owing in large part due to their solubility in nitrate salt. However, Cr is able to form a stable Cr_2O_3 as long as a stable iron oxide layer is present on top. This means that the passivating capability of Cr_2O_3 is present in the corrosion scales but is likely unreliable given the significant flaking and porosity of the iron oxide layers. Ni appeared to be relatively noble in elevated temperature Solar Salt, with corrosion of the other major alloying elements such as Cr and Fe resulting in significant Ni-enriched regions in the bulk metal surface. Over time, corrosion penetrated through bulk metal volumes resulting in Ni-rich phases embedded within the oxide layers. As highlighted above, Al is extremely beneficial to corrosion performance, with a thin Al_2O_3 layer able to completely passivate the material.

Other alloying elements such as Co, Cu, Mo, and Nb were readily observed to form metallic phases either on the oxide surface, within the oxide layers, or near the bulk metal surface. While this indicates relative stability of these elements in elevated temperature Solar Salt compared to Cr and Mn, these metallic phases and their associated elements do not appear to offer any significant benefit to the alloy in terms of corrosion resistance. Corrosion performance is however only one metric for selection of materials, and the best material for a given nitrate salt application will depend on many other factors including but not limited to strength, ductility, machinability, weldability, and cost. Like corrosion resistance, all of these material properties depend on the overall composition of the alloy.

Chapter 4 scoped several temperature steps between 570°C and 650°C enabling more sensitive detection of corrosion temperature dependencies in elevated temperature Solar Salt.

As expected, corrosion rates of 316SS were observed to significantly increase as temperature increased. More importantly, an inflection point in the rate of increase in corrosion rates was discerned at around 610°C through Arrhenius analysis. While Arrhenius analysis is unable to identify reaction processes associated with the extracted activation energies, the activation energies obtained were in line with diffusion of species such as oxygen for temperatures ≤610°C and alloying elements such as Cr for temperatures ≥610°C. If these processes are in fact the rate-controlling processes for corrosion in Solar Salt, this would indicate that at temperatures ≤610°C, the rate of nitrate salt decomposition is low enough such that the generation and diffusion of oxide species limits the corrosion rate of 316SS. This would also indicate that at temperatures ≥610°C, the amount of oxide species generated through nitrate salt decomposition is not fully limiting anymore, but rather it is the availability of alloying elements at the reaction interface.

This potential change in rate limiting process in corrosion has significant implications in context with the results from the Chapter 5 long-term corrosion study. A downward trend in the corrosion rates as exposure time increased was observed for all the materials examined, indicating that the corrosion scales exhibited by the material were protective to some degree. Alloy 601 exhibited significantly better corrosion performance than the steel samples, with corrosion rates three to eight times lower than 316H across all temperatures and exposure times. For example, 601 at ≤630°C performed better than 316H at 590°C (the lowest temperature examined). Regardless, a nonlinear corrosion time dependency was obtained for both materials, suggesting that as long as their respective oxide layers remained stable on the material surface (as opposed to flaking), diffusion of species is likely limited and further corrosion reduced.

The presence of a stable Cr_2O_3 layer as the innermost oxide layer indicates inward diffusion of oxygen species at least to near the metal-oxide interface. Nitrogen produced from nitrate salt decomposition was able to diffuse farther and into the metal surface. Microscopy revealed substantial over-nitriding of the bulk metal surface with the formation of CrN phases. For the steel materials, associated with this over-nitriding was the phase transformation of FCC austenite into BCC ferrite. Higher diffusivities in ferrite suggest that this phase transformation acts as a mechanism for increased corrosion for steel alloys through augmented diffusion of alloying elements such as Cr to the metal-oxide interface. This along with elemental composition considerations can explain why the corrosion rates for 316H and the other steel materials were substantially higher than that of 601.

Analysis of nitrate salt samples implied that the process of metal corrosion itself fosters increased decomposition of the nitrate salt due to the consumption of decomposition products. Increases in oxide concentration over time indicated that the nitrate salt became more corrosive to fresh samples as it aged. This was confirmed by corrosion rate data from 316-REF samples inserted at different times, which showed significant increases in 1000hr corrosion rates over time at the highest temperatures. This has significant implications for long-term applications utilizing elevated temperature nitrate salt, as fresh material may be introduced into the system during operation.

While significant corrosion data was obtained for a wide range of materials, exposure temperatures, and exposure times, the results in this dissertation highlight the need for additional areas of investigation. The potential galvanic effects observed for the N60 data in

Chapter 3 motivate targeted studies on galvanic corrosion and other effects in nitrate salt. Given that many different materials are likely to be used in a nitrate salt application, it is important to determine whether or not certain material combinations are compatible, especially if different materials are designed to be in intimate contact. Further investigations targeting the rate-controlling steps in elevated temperature nitrate salt corrosion are needed to ascertain the processes truly associated with the activation energies obtained through Arrhenius analysis in Chapter 4.

Nitrate salt aging effects revealed in Chapter 5 suggest exploration into potential chemistry control and monitoring methods. This includes study into the effects of changing gas space pressures and compositions, salt additions, and salt impurities. The flaking nature of oxide layers as well as the brittle nature of the aluminide coating urges examination into the effect of stresses on the stability of the corrosion scales and coatings. Concentrated solar plant applications demand consistent thermal cycling due to day/night cycles. Intermediate loops and heat storage systems for nuclear power plants prescribe thermal gradients and potentially significant flow stresses. These highlighted additional studies represent just some of the many variables in the overall parameter space that are not probed by the static corrosion tests presented in this dissertation. Further investigation is necessary for the continued development of materials suitable for elevated temperature nitrate salt applications.

References

1. Zinkle, S. J. & Was, G. S. Materials challenges in nuclear energy. *Acta Mater.* **61**, 735–758 (2013).
2. Forsberg, C., Sabharwall, P. & Sowder, A. *Separating Nuclear Reactors from the Power Block with Heat Storage: A New Power Plant Design Paradigm*. https://www.osti.gov/biblio/1768046 (2020) doi:10.2172/1768046.
3. Forsberg, C. Separating Nuclear Reactors from the Power Block with Heat Storage to Improve Economics with Dispatchable Heat and Electricity. *Nucl. Technol.* **208**, 688–710 (2022).
4. Caraballo, A., Galán-Casado, S., Caballero, Á. & Serena, S. Molten Salts for Sensible Thermal Energy Storage: A Review and an Energy Performance Analysis. *Energies* **14**, 1197 (2021).
5. Locatelli, G., Mancini, M. & Todeschini, N. Generation IV nuclear reactors: Current status and future prospects. *Energy Policy* **61**, 1503–1520 (2013).
6. Andreades, C. *et al.* Design Summary of the Mark-I Pebble-Bed, Fluoride Salt–Cooled, High-Temperature Reactor Commercial Power Plant. *Nucl. Technol.* **195**, 223–238 (2016).
7. Blandford, E. *et al.* Kairos power thermal hydraulics research and development. *Nucl. Eng. Des.* **364**, 110636 (2020).
8. Bryan, J., Meek, A., Dana, S., Islam Sakir, M. S. & Wang, H. Modeling and design optimization of carbon-free hybrid energy systems with thermal and hydrogen storage. *Int. J. Hydrog. Energy* (2023) doi:10.1016/j.ijhydene.2023.03.135.
9. Forsberg, C., Zheng, G. (Tony), Ballinger, R. G. & Lam, S. T. Fusion Blankets and Fluoride-Salt-Cooled High-Temperature Reactors with Flibe Salt Coolant: Common Challenges, Tritium Control, and Opportunities for Synergistic Development Strategies Between Fission, Fusion, and Solar Salt Technologies. *Nucl. Technol.* **206**, 1778–1801 (2020).
10. Soravilla, J. *et al.* GRIDRESERVE, TECHNICAL FEASIBILITY AND ECONOMICS OF A HYBRID SMALL MODULAR REACTOR AND THERMAL ENERGY STORAGE TO ENABLE NUCLEAR AS PEAKING PLANT.
11. Carling, R. W. & Mar, R. W. *Industrial use of molten nitrate/nitrite salts*. https://www.osti.gov/biblio/5257229 (1981) doi:10.2172/5257229.
12. Lovering, D. G. Molten salt technology. (1982).
13. Bohlmann, E. G. *HEAT TRANSFER SALT FOR HIGH TEMPERATURE STEAM GENERATION.* https://www.osti.gov/biblio/4595737 (1972) doi:10.2172/4595737.
14. Zhang, X., Tian, J., Xu, K. & Gao, Y. Thermodynamic evaluation of phase equilibria in NaNO3-KNO3 system. *J. Phase Equilibria* **24**, 441–446 (2003).
15. Ricker, R., Datta, P., Du, H. & Burnell-Gray, J. Corrosion of Intermetallics. in vol. 13 490–512 (2005).
16. Sieradzki, K. & Newman, R. C. A Percolation Model for Passivation in Stainless Steels. *J. Electrochem. Soc.* **133**, 1979 (1986).
17. Olsson, C.-O. A. & Landolt, D. Passive films on stainless steels—chemistry, structure and growth. *Electrochimica Acta* **48**, 1093–1104 (2003).
18. Choi, Y.-S., Nesic, S. & Young, D. Effect of Impurities on the Corrosion Behavior of CO2 Transmission Pipeline Steel in Supercritical CO2−Water Environments. *Environ. Sci. Technol.* **44**, 9233–9238 (2010).

19. D'Souza, B., Zhuo, W., Yang, Q., Leong, A. & Zhang, J. Impurity driven corrosion behavior of HAYNES® 230® alloy in molten chloride Salt. *Corros. Sci.* **187**, 109483 (2021).
20. Tsutsumi, Y. *et al.* Effect of Impurity Elements on Localized Corrosion of Zirconium in Chloride Containing Environment. *J. Electrochem. Soc.* **167**, 141507 (2020).
21. Guo, S., Zhang, J., Wu, W. & Zhou, W. Corrosion in the molten fluoride and chloride salts and materials development for nuclear applications. *Prog. Mater. Sci.* **97**, 448–487 (2018).
22. Raiman, S. S. & Lee, S. Aggregation and data analysis of corrosion studies in molten chloride and fluoride salts. *J. Nucl. Mater.* **511**, 523–535 (2018).
23. Covino, J. *et al. Corrosion in a temperature gradient*. https://www.osti.gov/biblio/899606 (2003).
24. Brough, B. J. & Kerridge, D. H. Reactions of Metals in Fused Nitrate Eutectic. *Inorg. Chem.* **4**, 1353–1356 (1965).
25. Brough, B. J., Kerridge, D. H. & Tariq, S. A. Molten lithium-potassium nitrate eutectic: The reactions of some compounds of chromium. *Inorganica Chim. Acta* **1**, 267–270 (1967).
26. Afanasiev, P. & Kerridge, D. H. Reactivity of V2O5, MoO3 and WO3 in molten KNO3, studied by mass spectrometry. *J. Alloys Compd.* **322**, 97–102 (2001).
27. Oryshich, I. V. & Kostyrko, O. S. Infleuence of molybdenum, tungsten, and cobalt on the corrosion of high-temperature strength nickel alloys in molten salts. *Met. Sci. Heat Treat.* **27**, 740–746 (1985).
28. Brough, B. J., Habboush, D. A. & Kerridge, D. H. The reaction of manganese dioxide with molten lithium-potassium nitrate eutectic. *J. Inorg. Nucl. Chem.* **30**, 2870–2872 (1968).
29. Smyrl, W. H. *Corrosion in molten salts used for solar thermal storage applications*. https://www.osti.gov/biblio/6273601 (1978).
30. Audigié, P. *et al.* High temperature molten salt corrosion behavior of aluminide and nickel-aluminide coatings for heat storage in concentrated solar power plants. *Surf. Coat. Technol.* **349**, 1148–1157 (2018).
31. Baraka, A., Abdel-Rohman, A. I. & Hosary, A. A. E. Corrosion of Mild Steel in Molten Sodium Nitrate–Potassium Nitrate Eutectic. *Br. Corros. J.* **11**, 44–46 (1976).
32. Boehme, D. R. & Bradshaw, R. W. *X-ray-diffraction analysis of corrosion products of Fe-Ni-Cr alloys formed in molten-nitrate salts*. https://www.osti.gov/biblio/6017111 (1983) doi:10.2172/6017111.
33. Bonk, A. *et al.* Influence of different atmospheres on molten salt chemistry and its effect on steel corrosion. *AIP Conf. Proc.* **2033**, 090003 (2018).
34. Bonk, A., Rückle, D., Kaesche, S., Braun, M. & Bauer, T. Impact of Solar Salt aging on corrosion of martensitic and austenitic steel for concentrating solar power plants. *Sol. Energy Mater. Sol. Cells* **203**, 110162 (2019).
35. Bradshaw, R. W. *Corrosion of 304SS by molten NaNO/sub 3/-KNO/sub 3/ in a thermal convection loop*. https://www.osti.gov/biblio/6624736 (1980) doi:10.2172/6624736.
36. Bradshaw, R. W. Thermal Convection Loop Study of the Corrosion of Incoloy 800 in Molten NaNO3-KNO3. *Corrosion* **43**, 173–178 (1987).
37. Bradshaw, R. W. & Goods, S. H. *Corrosion of Alloys and Metals by Molten Nitrates*. https://www.osti.gov/biblio/1545803 (2001) doi:10.2172/1545803.

38. Bradshaw, R. W. & Goods, S. H. *Corrosion resistance of stainless steels during thermal cycling in alkali nitrate molten salts.* https://www.osti.gov/biblio/1020472 (2001) doi:10.2172/1020472.
39. Soleimani Dorcheh, A. & Galetz, M. C. Slurry aluminizing: A solution for molten nitrate salt corrosion in concentrated solar power plants. *Sol. Energy Mater. Sol. Cells* **146**, 8–15 (2016).
40. Elbakhshwan, M., Lee, D. H. & Anderson, M. Corrosion resistance of high nickel alloys in solar salt at 600 °C for up to 4000 h. *Sol. Energy Mater. Sol. Cells* **245**, 111837 (2022).
41. Fernández, A. G., Galleguillos, H. & Pérez, F. J. Thermal influence in corrosion properties of Chilean solar nitrates. *Sol. Energy* **109**, 125–134 (2014).
42. Fernández, A. G., Cortes, M., Fuentealba, E. & Pérez, F. J. Corrosion properties of a ternary nitrate/nitrite molten salt in concentrated solar technology. *Renew. Energy* **80**, 177–183 (2015).
43. García-Martín, G., Lasanta, M. I., Encinas-Sánchez, V., de Miguel, M. T. & Pérez, F. J. Evaluation of corrosion resistance of A516 Steel in a molten nitrate salt mixture using a pilot plant facility for application in CSP plants. *Sol. Energy Mater. Sol. Cells* **161**, 226–231 (2017).
44. Gomes, A. *et al.* High-temperature corrosion performance of austenitic stainless steels type AISI 316L and AISI 321H, in molten Solar Salt. *Sol. Energy* **177**, 408–419 (2019).
45. Gomez-Guzman, N. B. *et al.* Behavior of Ni20Cr Alloy in Molten Nitrate Salts. *Int. J. Mol. Sci.* **23**, 7895 (2022).
46. Kramer, C. M., Smyrl, W. H. & Estill, W. B. Corrosion of Fe alloys in NaNO3-KNO3-NaNO2 at 823 K. *J. Mater. Energy Syst.* **1**, 59–65 (1980).
47. Kruizenga, A. & Gill, D. Corrosion of Iron Stainless Steels in Molten Nitrate Salt. *Energy Procedia* **49**, 878–887 (2014).
48. Kruizenga, A. M., Gill, D. D. & LaFord, M. E. *Corrosion of high temperature alloys in solar salt at 400, 500, and 680ÀC.* https://www.osti.gov/biblio/1104752 (2013) doi:10.2172/1104752.
49. Kruizenga, A. M., Gill, D. D. & LaFord, M. E. *Materials corrosion of high temperature alloys immersed in 600C binary nitrate salt.* https://www.osti.gov/biblio/1088090 (2013) doi:10.2172/1088090.
50. Liu, Q. *et al.* Effect of thermal cycling on the corrosion behaviour of stainless steels and Ni-based alloys in molten salts under air and argon. *Sol. Energy* **238**, 248–257 (2022).
51. McConohy, G. & Kruizenga, A. Molten nitrate salts at 600 and 680°C: Thermophysical property changes and corrosion of high-temperature nickel alloys. *Sol. Energy* **103**, 242–252 (2014).
52. Prieto, C., Ruiz-Cabañas, F. J., Madina, V., Fernández, A. I. & Cabeza, L. F. Corrosion performance of alloy 800H and alloy 625 for potential use as molten salts solar receiver materials in concentrating solar power tower plants. *J. Energy Storage* **55**, 105824 (2022).
53. Singh, M. P., Basu, B. & Chattopadhyay, K. Probing High-Temperature Electrochemical Corrosion of 316 Stainless Steel in Molten Nitrate Salt for Concentrated Solar Power Plants. *J. Mater. Eng. Perform.* **31**, 4902–4908 (2022).

54. Summers, K. L. & Chidambaram, D. Corrosion Behavior of Structural Materials for Potential Use in Nitrate Salts Based Solar Thermal Power Plants. *J. Electrochem. Soc.* **164**, H5357 (2017).
55. Sutter, F. *et al.* Dynamic corrosion testing of metals in solar salt for concentrated solar power. *Sol. Energy Mater. Sol. Cells* **232**, 111331 (2021).
56. Zhai, W. *et al.* Study on corrosion of metal materials in nitrate molten salts. *AIP Conf. Proc.* **1794**, 020016 (2017).
57. Zhang, X., Zhang, C., Wu, Y. & Lu, Y. Experimental research of high temperature dynamic corrosion characteristic of stainless steels in nitrate eutectic molten salt. *Sol. Energy* **209**, 618–627 (2020).
58. Moore, R. C., Siegel, N. P., Kolb, G. J., Vernon, M. E. & Ho, C. K. *Design considerations for concentrating solar power tower systems employing molten salt.* https://www.osti.gov/biblio/1008140 (2010) doi:10.2172/1008140.
59. Dorcheh, A. S., Durham, R. N. & Galetz, M. C. High temperature corrosion in molten solar salt: The role of chloride impurities. *Mater. Corros.* **68**, 943–951 (2017).
60. Goods, S. H. & Bradshaw, R. W. Corrosion of stainless steels and carbon steel by molten mixtures of commercial nitrate salts. *J. Mater. Eng. Perform.* **13**, 78–87 (2004).
61. Fernández, Á. G. *et al.* Compatibility of alumina forming alloys with LiNO3-containing molten salts for solar thermal plants. *J. Energy Storage* **48**, 103988 (2022).
62. Slusser, J. W., Titcomb, J. B., Heffelfinger, M. T. & Dunbobbin, B. R. Corrosion in Molten Nitrate-Nitrite Salts. *JOM* **37**, 24–27 (1985).
63. Tortorelli, P. F., Bishop, P. S. & DiStefano, J. R. *Selection of corrosion-resistant materials for use in molten nitrate salts*. https://www.osti.gov/biblio/5236321 (1989) doi:10.2172/5236321.
64. Brumm, M. W. & Grabke, H. J. The oxidation behaviour of NiAl-I. Phase transformations in the alumina scale during oxidation of NiAl and NiAl-Cr alloys. *Corros. Sci.* **33**, 1677–1690 (1992).
65. Yamamoto, Y. *et al.* Creep-Resistant, Al2O3-Forming Austenitic Stainless Steels. *Science* **316**, 433–436 (2007).
66. Brady, M. P. *et al.* The development of alumina-forming austenitic stainless steels for high-temperature structural use. *JOM* **60**, 12–18 (2008).
67. Muralidharan, G. *et al. Development of Cast Alumina-forming Austenitic Stainless Steel Alloys for use in High Temperature Process Environments*. https://www.osti.gov/biblio/1215573 (2015).
68. Dong, J., Sun, Y. & He, F. Formation mechanism of multilayer aluminide coating on 316L stainless steel by low-temperature pack cementation. *Surf. Coat. Technol.* **375**, 833–838 (2019).
69. Carling, R. W., Bradshaw, R. W. & Mar, R. W. Protective coatings for alloys in contact with molten drawsalt (NaNO3-KNO3). *J. Mater. Energy Syst.* **4**, 229–233 (1983).
70. Turchi, C. S., Vidal, J. & Bauer, M. Molten salt power towers operating at 600–650 °C: Salt selection and cost benefits. *Sol. Energy* **164**, 38–46 (2018).
71. Nagelberg, A. S. & Mar, R. W. *Thermochemistry of Nitrate Salts*. (1982).
72. Freeman, E. S. The Kinetics of the Thermal Decomposition of Potassium Nitrate and of the Reaction between Potassium Nitrite and Oxygen1a. *J. Am. Chem. Soc.* **79**, 838–842 (1957).

73. Sötz, V. A., Bonk, A., Forstner, J. & Bauer, T. Microkinetics of the reaction NO3-⇌NO2-+0.5 O2 in molten sodium nitrate and potassium nitrate salt. *Thermochim. Acta* **678**, 178301 (2019).
74. Sötz, V. A., Bonk, A., Steinbrecher, J. & Bauer, T. Defined purge gas composition stabilizes molten nitrate salt - Experimental prove and thermodynamic calculations. *Sol. Energy* **211**, 453–462 (2020).
75. Paniccia, F. & Zambonin, P. G. Thermodynamics of the systems NO–3= NO–2+½O2 and NO–3+½O2–2= NO–2+ O–2 in molten alkali nitrates. *J. Chem. Soc. Faraday Trans. 1 Phys. Chem. Condens. Phases* **72**, 1512–1518 (1976).
76. Bauer, T., Laing, D. & Tamme, R. Characterization of Sodium Nitrate as Phase Change Material. *Int. J. Thermophys.* **33**, 91–104 (2012).
77. Bauer, T. *et al.* Material aspects of Solar Salt for sensible heat storage. *Appl. Energy* **111**, 1114–1119 (2013).
78. Bonk, A., Braun, M., Sötz, V. A. & Bauer, T. Solar Salt – Pushing an old material for energy storage to a new limit. *Appl. Energy* **262**, 114535 (2020).
79. White, S. H. & Twardoch, U. M. Study of the interactions of molten sodium nitrate-potassium nitrate 50 mol % mixture with water vapor and carbon dioxide in air. Final report, June 2, 1980-June 30, 1981. *UNT Digital Library* https://digital.library.unt.edu/ark:/67531/metadc1053609/ (1981) doi:10.2172/5194427.
80. Kramer, C. M., Munir, Z. A. & Volponi, J. V. Screening tests of sodium nitrate and potassium nitrate decomposition. *Sol. Energy* **29**, 437–439 (1982).
81. Desimoni, E., Paniccia, F. & Zambonin, P. G. Solubility and detection (down to 30 p.p.b.) of oxygen in molten alkali nitrates. *J. Electroanal. Chem. Interfacial Electrochem.* **38**, 373–379 (1972).
82. Zambonin, P. G., Cardetta, V. L. & Signorile, G. Solubility and detection of water in the (Na,K)NO3 eutectic melt. *J. Electroanal. Chem. Interfacial Electrochem.* **28**, 237–243 (1970).
83. Marchiano, S. L. & Arvía, A. J. Potential/pO2− diagrams of iron, cobalt and nickel in molten sodium nitrite. *Electrochimica Acta* **17**, 861–871 (1972).
84. Osteryoung, R. A. *Corrosion of alloys in molten nitrates. First annual report, May 5, 1980-June 30, 1981*. https://www.osti.gov/biblio/6719273 (1982) doi:10.2172/6719273.
85. Bradshaw, R. W. *Thermal-convection-loop corrosion tests of 316SS and IN800 in molten nitrate salts*. https://www.osti.gov/biblio/5353081 (1982) doi:10.2172/5353081.
86. Bradshaw, R. W. *Oxidation and chromium depletion of Alloy 800 and 316SS by molten NaNO/sub 3/-KNO/sub 3/ at temperatures above 600/degree/C*. https://www.osti.gov/biblio/5103265 (1987) doi:10.2172/5103265.
87. Soleimani Dorcheh, A., Durham, R. N. & Galetz, M. C. Corrosion behavior of stainless and low-chromium steels and IN625 in molten nitrate salts at 600°C. *Sol. Energy Mater. Sol. Cells* **144**, 109–116 (2016).
88. Goods, S. H., Bradshaw, R. W., Prairie, M. R. & Chavez, J. M. *Corrosion of stainless and carbon steels in molten mixtures of industrial nitrates*. https://www.osti.gov/biblio/10141843 (1994) doi:10.2172/10141843.

89. Tortorelli, P. F. & DeVan, J. H. *Thermal-convection-loop study of the corrosion of Fe-Ni-Cr alloys by molten NaNo/sub 3/-KNO/sub 3/*. https://www.osti.gov/biblio/6630235 (1982) doi:10.2172/6630235.
90. Trent, M. C., Goods, S. H. & Bradshaw, R. W. Comparison of corrosion performance of grade 316 and grade 347H stainless steels in molten nitrate salt. *AIP Conf. Proc.* **1734**, 160017 (2016).
91. Winters, W. S., Bradshaw, R. W. & Hart, F. W. *Design and operation of thermal convection loops for corrosion testing in molten NaNO/sub 3/ - KNO/sub 3/*. https://www.osti.gov/biblio/5323425 (1980) doi:10.2172/5323425.
92. Malaret, F. & Yang, X.-S. Exact calculation of corrosion rates by the weight-loss method. *Exp. Results* **3**, e13 (2022).
93. Li, X., Cong, H., Gui, F., Brossia, C. S. & Frankel, G. S. Development of Liquid-Air-Interface Corrosion of Steel in Nitrate Solutions. *Corrosion* **70**, 230–246 (2013).
94. Yang, M. & Kainuma, S. Investigation of steel corrosion near the air–liquid interface in NaCl solution and soil environment. *Corros. Eng. Sci. Technol.* **56**, 690–702 (2021).
95. Xia, D.-H. *et al.* A novel approach used to study the corrosion susceptibility of metallic materials at a dynamic seawater/air interface. *Corros. Commun.* **6**, 62–66 (2022).
96. Mennicke, C., He, M.-Y., Clarke, D. R. & Smith, J. S. The role of secondary oxide inclusions ("pegs") on the spalling resistance of oxide films. *Acta Mater.* **48**, 2941–2949 (2000).
97. Yang, L. *et al.* Characteristics of oxide pegs in Ti- and Y-doped CoNiCrAl alloys at 1150 °C. *Rare Met.* **40**, 2059–2064 (2021).
98. Hubberstey, P., Sample, T. & Terlain, A. The Stability of Tritium Permeation Barriers and the Self-Healing Capability of Aluminide Coatings in Liquid Pb-17Li. *Fusion Technol.* **28**, 1194–1199 (1995).
99. Eduok, U., Ohaeri, E. & Szpunar, J. 8 - Self-healing composite coatings with protective and anticorrosion potentials: classification by healing mechanism. in *Self-Healing Composite Materials* (eds. Khan, A., Jawaid, M., Raveendran, S. N. & Ahmed Asiri, A. M.) 123–162 (Woodhead Publishing, 2020). doi:10.1016/B978-0-12-817354-1.00008-9.
100. Saburi, T., Murata, H., Suzuki, T., Fujii, Y. & Kiuchi, K. Oxygen Plasma Interactions with Molybdenum: Formation of Volatile Molybdenum Oxides. プラズマ・核融合学会誌 **78**, 3–4 (2002).
101. Ikeda, Y., Ito, H., Mizuno, T., Amioka, K. & Matsumoto, G. Sublimation behavior of molybdenum oxides. *High Temp Sci U. S.* **16:I**, (1983).
102. Wang, L., Li, M.-C., Xue, Z.-L., Zhang, G.-H. & Huang, A. Sublimation Behavior of Industrial Grade Molybdenum Trioxide. *Trans. Indian Inst. Met.* **74**, 1469–1477 (2021).
103. Blackburn, P. E., Hoch, M. & Johnston, H. L. The Vaporization of Molybdenum and Tungsten Oxides. *J. Phys. Chem.* **62**, 769–773 (1958).
104. Wu, C. *et al.* High-Temperature Reaction Mechanism of Molybdenum Metal in Direct Coal Liquefaction Residue. *Catalysts* **12**, 926 (2022).
105. Giletti, B. J. & Hess, K. C. Oxygen diffusion in magnetite. *Earth Planet. Sci. Lett.* **89**, 115–122 (1988).
106. Castle, J. E. & Surman, P. L. Self-diffusion of oxygen in magnetite. Effect of anion vacancy concentration and cation distribution. *J. Phys. Chem.* **73**, 632–634 (1969).

107. Jeon, B., Overmeere, Q. V., Duin, A. C. T. van & Ramanathan, S. Nanoscale oxidation and complex oxide growth on single crystal iron surfaces and external electric field effects. *Phys. Chem. Chem. Phys.* **15**, 1821–1830 (2013).
108. Korablev, G. A. & Zaikov, G. E. Calculation of activation energy of diffusion and self-diffusion. *Oxid. Commun.* **32**, 1–12 (2009).
109. Ping, S. B., Xie, F., Wang, R. K., Zheng, Z. J. & Gao, Y. Diffusion Kinetics of Chromium in a Novel Super304H Stainless Steel. *High Temp. Mater. Process.* **36**, 175–181 (2017).
110. Miley, H. A. Theory of Oxidation and Tarnishing of Metals: I . The Linear, Parabolic and Logarithmic Laws. *Trans. Electrochem. Soc.* **81**, 391 (1942).
111. Ophus, C. Four-Dimensional Scanning Transmission Electron Microscopy (4D-STEM): From Scanning Nanodiffraction to Ptychography and Beyond. *Microsc. Microanal.* **25**, 563–582 (2019).
112. Keiser, J. R., DeVan, J. H. & Lawrence, E. J. Compatibility of molten salts with type 316 stainless steel and lithium. *J. Nucl. Mater.* **85–86**, 295–298 (1979).
113. Kerridge, D. H. & Tariq, S. A. Molten sodium nitrite-potassium nitrite eutectic: the reactions of some compounds of chromium. *Inorganica Chim. Acta* **3**, 667–670 (1969).
114. Eweka, E. I. & Kerridge, D. H. Molten sodium nitrite-sodium nitrate-potassium nitrate eutectic: the reactions and spectra of chromium(III) chloride and chromium(VI) compounds. *Thermochim. Acta* **262**, 95–100 (1995).
115. Torbati-Sarraf, H. & Poursaee, A. 9 - Influence of the microstructure of the carbon steel reinforcing bar on its corrosion in concrete. in *Corrosion of Steel in Concrete Structures (Second Edition)* (ed. Poursaee, A.) 187–197 (Woodhead Publishing, 2023). doi:10.1016/B978-0-12-821840-2.00011-0.
116. Dong, H. S-phase surface engineering of Fe-Cr, Co-Cr and Ni-Cr alloys. *Int. Mater. Rev.* **55**, 65–98 (2010).
117. Borgioli, F. The “Expanded” Phases in the Low-Temperature Treated Stainless Steels: A Review. *Metals* **12**, 331 (2022).
118. Blawert, C., Mordike, B. L., Jirásková, Y. & Schneeweiss, O. Structure and composition of expanded austenite produced by nitrogen plasma immersion ion implantation of stainless steels X6CrNiTi1810 and X2CrNiMoN2253. *Surf. Coat. Technol.* **116–119**, 189–198 (1999).
119. Samandi, M. *et al.* Microstructure, corrosion and tribological behaviour of plasma immersion ion-implanted austenitic stainless steel. *Surf. Coat. Technol.* **59**, 261–266 (1993).
120. Holländer Pettersson, N., Lindell, D., Lindberg, F. & Borgenstam, A. Formation of Chromium Nitride and Intragranular Austenite in a Super Duplex Stainless Steel. *Metall. Mater. Trans. A* **50**, 5594–5601 (2019).
121. Sabioni, A. C. S. *et al.* About the Role of Chromium and Oxygen Ion Diffusion on the Growth Mechanism of Oxidation Films of the AISI 304 Austenitic Stainless Steel. *Oxid. Met.* **78**, 211–220 (2012).
122. Christiansen, T. L. & Somers, M. A. J. Determination of the concentration dependent diffusion coefficient of nitrogen in expanded austenite. *Int. J. Mater. Res.* **99**, 999–1005 (2008).

123. Takada, J., Yamamoto, S., Kikuchi, S. & Adachi, M. Determination of diffusion coefficient of oxygen in γ-iron from measurements of internal oxidation in Fe-Al alloys. *Metall. Trans. A* **17**, 221–229 (1986).
124. Takada, J. & Adachi, M. Determination of diffusion coefficient of oxygen in α-iron from internal oxidation measurements in Fe-Si alloys. *J. Mater. Sci.* **21**, 2133–2137 (1986).
125. Mizouchi, M., Yamazaki, Y., Iijima, Y. & Arioka, K. Low Temperature Grain Boundary Diffusion of Chromium in SUS316 and 316L Stainless Steels. *Mater. Trans.* **45**, 2945–2950 (2004).
126. Tőkei, Z., Hennesen, K., Viefhaus, H. & Grabke, H. J. Diffusion of chromium in ferritic and austenitic 9–20 wt-%chromium steels. *Mater. Sci. Technol.* **16**, 1129–1138 (2000).
127. Sharafat, S., Ghoniem, N. & Zinkle, S. Thermodynamic stability of oxide, nitride, and carbide coating materials in liquid Sn–25Li. *J. Nucl. Mater.* **329–333**, 1429–1433 (2004).